EVALUATION OF FUEL ROD PERFORMANCE IN MAINE YANKEE CORE I

TASK C

EPRI NP-218
(Research Project 586-1)

Final Report

November 1976

Prepared by

Combustion Engineering, Inc.
C-E Power System
1000 Prospect Hill Road
Windsor, Connecticut 06095

Principal Investigators
N. Fuhrman
V. Pasupathi
D. B. Scott
S. M. Temple
S. R. Pati
T. E. Hollowell

Prepared for

Electric Power Research Institute
3412 Hillview Avenue
Palo Alto, California 94304

Project Manager
Adrian Roberts

NOTICE

This report was prepared by Combustion Engineering, Inc. as an account of work sponsored jointly by the Electric Power Research Institute, Inc. (EPRI) and Combustion Engineering, Inc. Neither EPRI, members of EPRI, Combustion Engineering, Inc., nor any person acting on behalf of either: (a) makes any warranty or representation, express or implied, including the warranties of fitness for a particular purpose or merchantability, with respect to the accuracy, completeness, or usefulness of the information contained in this report, or that the use of any information, apparatus, method, or process disclosed in this report may not infringe privately owned rights; or (b) assumes any liabilities with respect to the use of, or for damages resulting from the use of, any information, apparatus, method, or process disclosed in this report.

ABSTRACT

This final report presents the results of a comprehensive performance evaluation of Maine Yankee Core I fuel prompted by observations of coolant iodine activity increases during Cycle 1. The program was initiated after the July 1974 shutdown and included a poolside fuel inspection and a hot cell examination of representative fuel rods. The hot cell work was conducted in two campaigns, an initial Combustion Engineering (CE) effort followed by a jointly-sponsored EPRI/CE study. The major objective of the overall program was to determine the primary cause of clad perforation. The opportunity was also afforded to obtain fuel rod performance data for evaluating fuel behavior codes.

The significant characteristics of the fuel rod perforation pattern were: (1) The perforated rods were virtually all located in high power positions in Batch B assemblies, and (2) based on coolant iodine activity history, perforations started to occur after an average core burnup of 5,000 Mwd/MTU and were mainly associated with two power change events--the first escalation to 88% core power (peak local power = 8.3 kw/ft) and later, the first escalation to 95% core power (peak local power = 9.0 kw/ft). During the period when perforations were occurring, Batch B assemblies were generally the highest power assemblies in the core.

Two populations of fractional fission gas release (less than 1% and 11.3 to 15.3%) were observed among rods operating under similar irradiation conditions. Metallography revealed equiaxed UO_2 grain growth only in the high gas release rods. Evidence of fission product redistribution was also observed only in high gas release rods. This consisted of: (1) Cesium gamma activity peaks located at pellet interfaces, (2) detection of cesium, iodine, and tellurium on the clad internal surface during a scanning electron microscopy (SEM) examination, and (3) finding cesium-rich interlayers in electron probe microanalyses of fuel-clad bonded regions. The higher temperature operation evident in the higher gas release rods is attributed to a densification-related fuel rod heat transfer reduction process.

Incipient cladding cracks were found in three high gas release Batch B rods originating at, and normal to, the clad internal surface. These were located in high power positions at pellet interfaces and near pellet cracks. Optical microscopy of metallographic surfaces indicated no evidence of mechanical deformation at the cracks. SEM fractography of a crack surface revealed the characteristic cleavage pattern ascribed to iodine stress corrosion cracking. Although an exhaustive metallographic examination was conducted in a search for incipient perforation in sound Batch B rods, no indication of primary hydriding was found. The evidence from the only perforated rod in Batch C, however, suggested primary hydriding as the cause of the cladding breach.

Based on the hot cell results and the strong power dependency of the rod perforation pattern, it is concluded that the most probable cause of initial cladding perforation was pellet cladding interaction assisted by fission product stress corrosion.

ACKNOWLEDGEMENTS

The authors wish to acknowledge the contributions of the Battelle-Columbus Laboratories where the hot cell examinations of both campaigns were performed under the supervision of V. Storhok and the Argonne National Laboratory, Material Science Division, where the SEM analyses of the internal cladding surfaces were performed under the direction of L. Neimark. The helpful discussions on internal fuel rod chemistry with D. Cubicciotti of the Stanford Research Institute are also gratefully acknowledged.

TABLE OF CONTENTS

TABLE OF CONTENTS (CONTINUED)

TABLE OF CONTENTS (CONTINUED)

TABLE OF CONTENTS (CONTINUED)

PREFACE

The EPRI/C-E Cooperative Project on PWR Fuel Performance (RP 586) is part of the Fuel Bundle Studies subprogram within the LWR Fuel Performance Program. Similar projects are currently ongoing with all of the U.S. fuel suppliers. EPRI's purpose in initiating fuels performance surveillance agreements with fuel vendors is to substantially increase the amount of detailed fuel performance data from large operating BWR's and PWR's which is readily available to the utilities.

The gathering of detailed fuel rod performance data under prototypic conditions is considered essential input for improving LWR fuel rod performance, reliability and safety. The resulting improvements in the understanding of fuel performance will assure that utilities can better specify fuel procurement and optimize operational maneuvers; the net effect will be decreased operations costs that result from easier and less frequent plant maintenance and from increased full-power plant availability.

This project (RP 586) is divided into three main tasks: (1) developing a comprehensive data base for the current 14 x 14 fuel assembly design based on the irradiation of three test assemblies in the Calvert Cliffs-I reactor; (2) providing data on a statistically significant sample of fuel rods at the earliest opportunity for evaluating the performance of the next generation of C-E fuel in the 16 x 16 fuel assembly design based on irradiation data from six assemblies in the Arkansas Nuclear One-2 reactor, and (3) providing a detailed evaluation of the performance of irradiated fuel rods that were removed from the Maine Yankee reactor at the end of cycle 1.

This report presents the results of the Maine Yankee evaluation. The program was prompted by observations of coolant iodine activity increases during cycle 1. The scope of work included a poolside fuel inspection and a hot cell examination of representative fuel rods, with the objective being to determine the primary cause of clad perforation. The hot cell work was conducted in two campaigns: an initial C-E effort followed by a jointly-sponsored EPRI/C-E study.

Based on extensive metallography data obtained from the hot cell studies and the strong power dependency of the fuel rod perforation pattern, it was concluded that the most likely cause of the initial cladding perforation was pellet cladding interaction assisted by fission product induced stress corrosion. The fuel rod failure mechanism appears to be a direct consequence of the combination of unstable (prone to densification) UO_2 fuel and the fact that the fuel rods were not initially pressurized. Current PWR fuel rod designs now routinely incorporate stable UO_2 fuels and are prepressurized with helium.

EVALUATION OF FUEL ROD PERFORMANCE IN MAINE YANKEE CORE I

1. INTRODUCTION

As part of the Joint EPRI/CE PWR Fuel Performance Evaluation Program, additional hot cell examinations of Maine Yankee Core I fuel after the first cycle of operation were performed. The results are presented in this final report.

An interim report[1] detailing the results of the initial effort, including the early CE hot cell examination campaign, has been issued previously. This initial investigation was prompted by evidence of perforated fuel rods, indicated by increases in the iodine activity of the coolant midway in the first cycle.

The Maine Yankee Core I fuel description and the operating history of the first cycle are summarized in Tables 1-1 and 1-2. The iodine activity history, simplified by presenting the estimated steady state levels (indicative of the number of perforated fuel rods present), as a function of time, is shown in Fig. 1-1. The figure shows that the first significant I-131 activity increase occurred at an average core burnup of 5,627 Mwd/MTU. Later, two major step increases occurred when the core power was escalated for the first time to 88% and 95% of full rating, respectively. It is estimated that the total number of perforated rods, corresponding to the steady state I-131 at the end of Cycle 1, was 225*.

---

* Based on an escape rate coefficient model from which the I-131 activity calculated for Maine Yankee conditions was 2.24×10^{-3} μCi/ml per perforated rod.

Table 1-1

MAINE YANKEE FUEL DESCRIPTION

Core	
Power, Mw(t)	2440
Average Linear Power,kw/ft @ 100% of rating	5.9
Fuel Assemblies	
Total Number of Fuel Assemblies	
Core	217
Batch A	69
Batch B	80
Batch C	24 (C_0), 36 (C_1), 8 (C_2)
Number of Fuel Rods Per Assembly	
Batch A	176 (no poison rods)
Batch B	160 (16 poison rods)
Batch C	176 (C_0), 164 (C_1-12 poison rods) 160 (C_2-16 poison rods)
Fuel Rod Array, Square	14 x 14
Fuel Enrichment, %	2.01 (A), 2.40 (B), 2.95 (C)
Fuel Assembly Material	All Zircaloy in core zone
No. of Control Element Assemblies (CEA)	85
No. CEA Guide Tubes per Fuel Assembly	5
Fuel Rods	
Clad Material	Zircaloy-4
Cold Helium Fill Pressure, psia	14.7
Clad OD, in.	0.440
Clad ID, in.	0.388
UO_2 Pellet Diameter, in.	0.3795
Active Fuel Length, in.	136.7
Pellet Density, % TD	93
Pellet L/D	1.7
Pellet Dish Depth, mils	15

Table 1-2

Maine Yankee Core I Operating History Highlights

Core Average Burnup at EOC, Mwd/MTU	10,368
Reactor Pressure, psi	
From BOL to 3800 Mwd/MTU	2,000
From 3800 Mwd/MTU to EOC	1,800
Time at Temperature, hr.	12.744
Time at Power (critical), hr.	11,820
Coolant Temperature, ^{o}F @ 2000 psi	536 (In)
	567 (Out)
@ 1800 psi	525 (In)
	570 (Out)
Highest Power Operation, % of Rating	95
Burnup at Highest Power Operation, Core Average Mwd/MTU	8,333
Rod Peak Power at Highest Power Operation, kw/ft.	9.0

Figure 1-1

I-131 ACTIVITY IN MAINE YANKEE

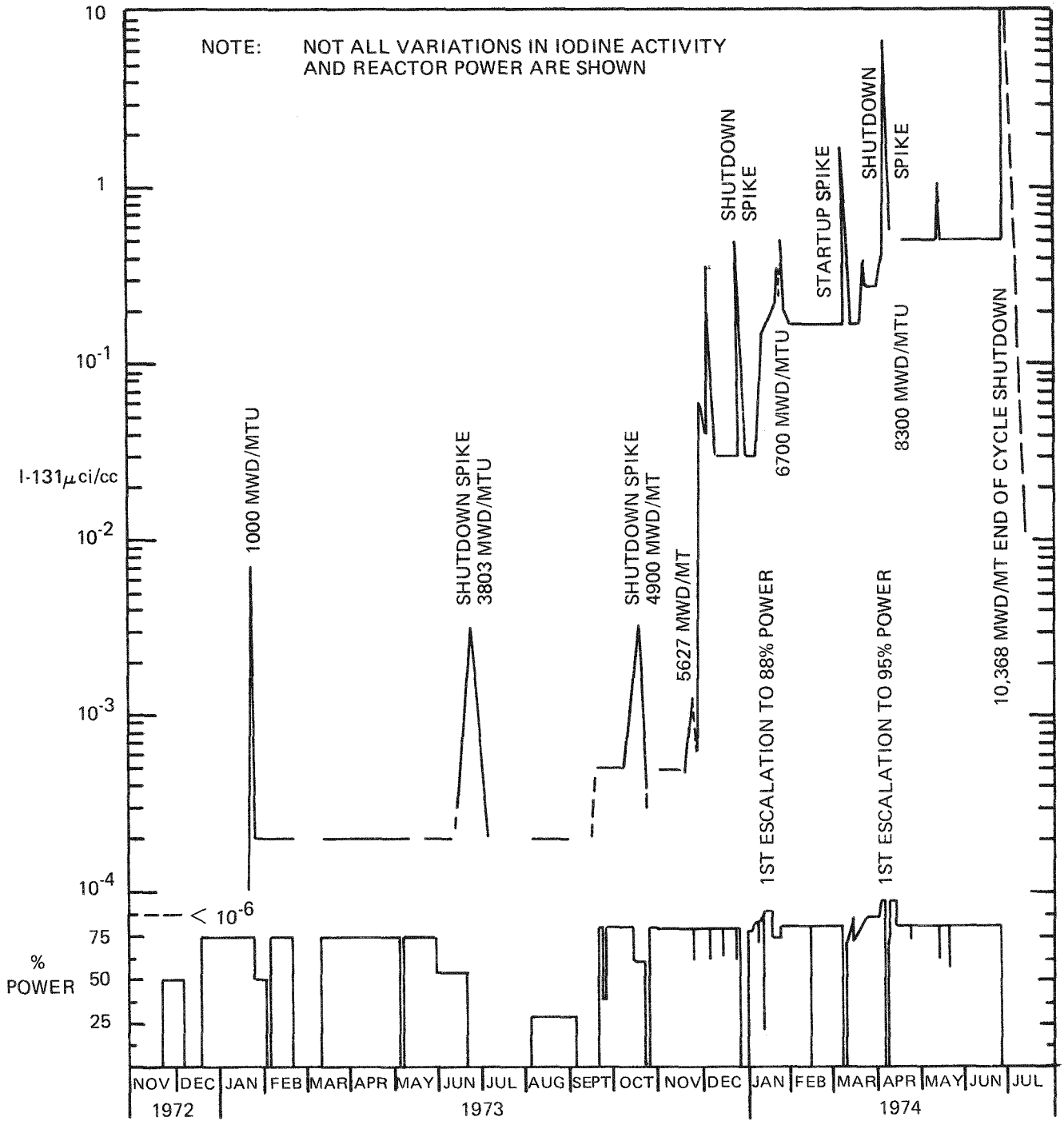

Figure 1-2

MAINE YANKEE CYCLE I

REACTOR CORE MAP

ASSEMBLY LOCATIONS

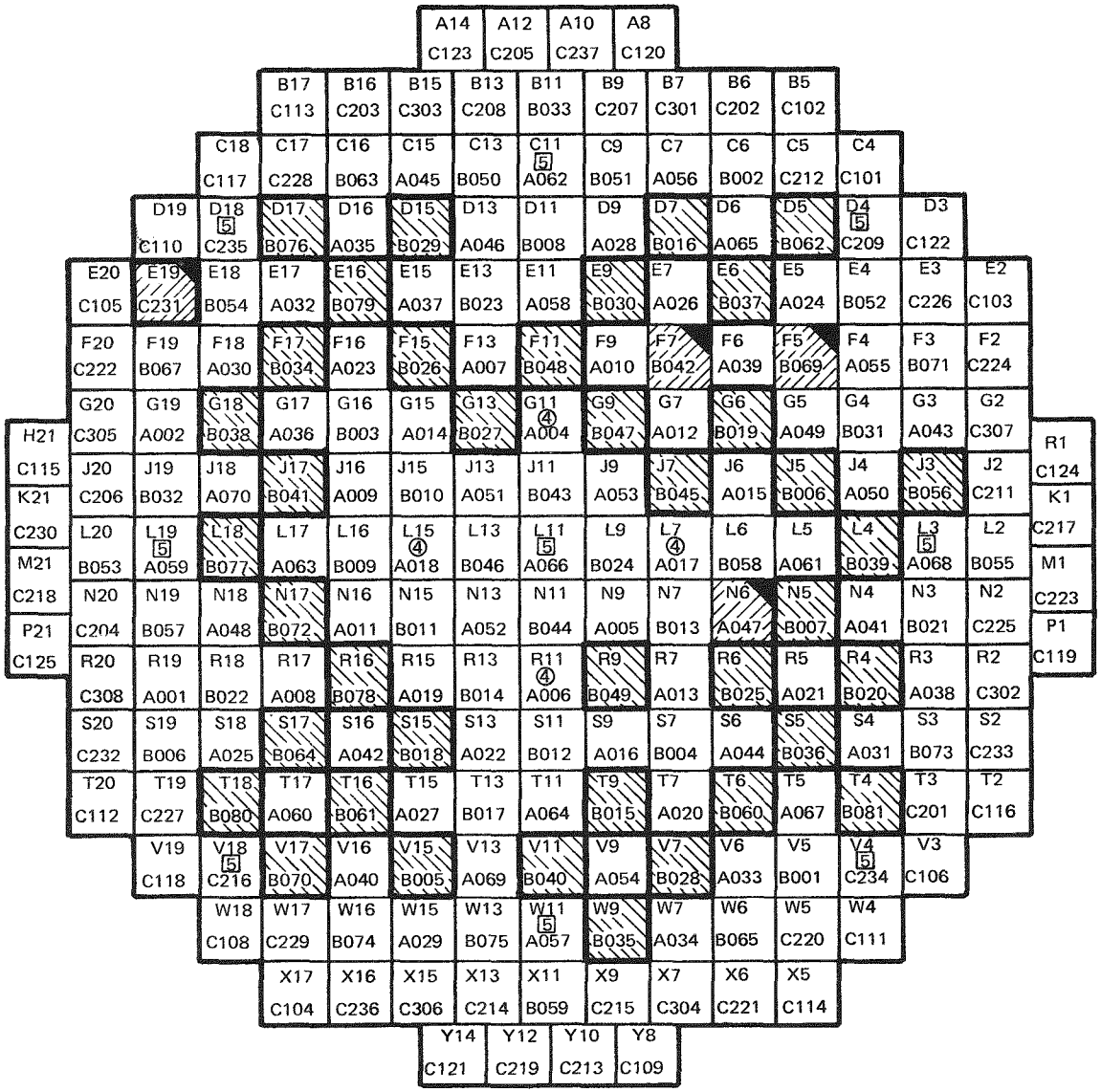

ASSEMBLIES WITH NO PERFORATED RODS

ASSEMBLIES WITH PERFORATED RODS

ASSEMBLIES WITH PERFORATED RODS DISASSEMBLED FOR DETAILED EXAMINATION

[5] CEA BANK No. 5

④ CEA BANK No. 4

CALLED NORTH

Sipping tests, performed during the first cycle shutdown in July 1974 on all 217 fuel assemblies in the core, identified a total of 43 assemblies with perforated rods; 41 from Batch B and only one each from Batches A and C. The location and identification of these assemblies can be seen in the Fig. 1-2 core map which also shows the positions of the control element assemblies (CEAs) of Banks Nos. 4 and 5. These were used for maneuvering during the first cycle, and it should be noted that they are located only in Batch A and C assemblies. Generally, the Batch B assemblies experienced the highest burnup (also the highest power operation) in the core; and, as shown in Fig. 1-3, the perforated fuel rods were predominantly in the higher power Batch B assemblies.

CE's initial program [1] was aimed at determining the mechanisms causing clad perforations which would account for the observed distribution of fuel assemblies with perforated rods in the core. The program consisted primarily of disassembly and non-destructive rod examinations of four assemblies at the Maine Yankee spent fuel pool and the hot cell examination of representative fuel rods from these assemblies. The assemblies included two from Batch B and each of the Batch A and C bundles with perforated rods. The results of the poolside non-destructive examination further demonstrated that the perforated rods in the Batch B assemblies were those operating at relatively high power in Cycle 1.

Thirty fuel rods were then sent to the Battelle-Columbus Hot Cells for a comprehensive examination involving the following activities:

	Total No. of Rods	No. of Perforated Rods
Visual Examination	22	5
Profilometry	16	2
Gamma Scanning	11	1
Fission Gas Collection and Analysis	13	-
Eddy Current Testing	13	-
Fuel-Clad Metallography (24 metallographic mounts)	8	1
Burnup Analysis (2)	1	-

Figure 1-3

HISTOGRAM SHOWING THE FRACTION OF BATCH B ASSEMBLIES WITH PERFORATED RODS IN EACH CORE SYMMETRIC POSITION AS A FUNCTION OF AVERAGE ASSEMBLY BURNUP FOR EACH POSITION

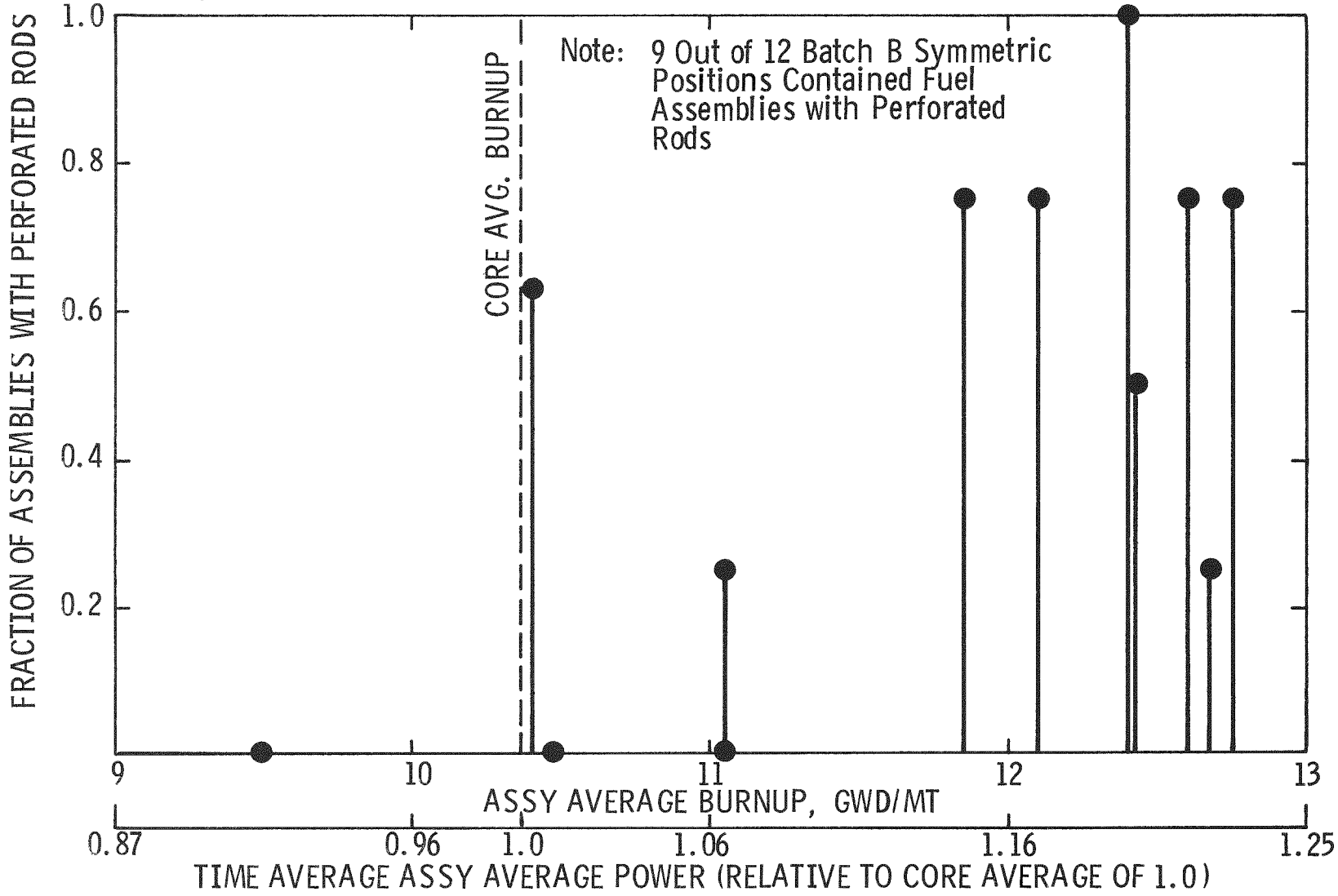

The results were highlighted by the discovery that Batch B fuel rods with similar power histories were exhibiting evidence of significantly different operating temperatures including two distinct fractional fission gas release populations: 11.3 to 13.5% and <1%.

An analysis of this finding indicated that as a consequence of UO_2 densification in the unpressurized rods of Maine Yankee Core I, a reduction in heat transfer occurred midway in Cycle 1 in certain fuel rods resulting in the higher gas release. Other rods operating at the same powers did not undergo the heat transfer reduction and were in the low gas release population. It is probable that the observed higher gas release occurred during a transient and was accompanied by release of a large inventory of reactive fission products (e.g., iodine and cesium) to the cladding in a short time period. This release could contribute to stress corrosion cracking.

Indeed, evidence of incipient perforation by a pair of cracks was found originating on the cladding internal surface of a high gas release Batch B rod, and their appearance was consistent with iodine stress corrosion cracking.

In view of these results, a second hot cell examination campaign and associated data analyses were undertaken under the Joint EPRI/CE PWR Fuel Performance Evaluation Program with the following objectives:

1. Examine the performance behavior of Maine Yankee Core I fuel to obtain data for evaluating fuel rod models.

2. Characterize the reduction in fuel rod heat transfer and determine the conditions under which it might occur.

3. Determine the relationship between reduction in fuel rod heat transfer and the resulting fission product release.

Another major objective was to confirm the tentative conclusion in the interim report that the most probable cause of initial cladding perforation in most of the perforated Maine Yankee Core I fuel rods was pellet-cladding interaction (PCI) in combination with stress corrosion by volatile fission products (e.g., iodine and/or cesium).

To accomplish these objectives, the work included an expansion of non-destructive testing (i.e., profilometry, gamma scanning and fission gas collection and analysis of available high burnup rods). Destructive examinations were also expanded to include:

1. Metallography to search for additional evidence of incipient cladding perforation in sound Batch B rods, as well as to map the extent of equiaxed grain growth in high gas release rods.

2. Density measurements to determine the densification/swelling behavior of the UO_2 fuel.

3. Microprobe analysis and other characterization techniques to determine local fission product concentrations in the fuel and on the cladding internal surface.

This final report details the results of the second hot cell examination campaign. Where pertinent data exist from the first campaign, they are consolidated with the new information in the appropriate section.

2.0 SUMMARY AND CONCLUSIONS

2.1 Post-Irradiation Examination Results

The significant results from the overall hot cell examination program and the data analyses are summarized below:

1. Fission Gas Release Behavior

The fission gas analysis data from the second hot cell campaign corroborated those from the first campaign in which two populations of fractional fission gas release were observed. Ultimately, 7 of the 10 sound Batch B rods shipped to the hot cell were in the population exhibiting the higher fractional gas release (11.3 to 15.3%). All of the rods in the lower gas release population exhibited less than 1% fractional release; yet, some of these rods operated under irradiation conditions similar to those of the higher gas release population. Metallography revealed extensive equiaxed UO_2 grain growth only in the higher gas release rods, indicative of higher operating temperatures. Grain growth typically extended over 90% of the fuel length and 25% of the fuel volume.

A higher gas release Batch A rod was also found; however, its fuel stack weight was relatively low, indicating an initial fuel density near the low end of the manufacturing tolerance. The result was not surprising in view of the role of densification propensity believed responsible for triggering the gas release. Fuel density measurements on pellets from this rod indicated an apparent densification of up to about 5% (from 92% to ~97% TD).

2. Fuel Rod Heat Transfer Reduction

The higher fission gas release behavior and attendant higher fuel temperatures are attributed to a fuel rod heat transfer reduction which was a consequence of UO_2 densification and became operative in unpressurized rods: At some point in life, after the fuel densified and the pellet-clad gap had increased, the fuel operated just below the temperature for equiaxed grain growth. A small power increase or a small

reduction of gap conductance was sufficient to increase the temperature and initiate equiaxed grain growth resulting in release of a large fraction of the fission gas from the grain growth region to further reduce the helium fill gas conductivity. The temperature of the fuel, thus, was increased by the reduced heat transfer, and the grain growth process spread to affect a larger volume of the fuel resulting in more gas release and additional reduction in fuel rod heat transfer. The mechanism was self-limiting in that fuel swelling and pellet relocation resulting from higher fuel temperatures reduced the pellet-clad gap and arrested the process.

The fact that all rods of a given design operating at similar power levels did not exhibit the above behavior is believed to be the result of variation in the actual fuel-to-clad gap during operation due to differences in as-built gap size and UO_2 pellet densification propensity. Larger starting gaps and greater UO_2 densification in-reactor would cause higher fuel temperatures. Rods with smaller starting gaps and less UO_2 densification would tend to run cooler at a given power, and, therefore, equiaxed grain growth would not have been initiated.

3. Volatile Fission Product Redistribution

Only the higher gas release rods exhibited cesium gamma scan peaks at pellet interfaces. Further evidence of fission product redistribution in these rods was observed in visual and scanning electron microscope (SEM) examinations of the internal clad surface. These revealed fuel-clad bonding mainly near pellet interface locations. Chemical characterization by X-ray spectrometry indicated the chemical composition of the fuel-clad bond region to be a mixture of cesium, uranium and zirconium combined with oxygen. Also, redistributed iodine and tellurium were detected on the clad surface. The presence of a Cs-Zr-U-O phase in the fuel-clad bond was confirmed by electron microprobe analysis of metallographic specimens.

4. Incipient Crack Metallography and Fractography

A total of 3 higher gas release Batch B rods were found with cladding cracks in high power regions, penetrating up to two-thirds of the clad wall. In all cases, the cracks were normal to and intersected the clad internal surface and were located at pellet interfaces and near pellet cracks. The optical microscopy features of the clad cracks appeared similar to those ascribed by other workers to iodine stress corrosion. Moreover, the cracks were tight and difficult to discern metallographically without etching the clad. Polarized light metallography showed no evidence of visible plastic deformation--also consistent with stress corrosion cracking (SCC).

A SEM fractography examination showed no ductile dimpling on the crack surface, confirming essentially no plastic deformation had occurred. Only flat cleavage planes and river patterns were observed. These are produced in Zircaloy by a stress corrosion cracking mechanism.

The only Batch C perforated rod in Core I showed evidence suggesting that primary hydriding may have been the cause of the cladding breach. Although an exhaustive metallographic examination was conducted at the hot cell in a search for internal cladding defects in sound Batch B rods, no incipient perforations due to primary hydriding were detected.

It is noteworthy that both the poolside and hot cell eddy current test indications, which were the bases for the metallographic specimen selection in the first campaign, invariably signaled regions of fuel-clad bonding rather than internal cladding defects. Therefore, in the second campaign, in which high gas release Batch B rods with no eddy current indications were examined, the selection was based on a combination of profilometry and cesium gamma scan data.

5. Grid-to-Fuel Contact Wear

An important outcome of the hot cell examination was the observation that the grid-to-fuel rod contact wear was insignificant, confirming the poolside inspection results, and thus, demonstrating successful wear-free operation of the Zircaloy grids in Maine Yankee Core I.

2.2 Cause of Clad Perforations

Based on an overall evaluation of all of the data obtained from the poolside inspection and both hot cell campaigns, it is concluded that in Batch B, where most of the perforated rods were located:

1. The most probable cause of initial clad penetration of the perforated rods was a pellet-cladding interaction (PCI) mechanism in which clad cracking was promoted by fission product (e.g., iodine and/or cesium) stress corrosion.

2. Primary hydriding was not the cause of initial clad penetration. (The hydride blisters visually observed on the Batch B perforated rods were virtually all secondary in nature caused by water ingress through the initial crack.)

The bases for these conclusions may be summarized as follows:

1. All of the evidence is consistent with a PCI mechanism with fission product-assisted stress corrosion:

a. The mechanism is strongly power dependent, and the perforated rods were predominately found in high power locations in Batch B assemblies.

b. A fuel rod heat transfer reduction occurred in some high power Batch B fuel rods causing a temperature increase, equiaxed UO_2 grain growth and higher fission gas release.

c. Other volatile fission products, cesium and iodine, were redistributed to pellet interfaces in high gas release rods. (The cesium promoted fuel-clad bonding which can enhance local stress concentration and iodine stress corrosion is a well-established phenomenon in Zircaloy.)

d. Evidence of equiaxed UO_2 grain growth and gamma scan cesium peaks was also observed in perforated rods consistent with higher gas release behavior.

e. Clad cracks penetrating up to two-thirds of the wall thickness were found in three (3) sound high gas release Batch B rods at pellet interfaces, characteristic of a PCI pattern.

f. SEM fractography and optical microscopy showed the crack morphology to be consistent with an SCC process.

g. An examination of the power history indicates why rod perforations were virtually all in Batch B assemblies. Very few rods other than those from Batch B ran at high power in Cycle 1 when gap conductance was minimized by UO_2 densification. Fuel rods from other batches were generally less susceptible to the heat transfer reduction process.

2. Hydriding is unlikely to have been a direct cause of initial clad penetration because the evidence is inconsistent with a primary hydriding pattern:

a. No evidence of incipient perforation by hydriding was uncovered during extensive hot cell examination of sound rods.

b. Instead of early-in-life, practically all perforations occurred later, after >5,000 Mwd/MTU average core burnup.

c. The incidence of perforation among rods was strongly power dependent instead of the random distribution usually observed.

d. Excessive moisture levels were not found in the manufacturing data or archive fuel pellet examination.

3. Hydriding predamage coupled with PCI to cause perforation late-in-life was also not a likely mechanism mainly because no evidence of primary hydride remnant cracks was detected in the hot cell program.

3.0 POOLSIDE INSPECTION PROGRAM

3.1 Preliminary Visual Inspection

As an adjunct to the sipping tests conducted during the July 1974 shutdown, 30 assemblies (14 with clad perforations and 16 without clad perforations) were visually examined with underwater viewing equipment. This consisted of a television camera and videotape recording apparatus to document the appearance of each of the four assembly sides and a periscope to obtain a magnified view of individual fuel rods both on the periphery and within the assembly. (Second row fuel rods are clearly visible over ∿25% of their surface.) No evidence of clad perforation was observed in the assemblies identified as sound by the sipping test. No perforated rods were evident from visual examination of assemblies A047 and C231, the only assemblies in Batches A and C with sipping indications of clad perforation. Twelve Batch B assemblies with sipping indications were inspected and ten contained rods with visible evidence of clad perforation. A total of 18 rods (all but one achieving a burnup greater than the core average) were identified as having perforations. (See Appendix A, Table A-1, for detail.) In view of the correlation of perforated assemblies with high burnup (i.e., high power) resulting from the sipping tests, it is not surprising that the perforated rods found were mostly in high burnup positions within the assemblies.

3.2 Bundle Disassembly and Fuel Rod Inspection

In September 1974, another, more extensive, poolside inspection program was undertaken involving the disassembly of four fuel bundles and the removal and examination of individual fuel rods. The major objectives were to characterize the mode(s) of the fuel rod perforation and to detect rods having incipient indications of perforation for possible further examination at a hot cell. The program consisted of three inspection steps: (1) Eddy current testing aimed at detecting and locating cladding anomalies which may be associated with incipient cladding cracks or other incipient penetrations, (2) viewing and videotape recording with the television system, and (3) detailed visual examination with a periscope.

The Batch B bundles selected for disassembly were B042 and B069 because they were representative of the symmetrical core positions exhibiting the highest incidence of assemblies with perforated rods. The other two bundles in the program were A047 and C231 representing the only assemblies with perforated rods other than those in Batch B. In view of the rod perforation pattern observed previously, the rods selected for testing were taken mainly from the high power positions, i.e., those adjacent to the water channels (around the guide tubes and between the guide tubes and bundle periphery), as shown in the assembly maps in Appendix A.

The number of fuel rods removed for the different examinations and data on the perforated rods found are summarized in Table 3-1. It is noteworthy that all of the perforated Batch B rods achieved a relatively high burnup and operated to relatively high power. The identification and description of the perforated rods are detailed in Appendix A (Table A-2). Their locations are also marked in the respective Appendix A assembly maps which also indicate the locations of all rods inspected.

All the perforated rods had visually observable blisters and bulges, presumably caused by hydriding. None exhibited evidence of axial cladding cracks as a form of perforation.

3.3 Observations of Grid Contact Wear

During the visual examination of fuel rods from the disassembled bundles using the periscope, slight wear was observed at the top grid contact points on Rod HBV-067 (from position C-13 of Assembly A047) and to a lesser degree, on Rod KCA-156 (from position N-14 of Assembly C231). The depth of the apparent maximum wear, at an arch contact point, on HBV-067 was found later in the hot cell examination to be 0.0035 in.

Table 3-1

Bundle Disassembly Program - Perforated Rod Data Summary

Assembly Number	No. of Fuel Rods Inspected by Eddy Current and TV	No.of Fuel Rods Examined with Periscope	Perforated Rod Data		
			No. of Perforated Rods Found	Range at End-of-Cycle	
				Relative Power+	Burnup (Mwd/MTU)*
B-042	84	37	11	1.183 - 1.267	12,786 - 13,629
B-069	73	13	4	1.230 - 1.284	12,744 - 13,535
A-047	88	11	1	1.073	12,453
C-231	154	17	1	0.969	9,661
TOTALS	399	78	17		

+ Relative to core average.

* Core average burnup - 10,368 Mwd/MTU.

As a result of these observations, all fuel rods from A047 and C231 not examined with the periscope were visually examined at the top grid region using a borescope. No evidence of wear was observed on any of the additional 309 rods inspected. A summary of the grid contact wear observations is presented in Table 3-2. Based on the results of this program (1021 grid regions containing 6126 contact points) grid contact wear was essentially absent, and it is concluded the Zircaloy grids exhibited wear-free operation.

3.4 Selection of Fuel Rods for Hot Cell Examination

Inasmuch as the poolside inspection did not develop conclusive data on the cause of initial clad perforation, it was decided to examine fuel rods further in a hot cell. The criteria used to select rods for shipment to the Battelle-Columbus hot cell were:

1. Inclusion of representative perforated rods and apparently sound rods containing possible incipient perforation indications or other internal surface anomalies based on eddy current test results.

2. Evidence of any wear at grid locations.

3. Inclusion of the different fuel lots with respect to perforated and sound rods, where possible.

It was recognized that secondary effects due to water ingress would tend to obliterate evidence of the initial clad perforation mechanism in perforated rods; therefore, the most important selection criterion was the inclusion of rods which appeared sound but produced eddy current signals ostensibly from non-perforating internal cladding surface cracks.

Table 3-2

Maine Yankee Core I Grid Contact Wear Observations

Assembly	Number of Rods Examined for Wear		
	Top Grid Only	All Grids	Total Rods
A-047	164	12	176
C-231	145	20	165
B-042, B-069	--	57	57
TOTAL	309	89	398

Total Rods Examined	398
Total Number of Grid Locations	1021
Total Number of Grid Contact Points Examined	6126

The eddy current data consisted of recorder traces, obtained with an encircling coil operating at excitation frequencies of 100 kHz and 400 kHz and oscilloscope signatures. Comparisons were available with similar data taken from calibration tube standards having known internal and external defects. A total of twelve sound rods were found containing various eddy current signals, some of which appeared to have originated from the cladding internal surface. Examples of the most prominent eddy current signals obtained are shown in Appendix B which, for comparison, also includes an eddy current signal from an internal surface calibration standard notch. Thirty fuel rods were selected for the hot cell examination program. (See Table 3-3 for rod identification and basis for selection.) Included are eight perforated fuel rods, all twelve rods with some type of eddy current test indication, three sound rods with visible indications of grid wear and seven sound rods with no eddy current indications.

Table 3-3

Maine Yankee Rod Selection for Shipment to Hot Cell

Bundle Number	Rod Position	Rod S/N	Fuel Lot	Fuel Wt.g	Shutdown Relative Power	Shutdown Burnup	Basis for Selection
B-042	L2	JBP-016	614	2532.9	1.264	13667	Perforated
	K13	JBP-084	614	2537.6	1.245	13526	Perforated
	B12	JBP-003	614	2545.2	1.267	13629	Perforated
	G9	JBP-044	614	2517.7	1.223	12896	Perforated
	J1	JBP-027	614	2533.6	1.181	12826	Eddy Current Indications
	E11	JBP-005	614	2548.8	1.213	13231	Eddy Current Indications
	N12	JBP-004	614	2541.6	1.197	13189	Eddy Current Indications
	C13	JBP-122	614	2540.8	1.265	13536	Sound
B-069	N2	JCN-151	622	2556.6	1.230	12744	Perforated
	M12	JBY-145	617	2553.9	1.284	13535	Perforated
	E11	JBY-157	617	2531.2	1.232	12935	Eddy Current Indication
	K1	JCN-182	622	2534.7	1.220	12635	Eddy Current Indication
	J5	JBY-142	617	2540.4	1.202	12321	Eddy Current Indication
	D2	JCN-199	622	2541.9	1.271	12842	Eddy Current Indication
	C13	JBY-097	617	2528.6	1.285	13349	Sound
	C2	JCN-196	622	2521.2	1.279	12904	Sound
A-047	F7	HBV-001	516	2531.0	1.073	12453	Perforated
	B6	HBU-198	516	2536.7	1.019	11478	Eddy Current Indications
	M10	HBV-007	516	2537.0	1.056	11946	Eddy Current Indications
	E4	HBU-169	515	2505.5	1.081	12410	Eddy Current Indications
	C13	HBV-067	516	2562.6	1.097	12437	Wear-Grid 8 Elevation
	I7	HBV-002	516	2526.8	1.075	12464	Sound
	J6	HBV-009	516	2532.0	1.030	11801	Sound
C-231	G10	KCA-109	719	2560.8	.969	9661	Perforated
	L2	KCA-019	719	2560.0	1.296	12762	Eddy Current Indication at Fuel Stack Bottom
	J13	KCA-185	719	2531.5	.998	9784	Eddy Current Indication
	N14	KCA-156	719	2555.5	1.060	10172	Wear-Grid 8 Elevation
	A14	KCA-125	719	2543.8	.689	6747	Wear-Grids 3 and 5
	E8	KCA-051	719	2566.8	.972	9743	Sound
	N6	KCA-058	719	2546.2	1.142	11165	Sound

4.0 HOT CELL EXAMINATION RESULTS

4.1 Summary of Scope

The hot cell examination of Maine Yankee fuel rods was conducted in two campaigns. In the first campaign, the major objective was to obtain evidence of the cause of initial clad perforation. During the second campaign, in addition to pursuing this objective, emphasis was placed on obtaining data relevant to fuel rod performance and data useful for evaluating fuel rod performance models. The selection of fuel rods and the specific examinations were particularly directed towards studying the fuel rod heat transfer reduction mechanism and related fission product release observed in the first campaign [1].

The specific types of examinations carried out in both campaigns are listed below:

1. Profilometry - Spiral scan and linear scans at two azimuthal orientations.

2. Visual examination.

3. Gamma scan - Gross gamma (1st campaign) specific isotope gamma scan (2nd campaign).

4. Fuel rod puncture and gas collection.

5. Hot cell eddy current testing.

6. Clad slitting for clad inner surface examination.

7. Fuel-clad metallography.

8. Cladding crack characterization by SEM.

9. Irradiated fuel density measurements.

10. Electron microprobe analysis of fuel-clad reaction zone, and

11. Burnup analysis.

The examinations performed on the individual fuel rods in both campaigns are listed in Table 4-1. The results of the overall hot cell program are presented in the following sections.

4.2 Profilometry (Fuel Rod Diameter Measurements)

4.2.1 Scope and Procedure

During the first hot cell examination campaign, continuous profilometry measurements were made on a total of 16 fuel rods (14 sound and 2 perforated) to characterize local fuel rod diameter and to determine the extent of ovality and cladding creepdown over the full length of the fuel rods. The measurements were performed in the standard rod rotating mode. During the second campaign, three additional sound rods were profiled. On two of the three rods, additional diameter traces were obtained in the non-rotating mode (linear traces) at two azimuthal orientations 0^{o} and 90^{o}.

The Battelle profilometer used for this work is shown schematically in Fig. 4-1. It consists of two linear variable differential transducers (LVDT) placed 180^{o} apart, which move axially along the fuel rod, a rod rotation mechanism, and a strip chart recorder. The fuel rod is held in position by guide rollers located above and below the transducer heads. The transducers respond to the changes in fuel rod diameter as they traverse axially along the rod, and these responses are converted electronically into strip chart recorder signals. The system is calibrated with a step standard, which is a cylindrical rod with precisely machined steps of different diameters. The standard used for the Maine Yankee fuel rods contained sections which ranged in diameter from 0.426 to 0.456 in. with steps of 2, 3, 4, 5 and 6 mils. The diameter of each section is known within $\pm$ 0.1 mil.

Table 4-1

Maine Yankee Hot Cell Examination Summary

Rod S/N	Assembly Location	Rod Avg. Burnup Mwd/MTU	Visual	Prof.	γ-Scan	Fission Gas	Eddy Current	Fuel Density No. of Samples	Clad-Fuel Metallography No. of Samples	Burnup No. of Samples	No. of Slit-Clad Sections
Ass'y B042											
JBP-027	J-1	12,826	X	X	X	X	-	-	2	-	1
JBP-003	B-12	13,629	X	X	(X)	Perforated Rod	-	-	(2)	-	-
JBP-004	N-12	13,189	X	X	(X)	X	X	(6)	-	-	(1)
JBP-005	E-11	13,231	X	X	X	X	X	-	6 + (2)	2	-
JBP-122	C-13	13,636	(X)	X	(X)	X	X	-	(3)	-	-
JBP-044	G-9	12,896	X	-	(X)	Perforated Rod	-	-	-	-	-
JBP-016	L-2	13,667	Broken Rod--No hot cell exam carried out.								
JBP-084	K-13	13,526	Broken Rod--No hot cell exam carried out.								
Ass'y B-069											
JBY-157	E-11	12,935	X	X	X	X	X	-	3	-	-
JCN-182	K-1	12,635	X	X	X	X	X	-	4	-	-
JBY-145	M-12	13,535	X	-	(X)	Perforated Rod	-	-	-	-	-
JCN-199	D-2	12,842	X	X	X	X	X	-	3	-	-
JBY-142	J-5	12,231	X	X	-	X	X	-	3	-	-
JCN-151	N-2	12,744	X	-	-	Perforated Rod	-	-	-	-	-
JCN-196	C-2	12,904	(X)	(X)	(X)	(X)	X	(3)	(3)	(2)	(2)
JBY-097	C-13	13,349	(X)	(X)	(X)	(X)	X	(2)	(5)	-	-

X = Test performed - 1st campaign.
(X) = Test performed - 2nd campaign.
- = Test not performed.

Table 4-1 (continued)

Maine Yankee Hot Cell Examination Summary

Rod S/N	Assembly Location	Rod Avg. Burnup Mwd/MTU	Visual	Prof.	γ-Scan	Fission Gas	Eddy Current	Fuel Density No. of Samples	Clad-Fuel Metallography No. of Samples	Burnup No. of Samples	No. of Slit-Clad Sections
Ass'y A-047											
HBU-198	B-6	11,478	X	X	X	X	-	-	-	-	-
HBV-007	M-10	11,946	X	X	X	X	-	-	-	-	-
HBV-002	I-7	12,464	(X)	(X)	(X)	(X)	X	-	-	-	-
HBU-169	E-4	12,410	X	X	(X)	(X)	X	(4)	(3)	(1)	(1)
HBV-067	C-13	12,437	X	-	-	X	-	-	2	-	-
HBV-009	J-6	11,801	X	-	-	(X)	X	-	-	-	-
HBV-001	F-7	12,453	Broken Rod--No examination.								
Ass'y C-231											
KCA-109	G-10	9,661	X	X	-	Perforated Rod	-	-	-	-	-
KCA-125	A-14	6,757	X	X	X	X	-	-	-	-	-
KCA-185	J-13	9,784	X	X	X	(X)	-	-	-	-	-
KCA-019	L-2	12,762	X	X	(X)	X	X	-	-	-	-
KCA-058	N-6	11,165	X	-	-	(X)	-	-	-	-	-
KCA-156	N-14	10,172	X	-	-	(X)	-	-	-	-	-
KCA-051	E-8	9,743	-	-	-	(X)	-	-	-	-	-

X = Test performed - 1st campaign.
(X) = Test performed - 2nd campaign.
- = Test not performed.

Figure 4-1

BATTELLE PROFILOMETER SYSTEM

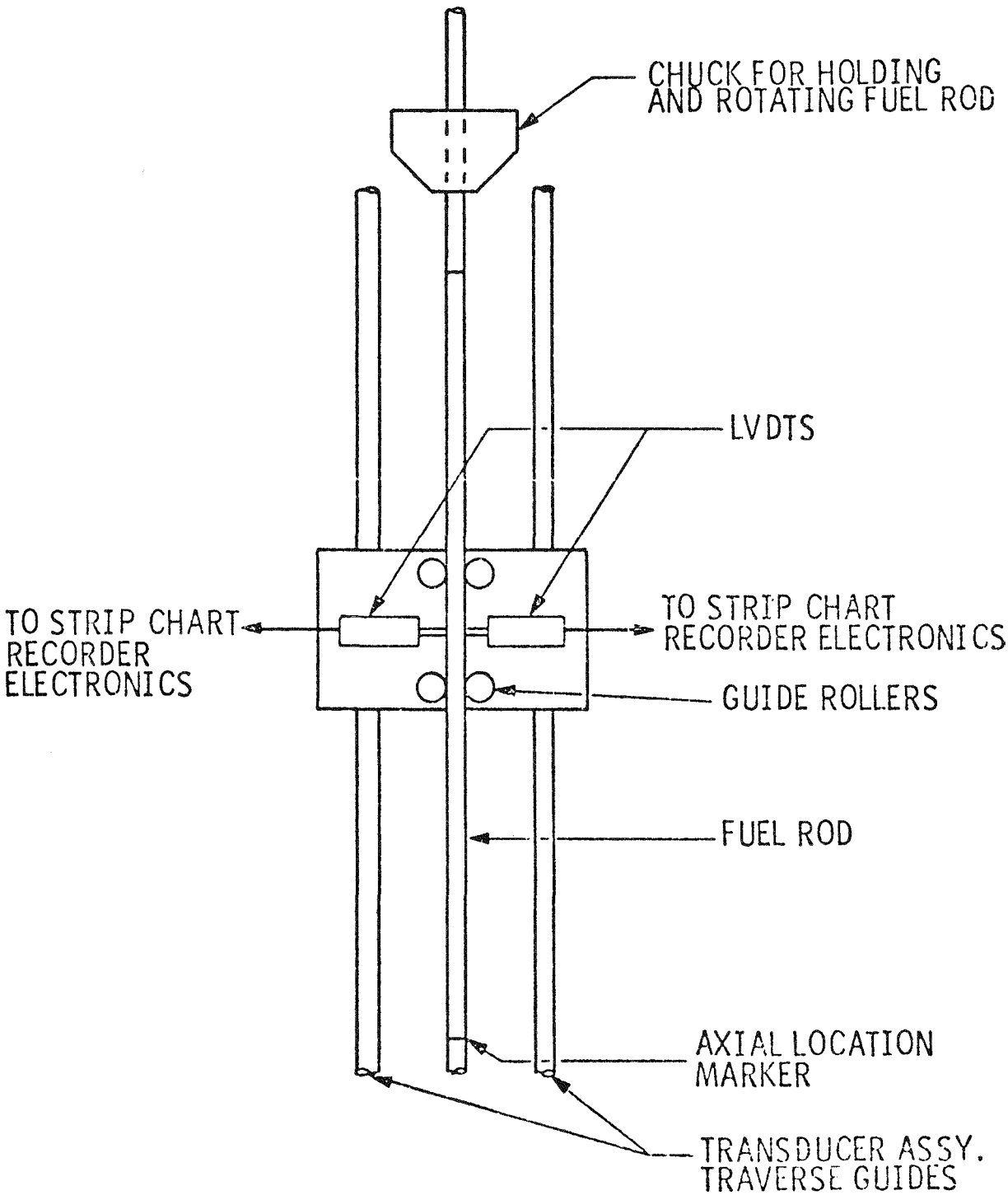

Prior to any measurements on a fuel rod, axial location markers were put on the fuel rod at 2-, 35-, 70-, 105-, and 140-inches from the bottom to provide a positive check on axial rod location. The axial location of any measurement is known within ±1/16 inch. Each rod was profiled with a rotational pitch of 8 revolutions/inch which produced an envelope of maximum-minimum diameters on the chart traces.

The accuracy of the profilometer system is ±0.0002 in. (95% confidence), and the precision of the measured mean diameter is ±0.0002 in. (95% confidence).

The results of the diameter measurements from the first and second campaigns are presented in Table 4-2 and discussed in the following sections.

4.2.2 Rod Ovality

The rod ovality (i.e., the difference between maximum and minimum diameter at a given axial location) ranged from 0.2 to 16.2 mils. Table 4-3 shows the cumulative lengths of various ranges of ovality found in some of the fuel rods. The cumulative length values were obtained by adding all the short lengths in a given range of ovality.

A typical range of ovality found among the rods can be seen in the selected profilometry traces in Fig. 4-2, 4-3 and 4-4, which show the largest ovality region, a typical region, and the plenum region of Rod JBP-005, respectively.

Only in two cases were the high ovality region of the rods associated with gaps in fuel stacks detected by gamma scanning of the rods. In one case, Rod JBY-157, the high ovality region is coincident with the gap region as shown in Fig. 4-5 (see also the Fig. 4-19 gamma scan trace) suggesting that the gap was contributory to ovalization. In the other case, Rod JBP-027, the highest ovality region is located just above the pellet gaps as shown in Fig. 4-6 (see also the Fig. 4-20 gamma scan trace). A possible explanation for this configuration is that in the region of high ovality, pellet hangup occurred resulting in a gap below in the cold conditi

Table 4-2

Profilometry Data Summary

Rod Number	Location and Assembly	Burnup Mwd/MTU	Shutdown Relative Power	Largest Ovality Mils and Location*	Average Diameters, in. Plenum @140*	Minimum and Location*	Max. Dia. Decrease Mils	Remarks
JBP-122	C13 B042	13,636	1.265	11.6 @ 112-1/2	.4395	.4366 @ 50 & 80	2.9	High gas release
JBP-003	B12 B042	13,526	1.245	5.2 @ 86-7/16	.4416	.4395 @ 90	2.1	Perforated
JBY-097	C13 B069	13,349	1.285	12.8 @ 88-1/10	.4405	.4377 @ 95	2.8	High gas release
JBP-005	E11 B042	13,231	1.213	11.6 @ 87-5/8	.4395	.4369 @ 80-100	2.6	High gas release
JBP-004	N12 B042	13,189	1.197	12.8 @ 83-7/8	.4388	.4354 @ 50 & 60	3.4	Low gas release
JBY-157	E11 B069	12,935	1.232	10.6 @ 40-9/16 10.4 @ 81-1/8	.4388	.4358 @ 80	3.0	Low gas release
JCN-196	C2 B069	12,904	1.279	4.0 @ 76	.4413	.4389 @ 80	2.4	High gas release
JCN-199	D2 B069	12,842	1.271	6.4 @ 58-7/16	.4416	.4395 @ 50 & 60	2.1	High gas release
JBP-027	J1 E042	12,826	1.181	6.4 @ 99-1/8	.4410	.4395 @ 70	1.5	High gas release
KCA-019	L2 C231	12,762	1.296	7.2 @ 42-7/8 & 53-9/16	.4419	.4392 @ 100	2.7	Low gas release
JCN-182	K1 B069	12,635	1.220	6.0 @ 78-1/8	.4394	.4377 @ 60	1.7	High gas release
HBV-002	I7 A047	12,464	1.075	11.8 @ 58-2/10	.4390	.4366 @ 85	2.4	Low gas release
HBU-169	E4 A047	12,410	1.081	14.6 @ 86-1/2	.4404	.4377 @ 60 & 80	2.7	High gas release
JBY-142	J5 B069	12,321	1.202	13.6 @64-1/2	.4392	.4370 @ 60 & 80	2.2	Low gas release
HBV-007	M10 A047	11,946	1.056	16.2 @ 117-1/4	.4397	.4368 @ 90	2.9	Low gas release
HBU-198	B6 A047	11,478	1.019	10.4 @124-1/2	.4400	.4374 @ 90	2.6	Low gas release
KCA-185	J13 C231	9,784	0.998	5.5 @ 53-5/8 & 103-1/2	.4390	.4368 @ 90,100,110	2.2	Low gas release
KCA-109	G10 C231	9,661	0.968	10.0 @ 2 (bulge) 1.8 @ 52-5/16	.4417	.4415 @ 70,90,100	0.2	Perforated
KCA-125	A14 C231	6,747	0.689	2.5 @ 69-1/8	.4407	.4391 @ 90	1.6	Low gas release

* Location in inches from bottom of rod.

Figure 4-2
PORTION OF PROFILOMETER TRACE OF JBP-005
SHOWING A LARGE OVALITY OF 10.6 MILS

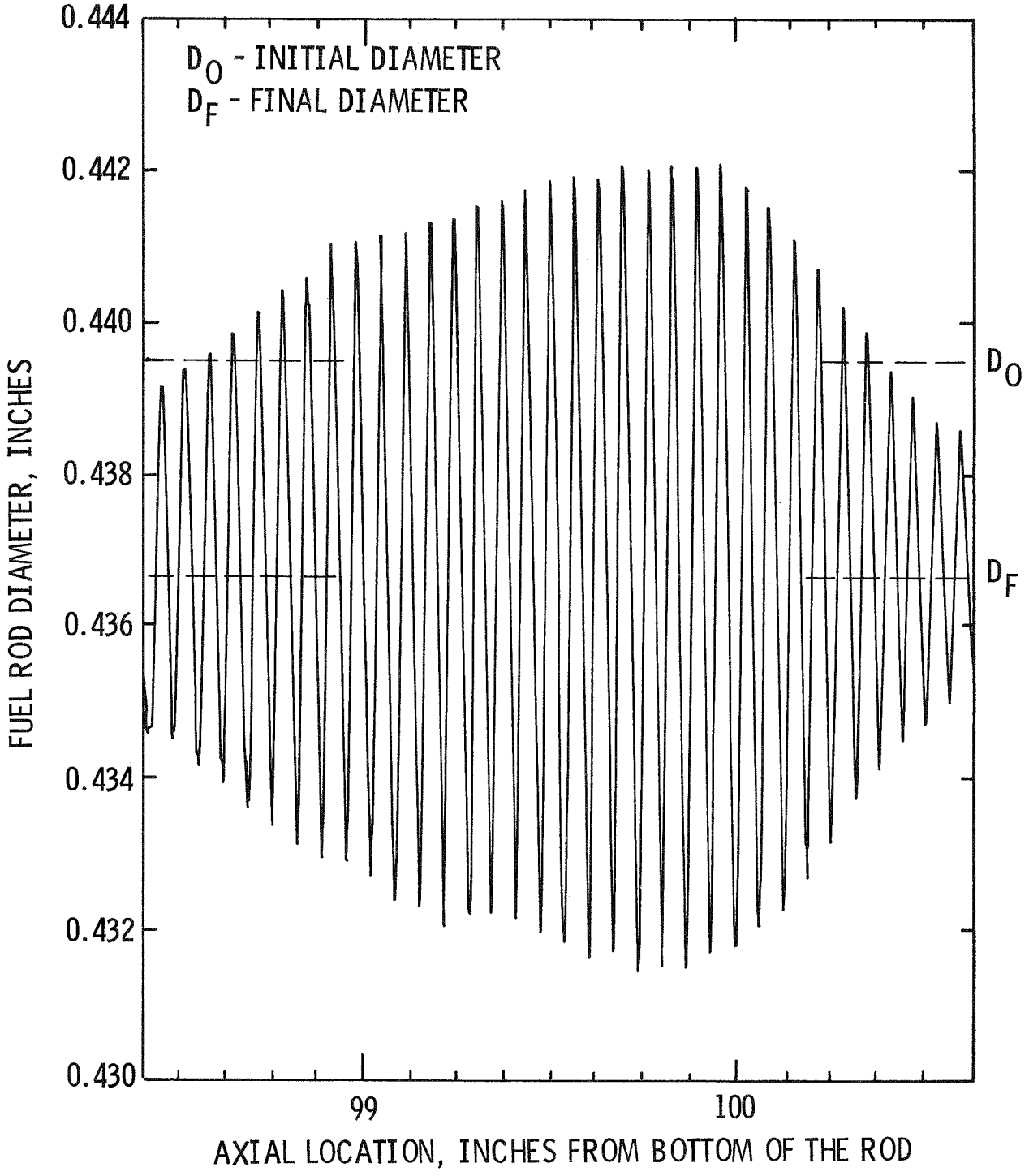

Figure 4-3
PORTION OF THE PROFILOMETER TRACE
OF JBP-005 SHOWING TYPICAL OVALITY
OF APPROX. 3.5 MILS

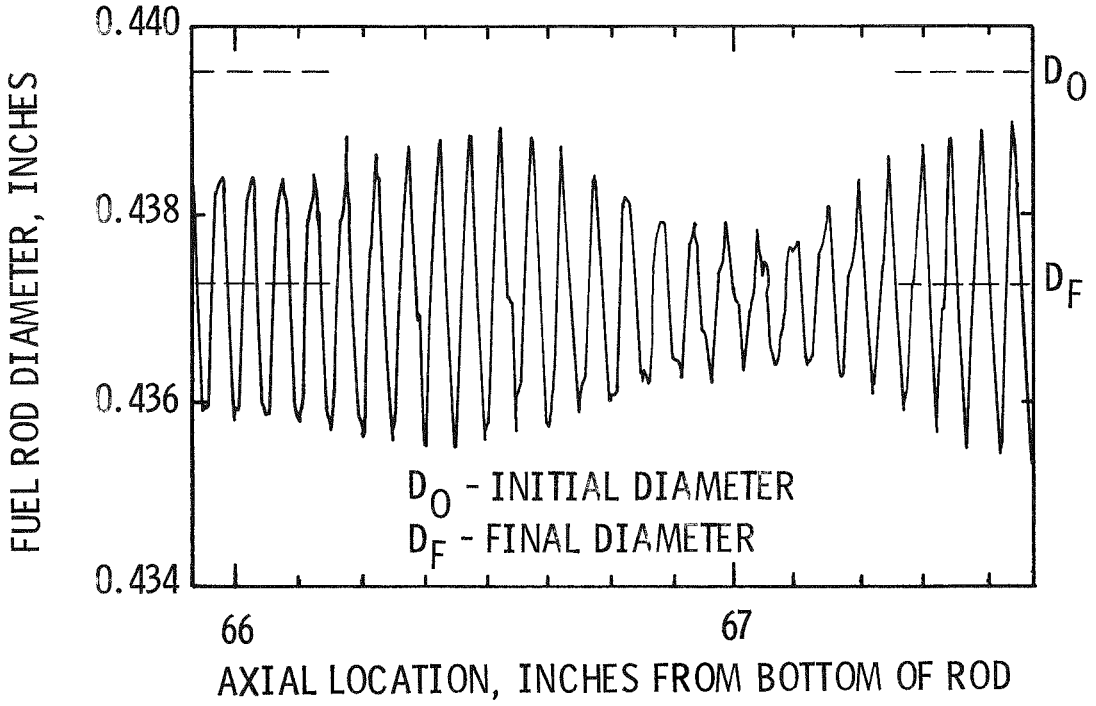

Figure 4-4
PORTION OF PROFILOMETER TRACE OF JBP-005
SHOWING PLENUM REGION

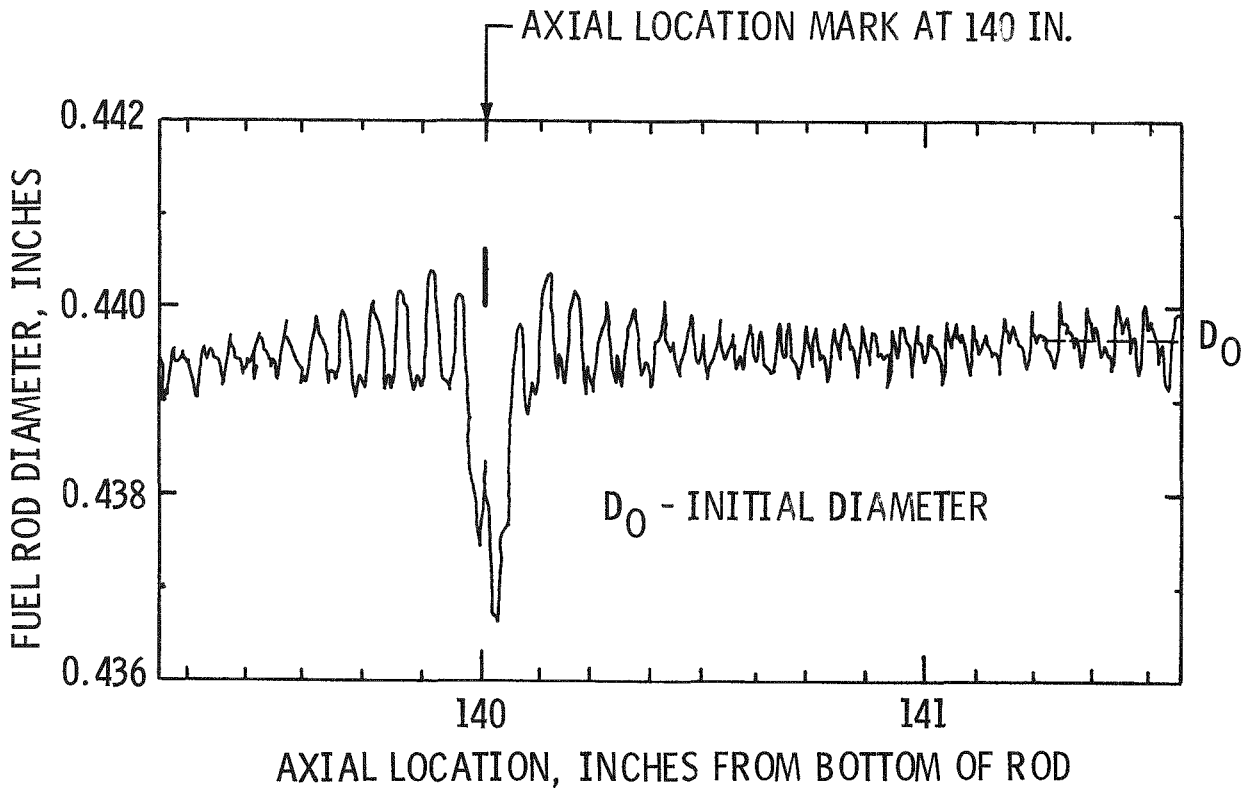

Figure 4-5
PORTION OF PROFILOMETER TRACE OF JBY-157
SHOWING AREA OF PELLET GAPS WITH
COINCIDENT HIGH OVALITY

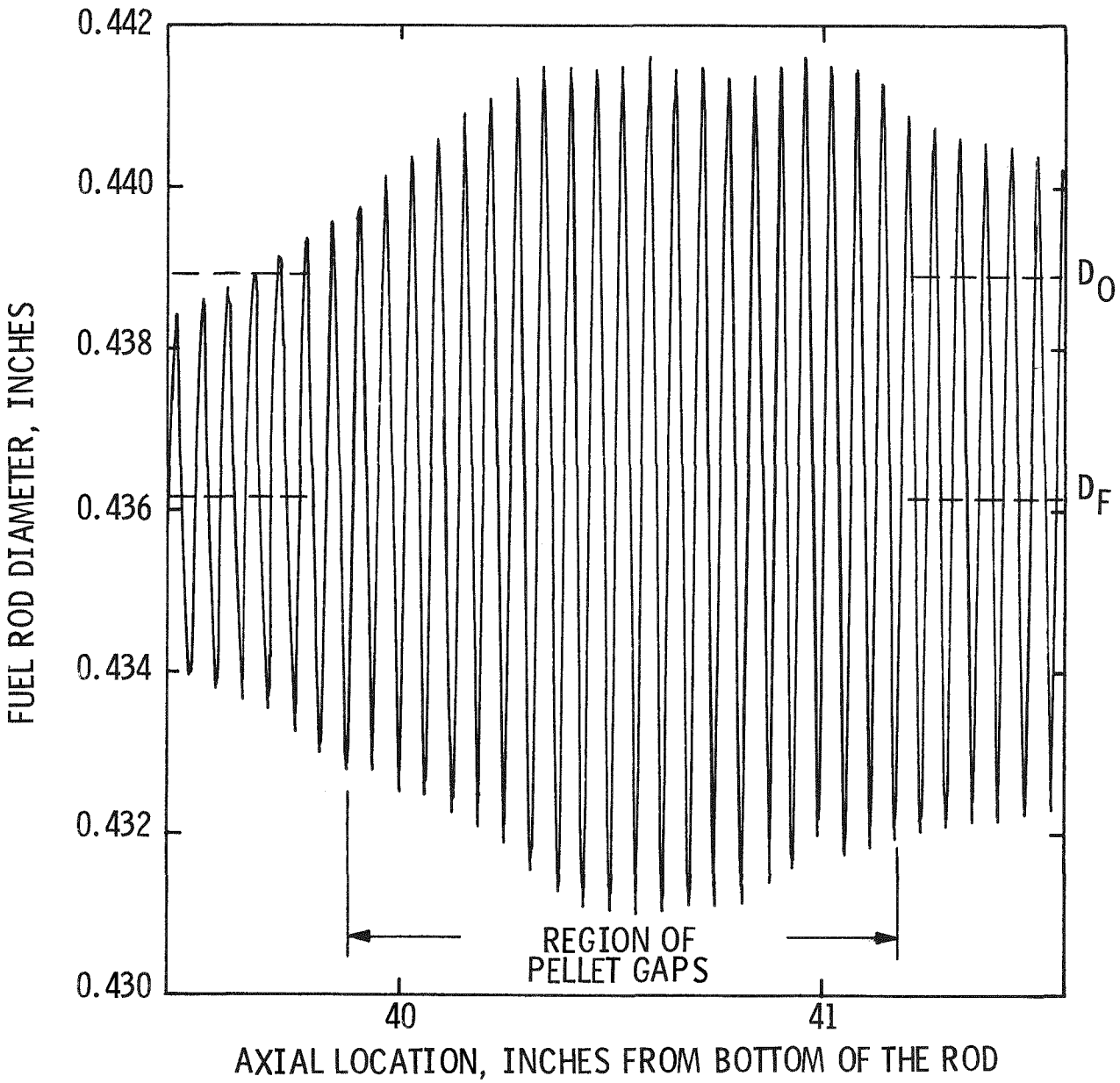

D_O - INITIAL DIAMETER
D_F - FINAL DIAMETER

Figure 4-6
PORTION OF PROFILOMETER TRACE OF JBP-027 SHOWING AREA OF PELLET GAP WITH HIGHEST OVALITY ON ROD JUST ABOVE THE GAP

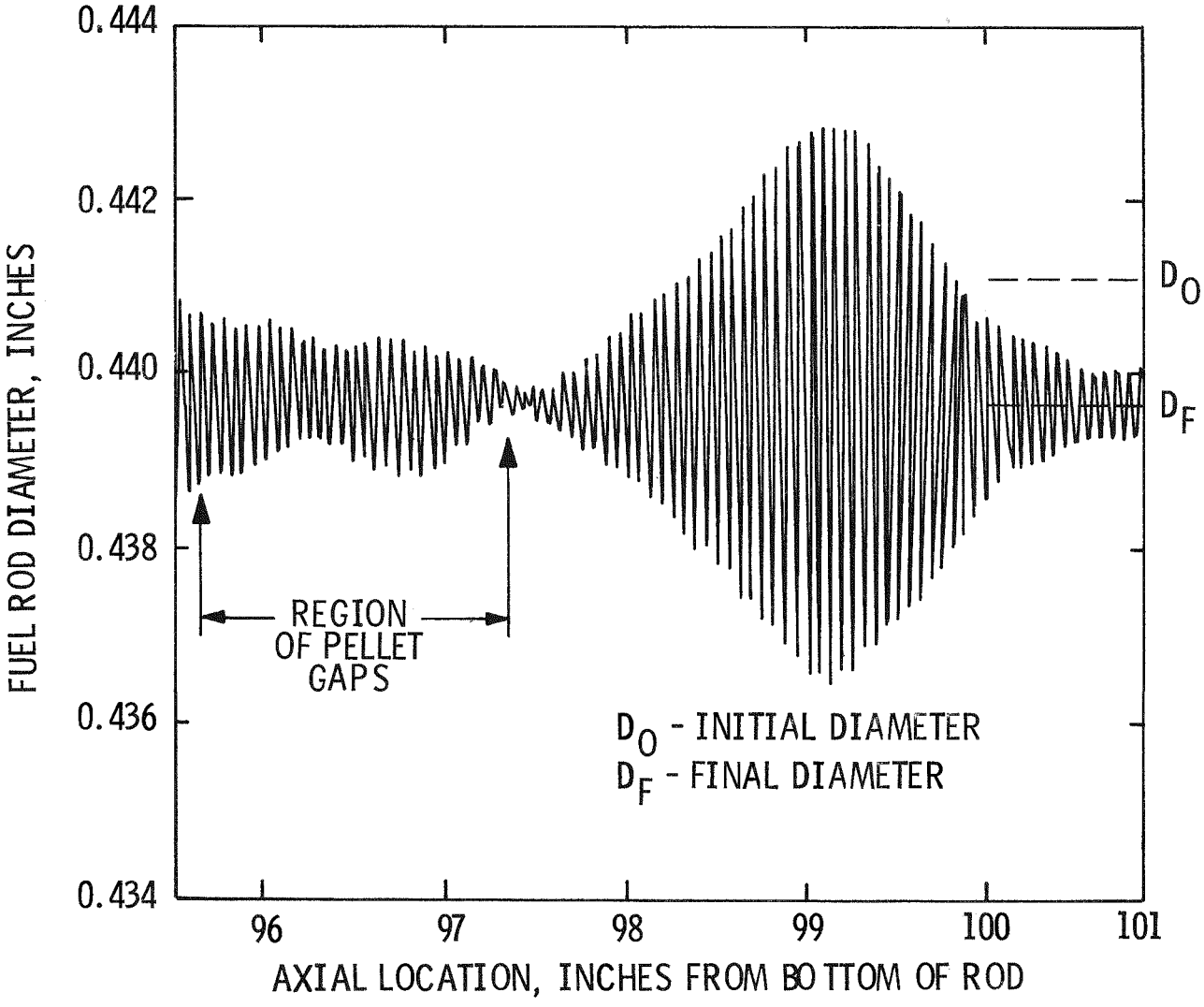

Table 4-3

Extent of Ovality in Selected Rods

Rod	Burnup	Cumulative Length of Rod Ovality in Range (in.)					Total Length (in.) with Ovality >2 mils
		<2 mils	2-4 mils	4-6 mils	6-8 mils	>8 mils	
JBP-122	13,636	25	39-7/8	37-1/2	28-1/8	12-5/8	118-1/8
JBP-027	12,826	97	41	4-3/4	1/4	None	46
JBP-005	13,231	42	50-1/2	31-1/4	12-5/8	6-1/2	100-7/8
JCN-182	12,635	100	34	9-1/8	None	None	43-1/8
JBY-157	12,935	46	41-3/4	30-7/8	18-3/4	5-5/8	97

The profilometry data also showed two significantly different degrees of rod ovality among high burnup rods. The maximum ovality in five (four from Batch B and one from Batch C) of the fourteen sound high burnup rods (>12,000 Mwd/MTU) was in the range of 4 to 7.2 mils, while the remainder had maximum ovalities in the range 10.4 to 14.6 mils.

Another observation of significance is the periodic change in the orientation of the major axis of ovality. Most of the changes in the orientation appear to be on the order of 90^{o} (i.e., the major axis shows a rotation by 90^{o}). Further, the change in orientation appears to be periodic and occurs gradually over a length of 3-4 inches. In almost all cases, the change occurs by going through a minimum in ovality. This is illustrated in Fig. 4-7 by the superposition of the linear traces in the two azimuthal orientations. The rotation in ovality is believed to be the result of the cladding tube fabrication process, which gives rise to a helical ovality pattern in the tubing. It could also be due to a small helical eccentricity in clad wall thickness, which could again be the result of the fabrication process.

4.2.3 Clad Ridging

The spiral diameter traces obtained during the first campaign showed slight indication of clad ridging on the order of 0.1 mil high in most of the fuel rods profiled. The ridges observed were predominantly located in the axial span between 70 and 120 inches from the bottom of the rods. A few pronounced ridges approximately 0.25 mil high were also found. Fig. 4-8 shows, for example, the more prominent ridges observed in Rod JBP-005.

Figure 4-7 SUPERPOSITION OF LINEAR DIAMETER TRACES AT 0^{o} AND 90^{o} FROM ROD JBY-097 SHOWING ROTATION IN FUEL ROD OVALITY

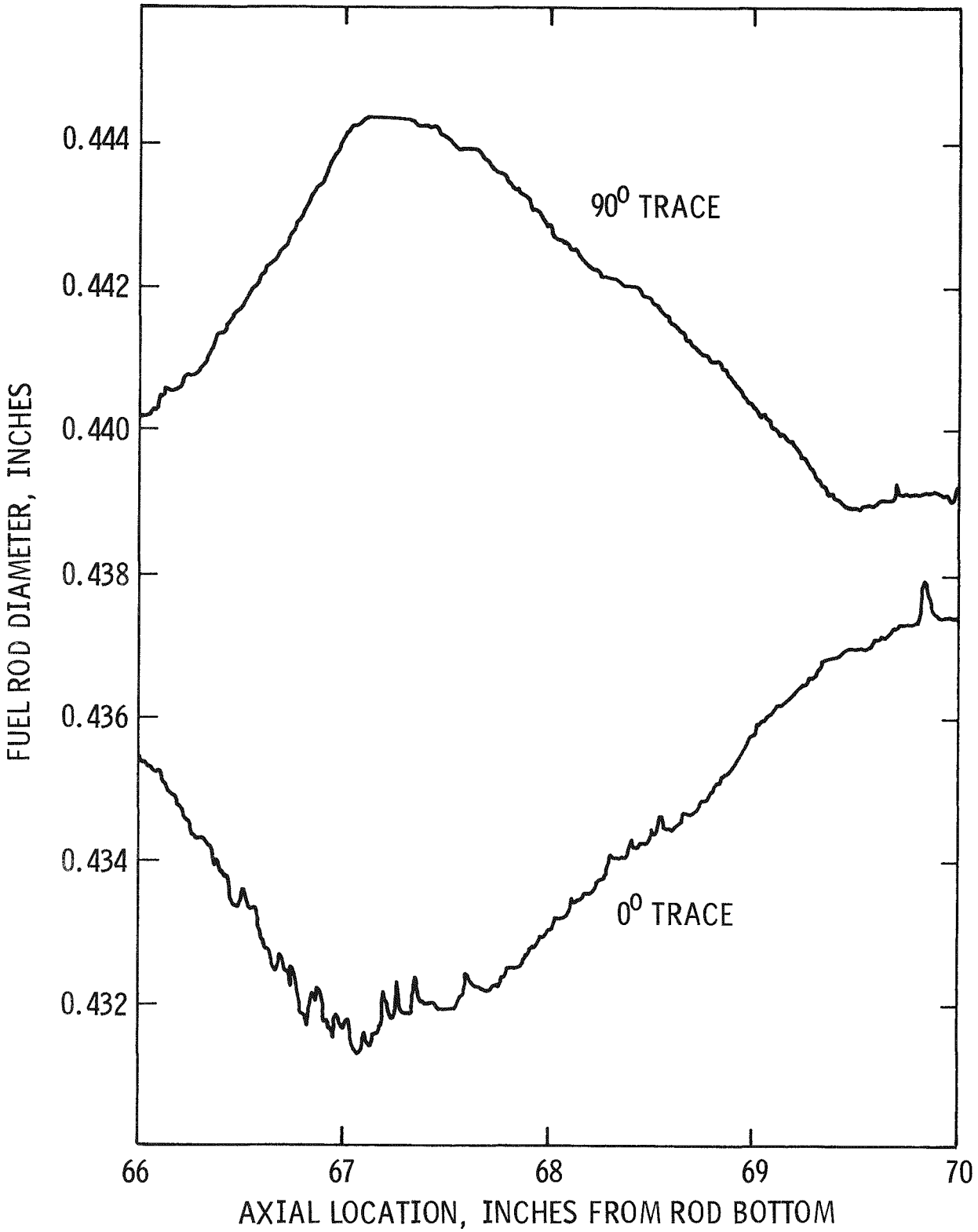

Figure 4-8
PORTION OF PROFILOMETER TRACE OF JBP-005
SHOWING FUEL PELLET RIDGING

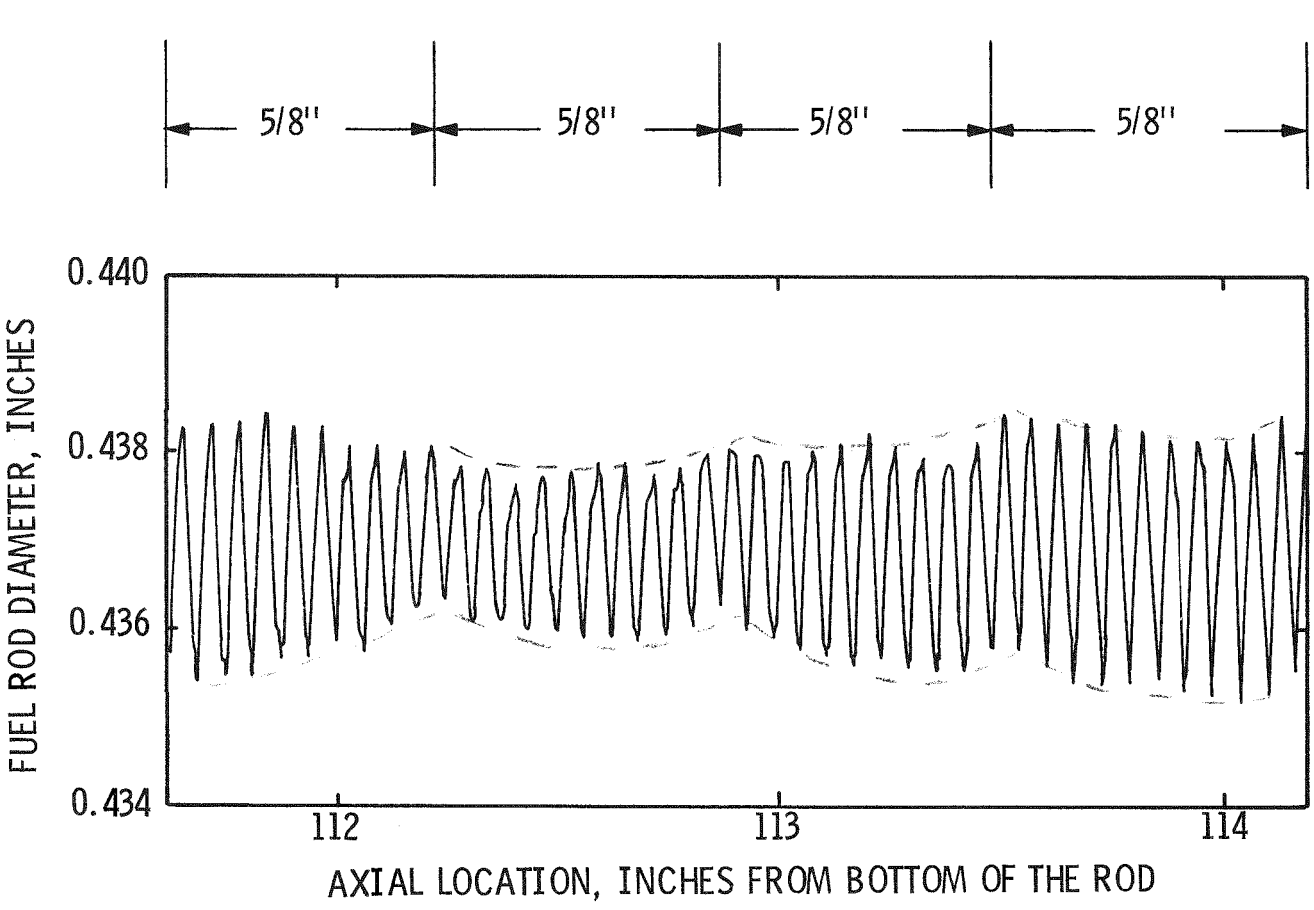

Linear diameter traces were obtained on two rods during the second campaign which more clearly showed the presence of clad ridging (ridges of up to 0.4 mils were observed). For example, Fig. 4-9 shows the clad ridging observed at pellet interfaces in Rod JBY-097. Note that additional ridges are seen away from pellet interfaces. These are believed to be related to the transverse pellet cracking pattern seen during longitudinal clad slitting and examination of fuel rods. Another observation of significance is the presence of ridges mostly at the minor axis of clad ovality as seen in Fig. 4-9. The fact that clad ridges are less frequently observed on the major axis of the clad ovality ellipse indicates that the ridges are real (i.e., not caused by crud particles) and are not continuous over the fuel rod circumference.

It is believed that the observation of clad ridging is significant from the point of view of identifying mechanisms for clad perforations. For example, the clad ridge in the 0^{o} linear trace shown in Fig. 4-9 at 88 in. from the bottom of Rod JBY-097 corresponds to the location of an incipient cladding crack observed by metallography (see also Section 4.8). The coincidence of pronounced clad ridging and an incipient crack lends support to the pellet-clad interaction-related mechanism.

4.2.4 Clad Creepdown

Table 4-2 summarizes the extent of diameter decrease obtained from the profilometer traces by assuming that the irradiated rod diameter in the plenum area (140 in. from the bottom of the rod) is representative of the as-fabricated rod diameter. These data indicate that the maximum diameter decrease for a fuel rod average burnup of approximately 13,000 Mwd/MTU is in the range of 2 to 3 mils.

Figure 4-9
SUPERPOSITION OF LINEAR AND SPIRAL DIAMETER TRACES
SHOWING CLAD RIDGING AT PELLET LENGTH INTERVALS
IN ROD JBY-097

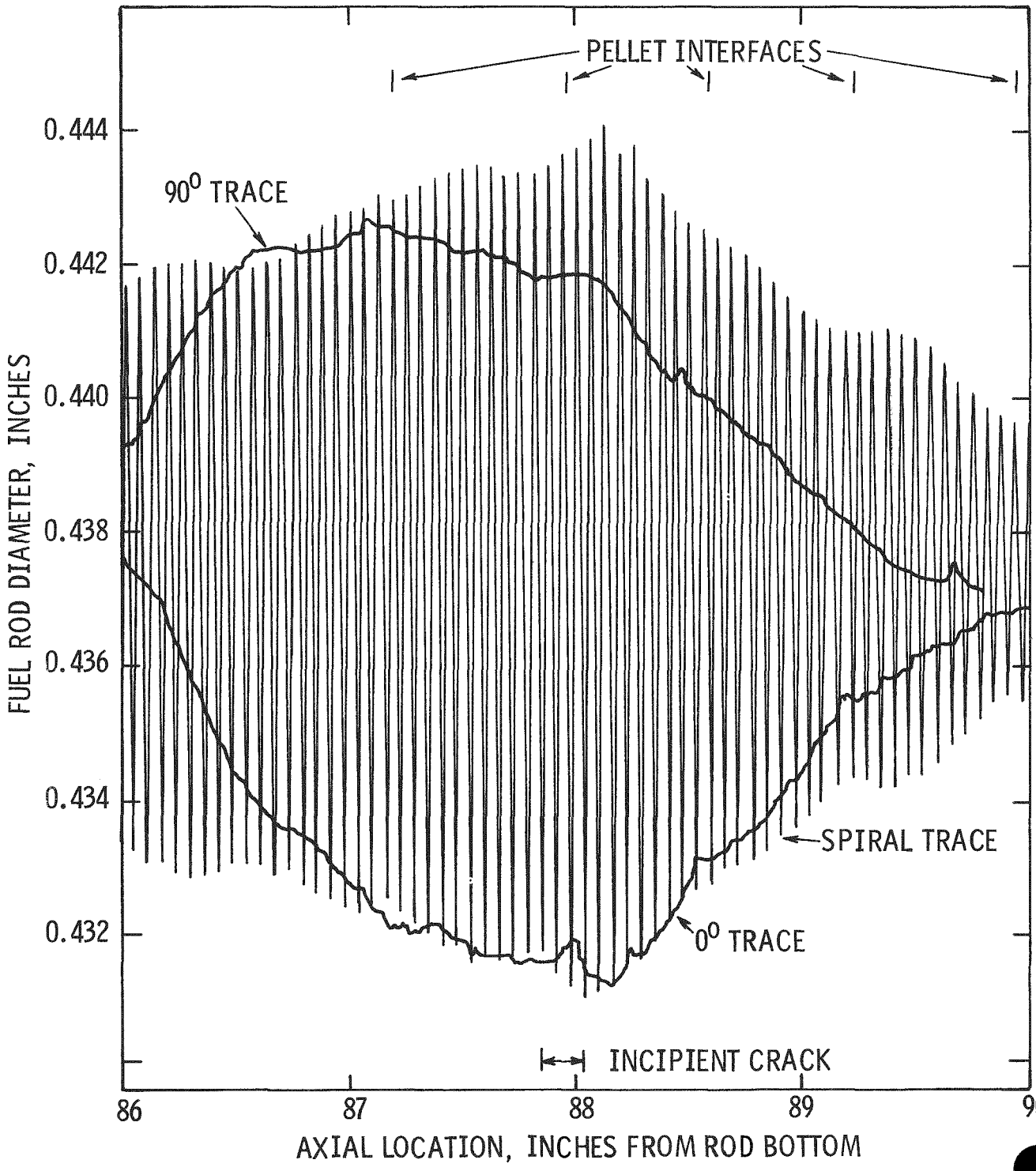

Four high burnup sound rods, namely, JCN-199, JCN-182, JCN-196 and JBP-027 exhibited less creepdown and significantly lower maximum ovalities (4 to 6.4 mils) compared to other sound rods of similar burnups. The fractional fission gas release in all four fuel rods was relatively high, 12.4% to 15.3% (see Section 4.4), but the lower creepdown could not be accounted for by the relatively higher rod internal pressure due to released fission gases. It should be noted that four other high gas release rods, JBP-122, JBP-005, HBU-169 and JBY-097, exhibited creepdown and ovalities similar to those of low gas release rods. Additional discussion of the profilometry data is presented in Section 6 (Data Analysis) of this report.

Also included in Table 4-2 are the data obtained for two of the perforated fuel rods, KCA-109 and JBP-003. It is likely that with perforated cladding the creepdown process is arrested as pressure equalization occurs. The data on diametral decreases, therefore, suggest that the cladding of Rod KCA-109 (the only perforated Batch C rod) was breached very early-in-life, and the cladding of Rod JBP-003 was perforated later-in-life.

4.3 Visual Examination

During the hot cell examination campaigns, a total of 26 (5 perforated and 21 sound) fuel rods were visually examined, and photographs were taken of penetration regions in perforated rods, crud deposits, and grid contact regions. In general, the observations of fuel rod appearance made during hot cell visual examination were in agreement with those made during poolside examination.

4.3.1 Sound Rods

The general appearance of the sound fuel rods was considered very good with no surface anomalies such as bumps, kinks or gouges. The crud on these rods was of two types:

1. An adherent deposit usually consisting of a very thin, blackish-grey material. Occasionally, heavier patches of red-orange crud were also seen. The thickness of most of the patches was estimated to be less than 0.1 mil based on the inability to detect crud in profilometry measurements.

2. Flaky light-tan crud which could be easily brushed off.

The hot cell examination confirmed the crud distribution observed at poolside in that the deposits appeared more textured at the lower elevations of the rods. "Plume-like" flow patterns were seen to some degree above each grid location but were more pronounced just above the retention grid (the lower most grid) and the lower spacer grids. Little or no crud deposition was observed in the plenum regions.

The amount of the adherent crud observed in the hot cell appeared to be the same as that observed during poolside examinations. However, the amount of light-tan flaky crud was considerably less that that observed during poolside examinations, probably due to losses during handling. Fig. 4-10 through 4-13 show typical appearance of various types of crud observed on the fuel rods during visual examination. In addition to the two types of crud, bands of crud were observed on several of the fuel rods. Fig. 4-14 shows a typical appearance of crud band observed in Rod JBY-157. A gamma scan of this region indicates the band is associated with a gap in the pellet stack caused by fuel densification (see Fig. 4-19).

4.3.2 Perforated Fuel Rods

Results of visual examination of five perforated fuel rods in the hot cells are summarized in Table 4-4. A general summary of these results is presented below:

1. Blisters were observed both with and without bulges in the cladding.

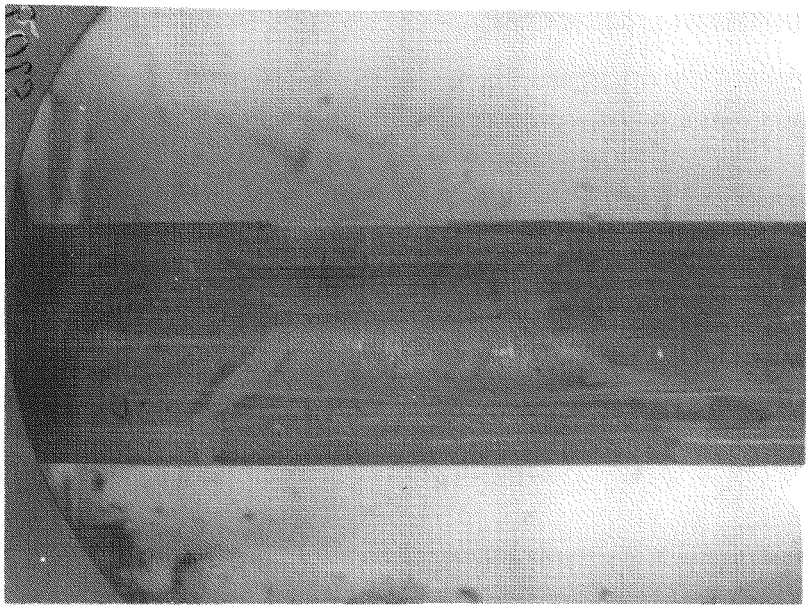

P 5709 3.5X

Figure 4-10 CRUD PATTERN IN ROD KCA-058 AT 37 3/4 INCHES

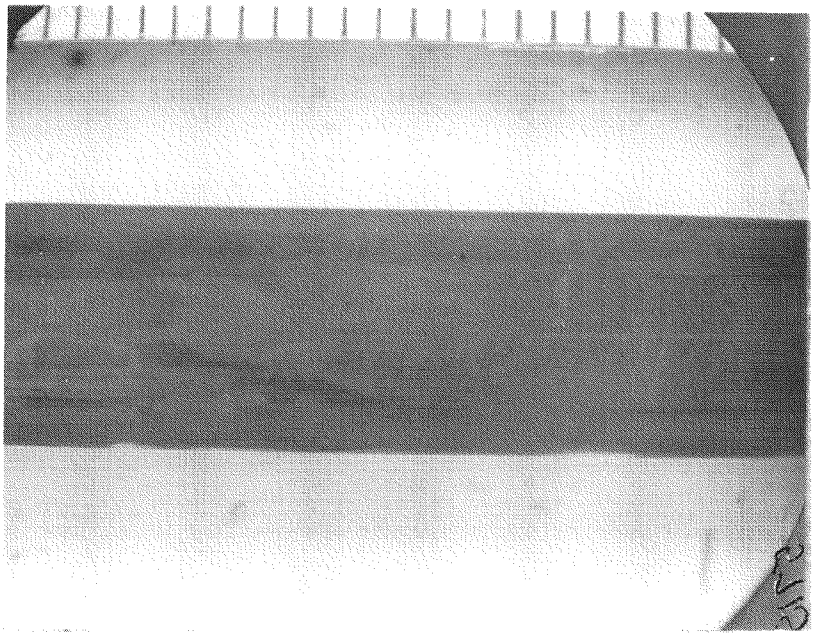

P 5715 3.5X

Figure 4-11 HEAVIER BLACK CRUD PATCH IN ROD HBV-009 AT 33 INCHES

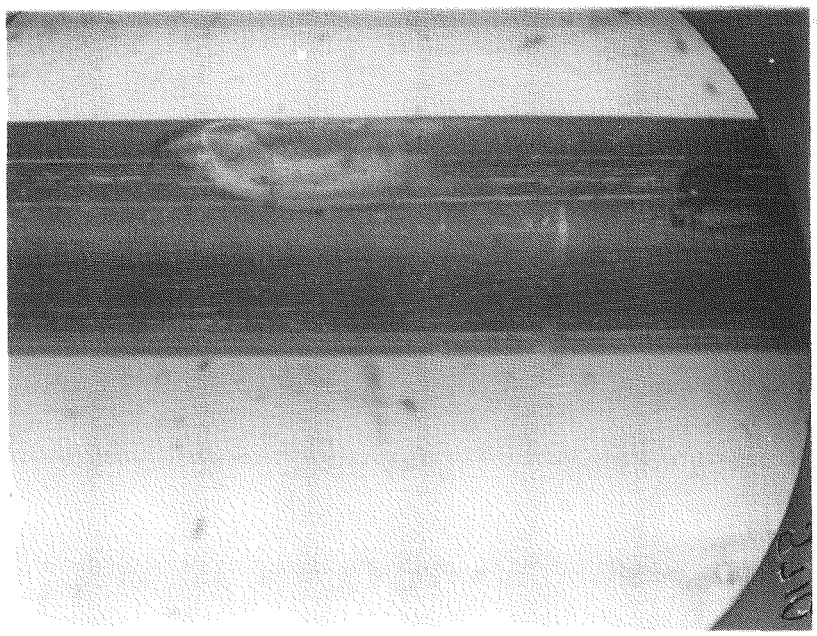

P5710 3.5X

Figure 4-12 PATCH OF BRIGHT-ORANGE COLORED CRUD IN ROD KCA-058 AT 85 1/2 INCHES

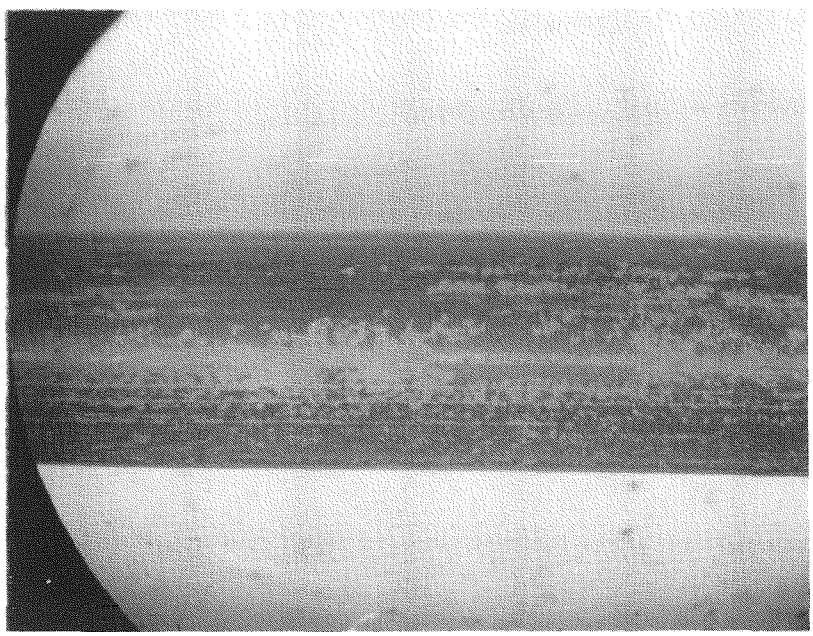

P 5716 3.5X

Figure 4-13 FLAKY CREAM-COLORED CRUD IN ROD HBV-009 AT 93 3/8 INCHES

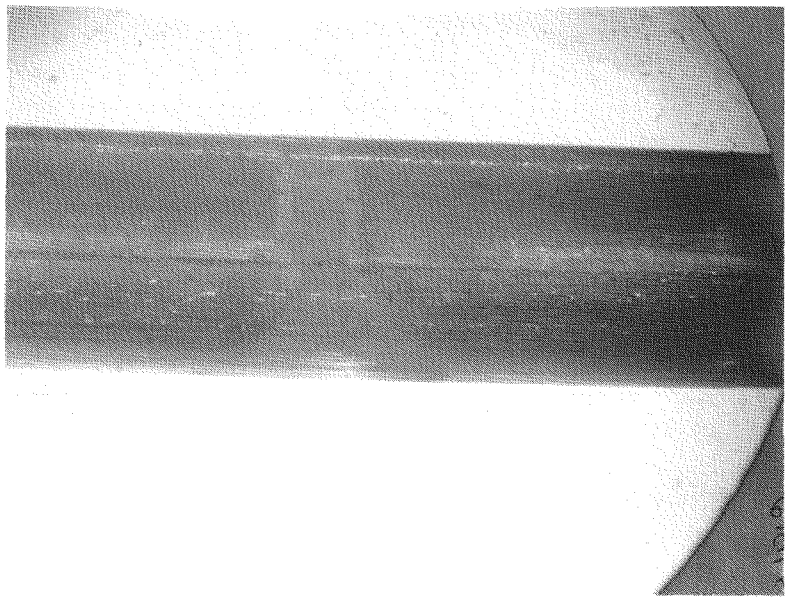

C1964 3.5X

Figure 4-14 APPEARANCE OF A TYPICAL CRUD BAND OBSERVED IN ROD JBY-157 AT 41 INCHES

Table 4-4

Summary of Data From Hot Cell Visual Examination of Maine Yankee Perforated Fuel Rods

Rod	Location and Assembly	Burnup Mwd/MTU	Hot Cell Visual Examination-Results*
KCA-109	G10 C231	9,661	Only one defect observed. Spalled blister 0.3 in. diameter at 88-1/2 in.
JBP-003	B12 B042	13,629	Small blisters at 13, 18-3/4, bulge at 88-3/4, cracked blister at 91-1/4, blister perforation (0.2 in. diameter) at 101-1/4, other blister-like areas at 38 and 76-3/8.
JCN-151	N2 B069	12,744	Defects observed are perforation (0.2 in. dia.) at 96-1/8, blister at 127-3/4, possible blisters at 58-1/2, 65-1/2, 65-3/4, 91 and 97 in. The bottom end cap broke off during poolside exam.
JBY-145	M12 B069	13,535	Bulges at 1-5/8, 2-5/8, blisters at 42-11/16, cracked blister (0.3 in. dia.) at 82-3/8, blister at 91, possible blister at 138-7/8.
JBP-004	G9 B042	12,896	Blisters at 73-1/8, 73-1/2, 83-3/16, 83-1/2, 101-1/2, 101-3/4, and 102-3/4. Blister-like areas at 108-5/16, 69-9/16, and 90-3/4.

* Defect locations are in inches from the bottom of the rod.

2. The blisters appear to be located predominantly in the span 70 to 105 inches from the bottom of the rod, although a few small blisters and bulges have been observed at other locations.

3. No cracks or splits in the cladding were observed except at large blister areas.

4. In general, the blister appearance and location observed at the hot cells is in good agreement with similar data taken at poolside.

Fig. 4-15 through 4-18 show the appearance of blisters and bulges observed in the perforated fuel rods.

4.4 Fuel Rod Puncture and Gas Collection

During the two hot cell examination campaigns, sixteen (16) fuel rods (ten from Batch B, five from Batch A, and one from Batch C) were punctured and the gases from these rods were collected and analyzed to determine the fractional fission gas release.

4.4.1 Procedure

The procedure used for puncturing these rods is summarized below:

1. The fuel rod is inserted through the gas tight punch chamber and sealed with teflon seals and brass nuts at each end of the chamber.

2. The entire system, punch chamber, expansion system, pressure gauges, and collection system is evacuated to a few microns pressure (generally $<5\mu$ Hg). Leak rates are established for both the in-cell portion of the system and out-of-cell portion of the system.

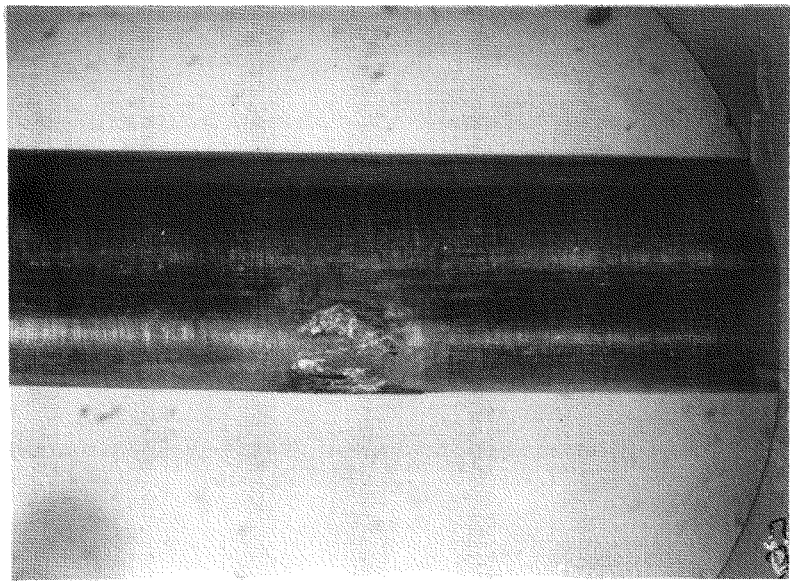

P5802 3.5X

Figure 4-15 APPEARANCE OF THE BLISTER AREA AT 101 1/4 IN. ROD JBP-003

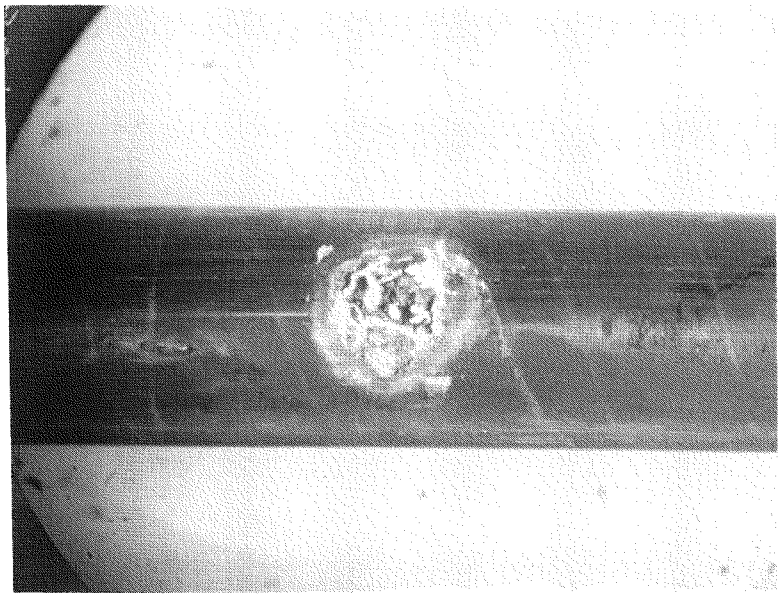

C1933 3.5X

Figure 4-16 PERFORATED BLISTER AT 88 1/2 IN. IN ROD KCA-109

C1994 3.5X

Figure 4-17 BULGED AREA AT 1 5/8 IN. IN ROD JBY-145

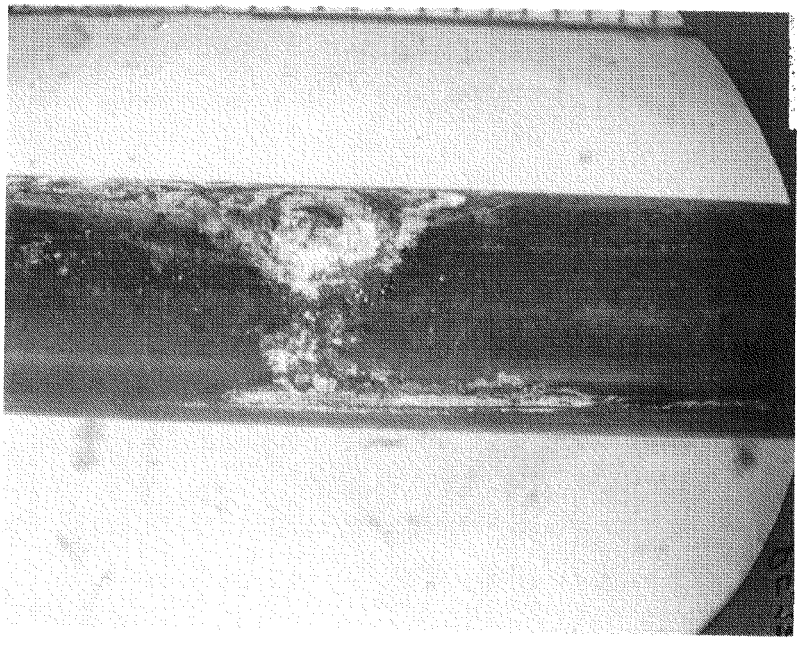

P5738 3.5X

Figure 4-18 PERFORATED BLISTER AREA AT 96 1/8 IN. ROD JCN-151

3. The system is again evacuated, the punch system pressure is recorded along with in-cell punch chamber temperature and collection vial temperature, and the rod is punctured.

4. Pressure readings from either the high pressure or low pressure gauge (depending on the amount and pressure of the gas in the rod) are recorded at the time of puncture at 2 min. and at 5 min. intervals, thereafter, until the system equilibrates.

5. The rod gas is expanded into a calibrated volume, and a second pressure is recorded. From these data and the rod void volume measured in a subsequent operation, the amount of gas contained in the rod can be calculated.

6. The rod gas is then expanded into the collection system and Toepler-pumped into two glass collection bulbs. These bulbs are removed from the system, and one is submitted for mass spectrometric analysis, and the other is retained as a backup.

The fuel rod void volume is then determined by backfilling of the punch chamber and the fuel rod to about 80 psi with helium and expanding into the calibrated volume. This procedure is repeated 10 times. Similar data are obtained by filling the chamber prior to puncturing the fuel rod, and the fuel rod void volume is determined from the difference between the two volumes.

4.4.2 Results

Tables 4-5 and 4-6 present the data obtained in the overall program. The leak checks performed during fuel rod puncture and the presence of the original He fill gas in the collected gas compositions shown in the tables confirmed that the rods listed were, indeed, free of through-wall penetrations. It can be seen that two categories of gas release values exist among high burnup rods, namely, high (11.3-15.3%) and low (<1%). The high gas release population included 7 of the 10 Batch B rods shipped to the hot cell and one Batch A rod. Because high gas release had only been observed among high burnup Batch B rods in the 1st campaign, it was at first surprising that a Batch A fuel rod (HUB-169) should have exhibited high fractional release. Examination of the pre-irradiation data on this rod showed the fuel stack weight to be significantly less than the nominal value. The equivalent fuel density calculated from the stack weight indicated that the average fuel density in Rod HBU-169 was 91.5% TD (compared to the nominal value of 93% TD). The propensity for in-pile densification in this type of fuel is expected to be greater the lower its density, and the post-irradiation density measurements obtained on fuel samples from this rod (see Section 4.11) show that the fuel has densified by about 5% TD. The stack shortening data obtained from the gamma scans of this rod also confirm the high propensity for densification of the fuel in Rod HBU-169. (See Section 4.5).

The significance of high gas release found in Rod HBU-169 is that it supports the densification-related reduction in fuel rod heat transfer mechanism proposed in Section 6 to explain the two distinct fission gas release populations.

Table 4-5

Fission Gas Release Data From Maine Yankee Fuel

Rod Serial No.	Location and Assembly	Calculated Rod Avg. Burnup Mwd/MTU	Time Averaged Relative Power(4)	End-of-Life Measured Void Vol.cc	Total Volume of Gas Coll. ccSTP(1)	Volume of He Collected ccSTP	Volume of(Xe+Kr) Collected ccSTP	Calculated Volume of (Xe+Kr) Generated ccSTP	Fractional Fission Gas Release %
JBP-027	J1 B042	12,826	1.237	36.58	152.49	30.95	120.36	891.1	13.5
JBP-005	E11 B042	13,231	1.276	34.26	150.20	33.19	116.91	919.1	12.7
JBP-004	N14 B042	13,189	1.272	36.04	35.70	30.32(2)	5.35(2)	916.2	0.58
JBP-122	C13 B042	13,636	1.315	34.35	136.38	28.91	107.29	947.3	11.3
JCN-182	K1 B069	12,635	1.218	36.18	142.94	34.16	108.61	877.7	12.4
JBY-157	E11 B069	12,935	1.247	35.27	41.02	32.32	8.66	898.6	0.96
JBY-142	J5 B069	12,321	1.188	35.44	32.13	28.56	3.51	855.9	0.41
HBU-198	B6 A047	11,478	1.107	36.86	31.96	29.18	2.72	797.4	0.34
HBV-007	M10 A047	11,946	1.152	36.96	40.56	35.36	5.15	829.9	0.62
KCA-125	A14 C231	6,747	0.651	38.63	29.26	25.42	2.82	468.7	0.60
HBV-067	C13 A047	12,437	1.199	34.93	23.81	20.71	3.05	864.0	0.35
JCN-199	D2 B069	12,842	1.238	34.85	142.28	23.60(3)	118.61(3)	892.1	13.3
JCN-196	C2 B069	12,904	1.244	36.28	163.62	25.85	137.28	896.4	15.3
HBU-169	E4 A047	12,410	1.196	38.57	150.08	26.41	123.56	862.1	14.3
JBY-097	C13 B069	13,349	1.288	36.32	163.72	39.13	124.36	927.3	13.4
HBV-002	I7 A047	12,464	1.202	37.19	40.98	34.83	6.01	865.9	0.69

(1) Average of two readings.

(2) Values corrected for 4.98% of air in gas sample.

(3) Values corrected for 1.14% of air in gas sample.

(4) Relative to core average of 1.0

Table 4-6

Fission Gas Composition Data on Maine Yankee Fuel Rods

Rod Serial No.	Location and Assembly	Calculated Rod Avg. Burnup Mwd/MTU	Total Volume of Gas Coll. ccSTP[1]	Composition, Volume Percent											Fractional Fission Gas Release %
				H_2	He	CH_4	H_2O	O_2	N_2	A	CO_2	Kr	Xe	Xe/Kr	
JBP-027	J1 B042	12,826	152.49	.12	20.3	<.01	<.1	.11	.58	<.01	<.01	9.33	69.6	7.46	13.5
JBP-005	E11 B042	13,231	150.20	<.1	22.1	<.01	<.1	<.01	<.01	<.01	<.01	8.94	68.9	7.71	12.7
JBP-004	N12 B042	13,189	35.70	<.01	80.7	<.01	<.1	.98	4.00	.07	<.01	1.76	12.5	7.1	0.58[2]
JBP-122	C13 B042	13,636	136.38	<.1	21.2	<.01	<.1	<.01	<.01	<.01	<.01	9.17	69.5	7.58	11.3
JCN-182	K1 B069	12,635	142.94	.08	23.9	<.01	<.1	<.01	.02	<.01	<.01	9.18	66.8	7.28	12.4
JBY-157	E11 B069	12,935	41.02	.04	78.8	<.01	<.1	<.01	<.01	.07	<.01	2.72	18.4	6.77	0.96
JBY-142	J5 B069	12,321	32.13	<.01	88.9	<.01	<.1	<.01	.01	.08	<.01	1.40	9.55	6.82	0.41
HBU-198	B6 A047	11,478	31.96	<.01	91.3	<.01	<.1	<.01	.10	.08	<.01	1.07	7.45	6.96	0.34
HBV-007	M10 A047	11,946	40.56	<.01	87.2	<.01	<.1	<.01	.03	.06	<.01	1.52	11.2	7.37	0.62
KCA-125	A14 C231	6,747	29.26	<.01	90.3	<.01	<.1	<.01	.03	.03	<.01	1.33	8.34	6.27	0.60
HBV-067	C13 A047	12,437	23.81	<.01	87.0	<.01	<.1	<.01	.05	.07	<.01	1.53	11.3	7.38	0.35
JCN-199	D2 B069	12,842	142.88	<.01	16.4	<.01	<.1	.21	.93	<.01	<.01	9.61	72.8	7.58	13.3[3]
JCN-196	C2 B069	12,904	163.62	.2	15.8	<.01	<.1	<.01	.02	.01	<.01	10.1	73.8	7.31	15.3
HBU-169	E4 A047	12,410	150.08	.08	17.6	<.01	<.1	<.01	.03	.01	<.01	9.63	72.7	7.55	14.3
JBY-097	C13 B069	13,349	163.72	.11	23.9	<.01	<.1	<.01	.01	.01	<.01	8.96	67.0	7.48	13.4
HBV-002	I7 A047	12,464	40.98	<.01	85.0	<.01	<.1	.02	.21	.08	<.01	1.77	12.9	7.29	0.69

(1) Average of two readings.

(2) Corrected for 4.98% air leak believed to have occurred during sample analysis.

(3) Corrected for 1.14% air leak believed to have occurred during sample analysis.

4.4.3 Additional Fission Gas Release Data

In addition to the fission gas release data shown in Tables 4-5 and 4-6, puncture data only (i.e., no gas collection and analysis) were obtained from 6 low burnup sound fuel rods. Five of these were from Batch C (KCA-019, KCA-051, KCA-058, KCA-156 and KCA-185) and the other from Batch A (HBV-009). In the case of all 6 rods, the pressure of released gases was comparable to those obtained on other low gas release rods. Thus, it was concluded that the fractional release in these rods was less than 1%.

4.4.4 Pressure Testing of Perforated Fuel Rods

During the first campaign, two of the perforated fuel rods, JBY-145 and KCA-109 were pressure tested to determine whether more than one through-wall defect was present. The areas of gross cladding perforations in the two rods were covered by short tubes of larger diameter and then the ends of the short tubes were sealed off with "Swagelok" end fittings. The rods were then punctured in a manner similar to that used for sound fuel rods. The punctured rods were then pressurized with helium to 80 psi, and the entire length of each rod was checked for leaks. Rod JBY-145 was found to contain a second through-wall perforation in the bulged area near the bottom end cap. Rod KCA-109 contained no other peforations. Since the observed blister in this rod was the only breach of the cladding, its metallographic character (see Section 4.8.3.5) suggests a conclusion that primary hydriding may have been the mechanism defecting the rod.

4.4.5 Xe/Kr Ratios

The Xe/Kr ratios shown in Table 4-6 were examined to establish any trends which would identify the burnup period during which high gas release occurred in some of the rods. It is believed that a burst of gas release occurring near the end-of-life would result in a higher Xe-Kr ratio, since the fission gas inventory in the fuel would reflect fission contribution from Pu-239*. The data, however, do not show any distinct categories of Xe/Kr ratio among the high gas release rods. Instead, a gradual increase in the value of the ratio is observed with increasing fuel rod burnup. This is consistent with the postulated contribution from Pu-239 fission. It is concluded that the measured Xe-Kr ratios are not useful for determining the comparative history of gas release among the rods.

4.5 Gamma Scanning

4.5.1 Gross Gamma Scans

During the first hot cell examination campaign, eleven fuel rods were gross gamma scanned to detect anomalies associated with the fuel stacks and to determine the relative burnup profile of the various fuel rods. The gamma scan charts showed that almost all the fuel rods contained very small distributed gaps at fuel pellet interfaces. Several large gaps were observed with the largest gap being approximately 0.4 inches. Fig. 4-19 and 4-20 show the gamma activity traces obtained on two rods, JBY-157 and JBP-027, in the region of the gaps.

The relative gamma activity observed among the various rods appeared to be consistent with the calculated rod average burnups for the rods. The peak gamma activity in all fuel rods was found to be in the region between 95 and 105 inches from the bottom of the rod.

---

* The Xe/Kr ratio from U-235 fission is approximately 7, while that from Pu-239 fission is approximately 15.

Figure 4-19
PORTION OF GAMMA SCAN OF JBY-157
SHOWING PELLET GAPS

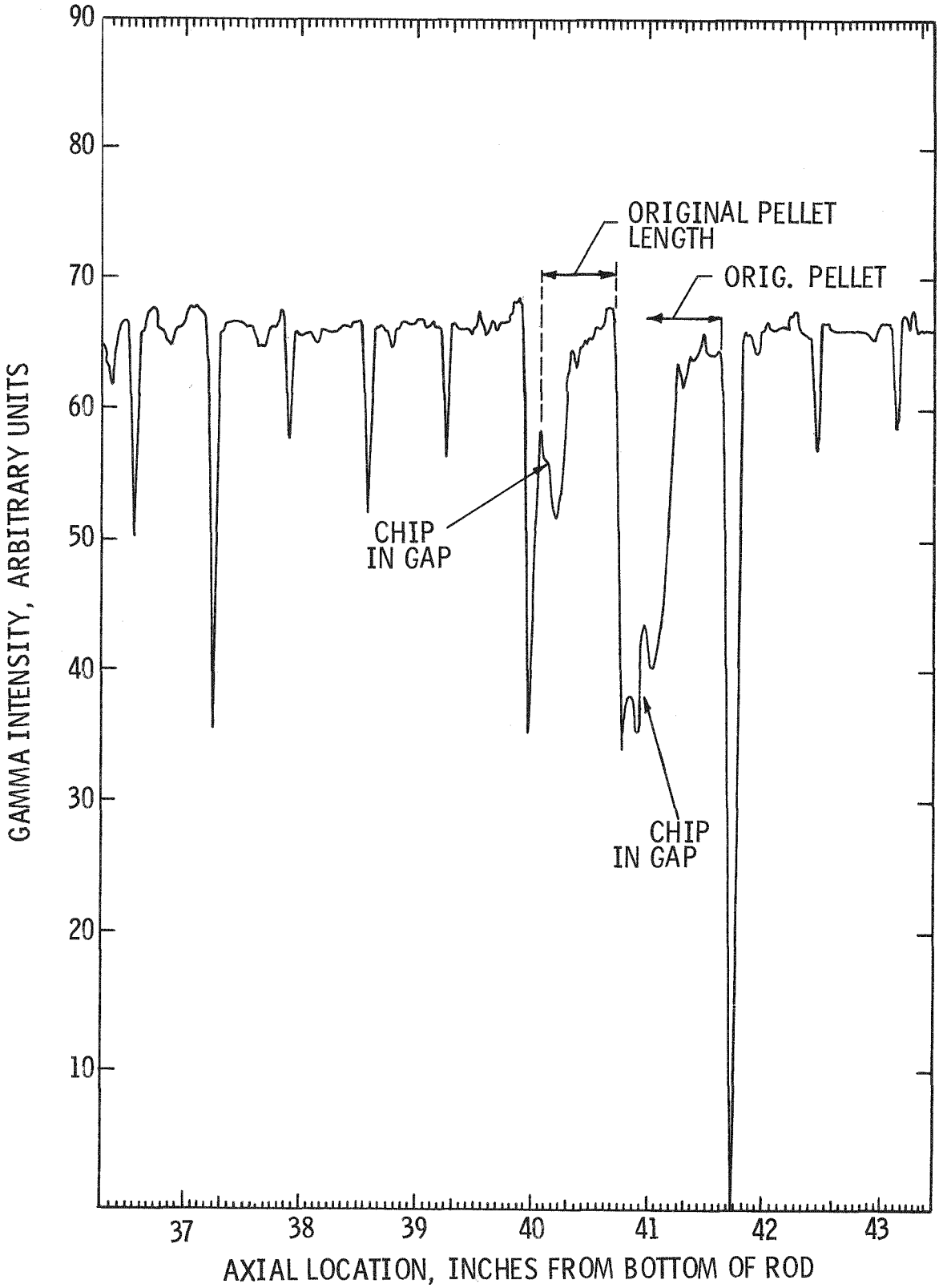

Figure 4-20
PORTION OF GAMMA SCAN OF JBP-027
SHOWING PELLET GAPS

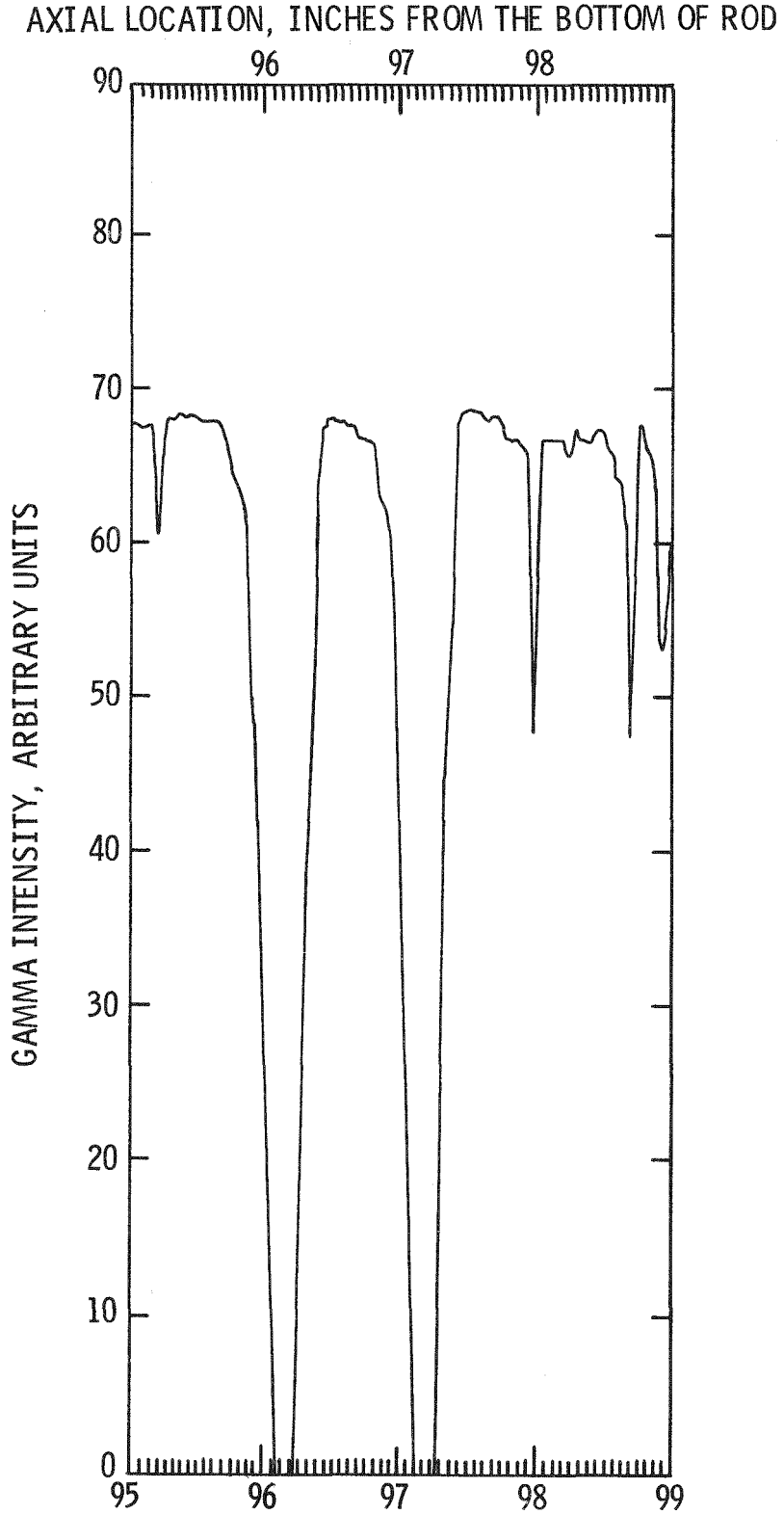

4.5.2 Specific Isotope Gamma Scans

4.5.2.1 Basis for Specific Isotope Approach

During the second hot cell examination campaign, ten fuel rods were scanned for gamma activity of the specific isotopes: Cs-137, Zr/Nb-95 and Cs-134. The decision to scan for specific isotopes was based on the results from the first campaign, as summarized below:

1. The results from visual examination of cladding internal surfaces and from fuel-clad metallography of specimens from high gas release rods showed significant amounts of fuel bonded to the cladding. Microprobe examination of one such bonded fuel area showed the presence of cesium-rich layer between the fuel and zirconium oxide layer. Thus, it was concluded that fuel bonding was associated with migration of fission product cesium to the cooler parts of the fuel pellets and deposition of cesium at pellet interfaces.

2. Some cesium redistribution was suspected when some of the gross gamma scans exhibited small peaks at pellet interfaces in Rods JCN-196 and JBP-005. During the first campaign, the gamma scan of Rod JBP-005 was repeated approximately 3-1/2 months after the first scan. As expected, the gamma activity was significantly lower and the collimator window was adjusted to increase the measured gamma activity. While the axial shape of the gamma activity profile remained the same, a larger number of spikes were observed at pellet interfaces. These spikes were attributed to fission product cesium which migrates to pellet interfaces during irradiation.

3. A comparison of the calculated burnup profile with the gross gamma scan of a given rod suggested that the gross gamma activity in the first campaign was predominantly from isotopes of shorter half-life (such as Zr/Nb-95). This implied that the gross gamma activity profile represents a later-in-life power history, rather than the life-averaged power history. It was believed that the distribution of cesium-137 in view of its longer half-life ($\sim$29 years) would more accurately represent the life-averaged burnup history of the rod.

The specific isotope scans were performed using a lithium-drifted germanium crystal. Table 4-7 shows the list of fuel rods scanned and the specific isotopes measured.

4.5.2.2 Sound Fuel Rod Results

An examination of the specific isotope gamma scans obtained on the sound fuel rods showed the following:

1. Strong periodic peaks of Cs-137 activity are observed in the scans of high gas release rods located at pellet interfaces which are discerned from Zr/Nb-95 scans (these show depressions at pellet interfaces). It is believed that the observed cesium peaking is the result of the release of cesium from the fuel pellet during operation and subsequent deposition on the cladding at pellet interfaces. Subsequent examination (including gamma scanning) of the cladding inner surface from the high gas release rod (see Section 4.7) supports this conclusion.

2. No Cs-137 peaking at pellet interfaces is observed in low gas release rods. Typical Cs-137 scans of high and low gas release rods at similar high power locations are compared in Fig. 4-21, demonstrating the marked difference in peaking. Also shown is the Zr/Nb-95 scan of the high gas release rod at the same axial location.

3. The axial extent of cesium peaking in high gas release rods typically ranges from 6 to 128 inches from the bottom of the fuel rod. This range is the same as that observed for the axial extent of equiaxed grain growth in the high gas release rods (discussed further in Section 4.8), confirming the association between high fuel temperatures and cesium redistribution.

4. The axial profile of Cs-137 in the high gas release rods is very similar to that in low gas release rods of comparable burnup, indicating an absence of gross axial migration of cesium.

Table 4-7

Summary of Maine Yankee Fuel Rod Isotopic Gamma Scanning

Rod Number	Gas Release Category	Isotope Scans
HBU-169	High	Zr/Nb-95 (complete rod) Cs-137 (complete rod) Cs-134 (complete rod)
JCN-196	High	Zr/Nb-95 (complete rod) Cs-137 (complete rod) Cs-134 (top 40 in.)
JBY-097	High	Zr/Nb-95 (complete rod) Cs-137 (complete rod) Cs-134 (top 40 in.)
JBP-004	Low	Zr/Nb-95 (complete rod) Cs-137 (complete rod) Cs-134 (top 40 in.)
JBY-145	Perforated Rod	Cs-137 (complete rod)
JBP-003	Perforated Rod	Zr/Nb-95 (complete rod) Cs-137 (complete rod)
JBP-044	Perforated Rod	Cs-137 (complete rod)
JBP-122	High	Cs-137 (complete rod) Cs-134 (top 40 in.)
KCA-019	Low	Cs-137 (complete rod)
HBV-002	Low	Cs-137 (complete rod)

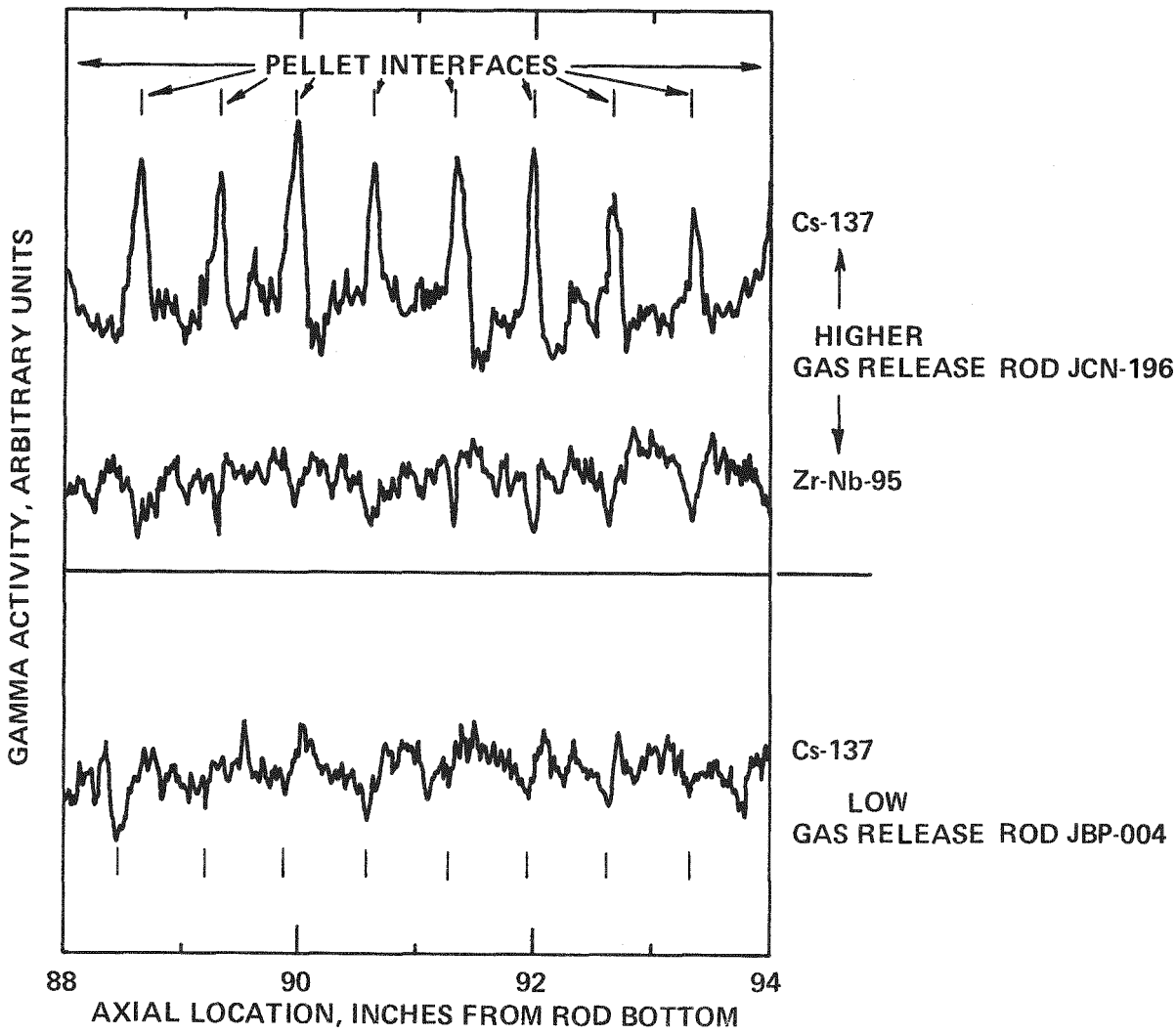

Figure 4-21
PORTIONS OF Cs-137 SCAN FROM THE PEAK POWER POSITION (88-94 IN) OF HIGH AND LOW GAS RELEASE RODS SHOWING THE DIFFERENCE IN Cs PEAKING AT PELLET INTERFACES

5. The axial distribution of Zr/Nb-95 is significantly different from that of Cs-137. Figure 4-22 shows the axial distribution of Cs-137 and Zr/Nb-95 in Rod JCN-196. Also shown for comparison is the distribution of gross gamma activity. It can be seen that the gross gamma activity scan is more similar to that of Zr/Nb-95, and the axial shape of these two scans are also similar to the axial power shape experienced by the fuel rod near the end-of-life. This confirms that the gross gamma scan represents power distribution near the end-of-life rather than the life-averaged burnup distribution. In view of its long half-life and observed lack of gross axial migration, the distribution of Cs-137 is believed to represent a life-averaged axial power shape and hence, the burnup distribution in the fuel rod. This aspect was confirmed by burnup data obtained from this rod which is discussed in Section 4.12. The significance of these results is that where there is a substantial shift in the axial power profile during reactor operation, the gross gamma scan cannot be used as an indicator of life-averaged power unless the measurement is made after the short-lived isotopes (e.g., Zr/Nb-95) are allowed to decay to relatively low levels.

4.5.2.3 Perforated Rods Results

The Cs-137 scans of the three perforated fuel rods exhibited cesium peaking at pellet interfaces similar to the high gas release rods. The axial range of peaks was also similar to that of the high gas release rods. However, the absolute level of activity exhibited significant variations as a function of axial position, when compared with a sound rod. This is probably due to further redistribution of cesium caused by reaction between cesium-rich fuel areas and the coolant water that entered the fuel rods.

4.5.3 Stack Length Changes

Fuel stack length changes, presented in Table 4-8, were obtained from the gross and specific isotope gamma scans. Also shown are the total length of gaps measured from the scans. It should be noted that all fuel rods exhibited a decrease in fuel stack length with the values ranging from 0.52 to 1.43%. The extent of stack length decrease is consistent with the expected amount of fuel densification. The largest

Figure 4-22

COMPARISON OF GROSS GAMMA SCAN PROFILE WITH SPECIFIC ISOTOPE GAMMA SCANS FOR ROD JCN-196

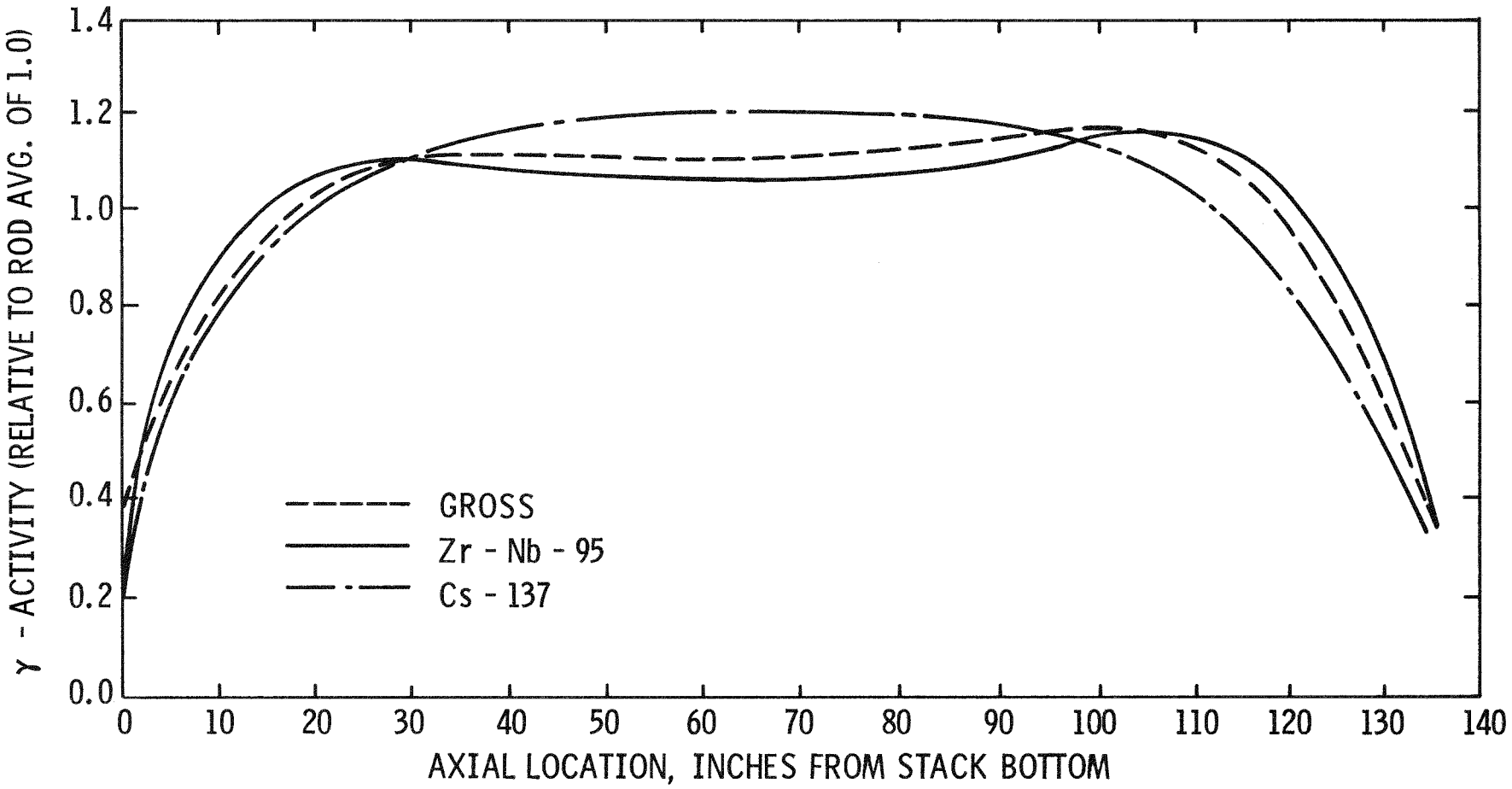

Table 4-9

Axial Locations of Eddy Current Defect Indications in the Sound Fuel Rods

Rod	Location and Assembly	Location of Indication*	Remarks
JCN-182	K1 B069	78-5/16 to 78-3/8	Long indication--similar signal was observed during poolside tests.
		81-1/2	Weak signal--not observed during poolside tests.
		76-13/16	Weak signal--not observed during poolside tests.
		74-7/16	Weak signal--not observed during poolside tests.
JCN-199	D2 B069	92-5/16	Corresponding poolside indication @ 91-3/16.
		87-1/2	Not observed at poolside.
		48-27/32	Not observed at poolside.
JBY-142	J5 B069	90-1/16	Not observed at poolside.
		87-9/32	Corresponding poolside indication @ 89-7/16.
		37-5/8	Corresponding poolside indication @ 37-5/16.
JBY-157	E11 B069	40-5/16	These indications were also seen at poolside. The locations coincide with gaps in fuel column observed in the gamma scan trace.
		40-5/32	
JBP-005	E11 B042	94-3/16	Several other weak signals were observed. All but one of these were seen at poolside.
		37-7/16	

* All locations are in inches from the bottom of the rod.

Figure 4-23

EDDY CURRENT TRACE OF ROD JCN-182 AT 100 KHZ SHOWING STRONG INTERNAL SURFACE INDICATION BETWEEN 78 5/16 AND 78 3/8 IN FROM THE BOTTOM

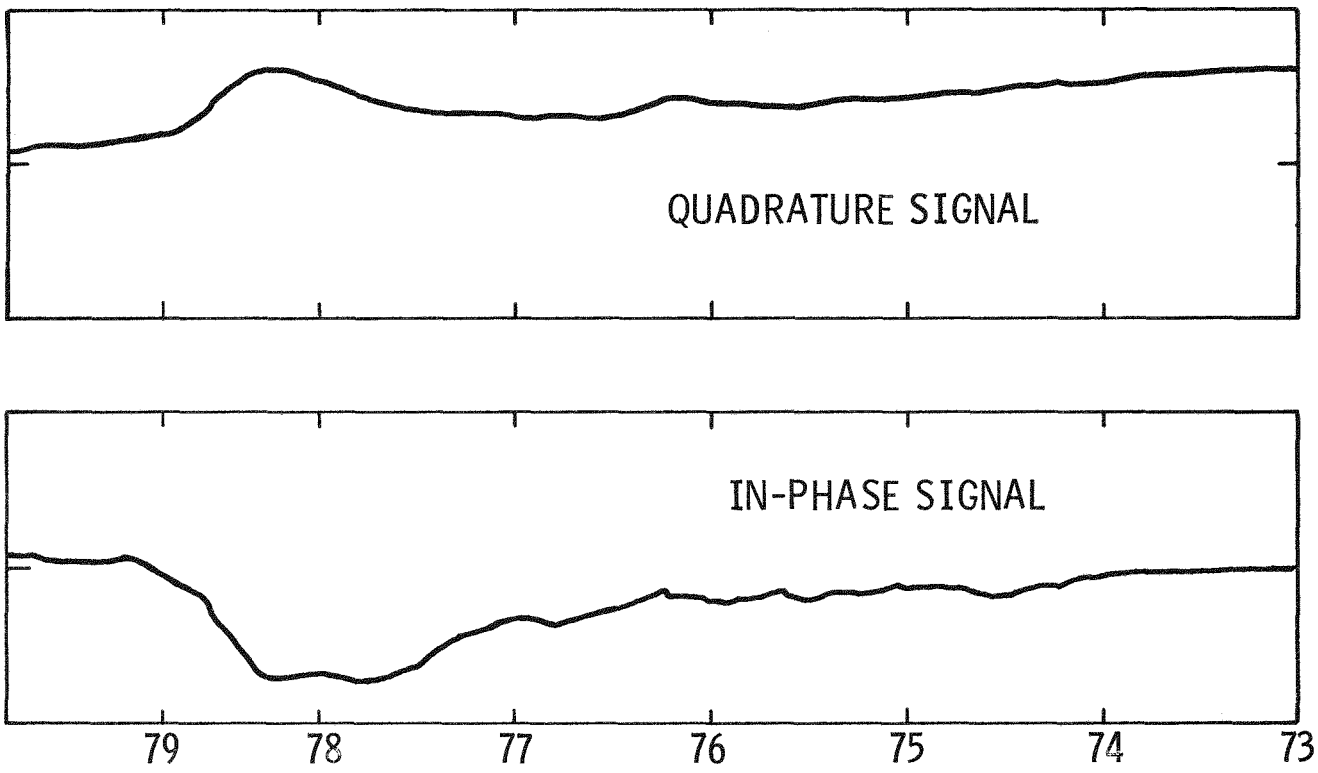

Figure 4-24
EDDY CURRENT TRACE OF ROD JCN-199 AT 100 KHZ SHOWING INDICATIONS AT 92 5/16 AND 87 1/2 IN FROM BOTTOM OF ROD

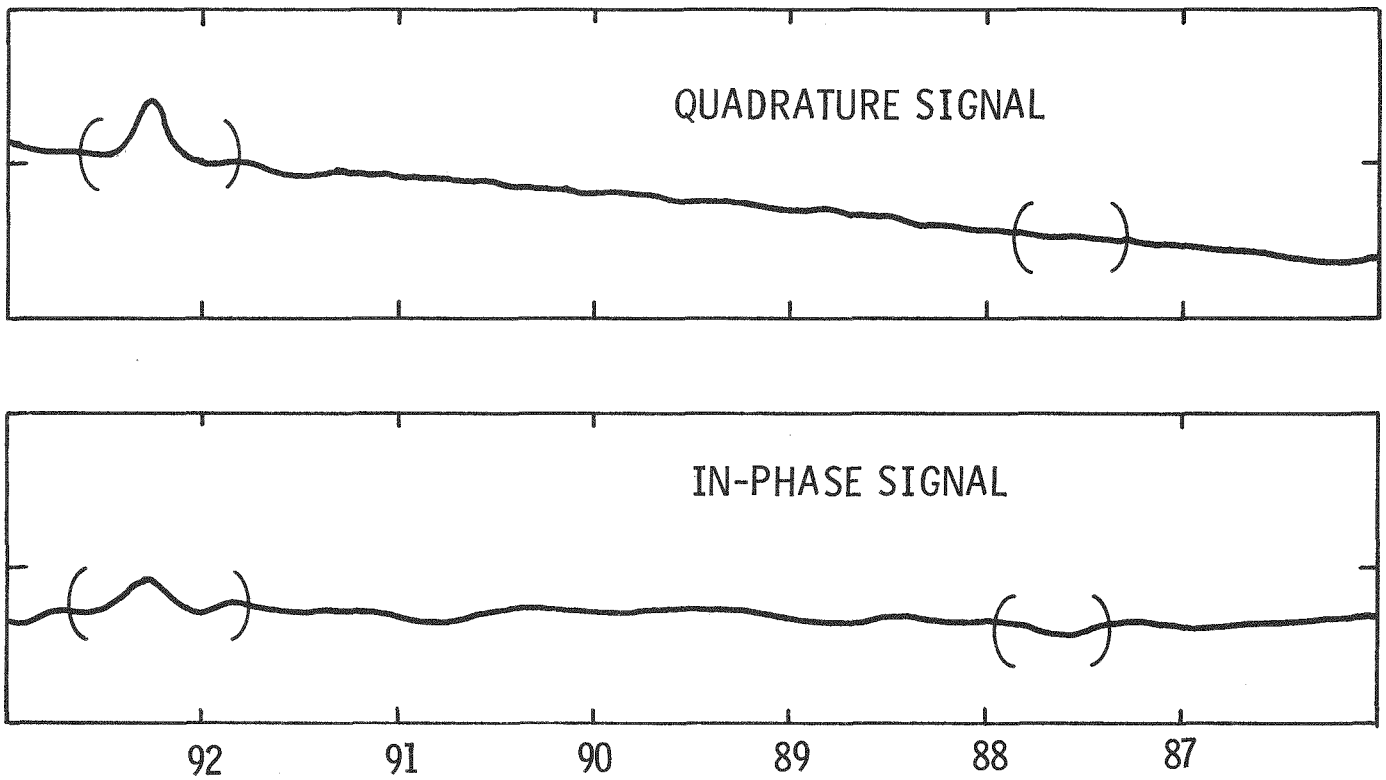

Figure 4-25
EDDY CURRENT TRACE OF ROD JBP-005 AT 100 KHZ SHOWING
INDICATION AT 94 3/16 IN FROM BOTTOM OF ROD

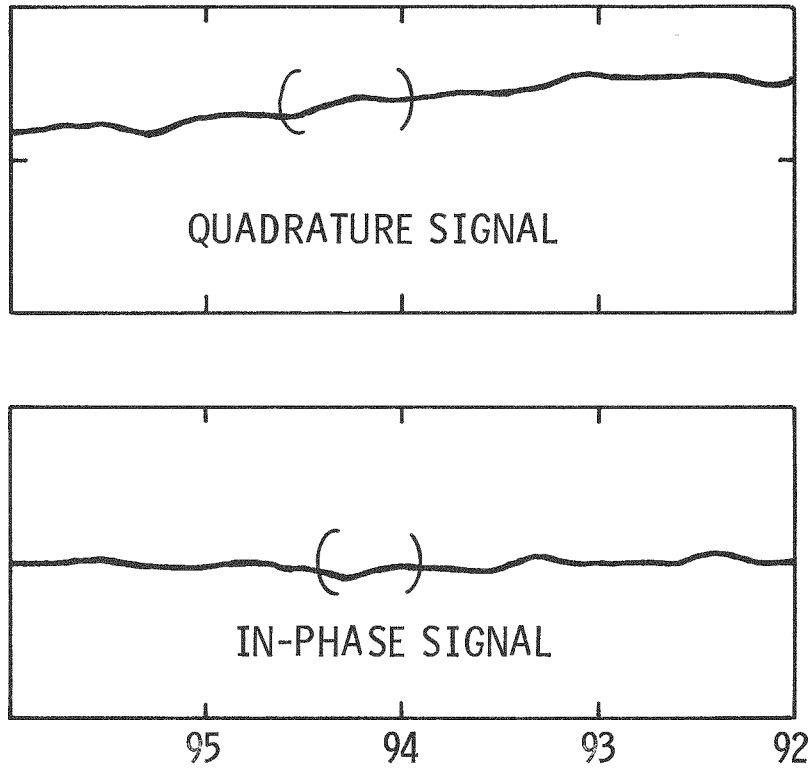

Figure 4-26

EDDY CURRENT TRACE OF CALIBRATION STANDARD SHOWING SIGNALS FROM INTERNAL AND EXTERNAL SURFACE DEFECTS IN ZIRCALOY-4 TUBING

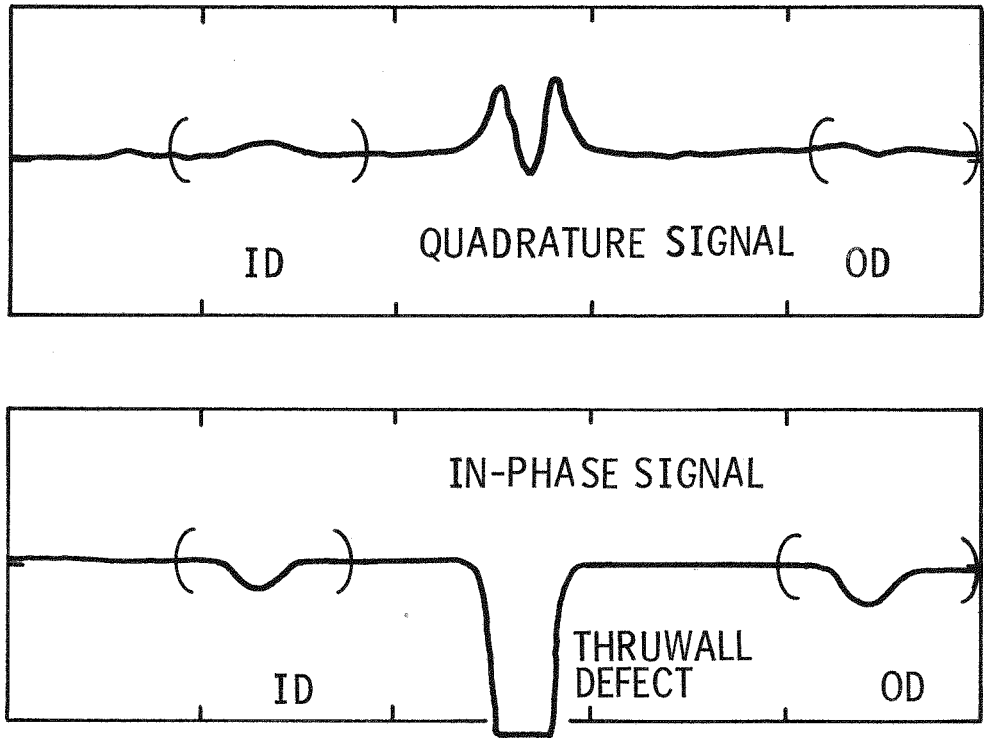

4.7 Cladding Internal Surface Examination

4.7.1 Scope

During the first hot cell campaign, the source of a prominent poolside eddy current signal from a high gas release rod (JBY-027) was pursued by visual examination of the cladding internal surface. The discovery of fuel-clad bonding in this case and the later metallographic examination results confirming the prevalence of the phenomenon in all high gas release rods prompted an effort in the second campaign to further characterize the cladding internal surface of representative rods. This involved sectioning fuel rods, slitting the cladding longitudinally, and removing the fuel.

The sections selected for examination are described in Table 4-10. Two of the four sections examined in the second campaign were taken from the same elevation of a high gas release Batch B rod and low gas release Batch B rod, respectively, to permit a comparison of cladding having approximately the same nominal power history. Also, at this elevation a section was taken from the only high gas release Batch A rod. The fourth section was taken from the bottom of the high gas release Batch B rod spanning the transition region between the occurrence and nonoccurrence of gamma scan cesium peaks.

In addition to the visual examination, representative samples from the slit cladding sections were further examined at Argonne National Laboratory (ANL) principally by scanning electron microscopy (SEM)and X-ray energy dispersive analysis to characterize the topography and chemical content of surface features.

4.7.2 Procedure for Clad Slitting

After cutting from the fuel rods, each section was subjected to a series of diametral measurements to locate the major and minor diameters. In all cases, an attempt was made to slit the cladding on the major diameter so that the region of minimum diameter could be more accessible for surface examination. With the section in a vise-holder arrangement,

Table 4-10

Cladding Internal Surface Examination

Hot Cell Campaign	Fuel Rod	Gas Release Category	Axial Location (Inches from rod bottom)	Reasons for Selection
1st	JBY-027	High	50 - 58-1/2	Strong eddy current indications at 53-1/4 in. (See Appendix B, Figure B-1)
2nd	JCN-196	High	1-1/4 - 13-1/4	Section spans the lower end of the rod where transition in gamma scan Cs peaking was observed.
2nd	JCN-196	High	80 - 91	High power with gamma scan peaks.
2nd	HBU-169	High	80 - 91	Only high gas release Batch A rod. Same elevation as above.
2nd	JBP-004	Low	80 - 91	Section from low gas release Batch B rod for comparison with high gas release rods.

slitting was performed with a circular saw. After the first cut, the section was turned 180^{o} for the second cut. The section was then opened up ("clam-shelled") and examined under a stereo microscope to characterize the fuel-clad configuration. This was followed by fuel removal, including brushing of the section to permit cladding surface examination of the two shells. The appearance of the fuel and cladding was documented by photographic scans.

4.7.3 Results of Slit-Clad Visual Examination

Examination of the section taken from JBY-027 revealed fuel particles tightly adhering to the cladding predominantly at pellet interfaces as can be seen in the two shell faces in Fig. 4-27. In addition to the objective of general characterization, a major reason for selecting this section was that it contained a strong poolside eddy current indication (at 53-1/4 inches from the bottom). Relatively large pieces of adhering fuel shown in Fig. 4-28 were observed near the location of this indication. No other anomalies, such as pits or cracks, were seen on the cladding surfaces. These observations, therefore, constituted the first evidence suggesting that an eddy current indication might be signaling unusual fuel-clad bonding in high gas release rods.

The significant findings from the additional examinations were as follows:

1. Fuel-clad bonding at pellet interfaces in the high gas release Batch B rod (JCN-196) appears to begin at 4 inches from the bottom. This is illustrated in the Fig. 4-29 montage of the 0^{o} shell face of the JCN-196 bottom section, which shows bonding present at all interfaces above this point. It is noteworthy that the whole rod Cs-137 gamma scan of this region, presented in Fig. 4-30 also shows cesium peaking at all the pellet interfaces in the section except those below the 4 inch point. The internal surface of this section also exhibited markings, associated with the pellet crack pattern, which can be seen in Fig. 4-29.

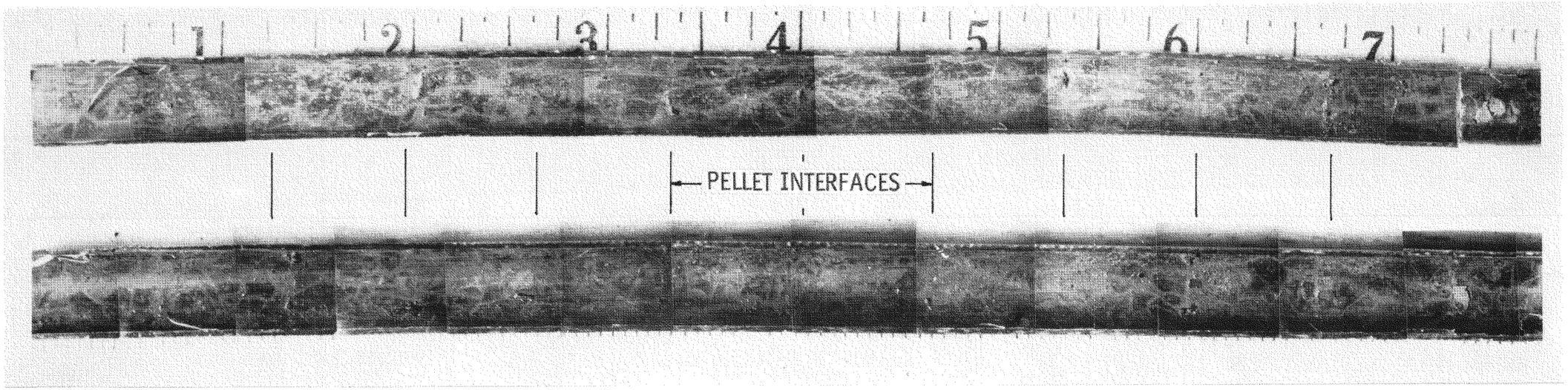

Figure 4-27 MONTAGE OF SLIT CLADDING SECTION FROM JBP-027 SHOWING THE TWO SHELLS WITH FUEL BONDED TO CLADDING AT PELLET INTERFACES.

P5597 5X

Figure 4-28 SECTION OF SLIT CLAD SHELL FROM ROD JBP-027 SHOWING PIECES OF BONDED FUEL.

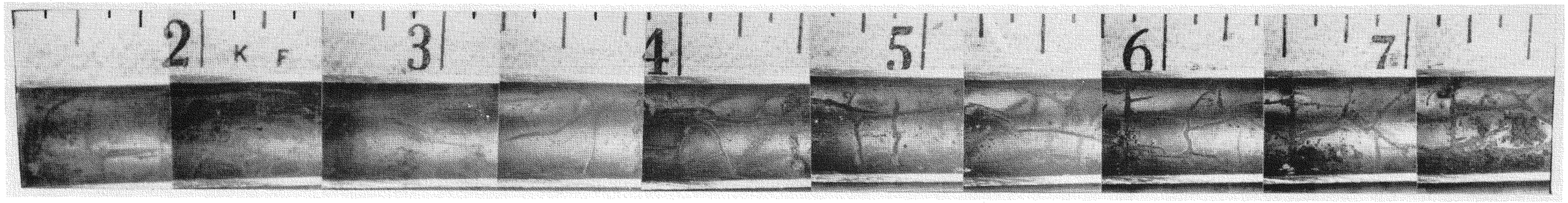

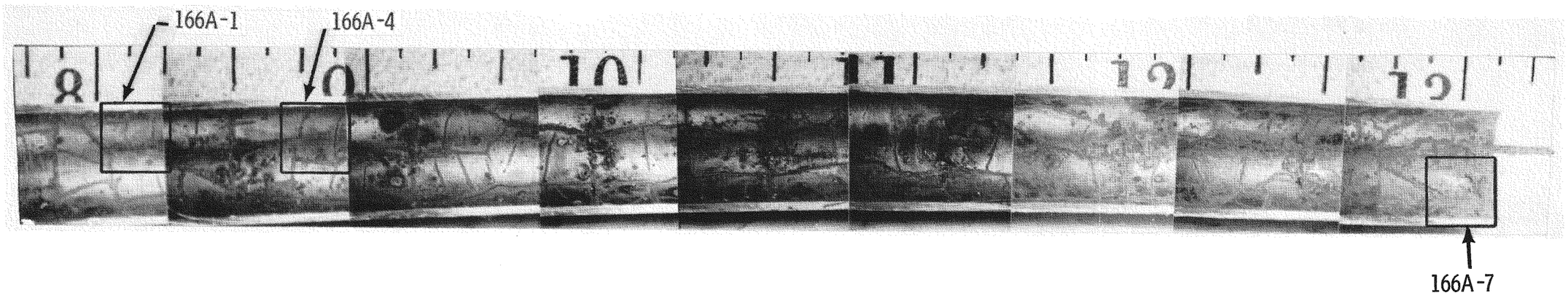

Figure 4-29 MONTAGE OF 0^{0} SHELL FACE OF SLIT CLAD SECTION FROM BOTTOM END OF JCN-196 (SECTION FROM 8 1/4 TO 13 1/4 INCHES) EXAMINED BY SEM AT ANL-APPROXIMATE LOCATION & IDENTIFICATION NUMBERS OF SAMPLES SHOWN .

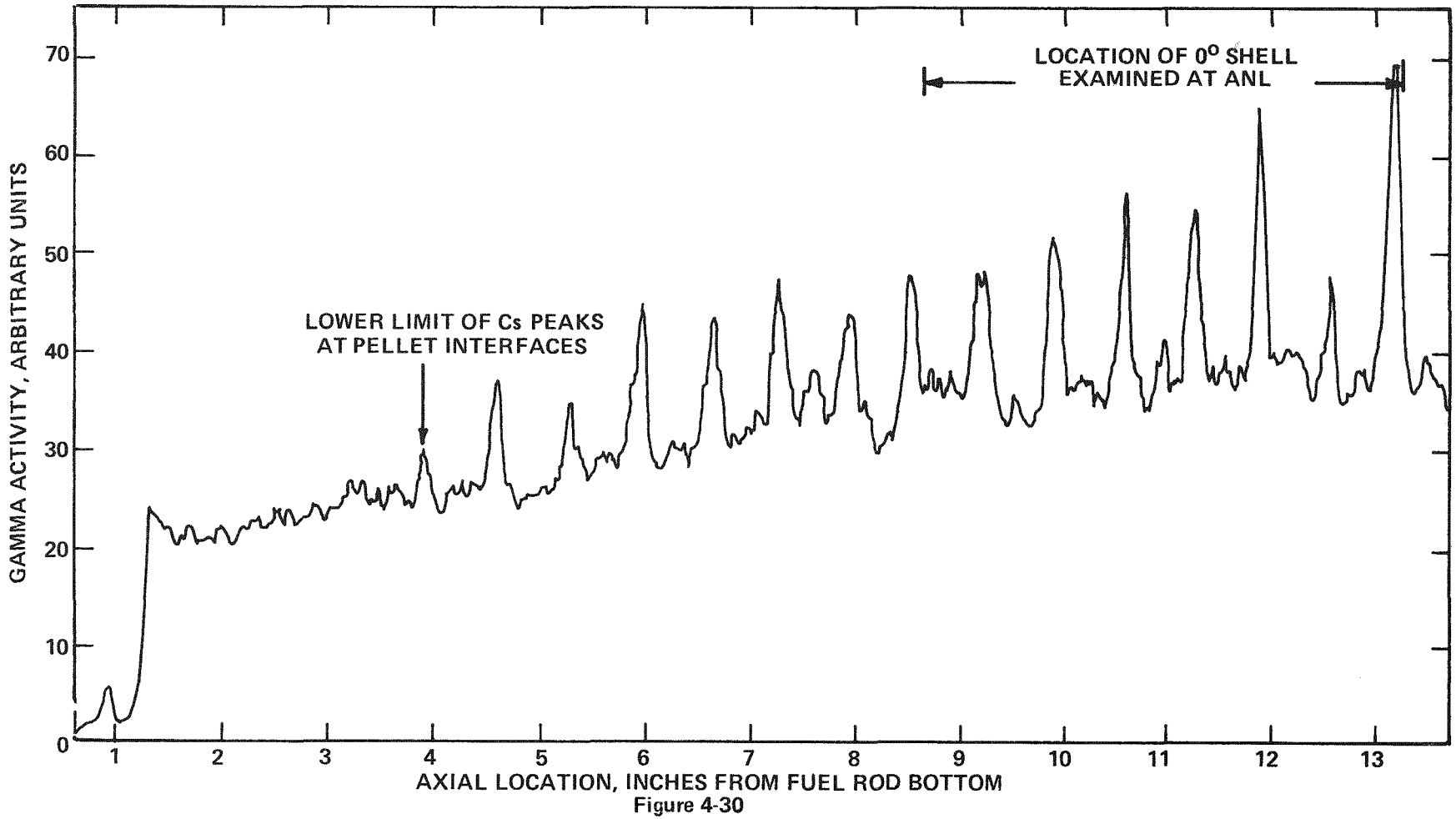

Figure 4-30

WHOLE ROD Cs-137 GAMMA SCAN OF BOTTOM END OF JCN-196 SUBJECTED TO CLADDING INTERNAL SURFACE EXAMINATION

2. Only in the case of the section at 80 to 91 inches in JCN-196 was it possible to preserve the fuel configuration after slitting, thus permitting a view of the pellet cracking pattern. Interestingly, many of the axial cracks, as shown in Fig. 4-31, appeared to continue from one pellet to the next maintaining the same azimuthal orientation. This would suggest that in modeling the cladding stress concentration pattern over pellet cracks at interfaces, it is proper to invoke a coincidence of azimuthal crack orientation from one pellet to the next.

3. As is evident in Fig. 4-32, the cladding internal surface of the low gas release Batch B rod (JBP-004) is substantially free of adhering material compared with that of high gas release rods examined in the same 86 to 91 inch location.

4. In contrast with the Batch B rods (JBP-027 in the first campaign and JCN-196 in the second campaign) the inner cladding surface of the high gas release Batch A rod (HBU-169) does not exhibit prominent fuel-clad bonding at pellet-pellet interfaces. However, circular "deposits" adhering to the cladding surface were observed, as shown in Fig. 4-33, which is a montage of the 90^{o} shell face. These deposits could be matched to circular spots on the UO_2 pellets in contact with the cladding before slitting. (See Fig. 4-34). On closer examination, another distinctive feature of the deposits, in addition to marked circularity, was their tendency to locate adjacent to pellet cracks and the pellet end faces. These features were not as readily discernible on the internal cladding surface of JCN-196 at the same position as shown in Fig. 4-32.

4.7.4 Topographical and Chemical Characterization

4.7.4.1 Specimen Selection

For further characterization of the features found on the internal cladding surface of high gas release rods, three representative specimens, each 5 inches long, were shipped from Battelle-Columbus hot cell facility to the Materials Science Division at ANL. The specimens were cut from the following locations:

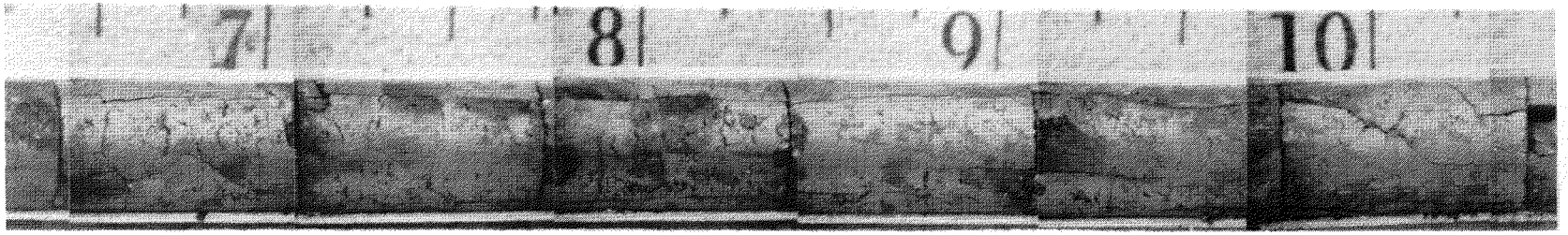

Figure 4-31 SECTION FROM JCN-196(86 1/2 TO 90 1/2 INCHES FROM BOTTOM)SHOWING CONTINUATION OF AXIAL CRACKS FROM PELLET TO PELLET

JCN-196
(86-91 INCHES)

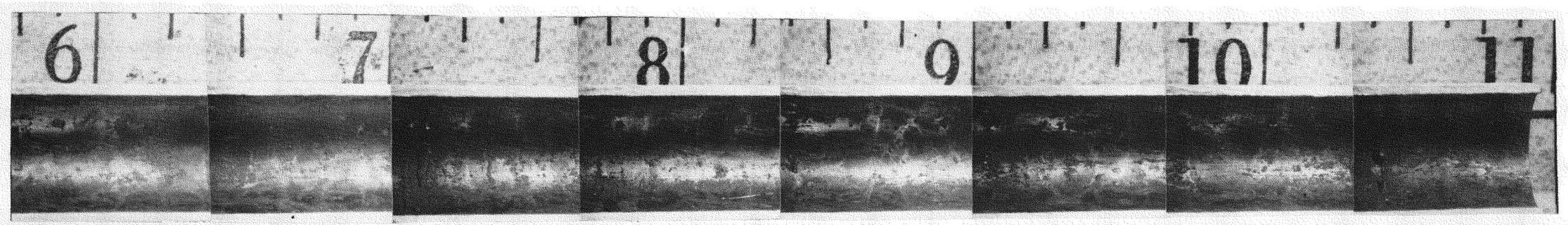

JBP-004
(86-91 INCHES)

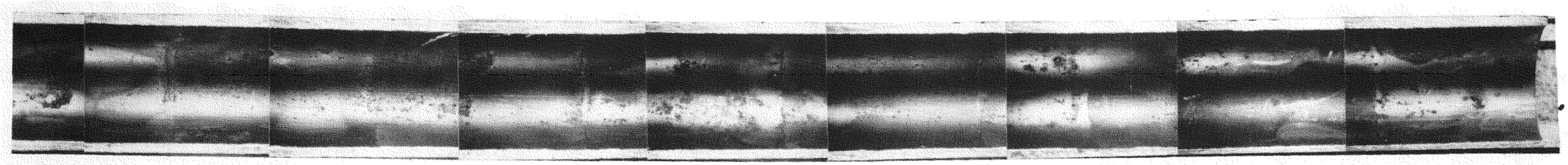

Figure 4-32 COMPARISON OF CLADDING INTERNAL SURFACE APPEARANCE IN HIGH-GAS RELEASE ROD JCN-196 WITH THAT IN LOW GAS RELEASE ROD JBP-004 AT 86-91 INCH AXIAL SPAN. (THE CLAD SECTION FROM ROD JCN-196 SHOWN ABOVE WAS SENT TO ANL FOR FURTHER EXAMINATION)

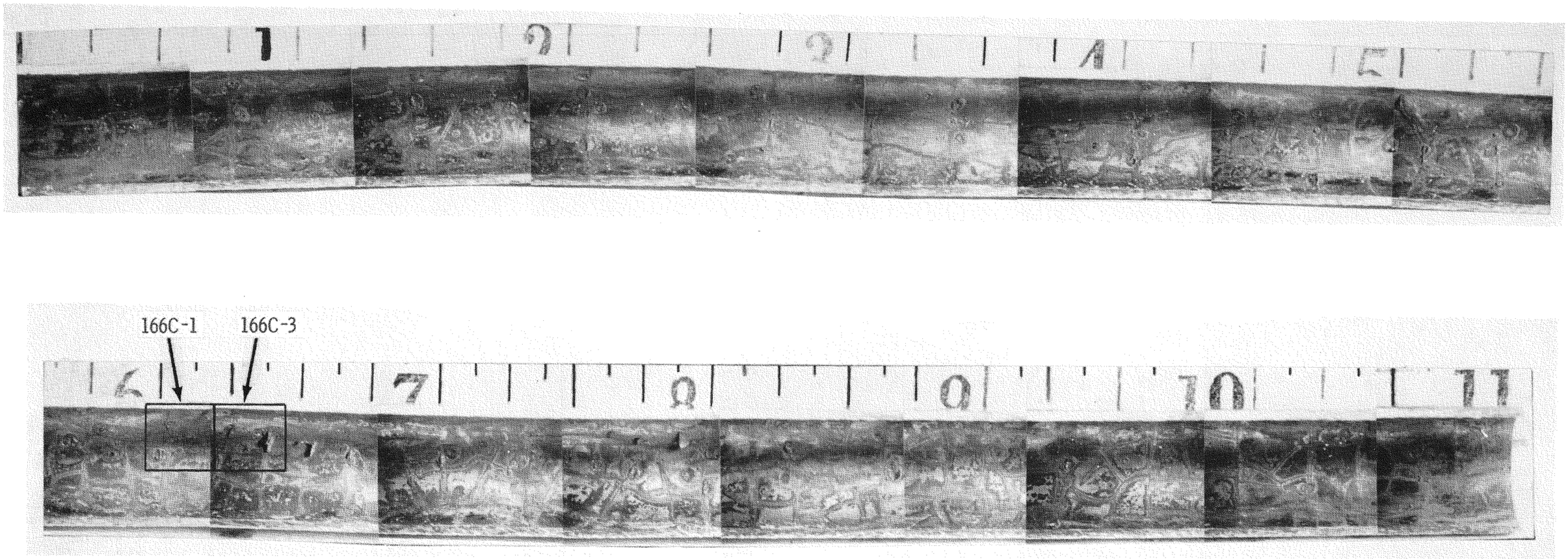

Figure 4-33 INTERNAL CLADDING SURFACE APPEARANCE IN THE HIGH GAS RELEASE BATCH A ROD (HBU 169-80 TO 91 INCHES FROM THE BOTTOM) EXAMINED BY SEM AT ANL-APPROXIMATE LOCATION AND IDENTIFICATION NUMBERS OF SAMPLES SHOWN.

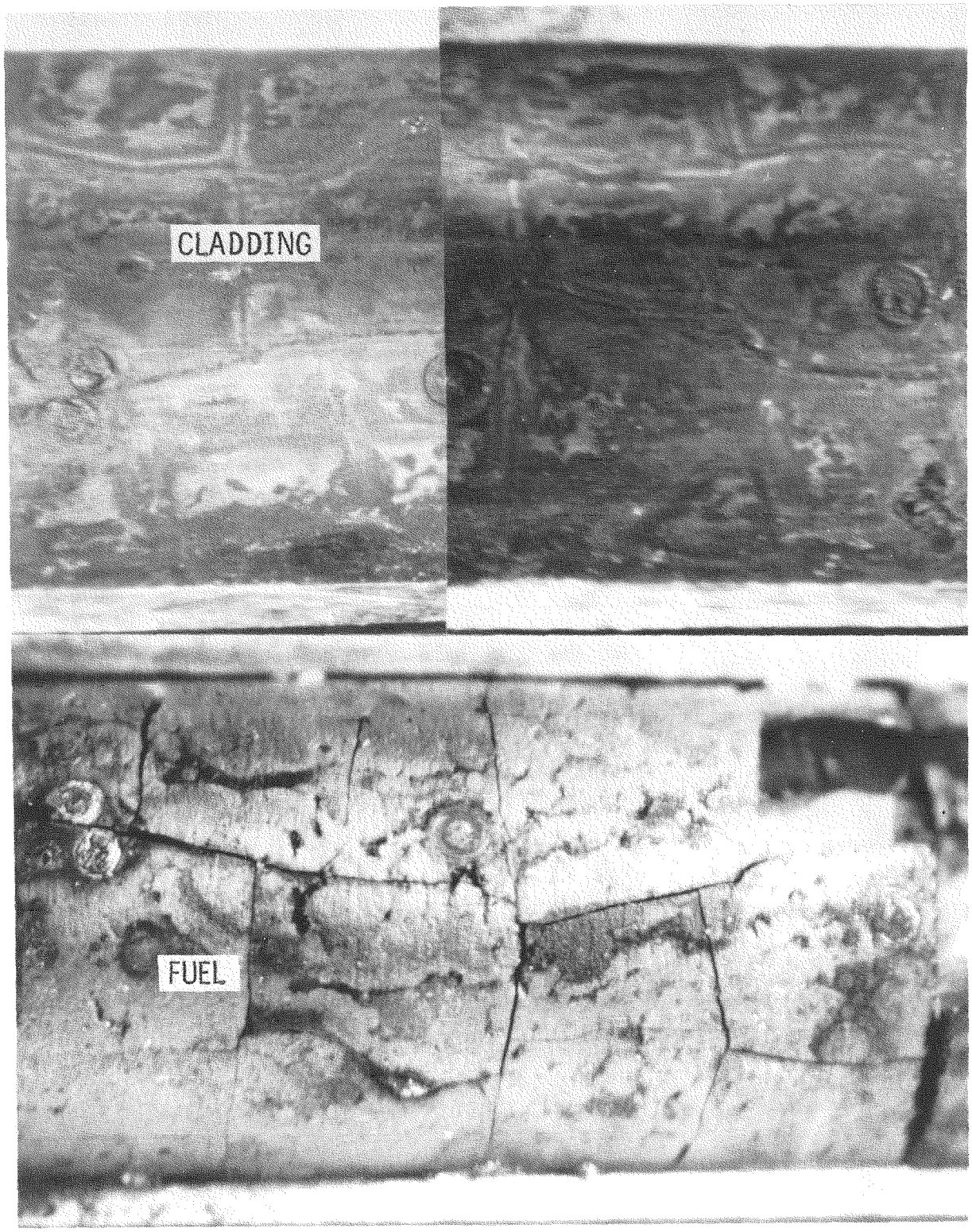

Figure 4-34
SLIT CLAD SECTION FROM ROD HBU-169 SHOWING CLADDING WITH CIRCULAR DEPOSITS ON THE INNER SURFACE AND CORRESPONDING SPOTS ON UO_2 PELLET

Rod S/N	Shell Face	Axial Location (in. from rod bottom)
JCN-196	180°	86 - 91
JCN-196	0°	8-1/4 - 13-1/4
HBU-169	90°	86 - 91

4.7.4.2 Gamma Scanning Results

Initially, each of the three shells was subjected to a series of gamma activity scans of the internal clad surface to determine the axial distribution and identity of the active species present. Each series consisted of a gross gamma scan and two specific isotope gamma scans for Cs-137 and Cs-134, respectively. The significant results from this work were as follows:

1. All three types of scans exhibited strong peaking at pellet interfaces indicating that cesium is the major gamma active fission product constituent of the material adhering to the cladding internal surface.

2. The whole rod gamma scans and the corresponding internal surface gamma scans exhibit similar cesium peaking patterns as shown in Fig. 4-35, suggesting that the adhering material is the source of the cesium concentrations measured in both cases.

3. As evident from Fig. 4-35, unlike the other two specimens, the specimen from HBU-169 exhibited fairly regular secondary cesium peaks between pellet interface locations. This appears to be consistent with the relatively more uniform axial distribution of adhering material observed in the visual examination of the HBU-169 shell face.

4.7.4.3 Scanning Electron Microscopy (SEM) Examination

Three representative samples were cut from the JCN-196, 0° shell face specimen and two from the HBU-169, 90° shell face specimen for examination in the Argonne shielded SEM. The locations of the specimens are indicated in Fig. 4-29 and 4-33, respectively. In addition to determining the topography of the inner cladding surface, X-ray energy dispersive analysis was used to identify the chemical elements present. This method

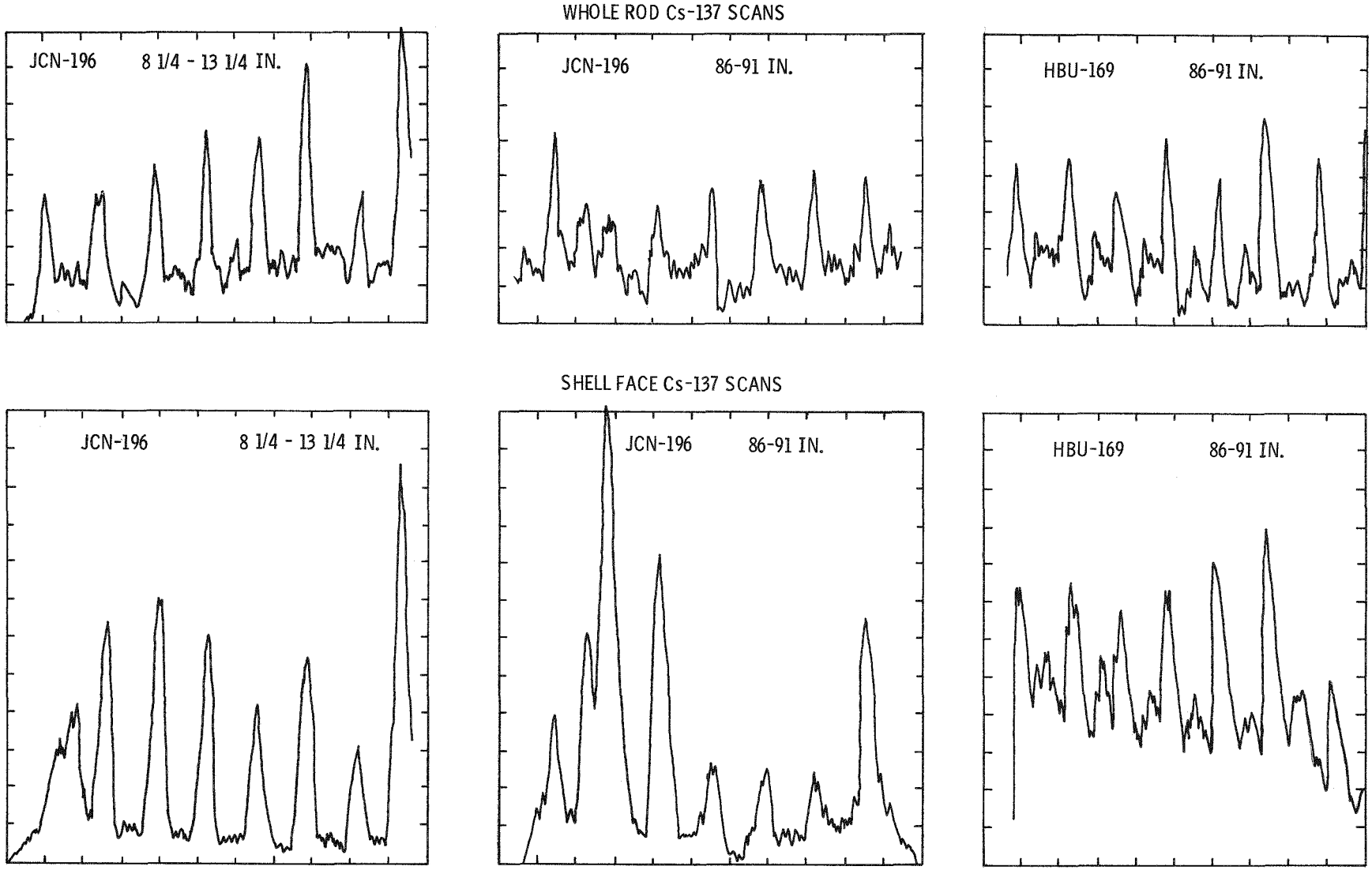

Figure 4-35 - COMPARISON OF WHOLE ROD AND SHELL FACE Cs-137 GAMMA SCANS SHOWING CESIUM CONCENTRATIONS AT PELLET INTERFACES

cannot detect elements with an atomic number less than that of sodium (Z=11); therefore, though oxygen (Z=8) is probably present in most of the adhering material in the form of oxides, it is not detectable.

Internal Surface of JCN-196 Cladding

The three samples (166 A-1, -4 and -7) examined from JCN-196 are shown as low magnification scanning photomicrographs in Fig. 4-36 and 4-37. All samples were initially 1/4 in. long by 1/4 of the cladding circumference. In the case of sample 166 A-7, the radioactivity was too high to permit X-ray analysis despite the use of a gold collimator to prevent saturation of the detector with background radiation. For chemical characterization, therefore, this sample was subdivided, yielding two additional samples (166 A-7-1 and 166 A-7-3) as shown in Fig. 4-37.

1. The pellet crack markings on the cladding, which are seen as stripes in the SEM photographs, consisted of a region of adhering microscopic particles of various sizes and shapes. Another interesting feature of the stripes is that they are bounded by a fairly uniform array of very small nodules running alongside. These observations are illustrated in Fig. 4-38, 4-39, 4-40 and 4-41, which show typical SEM photomicrographs of the stripe regions.

2. A typical X-ray spectrum shown in Fig. 4-42 of one of the small nodules indicates that it contains uranium and cesium, and that zirconium is apparently the major constituent. However, since these are very small particles, the zirconium X-rays may have emanated from the background.

3. More important were the results of chemical characterization of various particles lying in the stripe region. The X-ray analyses not only found cesium in relatively large quantities but also detected tellurium and iodine. For example, tellurium along with cesium, uranium and zironium are shown as constituents of a particle X-ray spectrum in Fig. 4-43. The X-ray spectra of the three small crystals (L, M and N)

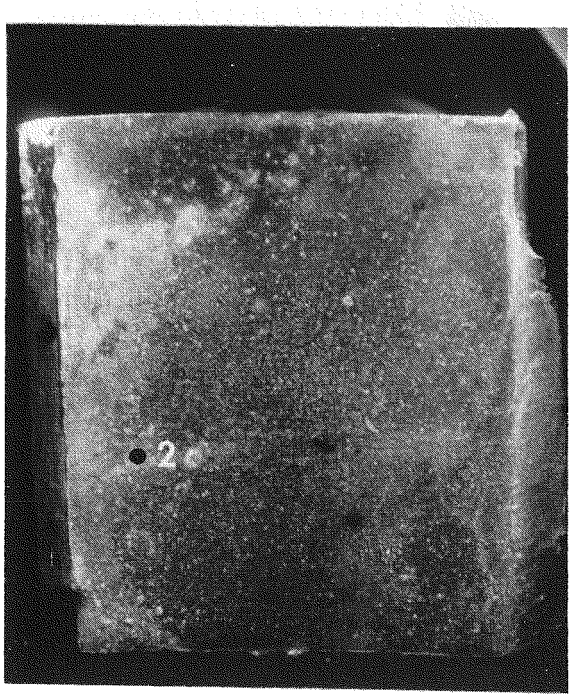

240B 166A-1 10X

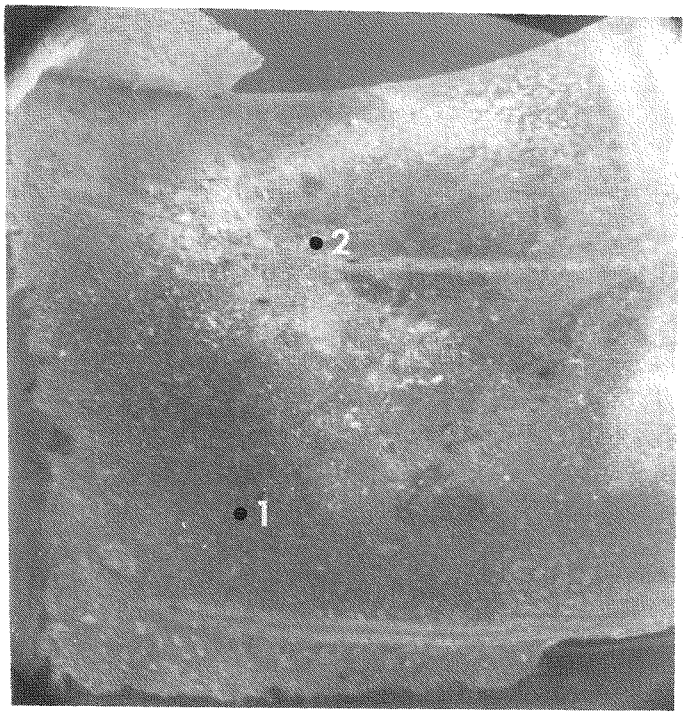

190 166A-4 15X

Figure 4-36 LOW MAGNIFICATION SEM PHOTOGRAPHS OF JCN-196 CLADDING SAMPLES

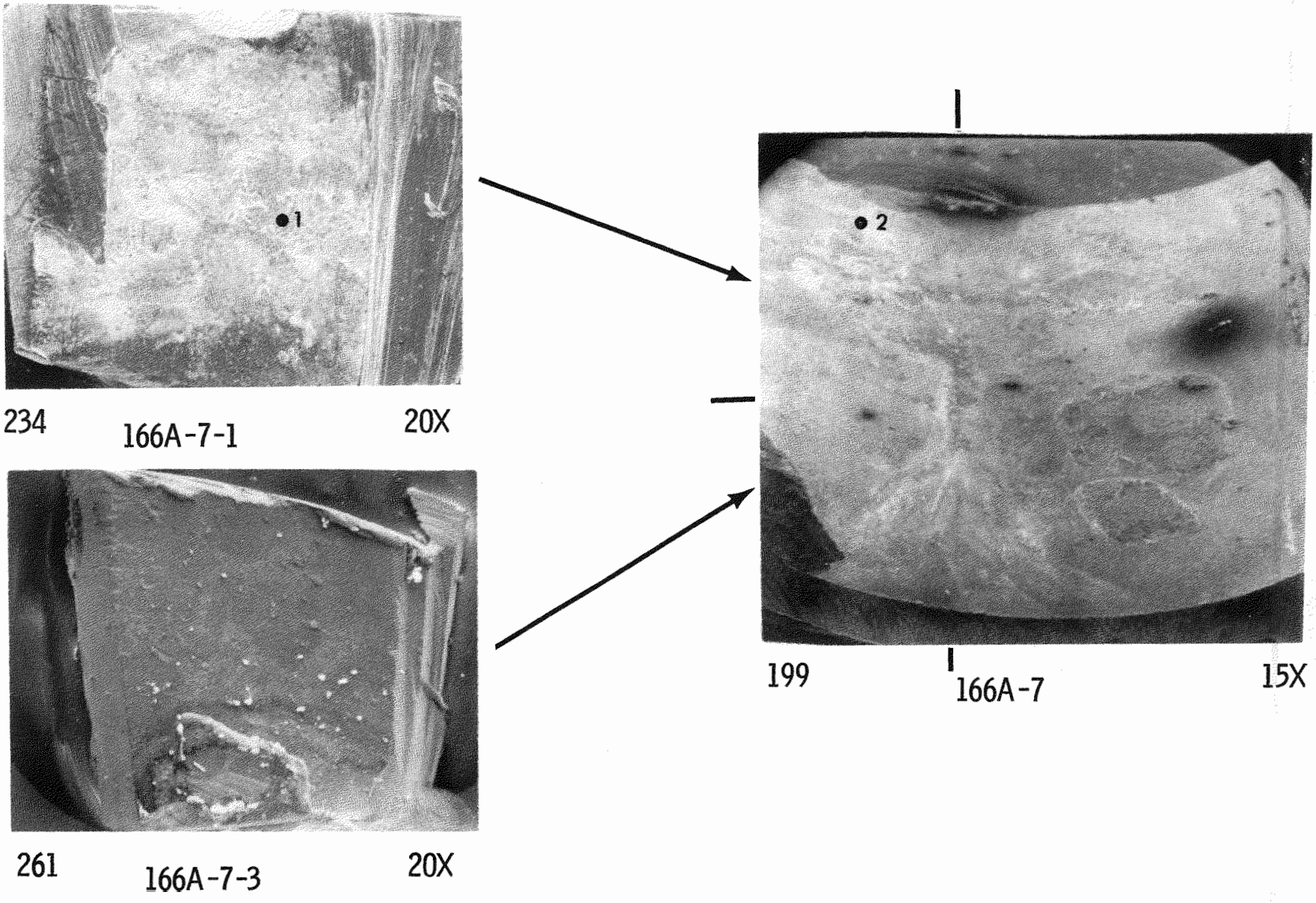

Figure 4-37 LOW MAGNIFICATION SEM PHOTOGRAPHS OF JCN-196 CLADDING SAMPLE 166A-7 SUBDIVIDED TO REDUCE RADIOACTIVITY

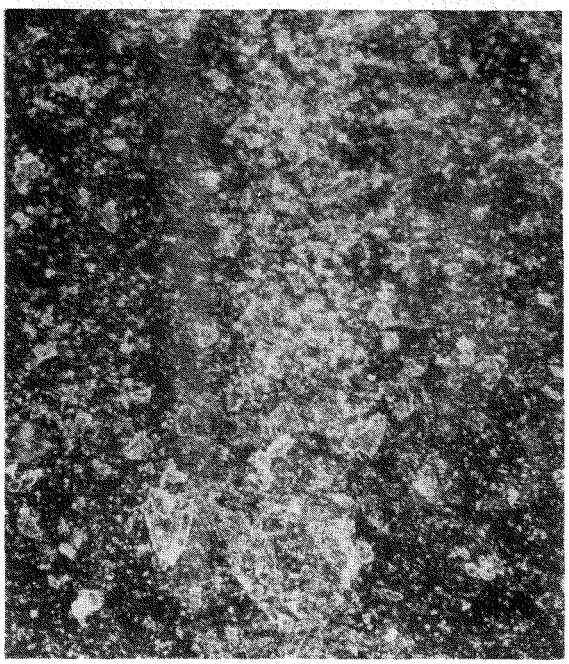

253 130X

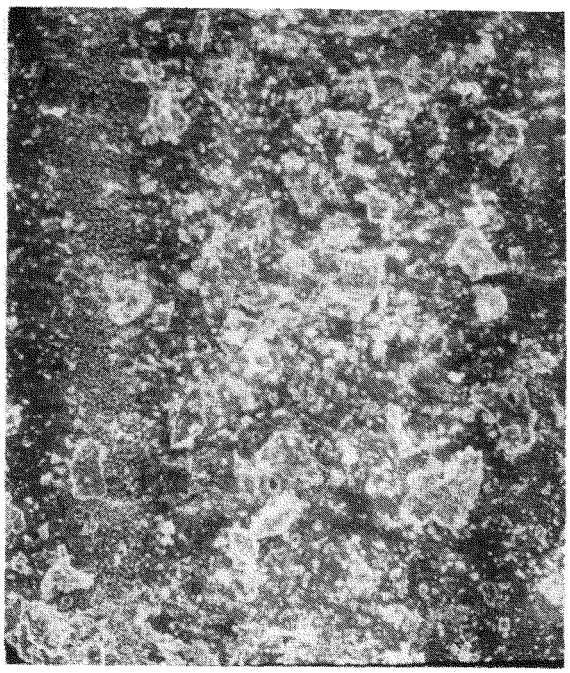

254 260X

Figure 4-38 SEM PHOTOGRAPH OF AREA NEAR POINT 2 OF 166A-1 (Figure 4-36) SHOWING PARTICLES CONCENTRATED ON A CLADDING STRIPE WITH A BAND OF UNIFORMLY SMALL NODULES TO THE LEFT

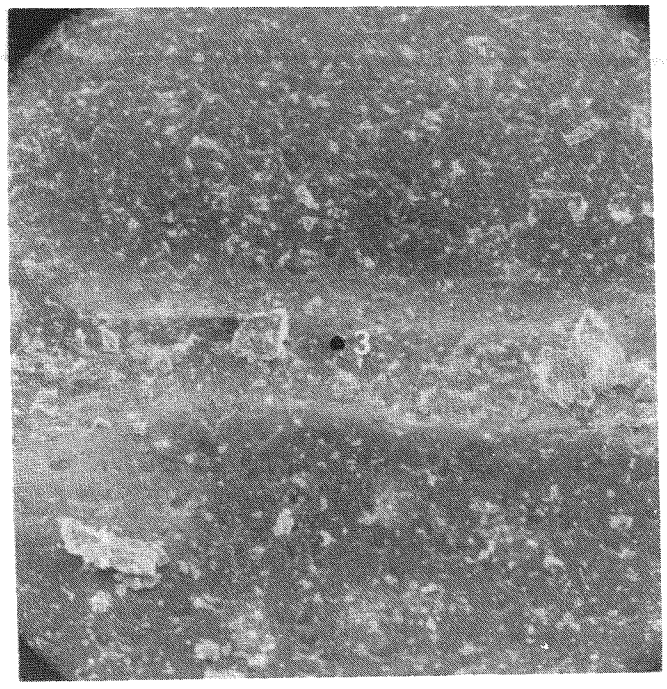

193 150X

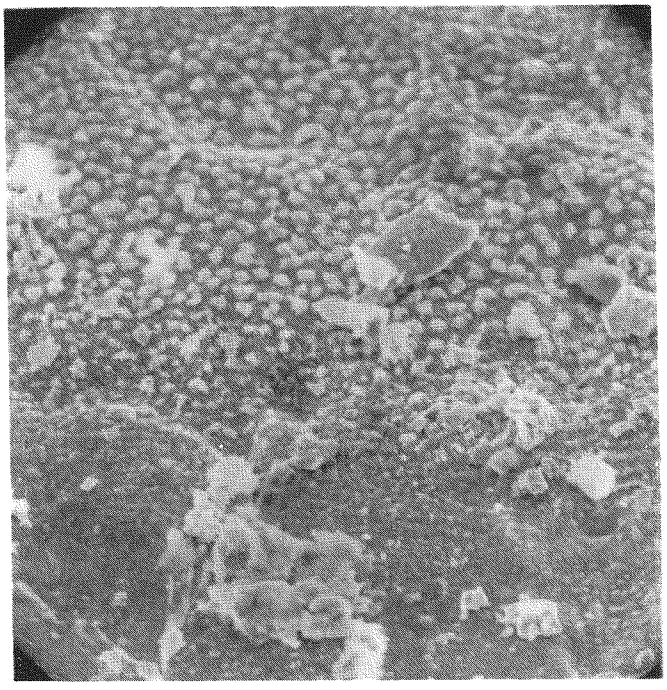

195 1200X

Figure 4-39 TOP - SEM PHOTOGRAPH OF AREA NEAR POINT 2 OF 166A-4 (Figure 4-36) SHOWING CLADDING STRIPE

BOTTOM - DETAIL NEAR POINT 3 IN TOP PHOTOGRAPH SHOWING THE BAND OF SMALL NODULES ABOVE THE STRIPE

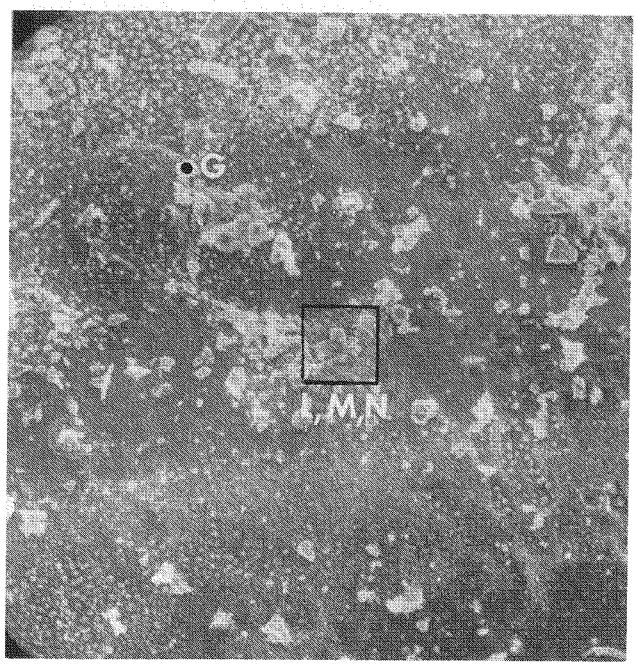

317 600X

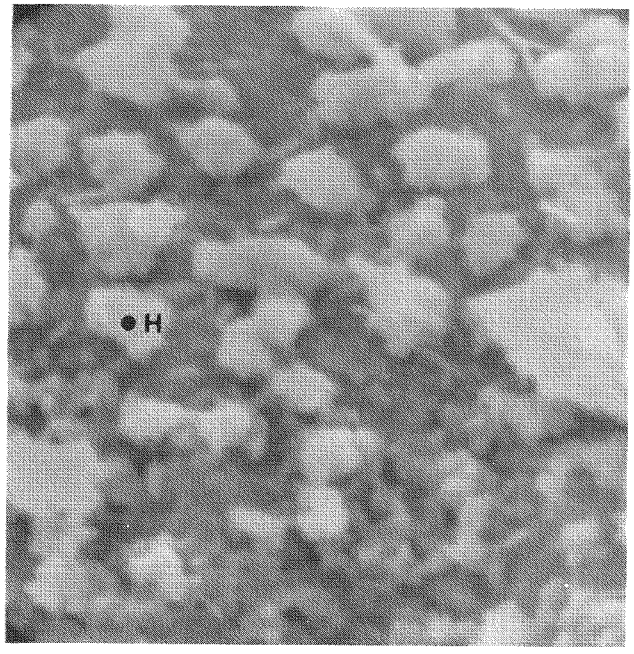

196 6000X

Figure 4-40 TOP - SEM PHOTOGRAPH SHOWING SMALL PARTICLES ON CLADDING STRIPE NEAR POINT 3 OF Figure 4-39 (TOP)

BOTTOM - HIGH MAGNIFICATION SEM PHOTOGRAPH OF NODULES IN Figure 4-39 (BOTTOM)

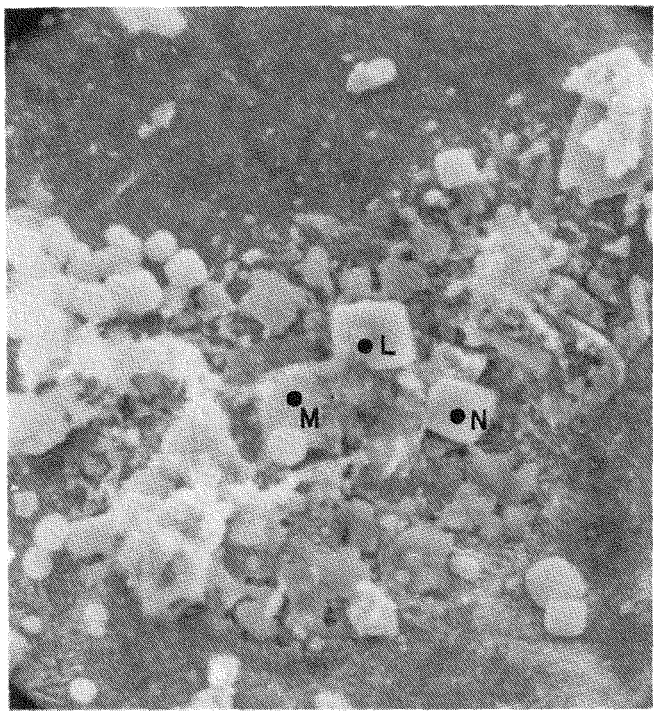

318 1500X

Figure 4-41 HIGH MAGNIFICATION SEM PHOTOGRAPH OF SMALL CRYSTALS IN STRIPE OF Figure 4-40 (TOP)

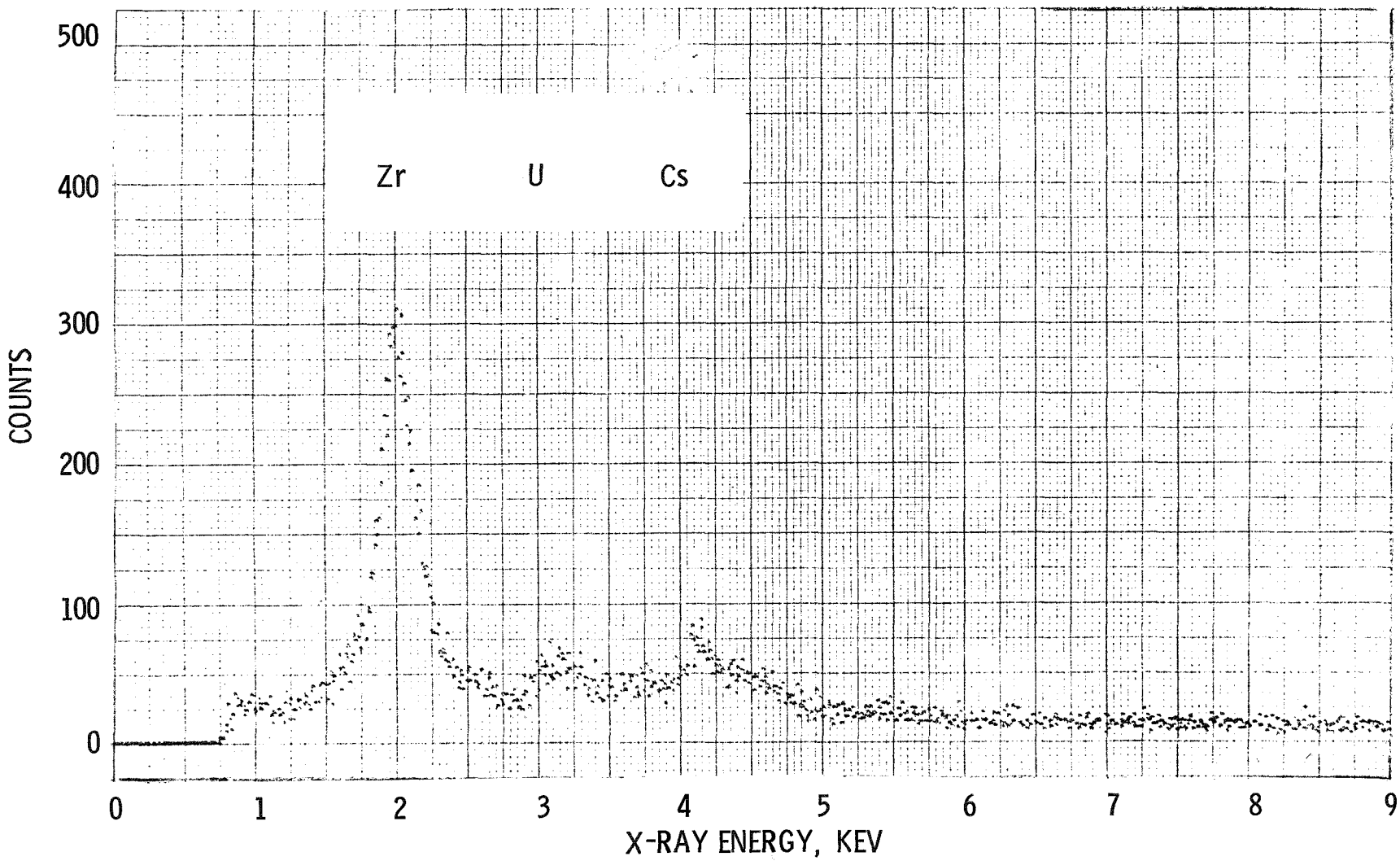

Figure 4-42 X-RAY SPECTRUM OF POINT H IN Figure 4-40 INDICATING THE PRESENCE OF Zr, Cs AND U IN THE NODULE.

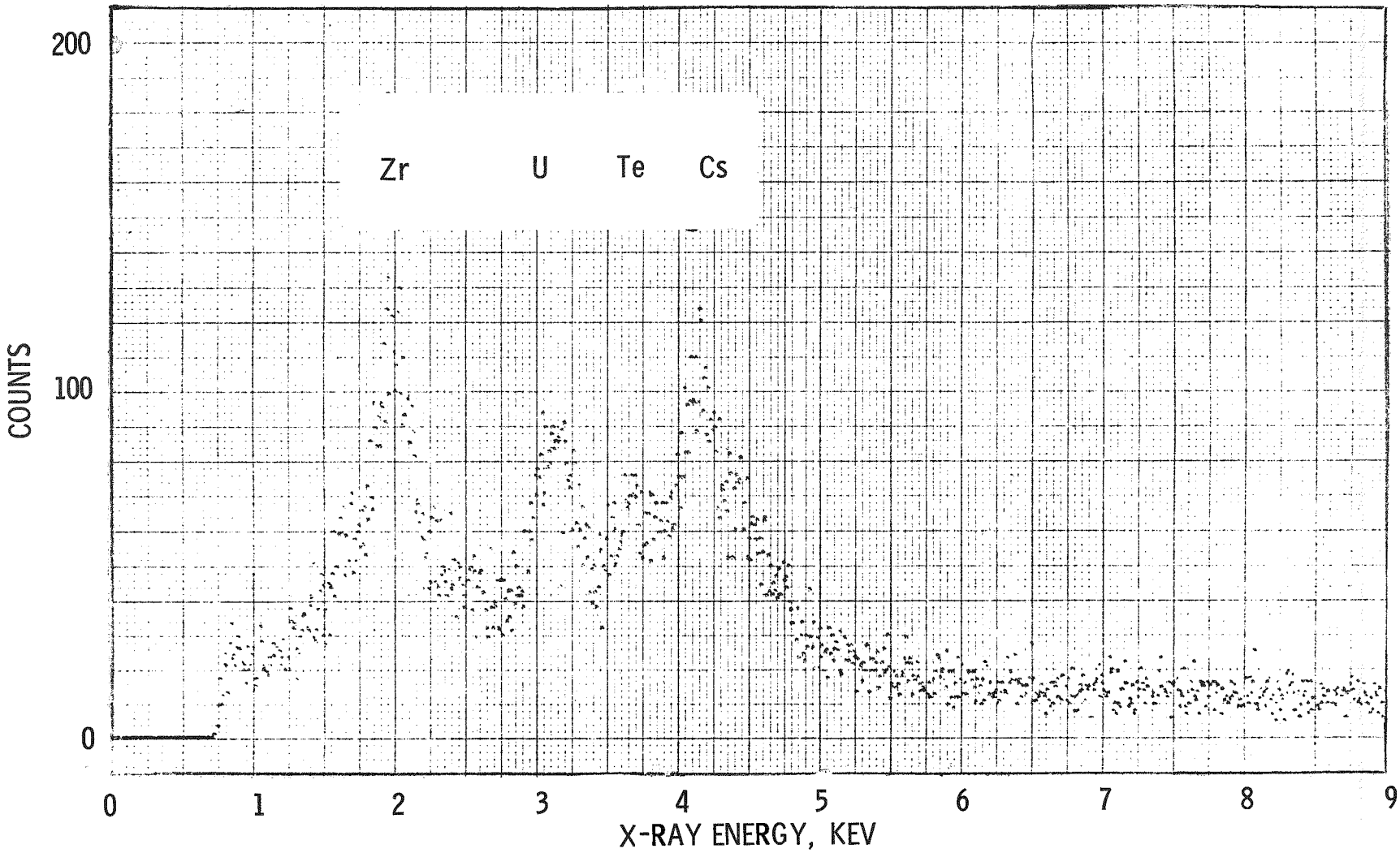

Figure 4-43 X-RAY SPECTRUM OF POINT G IN Figure 4-40 (TOP) SHOWING THE PRESENCE OF Zr, Cs, U AND Te.

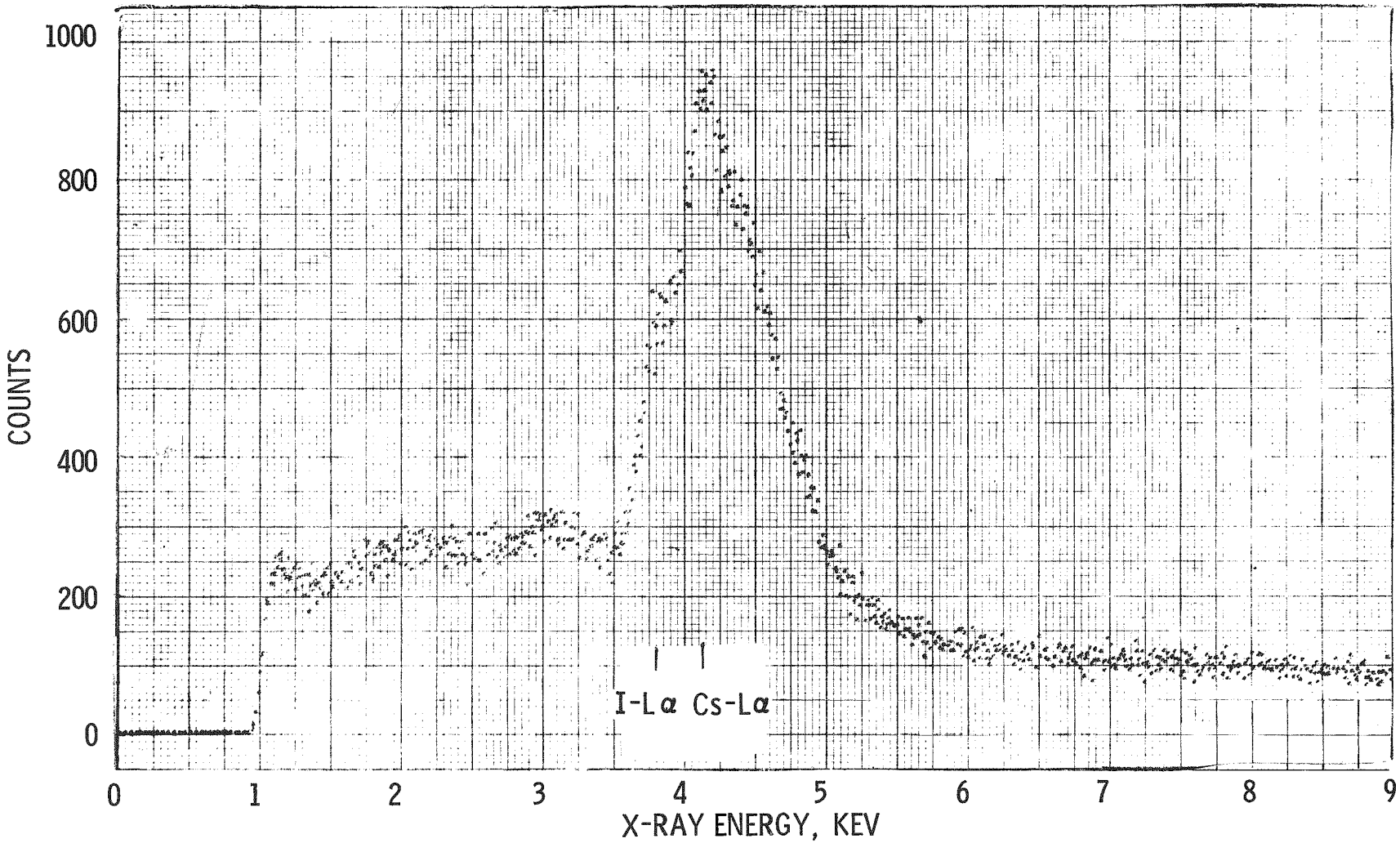

Figure 4-44 X-RAY SPECTRUM OF PARTICLE L IN Figure 4-41 SHOWING CESIUM AND IODINE AS THE MAJOR ELEMENTS PRESENT.

shown in Fig. 4-41 are of even greater interest in that they indicate mainly cesium and iodine are present. This can be seen in the Fig. 4-44 X-ray spectrum which was typical of those obtained for all three crystals. It should be noted that a sample of pure cesium iodide was analyzed in the same system to calibrate the X-ray spectrometer. The expected locations of the pertinent cesium and iodine X-ray peaks based on this analysis are shown in Fig. 4-44. In view of the prior exposure of the cladding specimen to laboratory air subsequent to the in-reactor environment, it is believed the chemical composition of the apparent crystals is more likely to be an oxidized and/or hydrated compound of cesium and iodine than pure cesium iodide. The significance of finding tellurium and iodine, along with cesium, on the cladding surface is that their presence (particularly iodine) on the cladding surface, though previously only suspected, has now been detected. Moreover, this result indicates that the relatively volatile tellurium and iodine, as well as cesium, are also redistributed in the high gas release rods. A subsequent analysis of a typical inner cladding surface in the ANL Ion Microprobe, which is much more sensitive than X-ray spectrometry, also confirmed the presence of these elements.

4. Small particles on the cladding internal surface away from the stripe regions were found to be typically composed of uranium and cesium. Fig. 4-45 shows such a particle, and Fig. 4-46 presents the corresponding X-ray spectrum. The finding of zirconium only in the Fig. 4-47 X-ray spectrum of the area adjacent to this particle confirms that the dark background is the cladding surface.

5. The large, thick deposits noted visually on the slit cladding shell surfaces (especially in the case of HBU-169) are also observed on the JCN-196 surface, as is evident in the SEM photographs of specimen 166 A-7 in Fig. 4-37. These appear to contain high concentrations of uranium and cesium, as indicated by X-ray analysis of such a deposit in specimen 166 A-7-1, as shown in Fig. 4-48. Attempts to analyze an area where this deposit appeared thinner were unsuccessful because high radioactivity saturated the X-ray detector. Since the beam reaching the detector is fairly

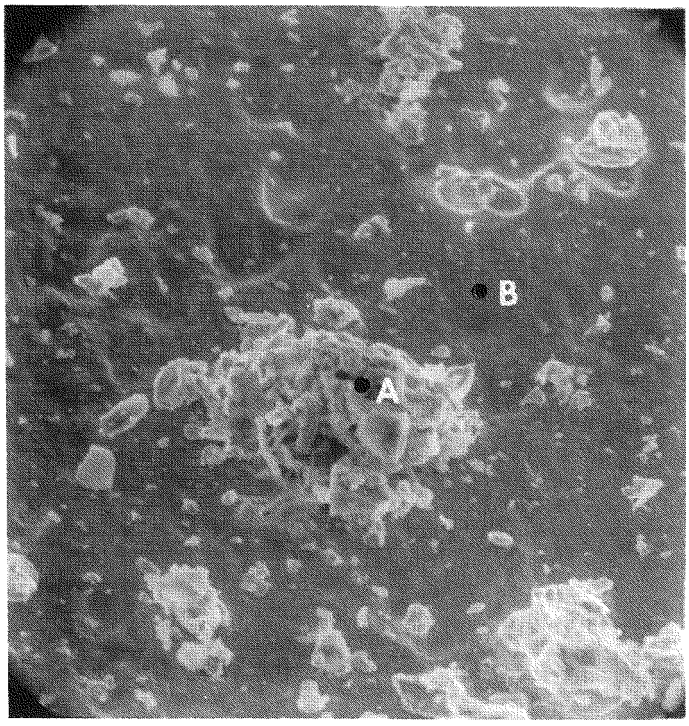

191 600X

Figure 4-45 SEM PHOTOGRAPH OF PARTICLE NEAR POINT 1 ON SAMPLE 166A-4 (Figure 4-36)

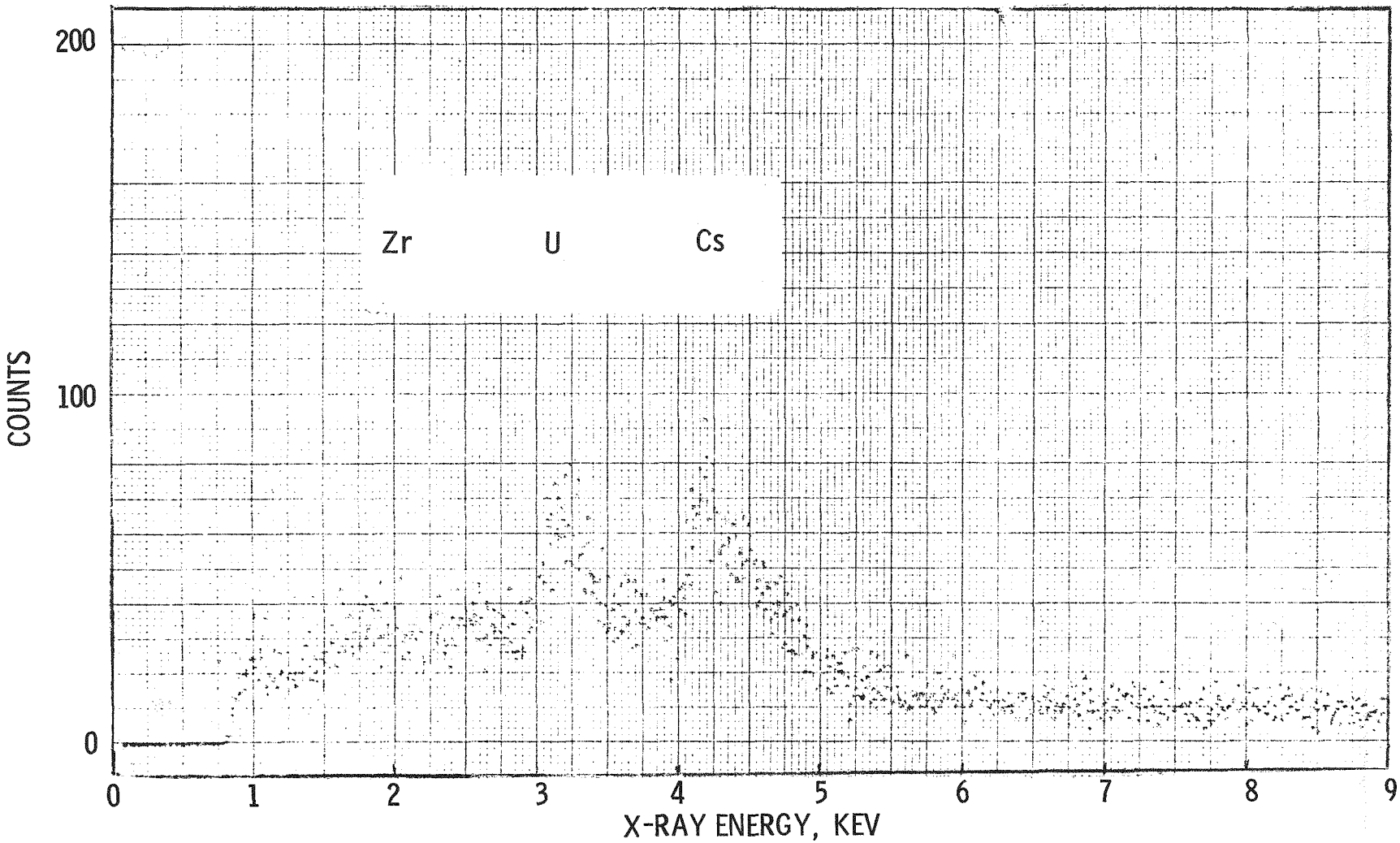

Figure 4-46 X-RAY SPECTRUM OF PARTICLE A IN Figure 4-45 SHOWING URANIUM AND CESIUM PRESENT.

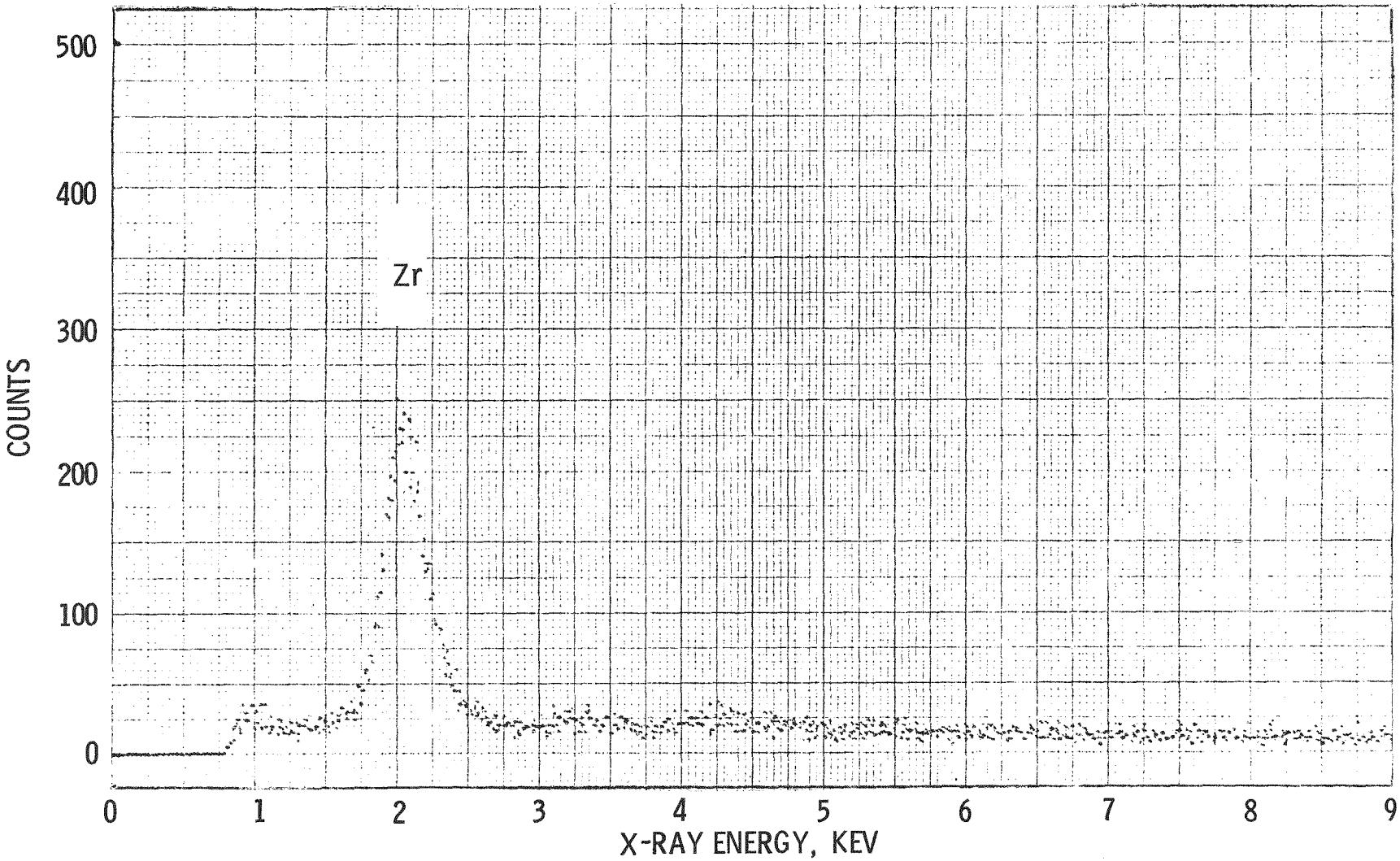

Figure 4-47 X-RAY SPECTRUM AT POINT B IN Figure 4-45 CONFIRMING ZIRCONIUM IN THE DARK BACKGROUND MATERIAL IN THE ZIRCALOY CLADDING SURFACE.

220 130X

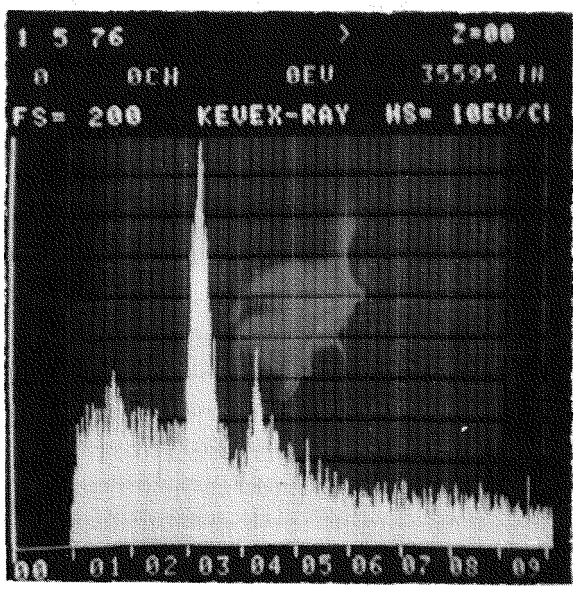

221

Figure 4-48 SEM PHOTOGRAPH OF AREA NEAR POINT 1 OF 166A-7-1 IN Figure 4-37 AND X-RAY SPECTRUM OF POINT C IN THE AREA SHOWING URANIUM AND CESIUM PRESENT

well collimated, this thinner area is concluded to have a higher activity than the area shown in Fig. 4-48, suggesting that the deposit material closer to the cladding surface has a relatively higher cesium content because cesium is the only significant activity source. These observations are consistent with the results of electron microprobe analyses of transverse metallographic sections through such deposits described in Section 4.10.

6. A major characteristic of these large, thick deposits was their circular or oval form. This circular tendency also extended to the apparent fracture pattern which results in concentric steps as shown in Fig. 4-49. Thus, such SEM evidence of circular morphology tended to confirm that the adhering material on the JCN-196 cladding was similar to the HBU-169 cladding deposits which appeared more obviously circular during the unaided visual examination.

Internal Surface of HBU-169 Cladding

The two samples cut from the HBU-169 section, one of which is shown in Fig. 4-50, were too radioactive for X-ray analysis. The SEM examination, therefore, was restricted to obtaining additional evidence of similarity with the topographical features of the JCN-196 samples. (Similar topography would also be evidence of similar chemical composition.)

As a result of this examination, it became clear that the HBU-169 deposits were virtually identical in appearance with those on the JCN-196 cladding. For example, Fig. 4-51 shows the circular features and the concentric step fracture pattern of a large deposit which could be considered replicas of a JCN-196 case illustrated in Fig. 4-49. Another example of the circular form of the HBU-169 deposits is shown in Fig. 4-52. The deposits on the two cladding specimens, then, most probably stem from similar fission product release and chemical processes.

212 120X

213 1200X

Figure 4-49 TOP - DEPOSIT NEAR POINT 2 OF 166A-7 IN Figure 4-37 SHOWING CIRCULAR FEATURES

BOTTOM - CONCENTRIC FRACTURE PATTERN DETAIL NEAR POINT A OF TOP PHOTOGRAPH

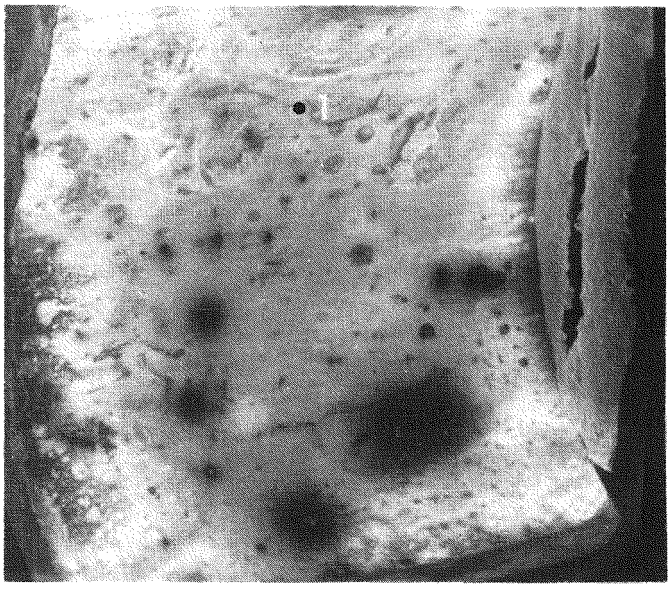

268 11X

Figure 4-50 LOW MAGNIFICATION SEM PHOTOGRAPH OF HBU-169 CLADDING SAMPLE 166C-3

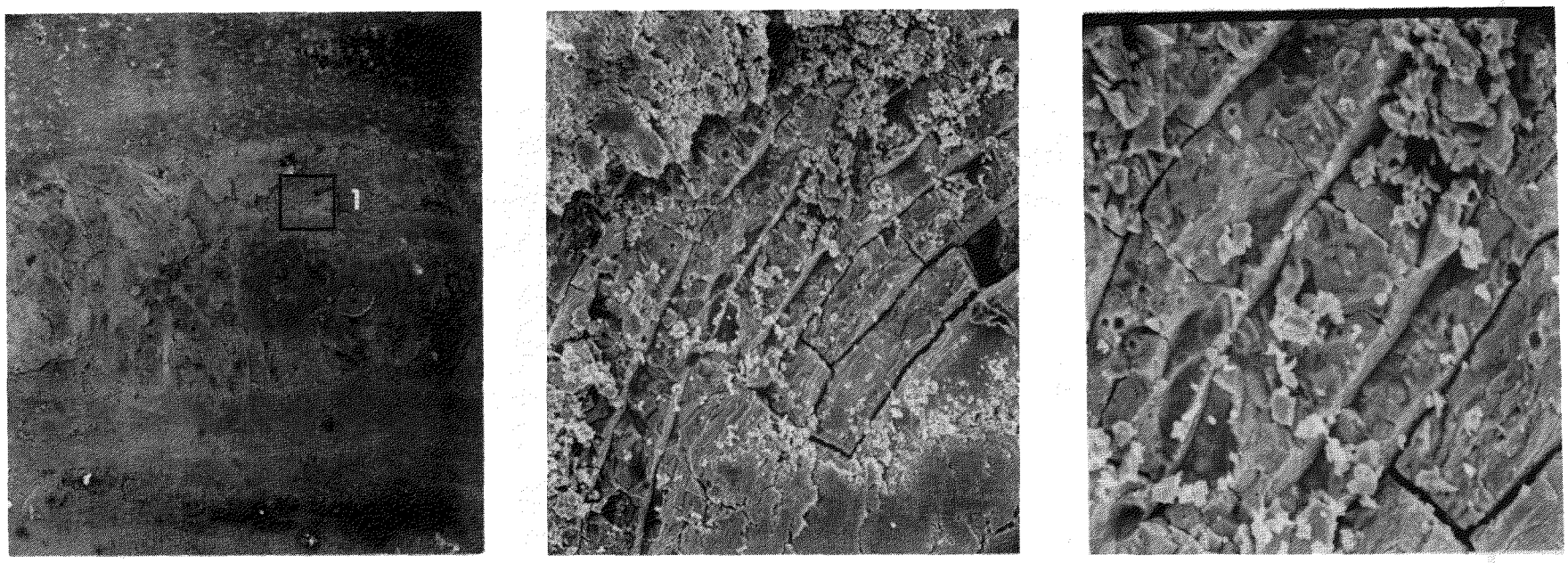

Figure 4-51 SEM PHOTOGRAPHS SHOWING CIRCULAR FEATURES AND CONCENTRIC FRACTURE PATTERN OF DEPOSIT NEAR POINT 2 OF 166C-1 IN Figure 4-50 (NOTE THE SIMILARITY WITH THE FRACTURE PATTERN OF Figure 4-49)

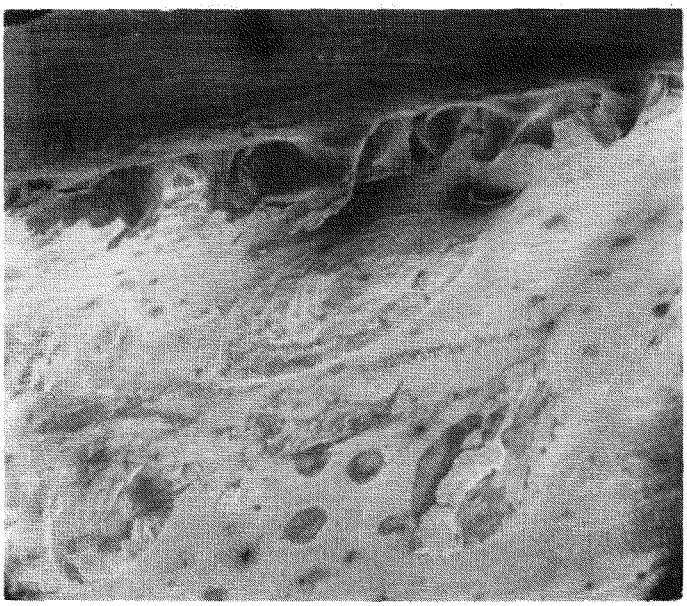

272 22X

273 44X

Figure 4-52 SEM PHOTOGRAPHS OF DEPOSITS NEAR POINT 1 OF 166C-3 IN Figure 4-50 SHOWING CIRCULAR TOPOGRAPHY

4.8 Fuel-Clad Metallography

4.8.1 Objectives

In addition to the slit cladding section examination, fuel rods were systematically sectioned for extensive fuel-clad metallography with the following primary objectives:

1. To search for evidence of incipient cladding perforation in sound rods using non-destructive test data as the basis for section selection.

2. To characterize the UO_2 microstructures, particularly to determine the extent of equiaxed grain growth in the high gas release fuel rods.

In the first hot cell campaign, eddy current data (both from the poolside and the hot cell tests) were the sole basis for the incipient crack search. However, because the eddy current indications were found, almost invariably, to be signaling fuel bonded to the cladding, the emphasis in the second hot cell campaign was shifted to the use of profilometry and gamma scan data to pinpoint possible locations of incipient cracks, e.g., the coincidence of circumferential ridging, high ovality and gamma scan cesium peaking at a high burnup position.

The underlying reason for concentrating this effort on sound rods rather than perforated rods was the recognition that the initial clad perforation features in perforated rods would most likely be masked by secondary hydriding due to water ingress. Further, in most conceivable circumstances, the finding of significant incipient perforation evidence in sound rods could serve as a basis for determining the cause of initial perforation in all the fuel rods.

4.8.2 Procedure

The procedure for the transverse metallography in both campaigns was the same. This involved one inch-long fuel rod sections, which were enclosed within a stainless steel supporting tube and then held in Bakelite premounts by means of epoxy resin. Azimuthal orientation was maintained by the use of a stainless steel pin fixed in the mount. A specimen for longitudinal metallography was mounted so that its cross section could be examined at the midplane, which was indicated by the presence of marking pins.

Generally, the specimens were ground and polished incrementally to permit examination of many surfaces. Progress through the specimens was followed by measuring the mount length with a micrometer when each new surface was reached. Grinding was performed with successively finer silicon carbide abrasive papers through 600 grit. This was followed by polishing with a 1μ alumina suspension in a 2% chromic acid solution. Each surface was examined both in the as-polished condition and after being etched with a freshly mixed acid solution of 48 v/o H_2O_2 (30%), 48 v/o HNO_3 (70%) and 4 v/o HF (48%) which revealed the hydride concentration and orientation in the cladding. The specimens intended solely for UO_2 microstructure characterization were ground through only a small number of steps. The etchant used to develop the fuel structure was composed of 85 v/o H_2O_2 (30%) and 15 v/o H_2SO_4 (98%).

In those cases where incipient cracks in the cladding were found, a modified procedure was used. Because the peroxide-based etchant would severely attack the cracked area, the specimen was lightly reground and repolished to remove about 0.01 in. of material and then etched with a less aggressive water-based composition [57.5 v/o H_2O, 39 v/o HNO_3 (70%) and 3.5 v/o HF (48%)]. The specimen was then anodized by the procedure described by Picklesimer [2] and Kaufmann, et al.[3] to facilitate examination of the cladding grain structure under polarized light.

The anodizing solution was:

50 grams oxalic acid
50 grams citric acid
50 ml H_3PO_4
100 ml lactic acid
350 ml H_2O
600 ml ethanol

A stainless steel strip was used as the cathode while the specimen cladding was the anode. A clamp applying a stainless steel pin to the specimen allowed the circuit to be completed with the application of 50 volts for 30 to 45 seconds.

4.8.3 Results of Metallography

The descriptions of all metallographic specimens examined at the hot cell in the first and second campaigns are presented in Tables 4-11 and 4-12, respectively. These tables include the specimen locations, the reasons for the examinations, and their results. The scope of this work may be summarized as follows:

1st Campaign

1. Total number of specimens- 24 (all transverse).

2. Seventeen (17) specimens to search for incipient cracks in sound rods using eddy current indications (ECI) observed during poolside and hot cell eddy current testing.

3. Four (4) specimens to characterize UO_2 microstructure, three from a high gas release rod and one from a low gas release rod (other UO_2 characterization data were obtained from specimens selected for ECI investigation).

Table 4-12

Table 4-11

Hot Cell Examination Metallography Summary - 1st Campaign

Mount Number	Rod Number	Indication Location †	Total No. of Surfaces Examined	Distance Ground Past ECI* Inches	Reason for Examination	Met. Exam Finding
X-330	JCN-182	78-5/16	23	0.110	ECI*	Extensive bonded fuel.
X-331	JCN-182	76-13/16	17	0.186	ECI	Some fuel bonding.
X-332	JBY-142	90-1/16	23	0.237	ECI	Very small (<0.002 in.) inner surface defect 98.6 mils past ECI.
X-333	JBY-142	87-9/32	17	0.106	ECI	Very little bonding.
X-334	JBY-142	37-5/8	21	0.162	ECI	Fuel very dense at center. Nothing else.
X-335	HBV-067	Grid #8	20	--	Grid Wear Mark	2 lower arch marks were 3.5 and 2.9 mils deep. Two spring marks were 3.0 and 1.0 mils deep.
X-336	HBV-067	Grid #2	10	--	Grid Wear Mark	Inconclusive due to shallowness of mark, maximum estimate of depth is 1.0 mils.
X-337	JBY-157	40-15/16	8	0.146	ECI	Some bonded fuel with no reaction zone.
X-338	JBY-157	40-5/32	7	0.099	ECI	No anomalies.
X-339	JCN-199	92-5/16	9	0.083	ECI	Extensive bonding. Electron microprobed.
X-340	JCN-199	87-1/2	9	0.113	ECI	Large amount of fuel bonding.
X-341	JCN-199	49-27/32	6	0.108	ECI	Large amount of fuel bonding.
X-342	JBP-005	94-3/16	12	0.083	ECI	Two radial cracks in cladding. Maximum depth 17.0 mils at 75^{o} and 12.2 mils at 80^{o}. Some bonding.
X-343	JBP-005	37-7/16	6	0.115	ECI	Very small amount of fuel bonding.
X-344	KCA-109	88-1/2	10	--	Only blister on perforated "C" rod.	Typical blister cross section.

* Eddy current indication of internal surface defect.

† Inches from bottom of the rod.

Table 4-12 (continued)

Hot Cell Examination Metallography Summary - 2nd Campaign

Mount Number	Rod Number	Axial Location†	Reasons for Selection	Total No. of Surfaces Examined	Results
Category I - Incipient Crack Search in Unfailed Rods - By Transverse Metallography (continued)					
X-421	JBY-097	87-3/8 - 88-3/8	1. Maximum ovality region with evidence of sharp ridging. 2. Cs peaking.	11	One crack in cladding observed. Specimen subjected to SEM fractography.
X-431	JBP-122	94 - 95	1. High burnup, high ovality region. 2. Evidence of ridging.	2	Four cracks in cladding observed. Specimen not examined further.
X-432	JBP-122	111-1/8 - 112-1/8	Maximum ovality region	7	No anomalies observed.
X-433	JBP-122	86-5/8 - 87-5/8	"Bump" in diameter trace.	7	No anomalies observed.
Category II - Incipient Crack Search in a Perforated Rod - By Transverse Metallography					
X-415	JBP-003 Plane of interest at 83-13/16	83-1/16 - 85-1/16	1. Sharp ridges. 2. Very small gap in stack. 3. Cs scan discontinuity. 4. Strong eddy current indication (from poolside exam)	2	Cladding oxidation and hydriding observed.
X-416	JBP-003 Plane of interest at 18-7/8	18-1/2 - 19-1/2	1. Sharp ridges 17-19 in. and one bump at 18-7/8. 2. Eddy current indication (from poolside exam) 3. Small Cs peaking.	1	

† Inches from bottom of rod.

Table 4-12 (continued)

Hot Cell Examination Metallography Summary - 2nd Campaign

Mount Number	Rod Number	Axial Location†	Reasons for Selection	Total No. of Surfaces Examined	Results
Category III - UO_2 Microstructure Characterization - By Transverse Metallography					
X-411	HBU-169	50-1/8	1. High ovality region. 2. High burnup location. 3. High gas release Batch A rod.	7	Equiaxed grain growth observed.
X-413	JBP-005	6	Complete data already available on this rod to determine the axial extent of equiaxed grain growth.	2	Equiaxed grain growth not observed.
X-414	JBP-005	128	Complete data already available on this rod to determine the axial extent of equiaxed grain growth.	2	Equiaxed grain growth observed.
X-422	JBY-097	6	Same location as from JBP-005 for comparison.	2	
X-426	JBY-097	128	Same location as from JBP-005 for comparison	2	
Category IV - Fuel-Clad Configuration - By Longitudinal Metallography					
X-425	JBY-097	35-5/8 - 36-5/8	Pellet interface ridge. Specimen examined at midplane.	2	Fuel-clad bonding observed near pellet interfaces.
			Total No. of Surfaces (all mounts)	114	

† Inches from bottom of rod.

4. One (1) specimen from the perforated rod from Batch C at the location of its only cladding breach.

5. Two (2) specimens to evaluate the depth of grid contact wear, one at a visibly worn area and one at a typical grid contact area.

2nd Campaign

1. Total number of specimens - 18 (17 transverse, 1 longitudinal).

2. Ten (10) transverse specimens to search for incipient cracks in sound rods using non-destructive test data from profilometry and gamma scanning as the basis for specimen selection and to examine the fuel-clad interface for fuel bonding characteristics.

3. Two (2) transverse specimens to search for incipient cracks in a perforated rod.

4. Five (5) transverse specimens to characterize UO_2 microstructures in high gas release rods and determine the axial extent of equiaxed grain growth.

5. One (1) longitudinal specimen for fuel-clad bonding characterization.

The major findings of this metallography program are presented in the following sections.

4.8.3.1 Fuel-Clad Bonding

One of the more striking results of the metallographic examination was the frequent observation of bonding of fuel to cladding in high gas release rods. Such evidence of adhering fuel, however, was not unexpected in view of the results from slit cladding internal surface examination which showed material adhering to the clad predominately at the pellet interface regions.

Fuel-clad bonding was originally observed in a specimen from Rod JBP-027 which had been selected because it spanned the location of a strong poolside eddy current indication at 59-5/16 inches. (As shown in Appendix B, Rod JBP-027 exhibited two strong poolside eddy current signals. On this basis, the rod was sectioned before the need for the hot cell eddy current testing was established.) During incremental grinding and examination, no anomalies were observed with the exception of fuel-clad bonding as illustrated in Fig. 4-53 through 4-55.

This early result suggested that the large eddy current signals obtained at poolside, as well as in the hot cell, might very well be associated with extensive fuel-clad bonding rather than a cladding defect. Confirmation was obtained when Mount No. X-330 of Rod JCN-182 exhibited no anomalies other than extensive bonding, such as shown in Fig. 4-56. This specimen had been selected because of the large internal surface ECI shown in the Fig. 4-23 hot cell eddy current trace.

As noted in Table 4-11, all of the specimens taken from high gas release rods in the first campaign exhibited some fuel-clad bonding. Little, if any, bonding was observed in metallographic specimens taken from the low gas release rods, i.e., JBY-142 and JBY-157.

In the second hot cell campaign, fuel-clad bonding was again observed in the high gas release rods on a frequent basis. For example, Fig. 4-57 shows typical bonded areas in transverse metallographic specimens. The Fig. 4-58 detail of the longitudinal specimen cross section shows examples of bonding at or near the pellet interfaces.

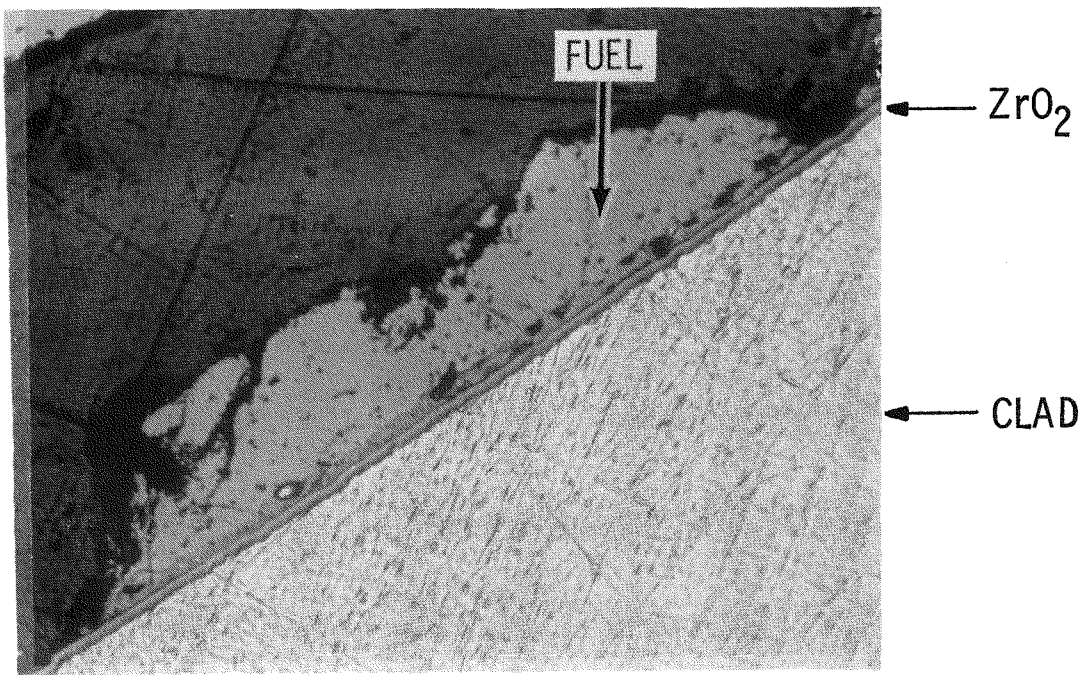

Figure 4-53 FUEL/CLAD BONDING IN ROD JBP-027, 59 1/8 INCH FROM BOTTOM (AS POLISHED)

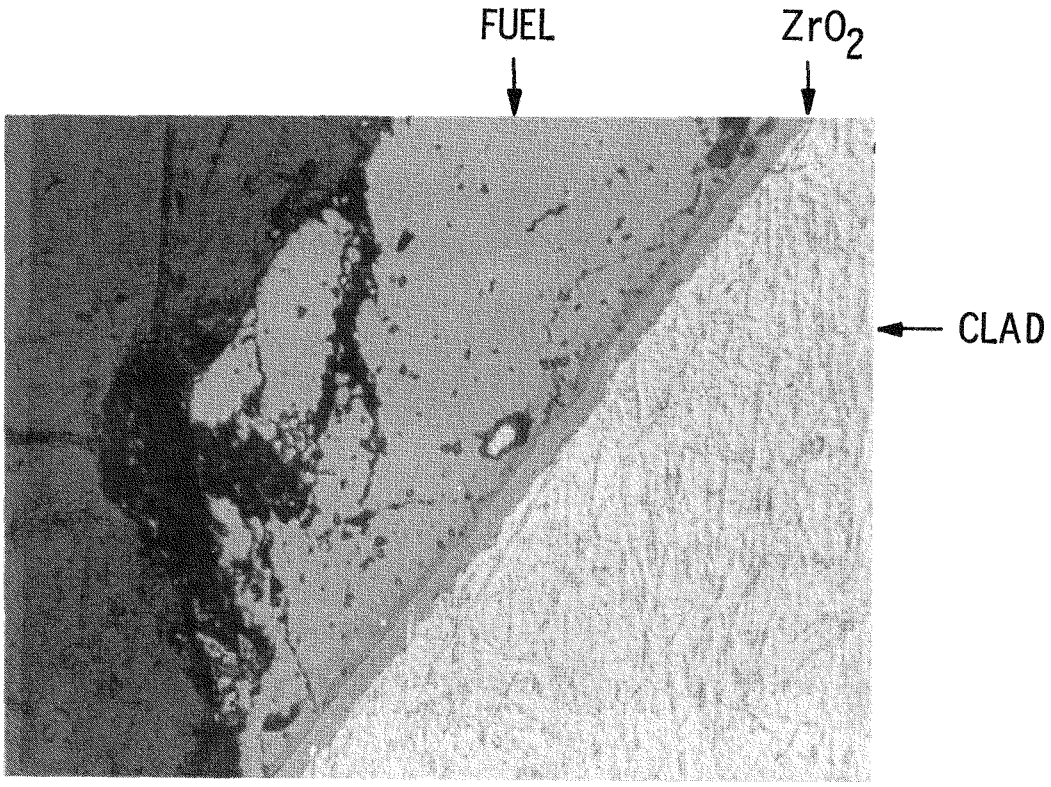

Figure 4-54 DETAIL OF FUEL/CLAD BONDING IN ROD JBP-027
Figure 4-53 (AS POLISHED)

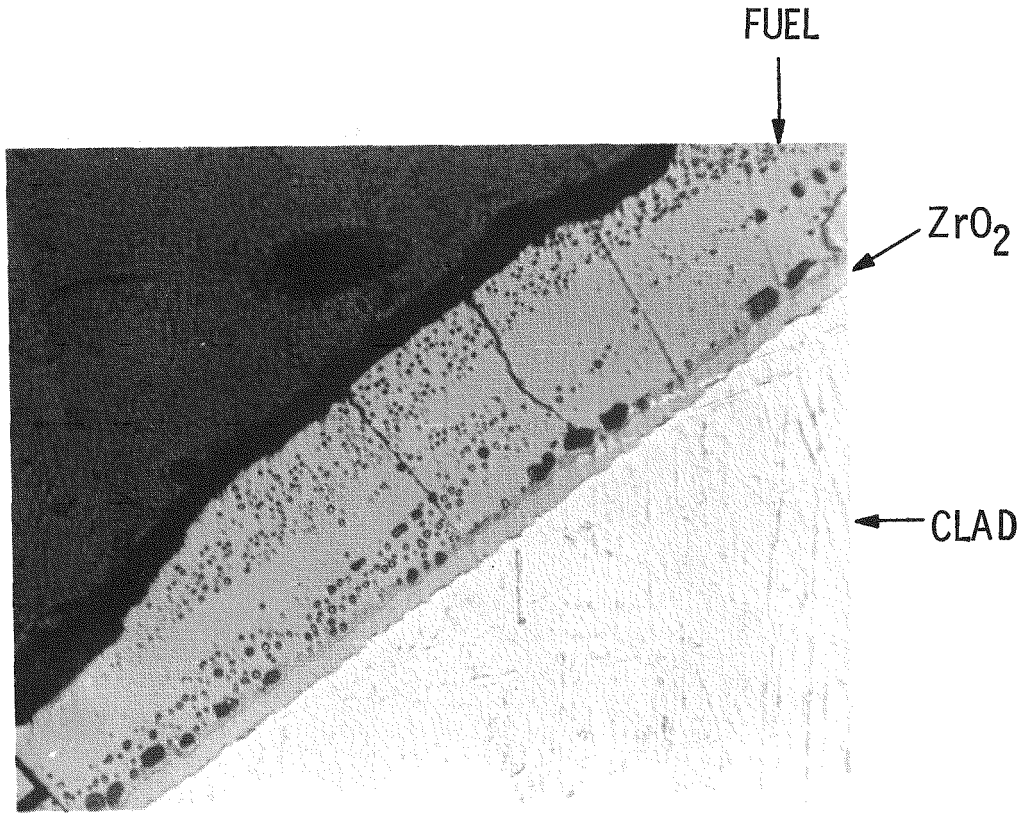

Figure 4-55 ANOTHER REGION OF FUEL/CLAD BONDING IN ROD JBP-027 AT 59 1/8 INCHES FROM BOTTOM (AS POLISHED)

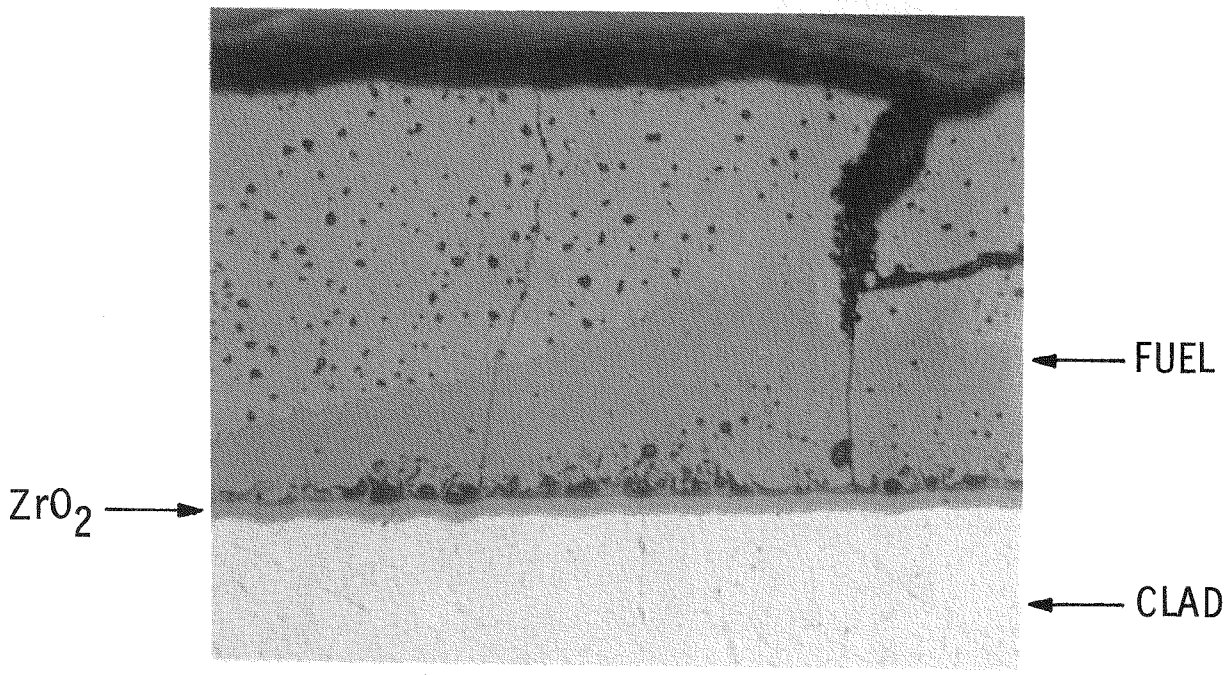

Figure 4-56 FUEL/CLAD BONDING IN MOUNT No. X-330 IN ROD JCN-182 ASSOCIATED WITH EDDY CURRENT SIGNAL IN Figure 4-23 NEAR 78-5/16 INCHES FROM BOTTOM (AS POLISHED)

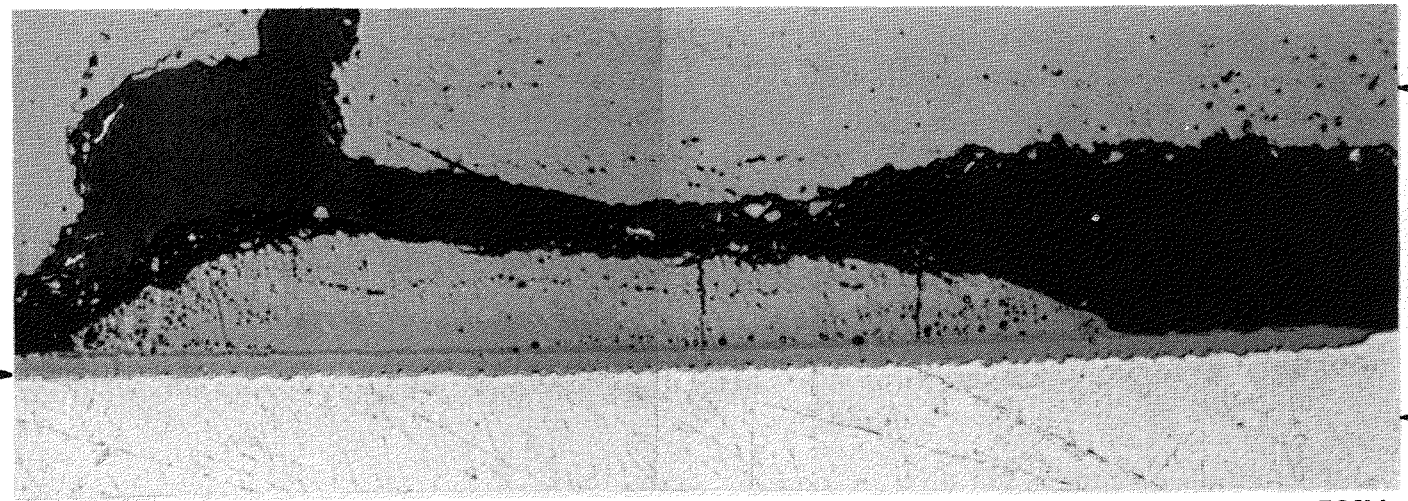

41596 & 41597 JBY-097 AT 45 7/8 IN. FROM THE BOTTOM 500X

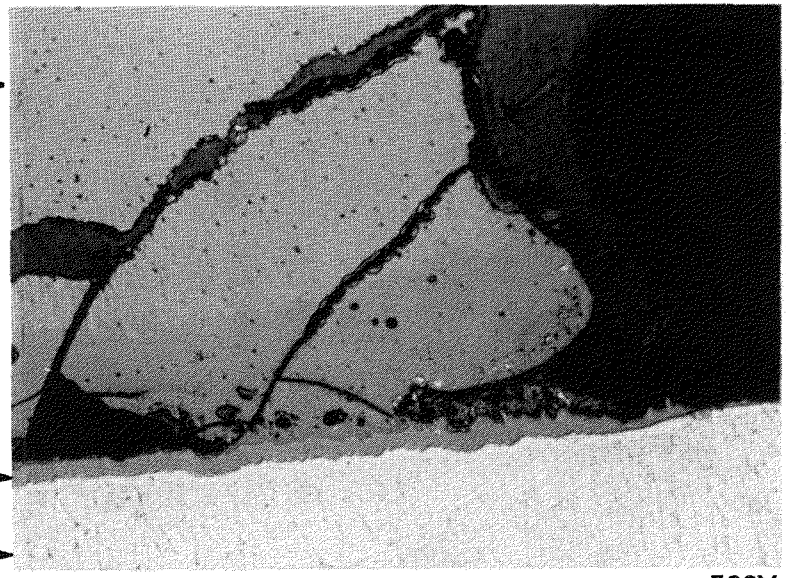

41870 500X

HBu -169 AT 50 3/8 IN. FROM THE BOTTOM

Figure 4-57

TYPICAL EXAMPLES OF FUEL/CLAD BONDING FOUND IN HIGH GAS RELEASE RODS IN SECOND CAMPAIGN (AS POLISHED)

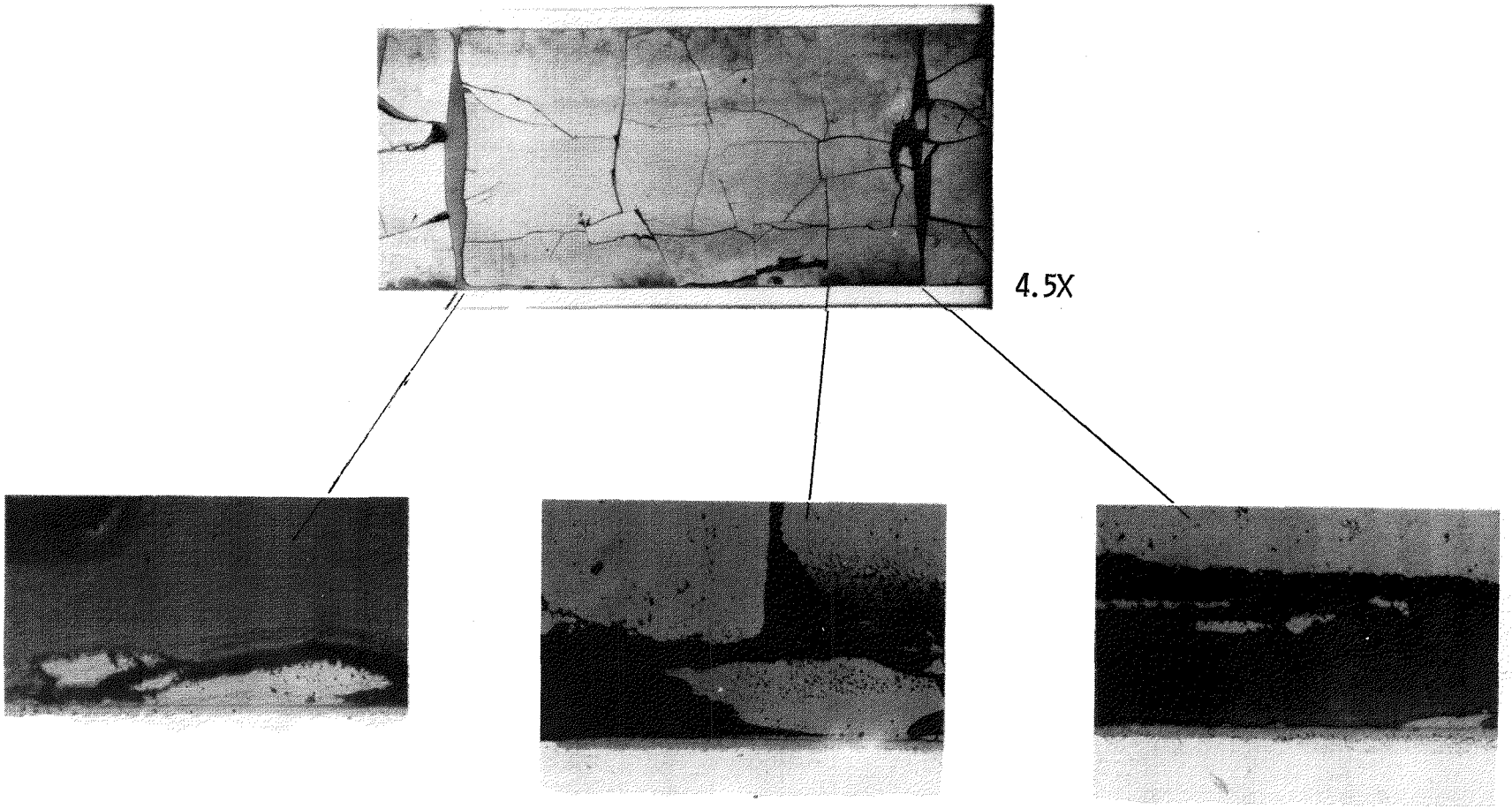

Figure 4-58 LONGITUDINAL SPECIMEN SHOWING FUEL/CLAD BONDING IN ROD JBY-097 AT 36 IN. FROM THE BOTTOM (AS POLISHED)

It should be noted that the metallographic appearance of the fuel-clad bonding is characterized by a relatively thick local ZrO_2 layer ($\sim 5\mu$) to which is adhered one or more dark grey fuel layers of varying thickness and distinctly different from the grey UO_2. The SEM examination of the adhering material on the slit clad sections described earlier in Section 4.7 and the electron microprobe analyses of typical bonded fuel regions described later in Section 4.10 indicate that the layers immediately adjacent to the ZrO_2 consist of a reaction zone containing cesium and zirconium, as well as uranium.

4.8.3.2 Incipient Cladding Perforations

1st Campaign

In the first campaign, only two sections exhibited cladding defects of any significance. One of these is a small cracked area found in Mount No. X-332 from a low gas release rod, JBY-142, as shown in Fig. 4-59 and 4-60. The depth of penetration was approximately 5% of the wall thickness. It appears to be a tube fabrication blemish, viz., a rolled-in chip or a lap and is considered to have been in the tube before irradiation.

The other defect, consisting of two internal surface cladding cracks, was found in Mount X-342 from Rod JBP-005 containing the ECI shown in the Fig. 4-25 trace at 94-3/16 inches from the bottom of the rod. (Note that this is in a relatively high burnup position of a high gas release rod.) One of the two cracks was observed immediately on the first surface examined at a pellet-pellet interface as shown in Fig. 4-61 and 4-62. Further metallography of successive surfaces was performed to characterize the crack and establish its axial length. Upon grinding 4 mils to the second surface, the second crack was found adjacent to the first crack. Both cracks were observed on the next five surfaces over a distance of 61 mils. The typical appearance of the cracks is illustrated in the photographs of the sixth surface shown in Fig. 4-63 through 4-66. After grinding a total of 93 mils from the first surface, both cracks disappeared. From a

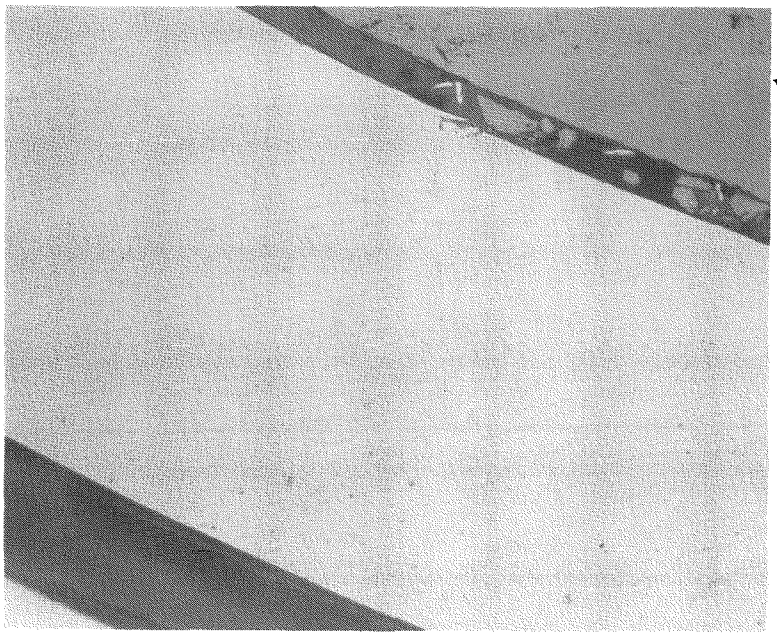

Figure 4-59 DEFECT ON INNER CLADDING SURFACE OF ROD JBY-142 AT 90-11/32 INCHES FROM BOTTOM (AS POLISHED)

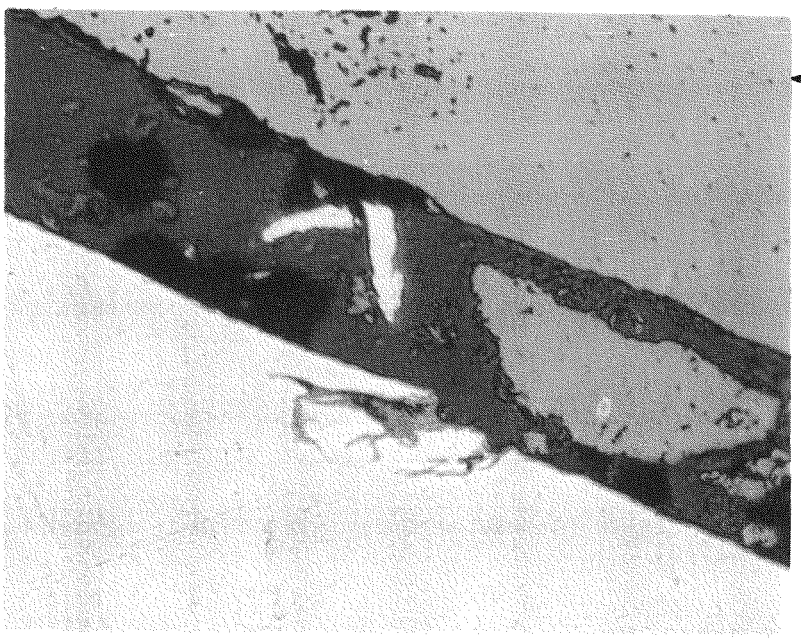

Figure 4-60 DETAIL OF Figure 4-59 CLADDING DEFECT IN ROD JBY-142 (AS POLISHED)

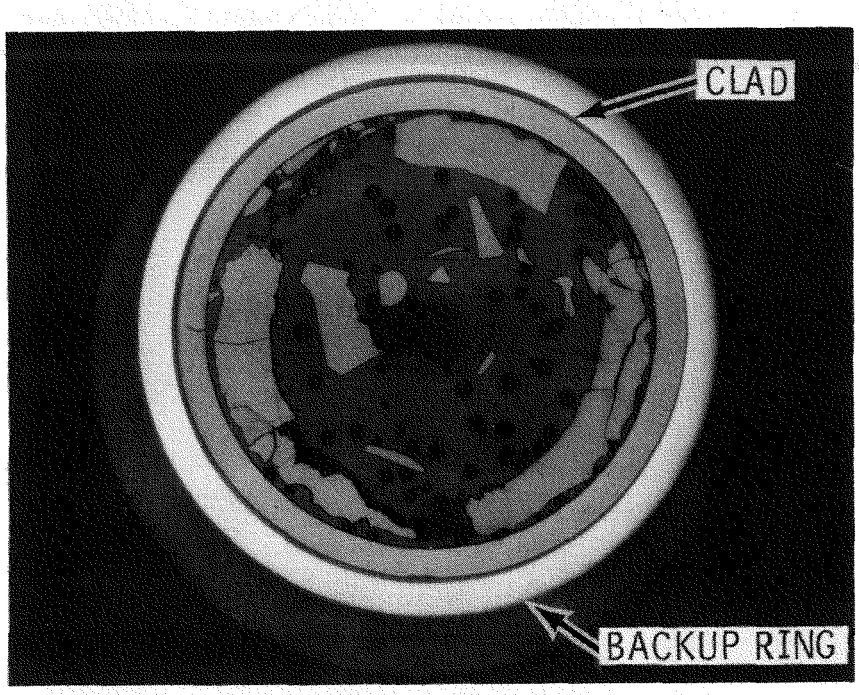

HC41254 6.5X

Figure 4-61 MACROPHOTOGRAPH OF CRACK AT PELLET-PELLET INTERFACE IN MOUNT X-342 FROM ROD JBP-005 (ABSENCE OF FUEL IS DUE TO PELLET END DISHING).

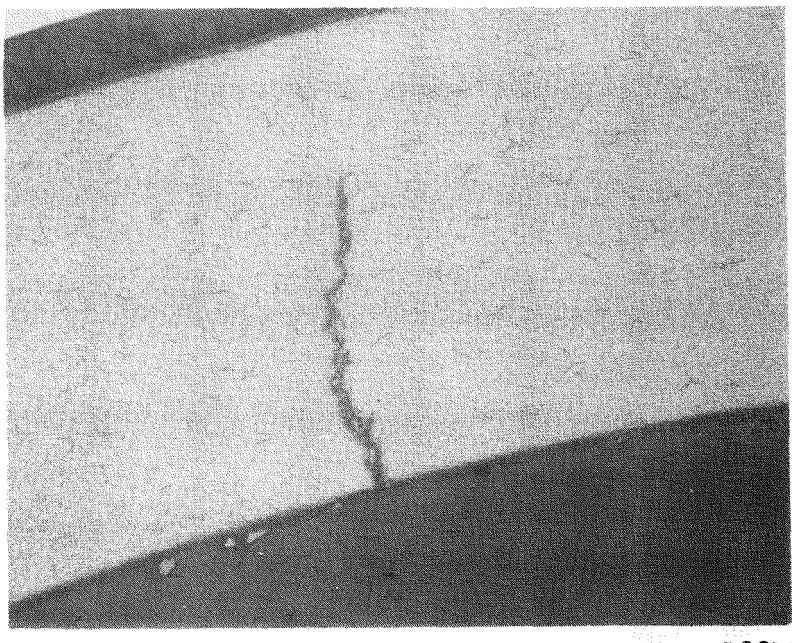

HC41239 100X

Figure 4-62 CRACK AT 75^{o} IN MOUNT X-342 FROM ROD JBP-005 AT PELLET INTERFACE 1st SURFACE (ETCHED).

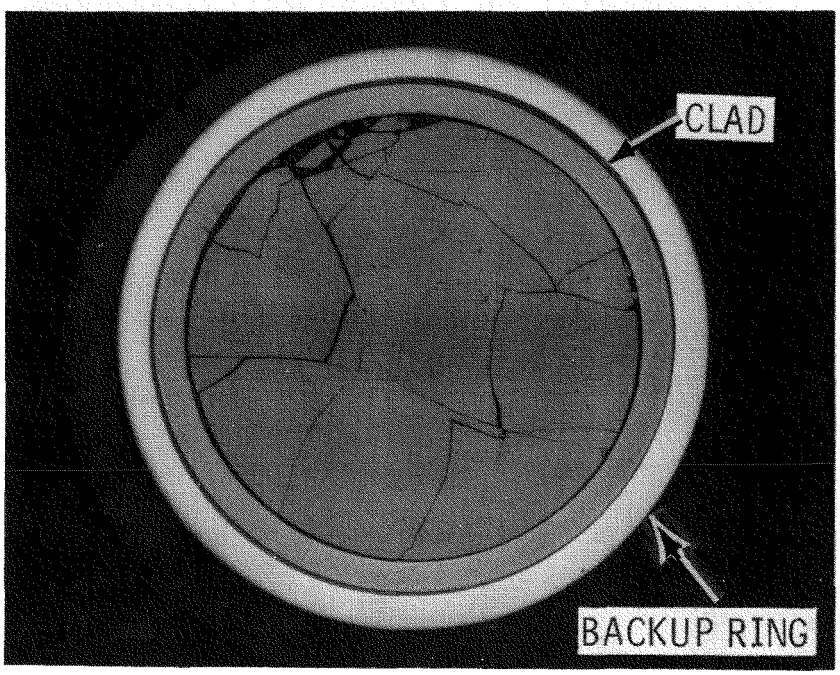

HC41420 6.5X

Figure 4-63 MACROPHOTOGRAPH OF CRACKS IN MOUNT X-342 FROM ROD JBP-005 - 6th SURFACE (ETCHED)

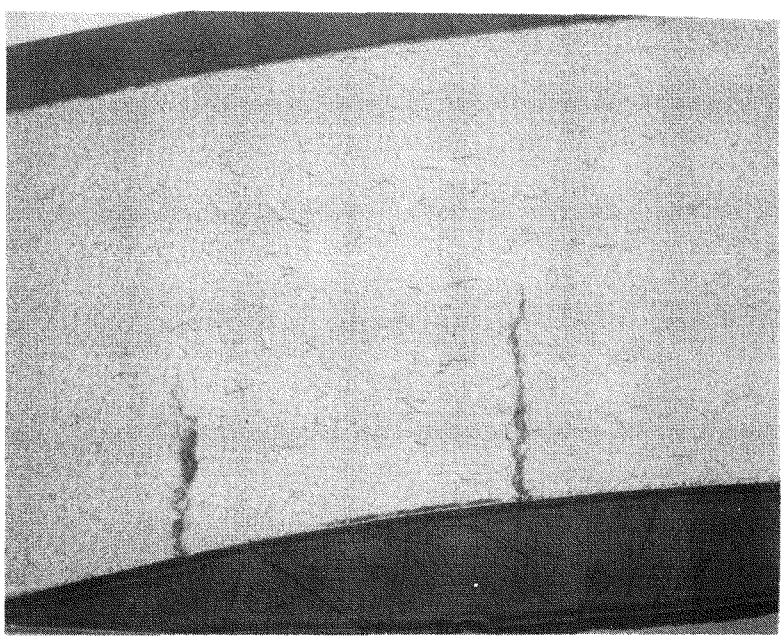

HC41415 100X

Figure 4-64 CRACKS AT 75^{0} AND 80^{0} IN MOUNT X-342 FROM ROD JBP-005 - 6th SURFACE (ETCHED)

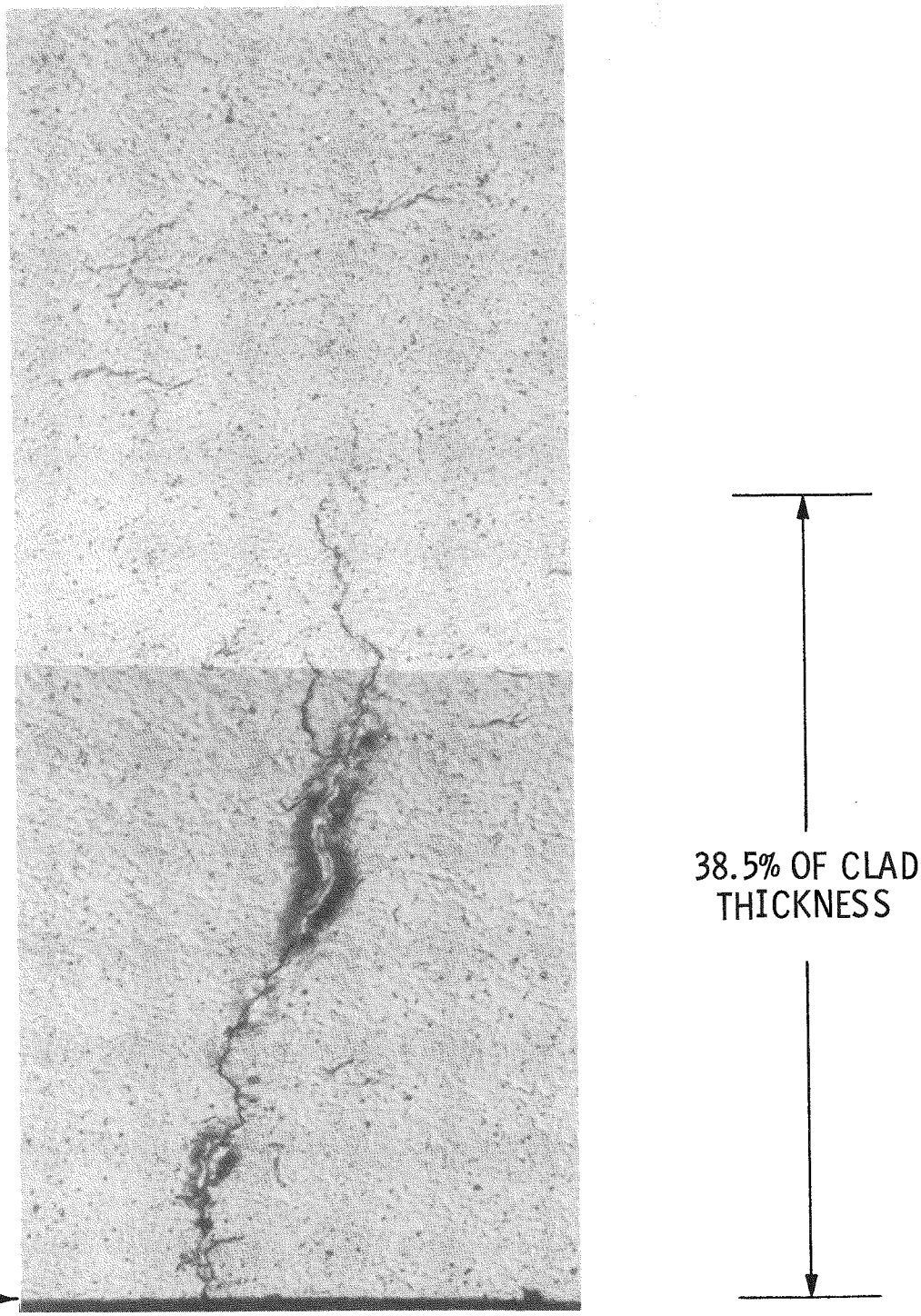

Figure 4-65 CRACK IN MOUNT No. X342 FROM ROD JBP-005 AT 75^{0} - 6th SURFACE (ETCHED).

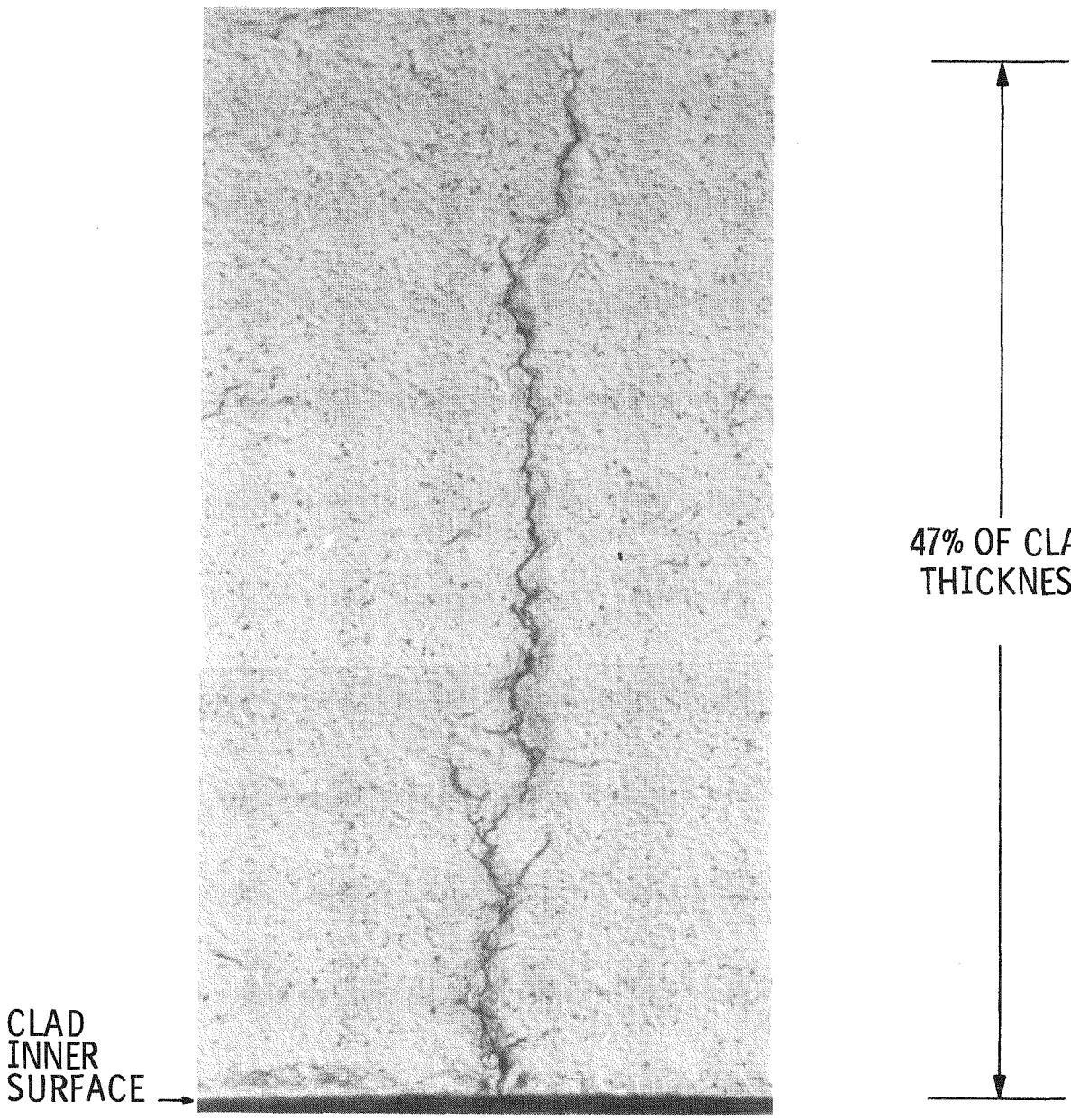

Figure 4-66 CRACK AT 80° IN MOUNT No. X342 FROM ROD JBP-005 - 6th SURFACE (ETCHED).

"map" of the two cracks shown in Fig. 4-67, it can be seen that the maximum wall penetration of the first crack was 65% and that of the second crack 45%. The axial length of the deeper crack is in the range of 1/8 to 3/16 inch, while that of the other crack is approximately 1/16 inch. It should be noted that the cracks were tight and difficult to detect in the as-polished condition; therefore, etching was necessary not only to characterize their appearance but to reveal their presence.

At this point in the program, consideration only of the location at a pellet-pellet interface and the optical microscopic characteristics (tightness and branching) of the cracks suggested that they were caused by a stress corrosion assisted pellet-cladding interaction mechanism. This conjecture was reinforced by a comparison of the photomicrographs generated in this study with those reported by others. For example, Bain, et al.[4] have published photomicrographs of stress corrosion-related cracks in cladding (some caused by iodine), as shown in Fig. 4-68. A comparison with a cladding crack from JBP-005, also shown in Fig. 4-68, demonstrates the similarity in appearance.

Three fuel rod sections were identified as having the same hot cell eddy current signals as that of the pair of cracks in JBP-005. One was from another region of JBP-005 (Mount No. X-357) and the other two were from another high gas release rod, JCN-182 (Mount No. X-355 and X-356). Exhaustive metallographic examination involving grinding and polishing of many surfaces found no evidence of cracking. It was concluded that the discovery of the original cracks involved some element of chance instead of being pinpointed by an eddy current signal indication.

2nd Campaign

The selection of specimens for the incipient crack search in the second campaign was based primarily on non-destructive tests other than eddy current. Table 4-12 lists the pertinent specimen characteristics obtained from profilometry and gamma scan data. Because of the additional high gas release rods found and the mounting evidence for a causal relationship between fission product release and initial clad perforation

Figure 4-67
MAP OF TWO CRACKS IN MOUNT X-342
FROM ROD JBP-005 AT 94-3/16 IN.
FROM BOTTOM OF ROD

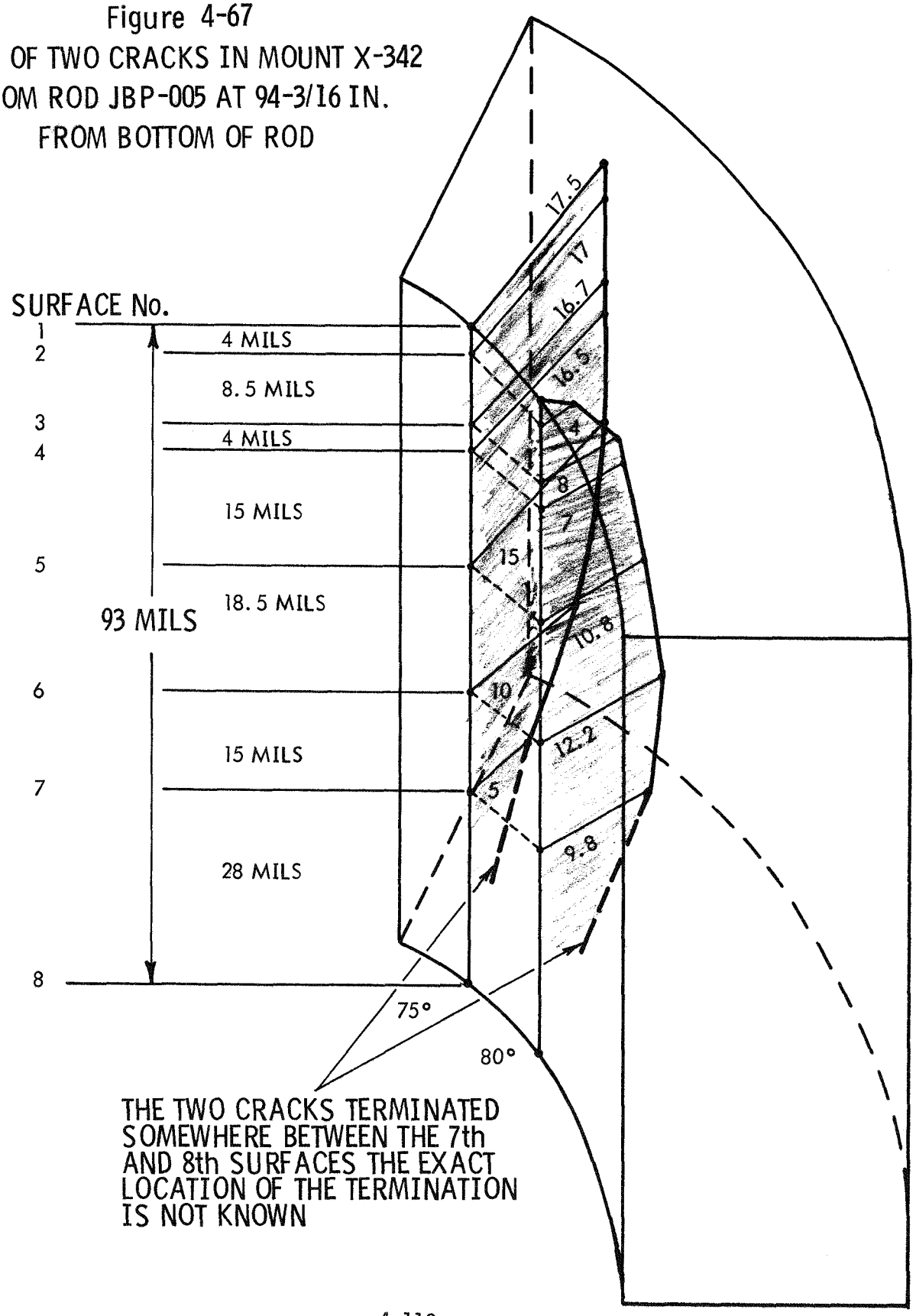

THE TWO CRACKS TERMINATED SOMEWHERE BETWEEN THE 7th AND 8th SURFACES THE EXACT LOCATION OF THE TERMINATION IS NOT KNOWN

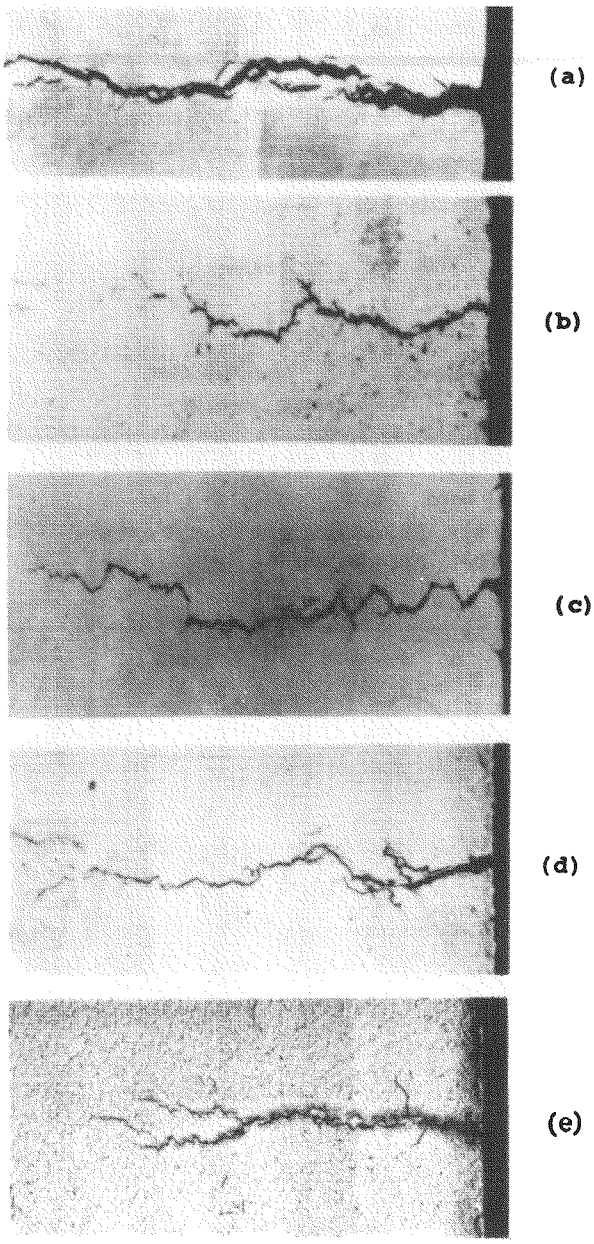

APPROX. 270X

Figure 4-68 CRACKS IN ZIRCALOY CLADDING FROM REF. 4 (a-d) COMPARED WITH A MAINE YANKEE CLADDING CRACK (e).
a. UNIRRADIATED CRACKED IN IODINE VAPOR AT 300°C.
b. IRRADIATED (7×10^{24} N/M^2 E>1 Mev), CRACKED IN IODINE VAPOR AT 300°C.
c. SHEATH OF ELEMENT THAT FAILED AFTER AN INCREASE IN POWER IN A TEST REACTOR.
d. SHEATH OF AN INTACT ELEMENT FROM A BUNDLE THAT DEFECTED AFTER AN INCREASE OF POWER IN A POWER REACTOR.
e. CRACK AT 80° IN MOUNT X-342 FROM ROD JBP-005 7th SURFACE (ETCHED)

the sound rods selected for clad metallography were all from the high gas release population, i.e., Batch B Rods JCN-196, JBY-097 and JBP-122 and Batch A Rod HBU-169.

Of the ten (10) specimens metallographically examined for evidence of incipient perforation, two were found to have cladding cracks similar to those in JBP-005. One crack was found in Rod JBY-097 (Mount X-421) as shown in Fig.4-69 and 4-70, and a set of cracks was found in Rod JBP-122 (Mount X-431) as shown in Fig. 4-71 through 4-74. As in the case of JBP-005, the cracks were found at pellet interfaces in the vicinity of pellet cracks. They were also extremely tight and generally not observed in the as-polished condition.

It is noteworthy that JBP-122 and JBP-005 came from the same quadrant of assembly B-042, and the clad cracks discovered in both rods were at the same elevation (∿95 in. from the bottom). Rod JBY-097 had been selected from assembly B-069, and its crack was found at ∿88 in. from the bottom which is also a relatively high power position. The crack in Rod JBY-097, which was found first, was subsequently characterized by scanning electron microscopy (see Section 4.9). The crack in Rod JBP-122 was found later as part of a secondary effort to demonstrate a search technique; therefore, it was not characterized beyond optical microscopy. In both cases the cladding surfaces containing the cracks were characterized by polarized light metallography. For this purpose, the specimens were briefly reground, polished, etched with the slower acting etch, and then anodized. Under polarized light and/or sensitized tint illumination, all cracks were found to be transgranular with no evidence of twins or slip in or around the cracks indicating no plastic deformation occurred. This morphology along with the branching characteristics, is consistent with stress corrosion cracking.

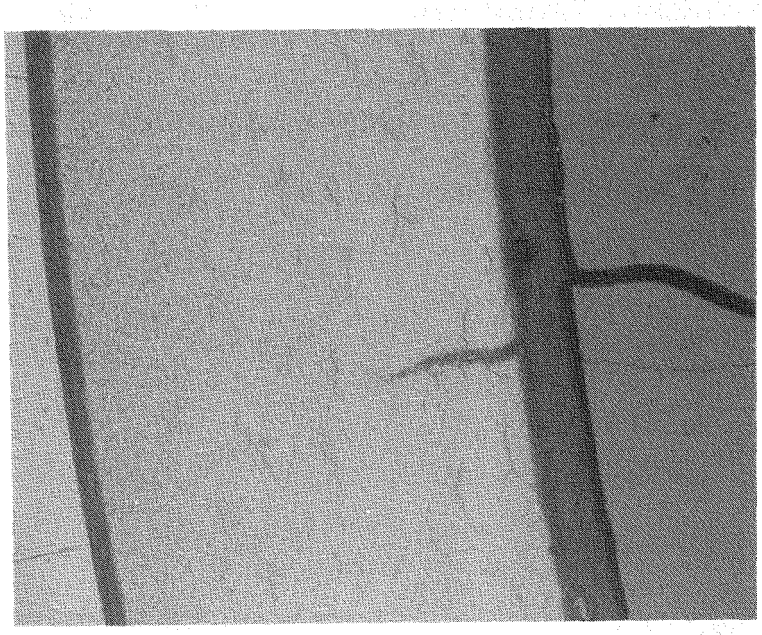

41854 100X

Figure 4-69 PHOTOMICROGRAPH OF INCIPIENT CLADDING CRACK IN ROD JBY-097 AT 88 3/8 IN. FROM THE BOTTOM (ETCHED)

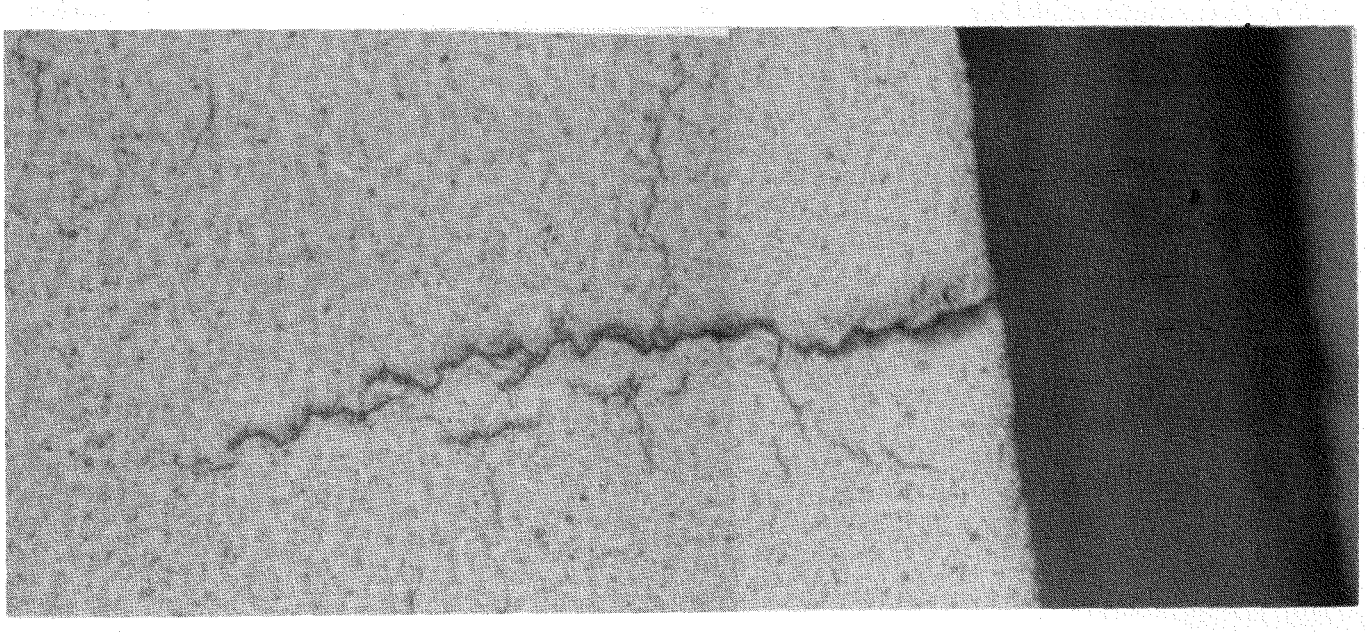

41857 & 41858 550X

Figure 4-70 DETAIL OF INCIPIENT CLADDING CRACK IN ROD JBY-097 SHOWN IN Figure 4-69 (ETCHED)

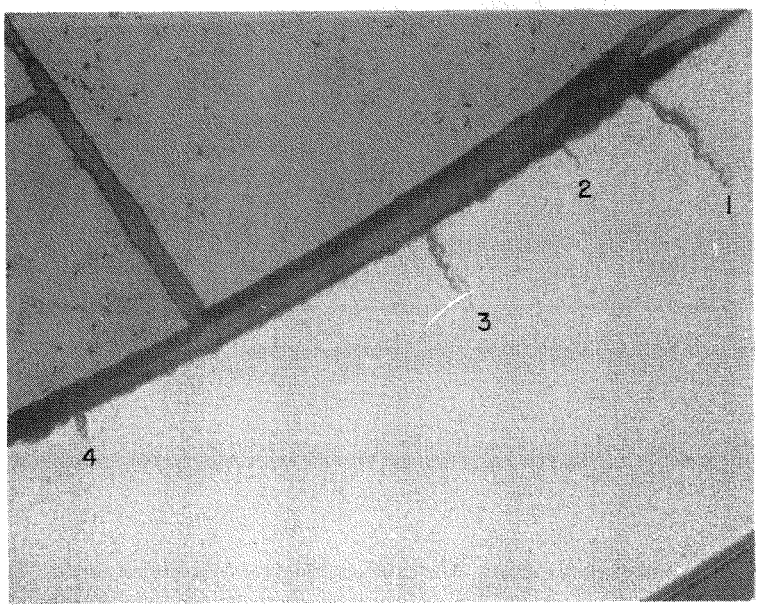

42078 100X

Figure 4-71 PHOTOMICROGRAPH OF INCIPIENT CLADDING CRACKS IN ROD JBP-122 AT 95 IN. FROM THE BOTTOM (ETCHED)

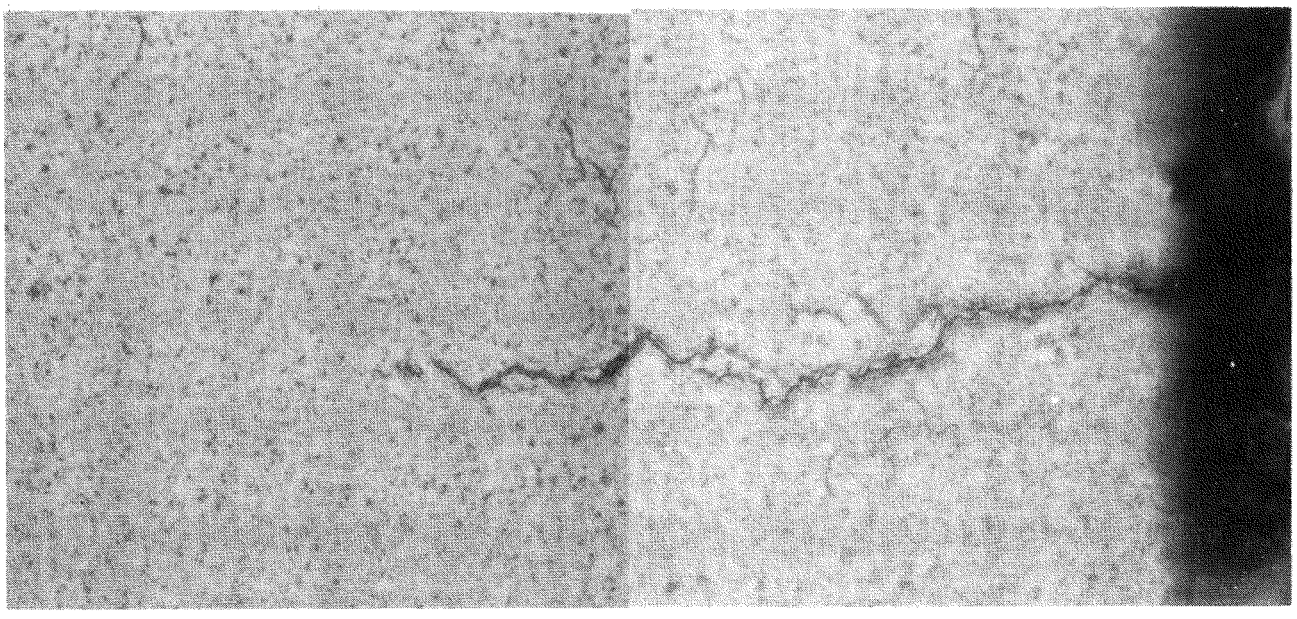

42189 & 42190 550X

Figure 4-72 DETAIL OF INCIPIENT CLADDING CRACK No. 1 IN ROD JBP-122 SHOWN IN Figure 4-71 (ETCHED)

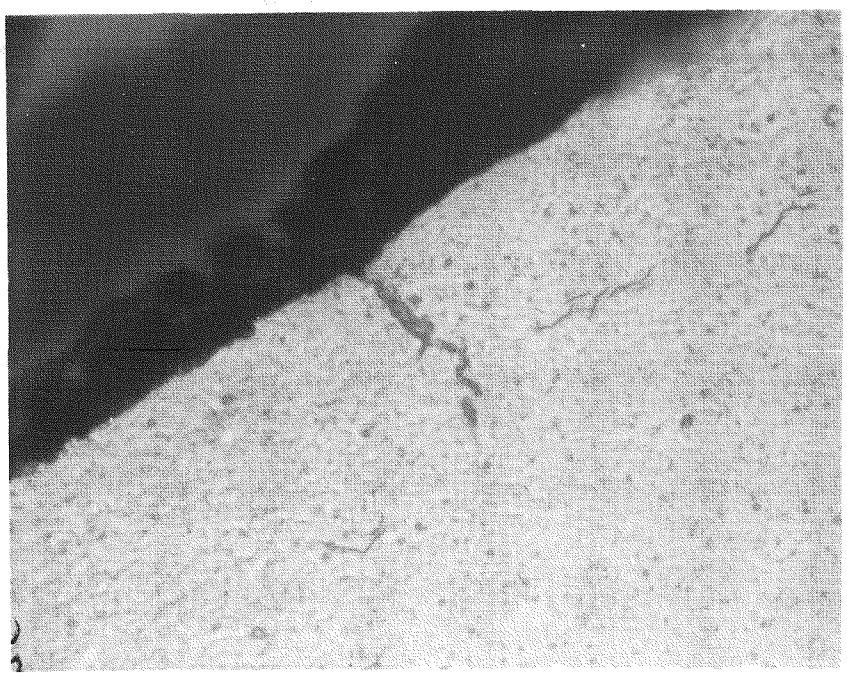

42082 550X

Figure 4-73 DETAIL OF INCIPIENT CLADDING CRACK No. 2 IN ROD JBP-122 SHOWN IN Figure 4-71 (ETCHED)

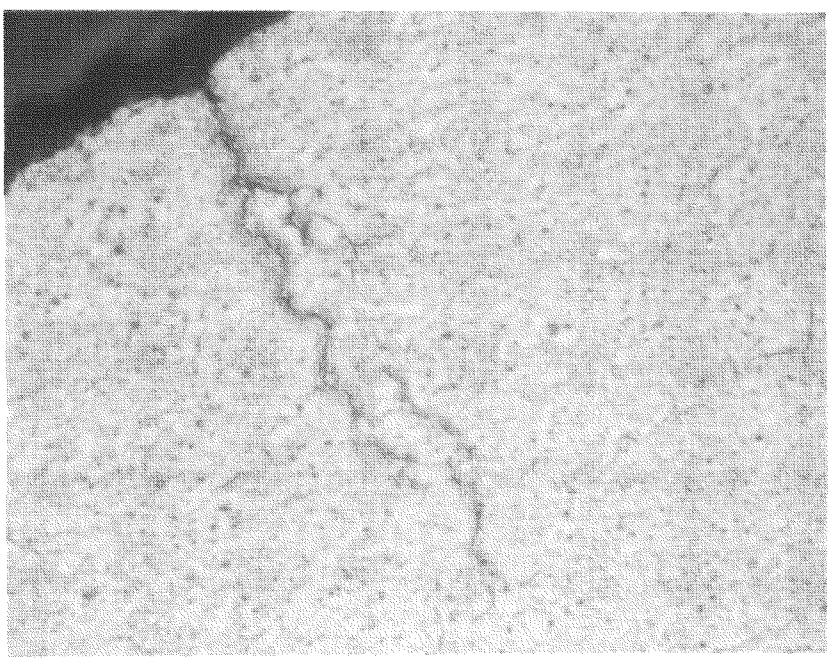

42081 550X

Figure 4-74 DETAIL OF INCIPIENT CLADDING CRACK No. 3 IN ROD JBP-122 SHOWN IN Figure 4-71 (ETCHED)

It is considered unlikely for these incipient cracks to have been present during fabrication, since all cracks were observed to follow a radial direction which is the most easily detected by the ultrasonic techniques used in inspecting the starting tube material. Fabrication defects tend to be at an angle to the radial direction. Most important, these cracks were all at pellet interfaces which would be too much of a coincidence if they were present as fabricated.

4.8.3.3 UO_2 Microstructure Characterization

Most of the transverse metallographic specimens sectioned in the search for defects on the cladding internal surface were also examined to characterize the UO_2 microstructure. Additional specimens were specifically selected for this purpose. The section locations and other pertinent fuel rod data are presented in Table 4-13. As indicated in the table, all high gas release rods exhibited equiaxed grain growth and grain boundary fission gas bubbles. These structures are indicative of relatively high temperature operation. Specimens from the low gas release rods (JBY-142 and JBY-157) exhibited no significant grain size transition even though their power histories were similar to those from the high gas release rods. This difference in appearance is illustrated by comparing the microstructure montage of the highest burnup region of JBP-005 in Fig. 4-75 with that of JBY-157 in Fig. 4-76.

Specimens from a perforated rod, e.g., JBP-003, also exhibited equiaxed grain growth. While this is consistent with the rod having high gas release, grain growth could also be due to the fuel operating hotter after water ingress.

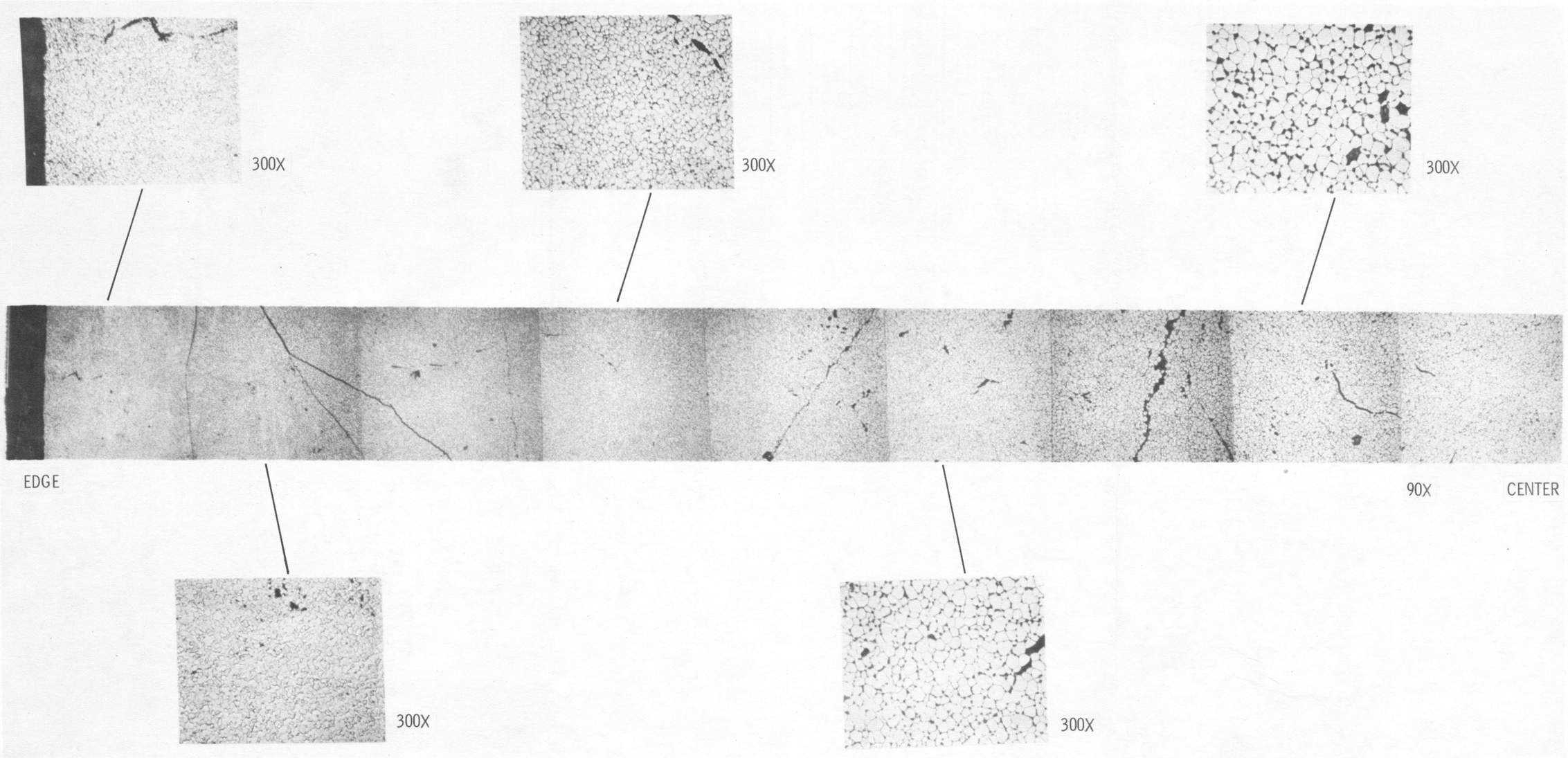

Figure 4-75 UO_2 MICROSTRUCTURE OF ROD JBP-005 AT 94-7/16 INCHES FROM THE BOTTOM SHOWING EQUIAXED GRAIN GROWTH.

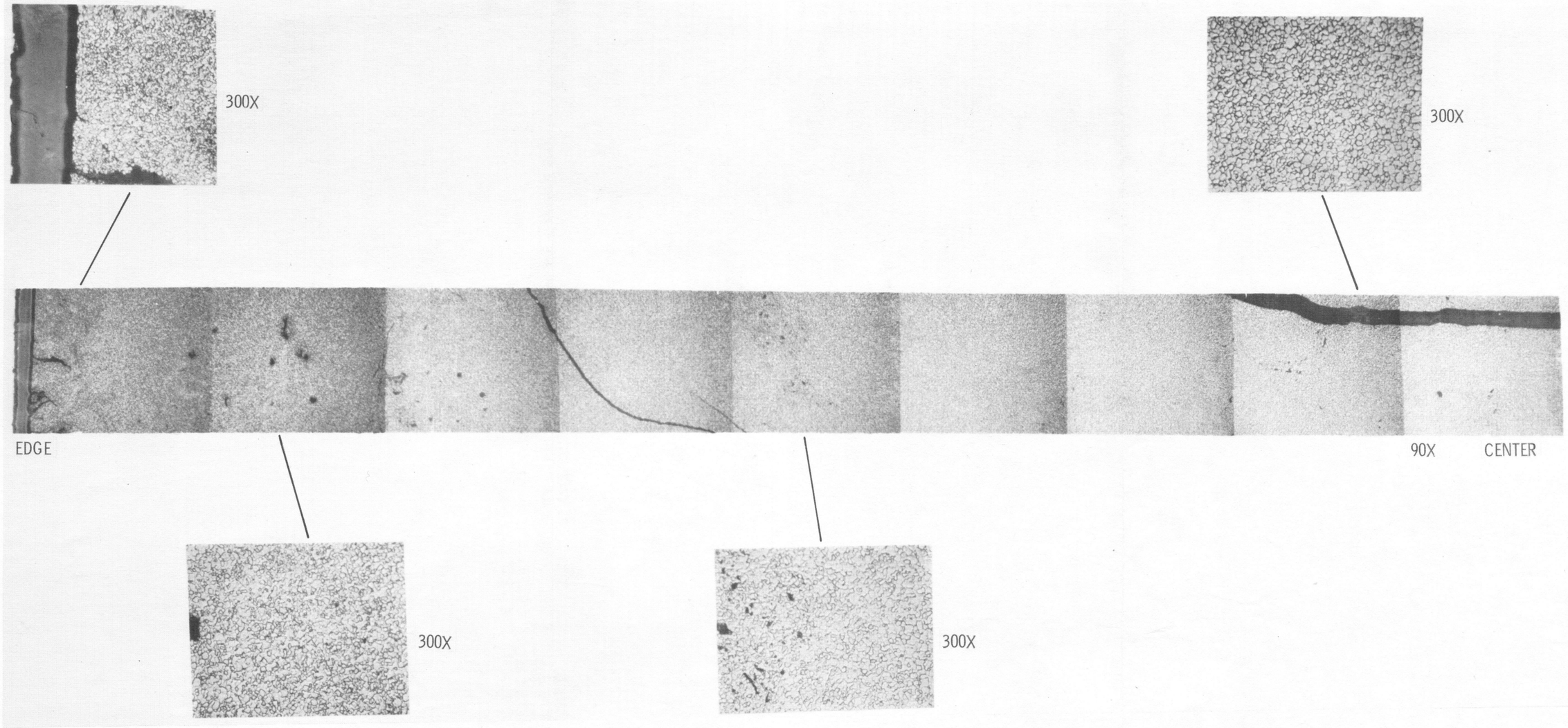

Figure 4-76 UO_2 MICROSTRUCTURE OF ROD JBY-157 AT 96 INCHES FROM BOTTOM SHOWING NO GRAIN STRUCTURE TRANSITION.

Having established that the high gas release was accompanied by equiaxed grain growth, sections were taken to determine the axial extent of the equiaxed grain growth region. These included specimens from 6 in. and 128 in. from the bottom of two rods, JBP-005 and JBY-097. Both Rod JBY-097 specimens exhibited some equiaxed grain growth. In Rod JBP-005, which exhibited such grain growth at about 10 in. from the bottom, no grain growth was found 6 in. from the bottom; however, it was observed at 128 in. from the bottom. Montages of these latter two cross sections are shown in Fig. 4-77 and 4-78, respectively. The equiaxed grain growth radii of most of the specimens listed in Table 4-13 were measured* and are plotted as a function of axial position in Fig. 4-79. From this figure, equiaxed grain growth is estimated to extend over approximately 90% of the fuel length and 25% of the fuel volume in a typical high gas release rod.

4.8.3.4 Cladding Characterization

Zirconium Oxide Film Thickness Measurements

Measurements of zirconium oxide layer thickness were obtained on several of the specimens from high burnup rods using 500X photomicrographs of inner and outer cladding surface cross sections. Fig. 4-80 shows the typical appearance of the oxide layer on the outer surface of the cladding. The measurements obtained for the outer surface oxide layers were in the range of 0.08 to 0.22 mils (2 to 5.6μ) with the predominant value being 0.1 mil (2.5μ). These values are in good agreement with typical long-term corrosion rates reported for Zircaloy-4 in PWRs[5] (as well as out-of-reactor), assuming an average outer surface cladding temperature of 600°F.

---

* The criteria for locating the outer equiaxed grain growth boundary are presented and discussed in Section 6.4.

Table 4-13

UO_2 Microstructure Characterization Results

Mount Number	Rod Number	Gas Release	Calculated Rod Average Burnup Mwd/MTU	Axial Location Inches from Bottom	Remarks
1st Campaign					
X-339, X-341, X-340	JCN-199	High	12,842	92-7/16, 49-3/32, 87-3/4	Equiaxed grain growth.*
X-342, X-343, X-358, X-359, X-360	JBP-005	High	13,231	94-7/16, 37-11/16, 24-1/8, 16-1/4, 10-7/8	Equiaxed grain growth.
X-330	JCN-182	High	12,635	78-1/2	Equiaxed grain growth.
--	JBP-027	High	12,826	59-1/4	Equiaxed grain growth.
X-345	JBY-157	Low	12,935	96	No equiaxed grain growth.
X-332	JBY-142	Low	12,321	89-13/16	No equiaxed grain growth.
X-344	KCA-109	(Perforated Rod)	9,661	89	Equiaxed grain growth.
2nd Campaign					
X-411	HBU-169	High	12,410	50-1/8	Equiaxed grain growth.
X-413	JBP-005	High	13,231	6	No equiaxed grain growth.
X-414	JBP-005	High	13,231	128	Equiaxed grain growth.
X-422	JBY-097	High	13,349	6	Equiaxed grain growth.
X-426	JBY-097	High	13,349	128	Equiaxed grain growth.
X-419	JCN-196	High	12,904	75-5/8	Equiaxed grain growth.
X-415	JBP-003	(Perforated Rod)	13,629	84-1/16	Equiaxed grain growth.
X-416	JBP-003	(Perforated Rod)	13,629	18-1/4	Equiaxed grain growth.

* Defined by the presence of grain boundary fission gas bubbles in the center of the grain growth region.

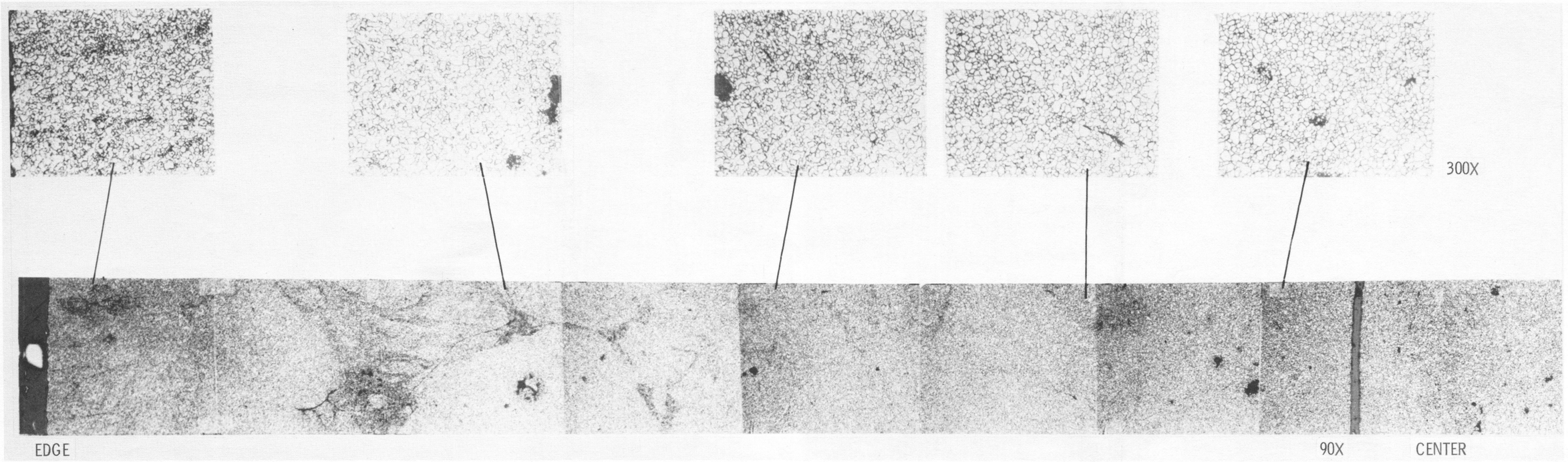

Figure 4-77 UO_2 MICROSTRUCTURE OF ROD JBP-005 AT 6 INCHES FROM THE BOTTOM SHOWING NO TRANSITION TO EQUIAXED GRAIN GROWTH.

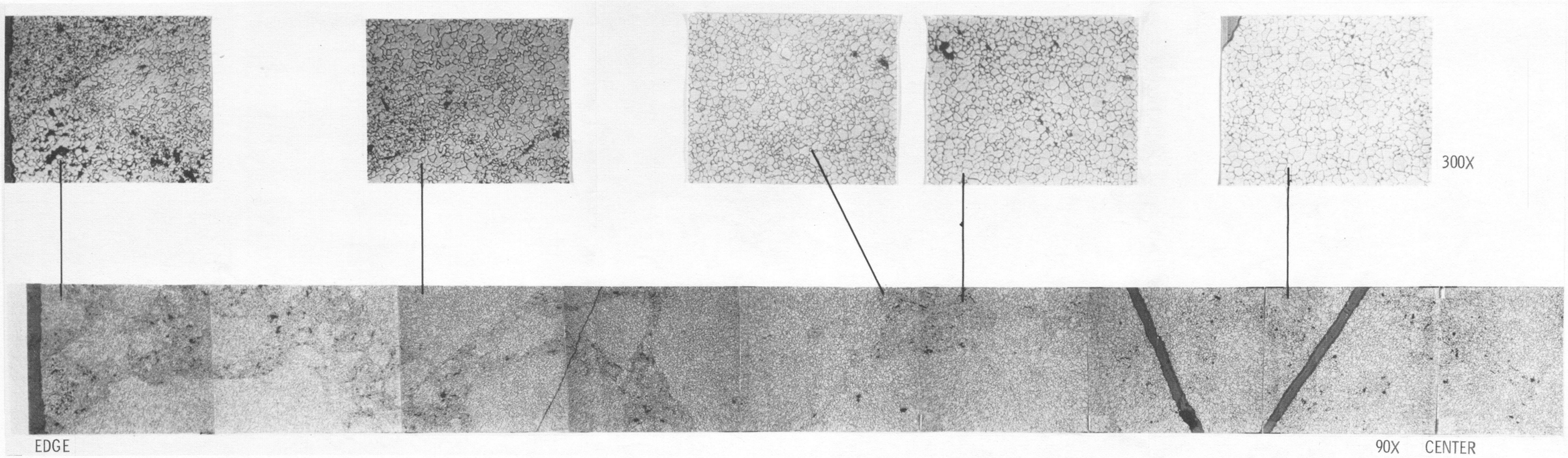

Figure 4-78 UO_2 MICROSTRUCTURE OF ROD JBP-005 AT 128 INCHES FROM BOTTOM SHOWING EQUIAXED GRAIN GROWTH.

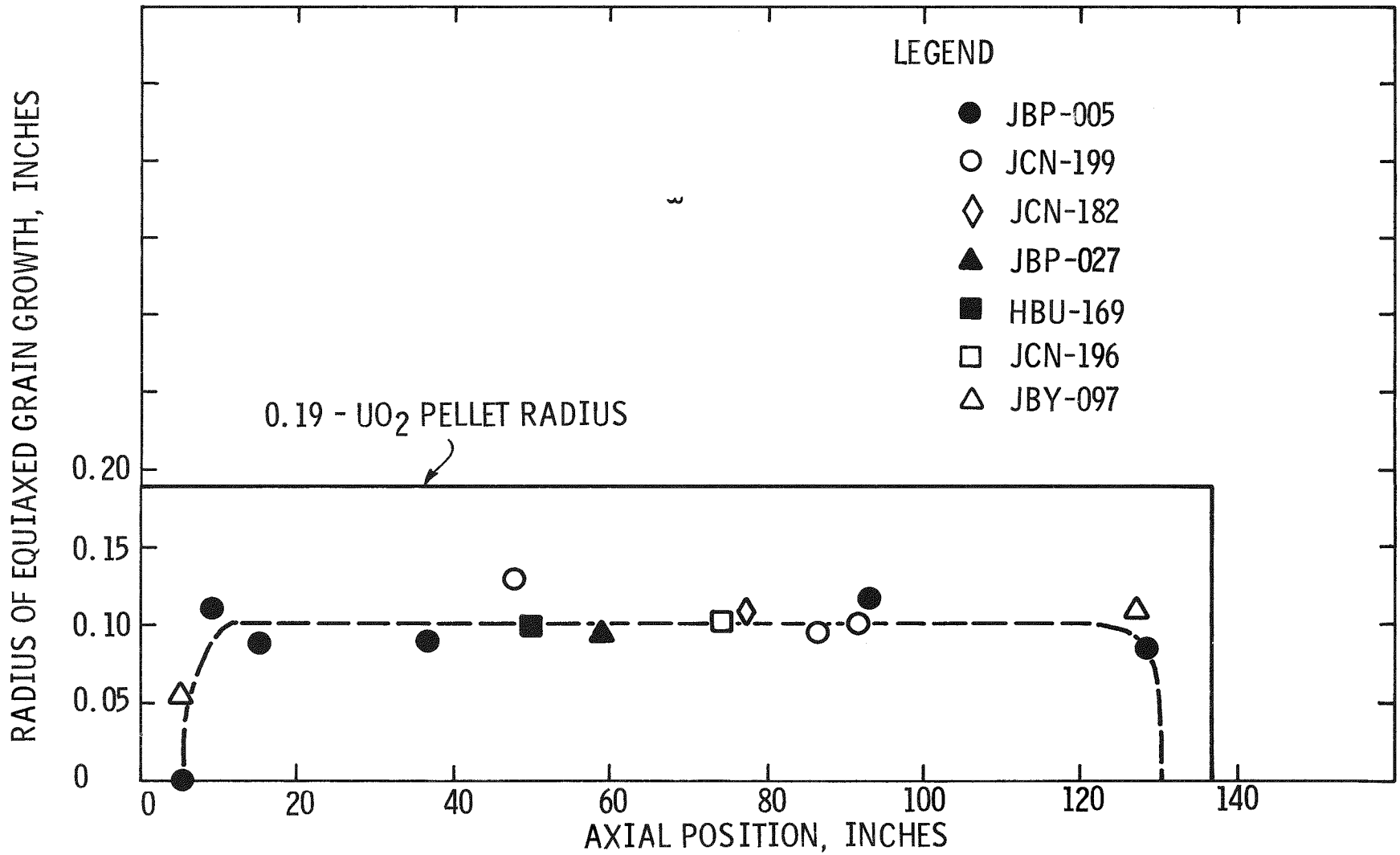

Figure 4-79 EXTENT OF EQUIAXED GRAIN GROWTH IN HIGHER GAS RELEASE RODS

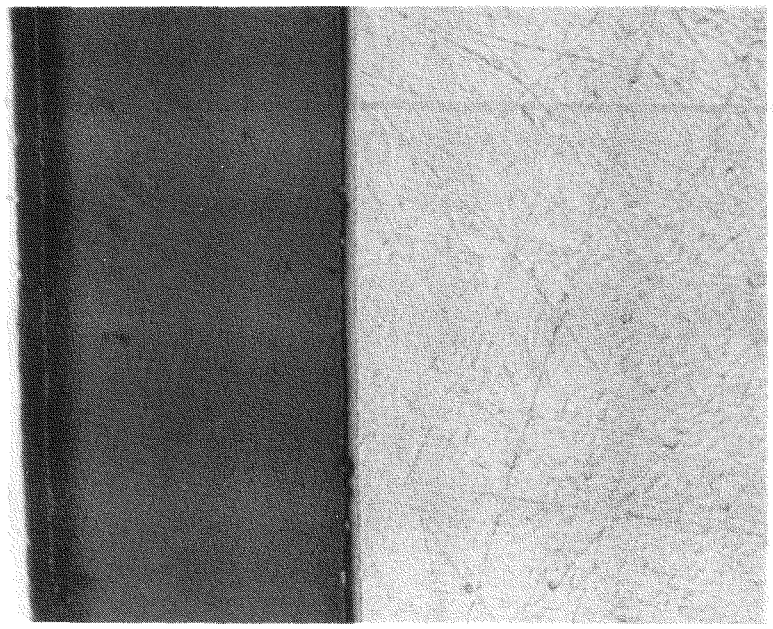

HC41189 500X

Figure 4-80 APPEARANCE OF ZrO_2 LAYER ON THE OUTER SURFACE OF THE CLADDING OF MOUNT No. X-330 (AS POLISHED)

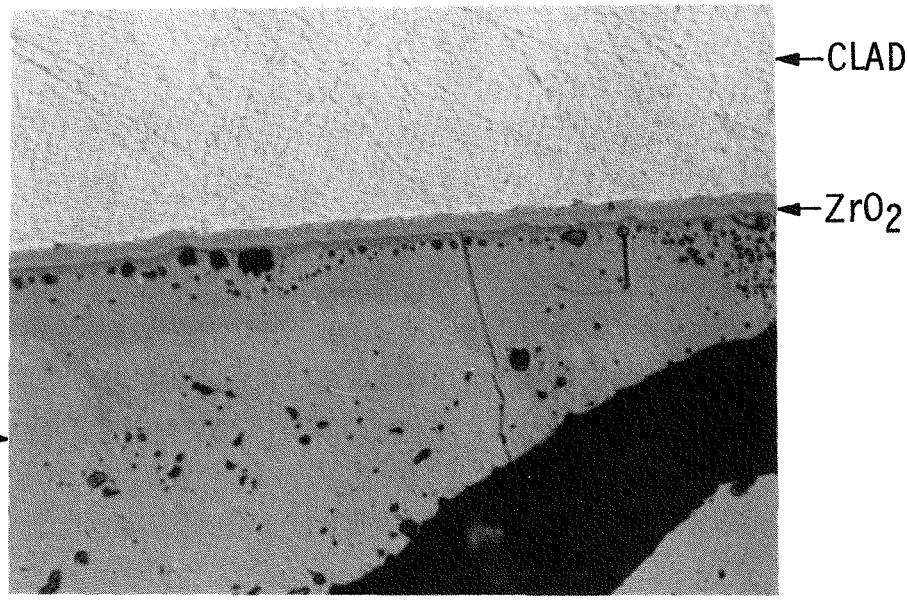

HC40886 500X

Figure 4-81 APPEARANCE OF ZrO_2 LAYER ON THE INNER SURFACE OF THE CLADDING OF MOUNT X-331 AT THE LOCATION OF FUEL-CLAD BONDING (AS POLISHED)

On the inner surface of the cladding, measurable oxide layers were found only where significant contact between the fuel and the cladding was evident, as shown in Fig. 4-81. In other areas, the oxide film was not detectable at 500X magnification. The thickness of the oxide layer in the areas of fuel bonding was in the range of 0.16 to 0.24 mils (4 to 6 μ). This is similar to the oxide thickness observed in a Yankee Rowe Core V fuel rod, where intimate contact between fuel and cladding occurred due to the presence of an oversized pellet [6].

Hydrogen Concentration in the Cladding

Many of the metallographic specimens were examined in the etched condition to evaluate the concentrations of hydrogen in the cladding. The examinations, in general, showed the hydride precipitates to be randomly distributed and of low concentrations. Fig. 4-82 shows the typical appearance of hydrides observed in the cladding. The amount of hydrogen in the cladding was estimated from the photomicrographs to be 60-70 ppm based on published metallographic comparison photographs [7, 8]. The amount of hydrogen pickup (∿50 ppm) from the coolant is consistent with that expected from the time at temperature for the Zircaloy-4 clad fuel rods[5].

One of the specimens from Rod JBP-027 exhibited microscopic features on the inner surface of the cladding which appeared to be radially-oriented hydrides, as shown in Fig. 4-83. The overall concentration of the hydrides are similar to those shown in Fig. 4-82. The radial orientation of the apparent hydride platelets may be the result of highly localized directional stresses in the cladding.

4.8.3.5 Perforated Rod Metallography

Because of difficulties in unambiguously distinguishing between cause and effect of initial clad perforation, metallographic examination of perforated rods in the first campaign was limited to an investigation of the fuel-clad region in the vicinity of the only cladding breach detected in the perforated Batch C rod (even after pressure testing).

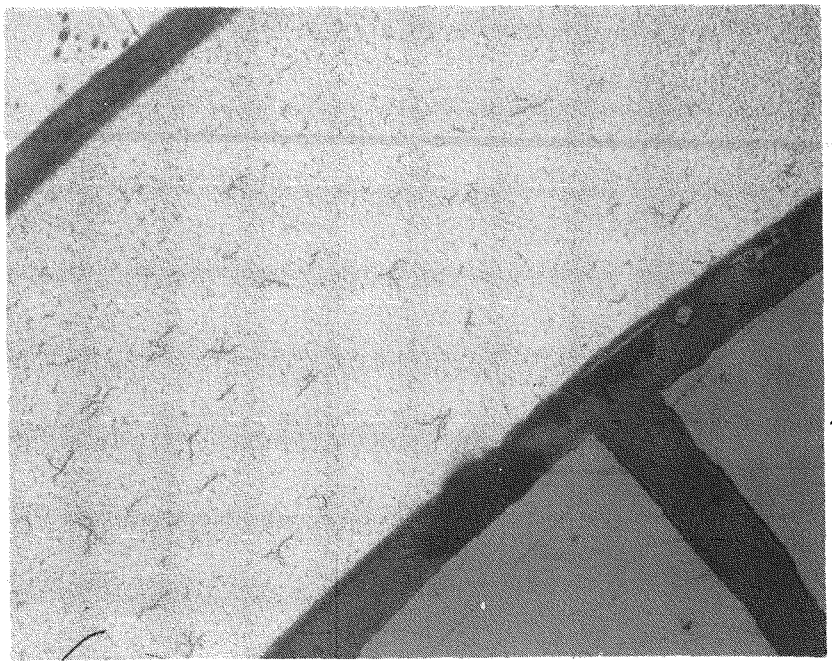

HC40042 100X

Figure 4-82 TYPICAL APPEARANCE OF HYDRIDE PRECIPITATES IN THE SPECIMEN FROM ROD JBP-027 (ETCHED).

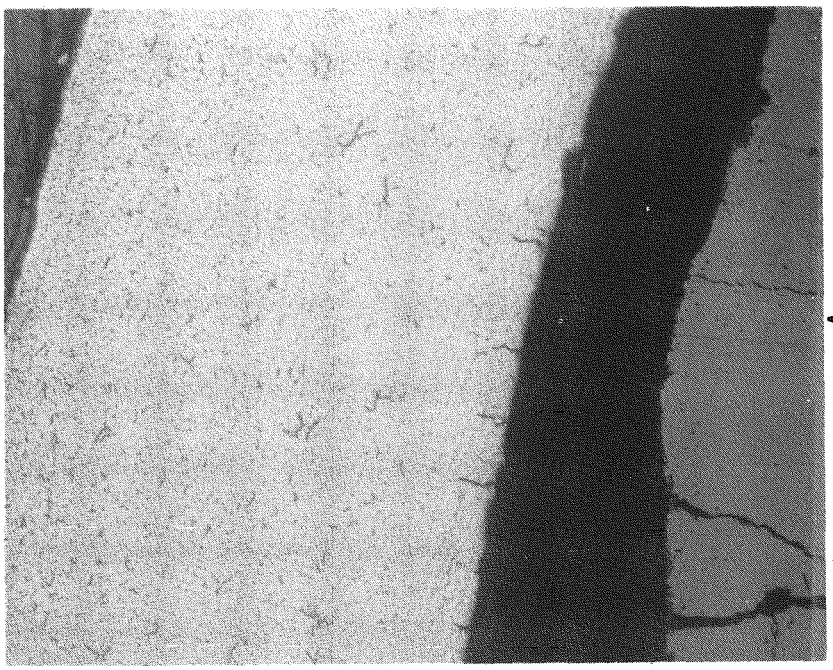

HC40057 100X

Figure 4-83 APPEARANCE OF RADIALLY ORIENTED HYDRIDES ON THE INNER SURFACE OF THE CLADDING IN THE SPECIMEN FROM ROD JBP-027 (ETCHED).

Photographs of the perforation area in Fig. 4-84 and 4-85 show the characteristics of the later stages of a hydriding attack, i.e., the divergent solid hydride distribution near the cladding outside surface suggests it was originally concentrated at the internal surface. Since this is the only cladding breach and little cladding creepdown was observed (see Rod KCA-109 in Table 4-2), it is likely that the rod failed early-in-life because of primary hydriding (i.e., a localized attack due to an internal source of hydrogen).

During the second campaign, two sections from Rod JBP-003 were examined to search for incipient cracks. In neither case were incipient cracks found. The first specimen, located 7 in. from a perforation, showed severe steam attack on the internal surface of the clad; a hydride rim on the external surface of the clad; and, in one position, the remnants of a secondary hydride sunburst. The cladding of the sound specimen, much farther away from the perforation, was similar to that of sound rods except for a hydride rim at the external surface.

4.9 Cladding Crack Characterization by SEM

After the cladding crack in Rod JBY-097 at ∿88 in. from the bottom was examined metallographically, the specimen was removed from the mount and the crack was opened for fractographic examination by SEM. Work by Wood, et al. [9] has shown that characterization of Zircaloy fracture patterns can provide evidence of the cause of fracture particularly in instances of stress corrosion.

4.9.1 Procedure

The following operations were used in the preparation of the sample:

1. The fuel-clad specimen was removed from the mount by dissolving the mounting epoxy in glacial acetic acid. The fuel fell out of the cladding during this operation.

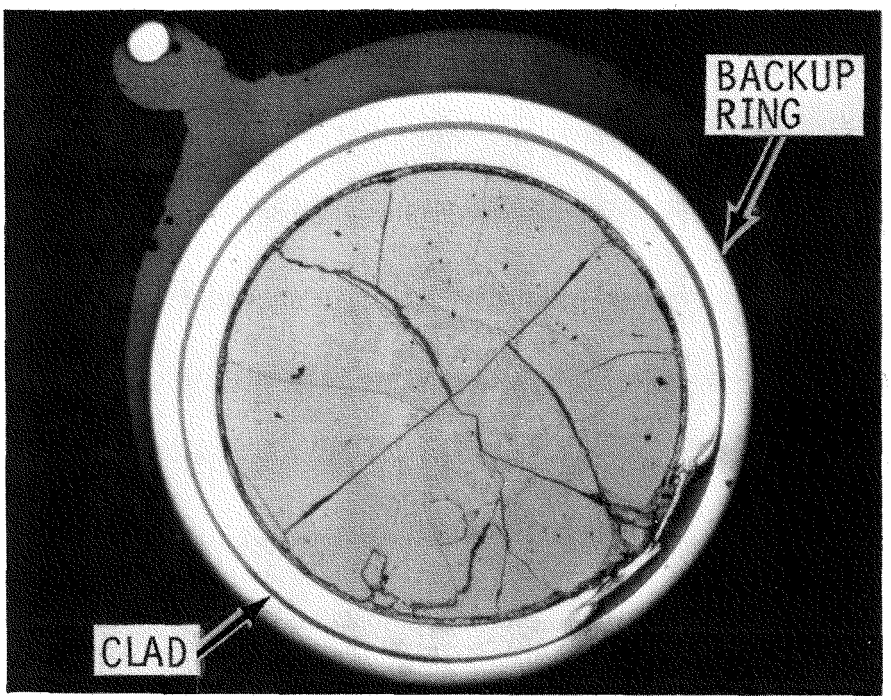

HC41285 6.5X

Figure 4-84 MACROPHOTOGRAPH OF PERFORATION AREA IN. MOUNT No. X344 OF ROD KCA-109 (AS POLISHED)

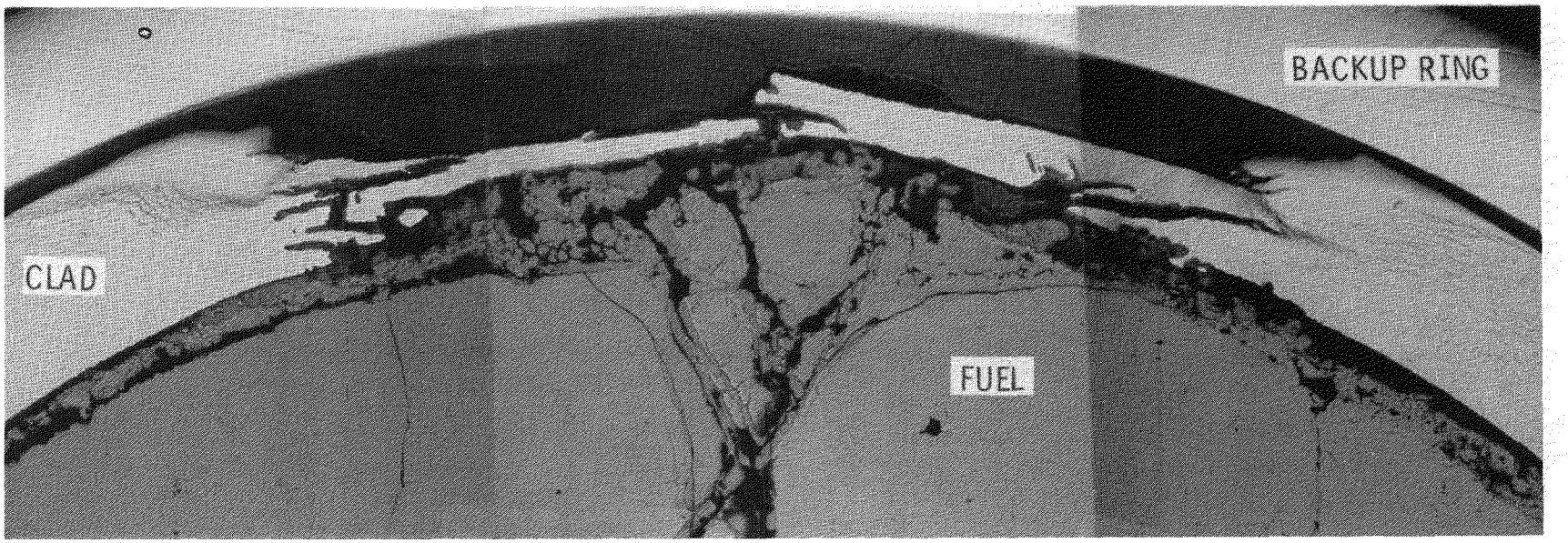

HC41282, HC41283 AND HC41284 100X

Figure 4-85 PERFORATION AREA DETAIL IN MOUNT No. X344 OF ROD KCA-109 (AS POLISHED)

2. The resulting clad specimen was cut to 3/8 in. length with a wet cutoff wheel.

3. The sample was then slit axially by cutting through the 90-270° plane with a jeweler's saw. After cutting, the internal surface was visually examined, and the crack was barely visible to the unaided eye.

4. To permit transfer to the SEM, the sample surface was decontaminated by repeated ultrasonic cleaning in a water-detergent solution and finally, ultrasonically cleaned in alcohol.

5. The crack was then opened by applying a three-point load. At this point, the crack was sufficiently opened so that only a thin ligament held the two pieces together. The ligament was broken with pliers.

6. The two halves of the fracture were then mounted in separate SEM specimen holders, held with Plasticine, and the Plasticine painted with "Dag" (a graphite in alcohol suspension) to form an electrically conducting surface. The fracture surfaces of the specimen were then examined in the SEM.

4.9.2 Results of the SEM Examination

An overall view of the fracture is presented in the SEM photograph of Fig. 4-86 in which the area subjected to detailed study is outlined. Low power examination of the fracture surfaces showed four separate zones. Proceeding from the internal to the external surfaces of the cladding, the zones are described in the following paragraphs and shown in Fig. 4-87.

1. The crack face immediately adjacent to the inside clad surface exhibited surface characteristics attributed to contact with an oxidizing medium which may have come from the in-reactor environment or from the anodizing etch used as part of the metallographic examination.

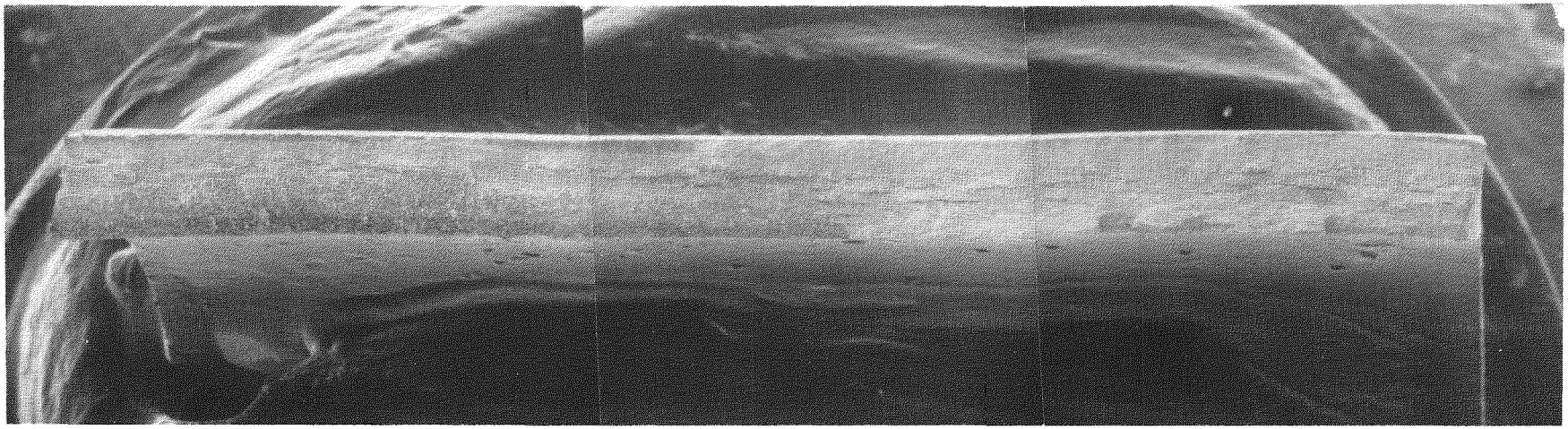

23X

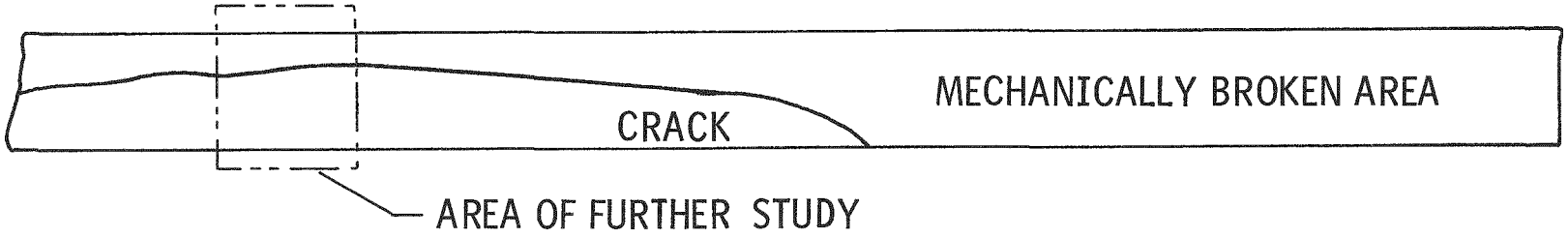

Figure 4-86
SEM OVERALL VIEW OF FRACTURE AREA FROM ROD JBY-097 AT — 88 IN. FROM THE BOTTOM

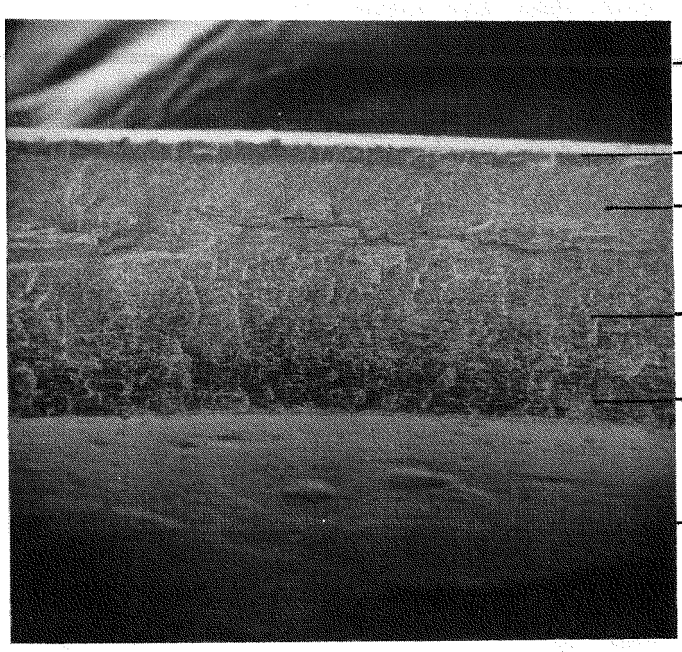

Figure 4-87 LOW MAGNIFICATION SEM-PHOTOGRAPH OF FRACTURE

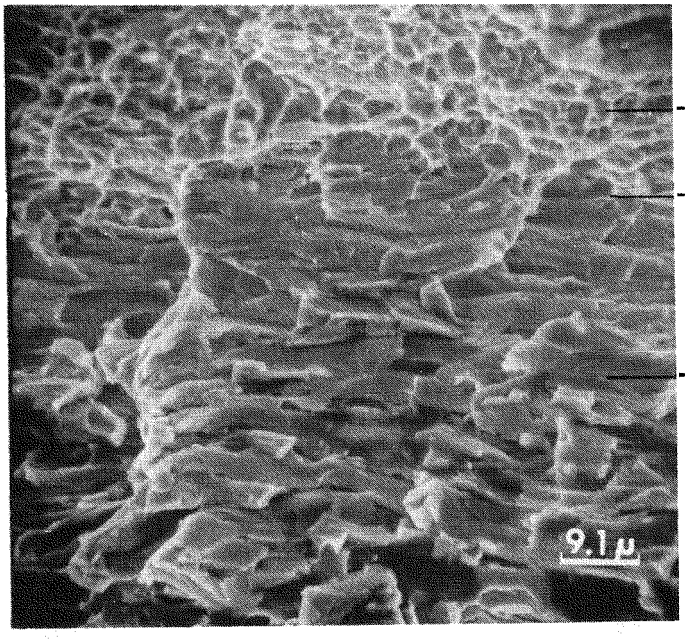

Figure 4-88 FRACTURE SURFACE AT CRACK TIP

2. The continuation of the original crack into the cladding was the next zone. This fracture surface appeared free of oxidation and exhibited the characteristic flat cleavage planes observed by Wood, et al.[9] and ascribed to iodine stress corrosion of Zircaloy based on out-of-reactor tests.

3. The third zone had a fracture surface distinctly different from the original crack face. This was the fracture zone caused by the mechanical opening of the original crack, and it was characterized by the ductile dimpling associated with such a cracking process.

4. The last zone was the smeared surface region that corresponded to the final break made with pliers to separate the crack.

The examination also revealed that the original crack penetrated approximately 50% of the cladding thickness and extended approximately 3/16 inch axially.

After the general examination of the fracture surface, attention was then focused on the second zone, i.e., the original crack from the oxidized portion to the crack tip. As may be seen from Fig. 4-88 through 4-91, this portion shows transgranular cleavage with river patterns and some fluting. Stereo-pair photomicrographs, presented in Fig. 4-92 through 4-94, verify the transgranular cleavage and the complete absence of ductile dimpling. This is the same type of fracture reported by Wood, et al. [9] and Garlick [10] as characteristic of in-reactor clad cracks with a morphology similar to that of fractures caused out-of-reactor by iodine stress corrosion cracking (SCC). In this connection, it is worthwhile quoting the Cox and Wood [11] review on the subject of SCC in Zircaloy;

> "The only features that are unique indicators of the occurrence of SCC in the Zircaloys are the flat cleavage planes. No other conditions (e.g., fracture at low temperature, low ductility tensile failure after irradiation) give rise to cleavage in Zircaloys. Fractures always show ductile features when caused mechanically."

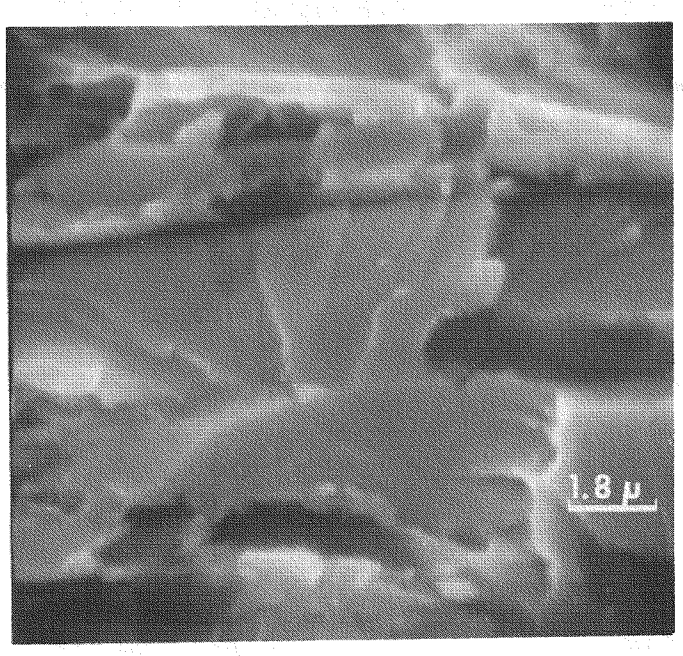

A21 5500X

Figure 4-89 HIGH MAGNIFICATION OF CENTER OF Fig. 4-88

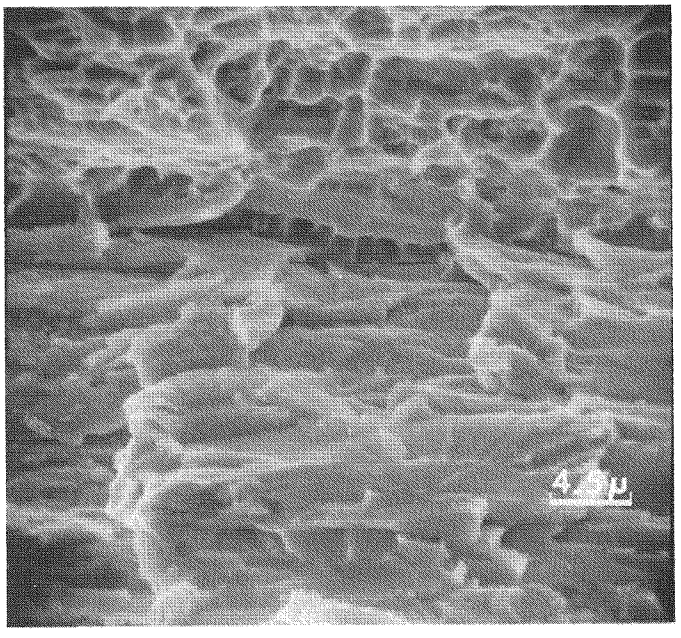

A18 2200X

Figure 4-90 HIGH MAGNIFICATION OF TRANSITION BETWEEN ZONES 2 AND 3

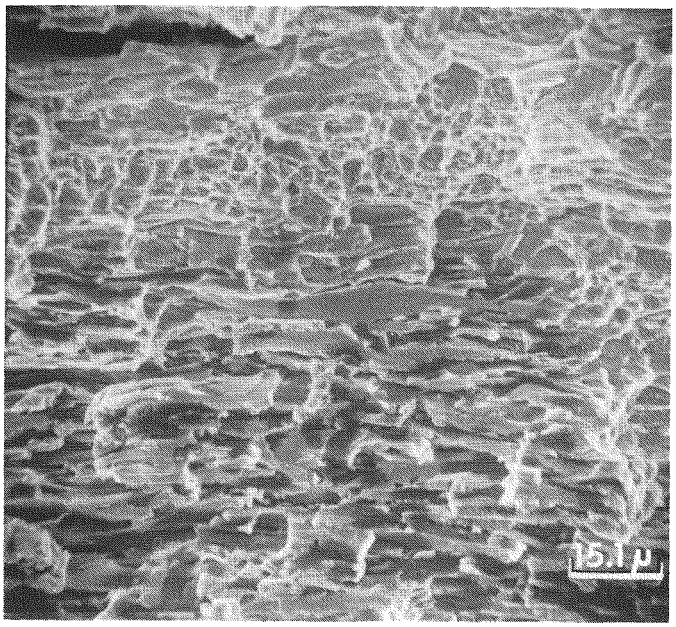

B9 650X

Figure 4-91 FRACTURE SURFACE AT CRACK TIP

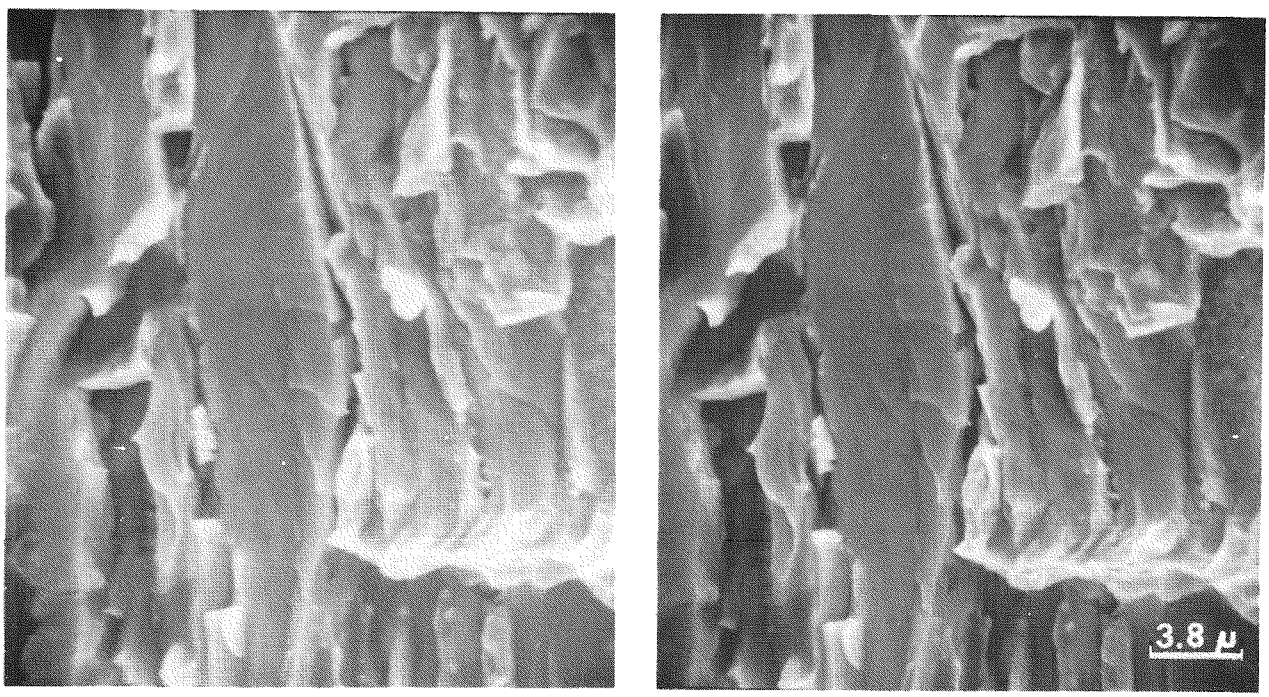

B11 LEFT 2600X B10 RIGHT 2600X

ure 4-92 HIGH MAGNIFICATION STEREO PAIR OF CENTER OF Figure 4-90 ROTATED 90°

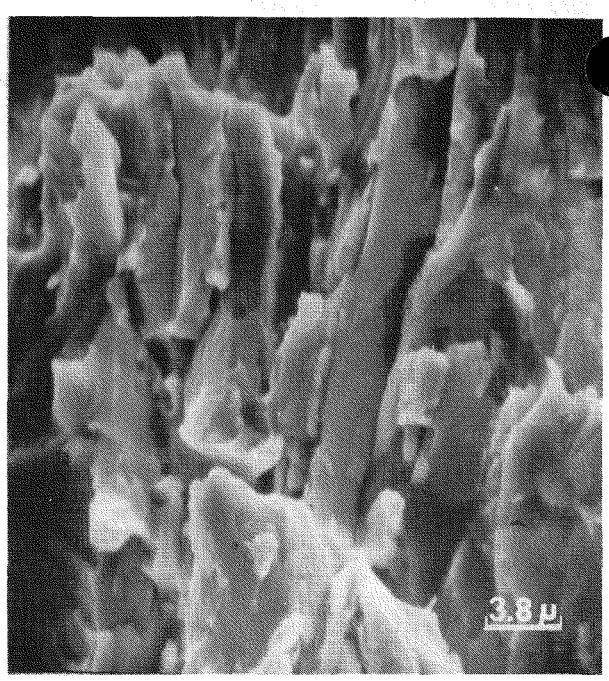

B8 LEFT B7 RIGHT 2600X

Figure 4-93 STEREO PAIR OF ZONE 2 SHOWING CLEAVAGE

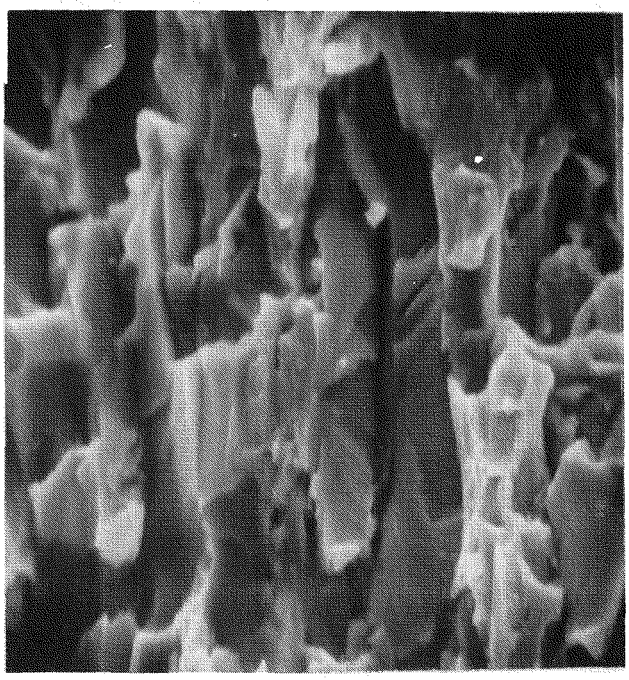

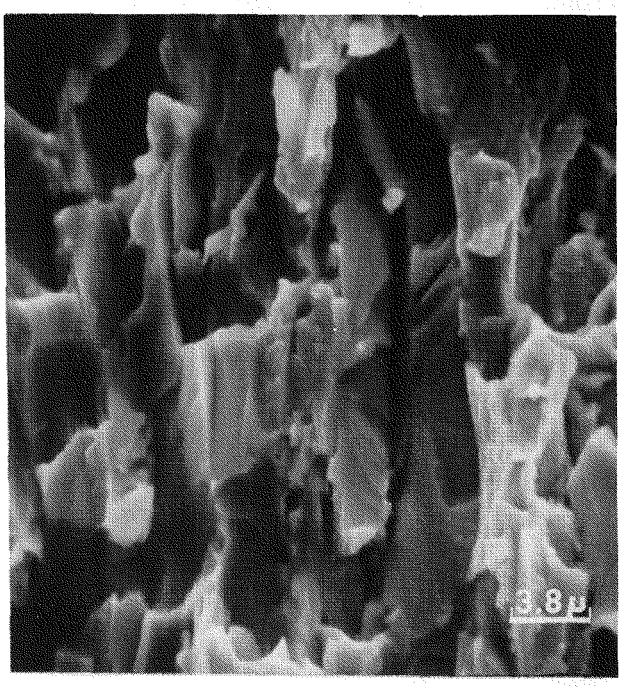

B6 LEFT B5 RIGHT 2600X

Figure 4-94 STEREO PAIR OF ZONE 2 SHOWING RIVER PATTERNS AND CLEAVAGE

Thus, these SEM results constitute strong evidence that SCC was the cause of the cladding crack found in JBY-097 at ∿88 in. from the bottom of the rod.

Table 4-14 summarizes all of the internal cladding crack characteristics found in the three sound, high gas release, Maine Yankee Batch B fuel rods. In all cases, cladding cracks were observed at or near pellet interfaces. Further, all cladding cracks were at or near cracks in pellets. Most important, all of the cracks are similar in appearance, suggesting the same cause. Based on the SEM observations and the optical microscopy showing transgranular cracking without twinning or slip, it is believed that stress corrosion-assisted pellet-clad interaction caused all of these incipient cracks. While the work of others [9, 10, 11] points to iodine as the chemical species involved in the SCC mechanism, the role of iodine has not been conclusively established. This program's finding of redistributed cesium and tellurium on the internal cladding surface raises the possibility that other aggressive chemical species could contribute to SCC mechanism.

4.10 Electron Microprobe Analysis of Fuel-Clad Reaction Zones

4.10.1 Scope

As described in Section 4.8, fuel-clad bonding was frequently observed during metallographic examination of fuel rod sections from high gas release rods. The bonded areas exhibited various phases characterized by different shades of grey, all darker than the UO_2 fuel. At ANL, specific isotope gamma scans of the internal surfaces of slit cladding sections and the X-ray spectometry of material adhering to these surfaces indicated that cesium, uranium and zirconium were the principal elements present with traces of iodine and tellurium. It is evident that some of this material was involved in the fuel-clad bonding observed in metallography. To characterize the chemical composition of typical fuel-clad reaction zones more completely, electron microprobe analyses were carried out on three samples. During the first campaign, a qualitative analysis of a specimen from Rod JCN-199 was performed. During the second campaign, a more quantitative approach was taken with one each from Rods JCN-196 and JBY-097.

Table 4-14

Summary of Internal Cladding Crack Characteristics in Maine Yankee Sound Batch B Fuel Rods

Rod No.	JBP-005	JBY-097	JBP-122
Assembly/Rod Positions	B042/E11	B069/C13	B042/C13
Fractional Fission Gas Release, %	12.7	13.4	11.3
Axial Location of Crack, in. from Rod Bottom	94.21 to 94.30	88.035	94.895
Burnup at Location, Mwd/MTU	14,850 (measured)	15,800 (estimated)	15,800 (estimated)
Maximum Steady State Power at Location, kw/ft.	∿8.35	∿8.7	∿8.7
Comments:	1. Two cracks adjacent to each other were observed. 2. Larger crack (∿65% penetration) was observed at a pellet interface. 3. Ovality at this location was low (∿4.5 mils). 4. Equiaxed grain growth observed in the fuel. 5. Cracks opposite pellet chip (fuel missing). 6. Minor fuel-clad bonding adjacent to crack. 7. Crack length estimated 1/8 to 3/16 in. by progressive grinding. 8. Optical microscopic features consistent with stress corrosion cracking.	1. Single crack observed subtending pellet interface. 2. The extent of penetration was ∿50%. 3. Region of maximum ovality (∿13 mils), crack observed near the major axis of ovality ellipse. 4. Equiaxed grain growth observed in the fuel. 5. Crack opposite crack in pellet. 6. Fuel adhering to clad adjacent to crack. 7. Crack length found to be about 3/16 in. by fractographic examination. 8. Optical and scanning electron microscopic features consistent with stress corrosion cracking.	1. Four cracks adjacent to each other observed very near pellet interface (within 1/16 in.) 2. Extent of penetration was ∿25% on metallographic surfaces examined. 3. Region of large ovality (∿10 mils), cracks observed near minor axis of ovality ellipse. 4. Equiaxed grain growth present in fuel. 5. Cracks very near pellet crack. 6. Crack lengths not known. 7. No fuel adhering to clad in vicinity of cracks. 8. Optical microscopic features consistent with stress corrosion cracking.

4.10.2 Procedure

Transverse metallographic specimens were first coated with a thin layer of carbon to make them electrically conductive. They were then subjected to combinations of the following procedures:

1. Two theta (2θ) scans to identify the elements present at selected points in the area of interest [elements of atomic numbers 14 (Si) through 94 (Pu) are detectable with the exceptions of atomic numbers 31 through 35 (Ga, Ge, As, Se and Br)].

2. X-ray imaging to pictorially illustrate the relative distribution of the elements present in the area, and

3. Quantitative analysis by point counting to determine the composition of the phases from the cladding through the fuel-clad bond region to the pellet center.

4.10.3 Results

4.10.3.1 First Campaign - Sample from Rod JCN-199 at 92-9/16 in.

The analysis of this sample included 2θ scans and X-ray imaging of the elements detected in the area of interest. Only uranium, zirconium and cesium were detected in the 2θ scans. Fig. 4-95 shows the photomicrograph of the area studied and X-ray images for the three elements present in the area. It can be seen from the X-ray images that the concentration of cesium is low in the fuel, intermediate in the light grey reaction zone, and high in the dark grey layer adjacent to the zirconium oxide layer. From the relative cesium intensities of the 2θ scans, the amounts of cesium in the three zones were estimated to be approximately 1, 2 and 5 percent by weight, respectively. Based on these results, it was concluded that the bonding of fuel to clad was promoted by the presence of redistributed cesium at the fuel-clad interface in the high gas release rods.

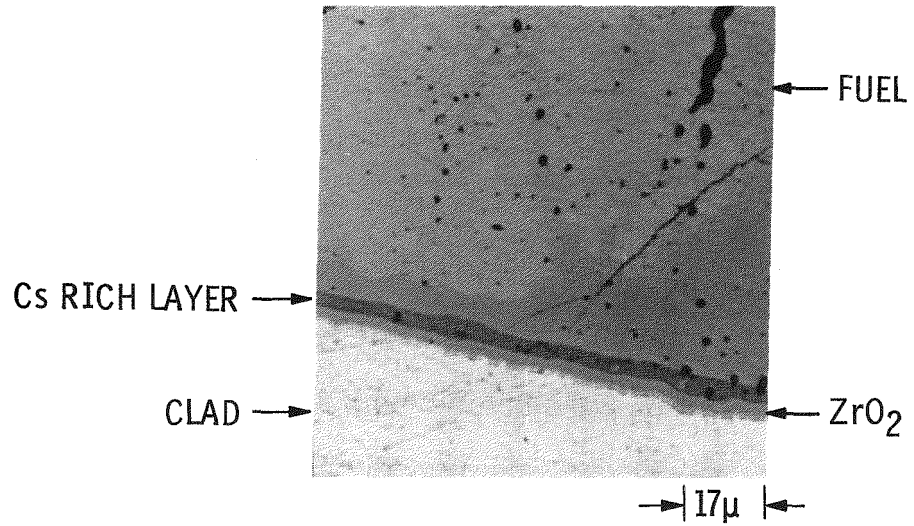

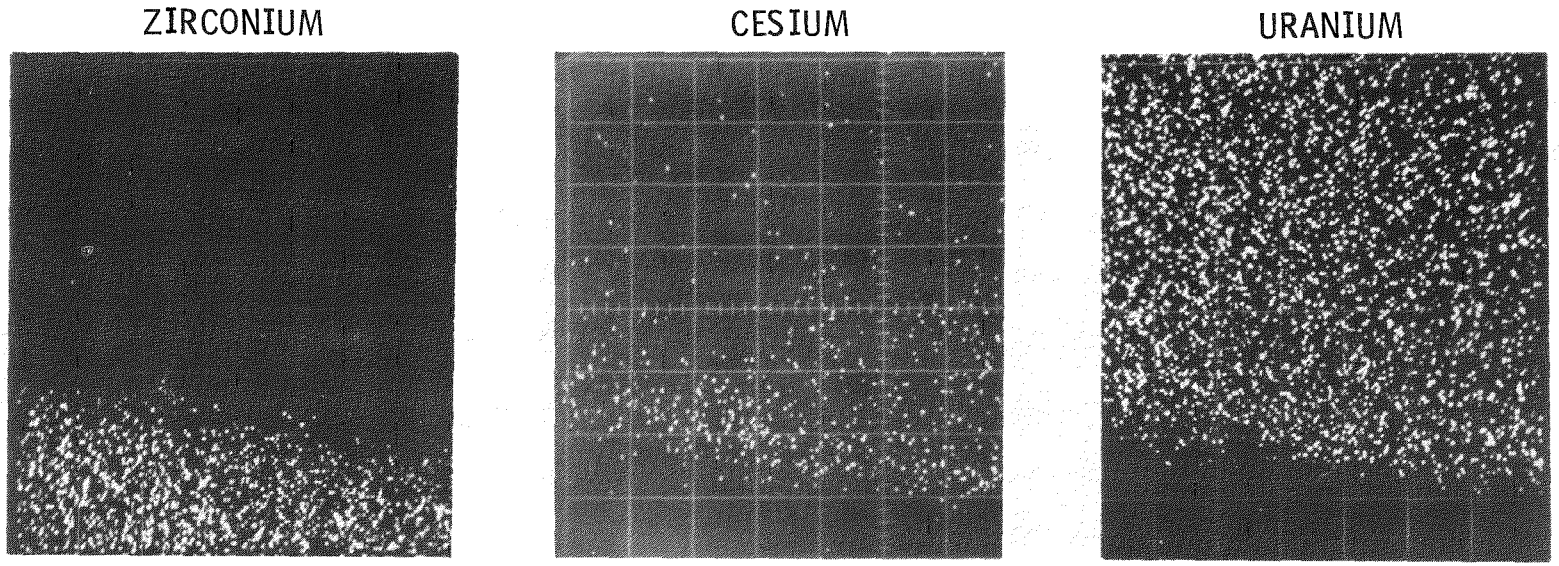

Figure 4-95 AREA OF FUEL/CLAD BONDING IN MOUNT No. X-339 OF ROD JCN-199, SELECTED FOR MICROPROBE ANALYSIS, ASSOCIATED WITH EDDY CURRENT SIGNAL SHOWN IN Figure 4-24 NEAR 92-5/16 IN. FROM BOTTOM. X-RAY IMAGES ARE SHOWN IN BOTTOM PHOTOGRAPHS. 600X

4.10.3.2 Second Campaign

Sample from Rod JCN-196 at 75-5/8 in.

This specimen was extensively examined, including quantitative analysis to determine the composition of the bonded fuel area. The 2θ scan of a point within the area exhibited the presence of uranium, cesium and zirconium. In addition, the presence of tellurium was detected. Detection of tellurium was unexpected, based on the 2θ scan results from the first campaign microprobe analysis. Subsequent X-ray imaging of the bonded area showed that tellurium was concentrated only in one small isolated area, which coincidentally was the location subjected to 2θ analysis. Fig. 4-96 shows a photomicrograph of the area studied and the relative concentrations of uranium, cesium, zirconium and tellurium, as shown by X-ray imaging. Attempts were also made to determine if isolated concentration pockets of molybdenum were present, similar to that of tellurium. However, the concentration of molybdenum in the entire area was too low to produce a satisfactory X-ray image. The X-ray images, in general, showed that cesium is highly concentrated in the dark grey band adjacent to the zirconium oxide layer and is also randomly distributed in the other grey areas. These observations are similar to those from the first campaign.

Quantitative data on the uranium, zirconium and cesium contents were obtained across the specimen cross section by performing a series of point counts. The path of the analysis started at a point in the clad inner surface and proceeded to the center of the fuel pellet. In the region of the fuel-clad interface, the points analyzed were approximately 2 microns apart. Beyond this area of primary interest, the steps were increased to 10 microns and finally to 50 microns. The counting time at all points was 10 seconds.

The point counting data were converted to absolute weight fraction through the use of the MAGIC computer code, which compares the count rates obtained from the sample with those from standards and corrects for the X-ray absorption characteristics of the matrix. The sum of the weight fractions of uranium, zirconium and cesium was always less than 100%.

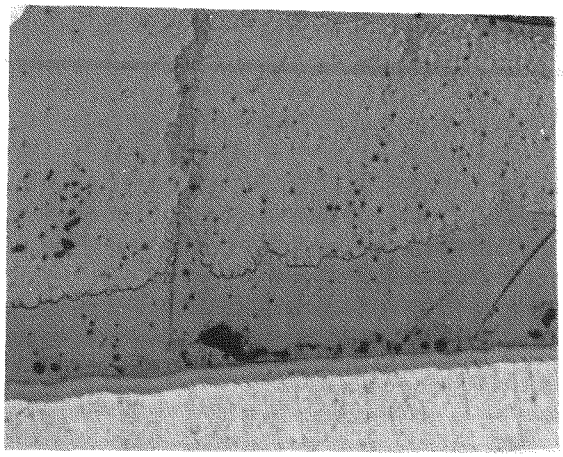

a) PHOTOMICROGRAPH →| 20μ |←

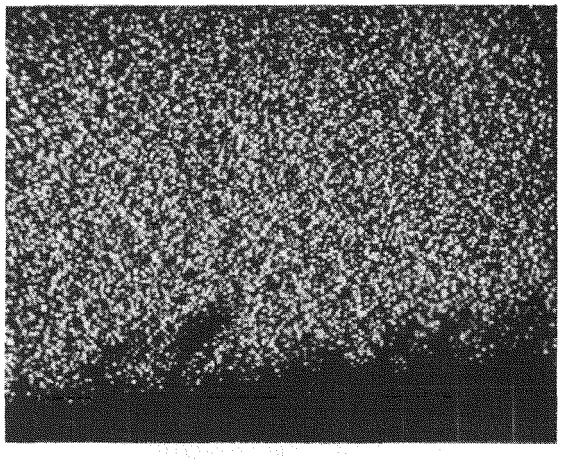

b) $U_{M\alpha}$ X-RAY IMAGE

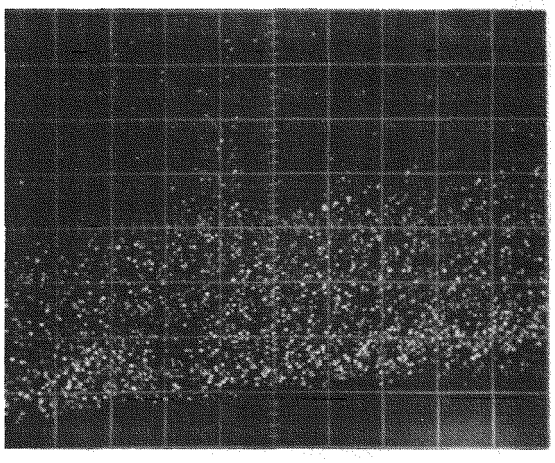

c) $Cs_{L\alpha}$ X-RAY IMAGE

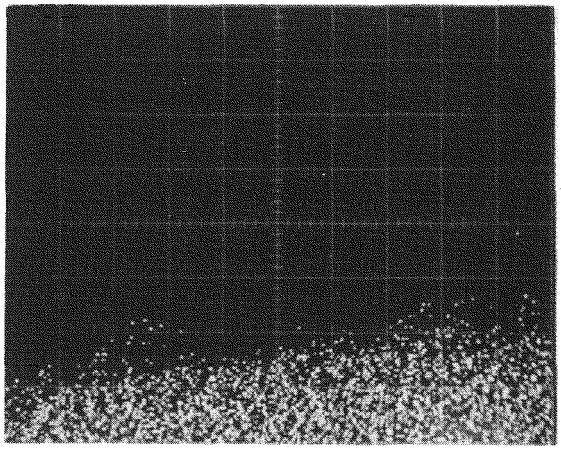

d) $Zr_{L\alpha}$ X-RAY IMAGE

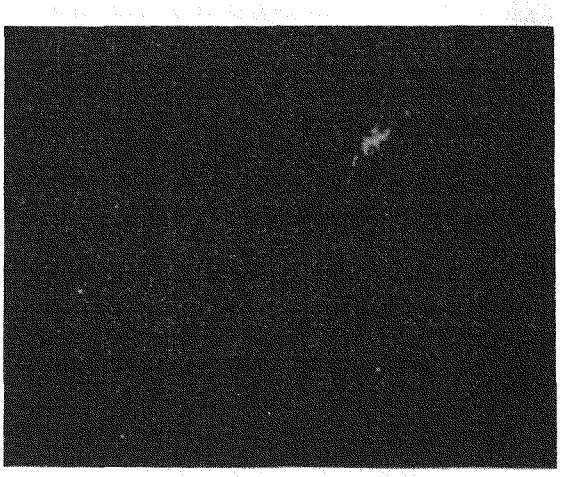

e) $Te_{L\alpha}$ X-RAY IMAGE

Figure 4-96 MICROPROBE ANALYSIS OF FUEL/CLAD BONDING IN ROD JCN-196 AT 75-5/8 IN. FROM BOTTOM. PHOTOMICROGRAPH AND X-RAY IMAGES OF AREA ARE SHOWN.

The balance was assumed to be oxygen. Fig. 4-97 shows the concentration profiles of the three elements in the fuel-clad reaction zone. It can be seen that beyond the region of the fuel-clad reaction zone, the concentrations of zirconium and cesium are negligible. Fig. 4-98 shows the concentration profile of cesium across the pellet cross section to the fuel centerline. No cesium concentration variations are detectable except near the fuel-clad interface.

Sample from Rod JBY-097 at 44-1/8 in.

The examination of the specimen from JBY-097 at 44-1/8 in. was similar to that for the specimen from JCN-196 at 75-5/8 in. except that no 2θ scans were performed. In this case, in addition to the X-ray imaging and point counting from the clad into the pellet, point counting was carried out along a short circumferential path (approximately 55 microns) over the dark grey phase adjacent to the cladding. The path of the point counting analyses is shown in Fig. 4-99.

The X-ray images showed essentially the same relative distribution of cesium, zirconium and uranium in the various grey phases as in the other samples; however, no tellurium was found. The point counting along the circumferential path showed the concentration of cesium and uranium to be nearly constant over the path. The concentration of zirconium, however, varied widely with the lowest value found at the right hand edge of the area adjacent to a large void. The point counting analysis carried out across the pellet radius showed the concentration profiles for uranium, cesium and zirconium to be similar to that of the specimen from JCN-196 at 75-5/8 in.

4.10.4 Discussion of Results

The results of the microprobe analysis presented above show that bonding of fuel to cladding is associated with a cesium-rich layer which stemmed from the redistribution of the fission product cesium in high gas release rods.

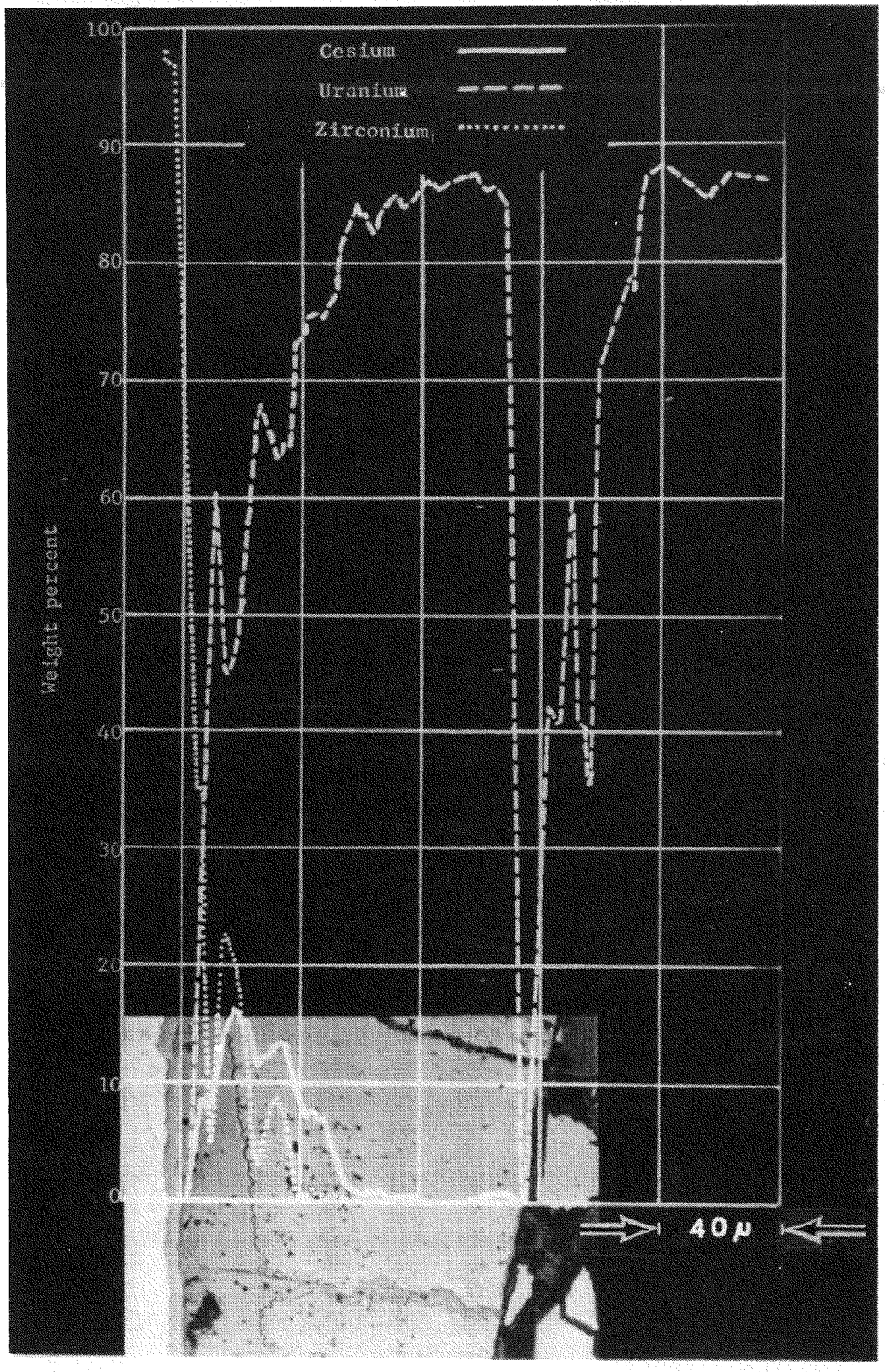

Figure 4-97 URANIUM, CESIUM AND ZIRCONIUM CONCENTRATION PROFILES OF FUEL/CLAD BOND REGION IN ROD JCN-196 AT 75-5/8 FROM BOTTOM. PATH OF ANALYSIS CORRESPONDS TO LOCATION OF ABSCISSA ON PHOTOMICROGRAPH.

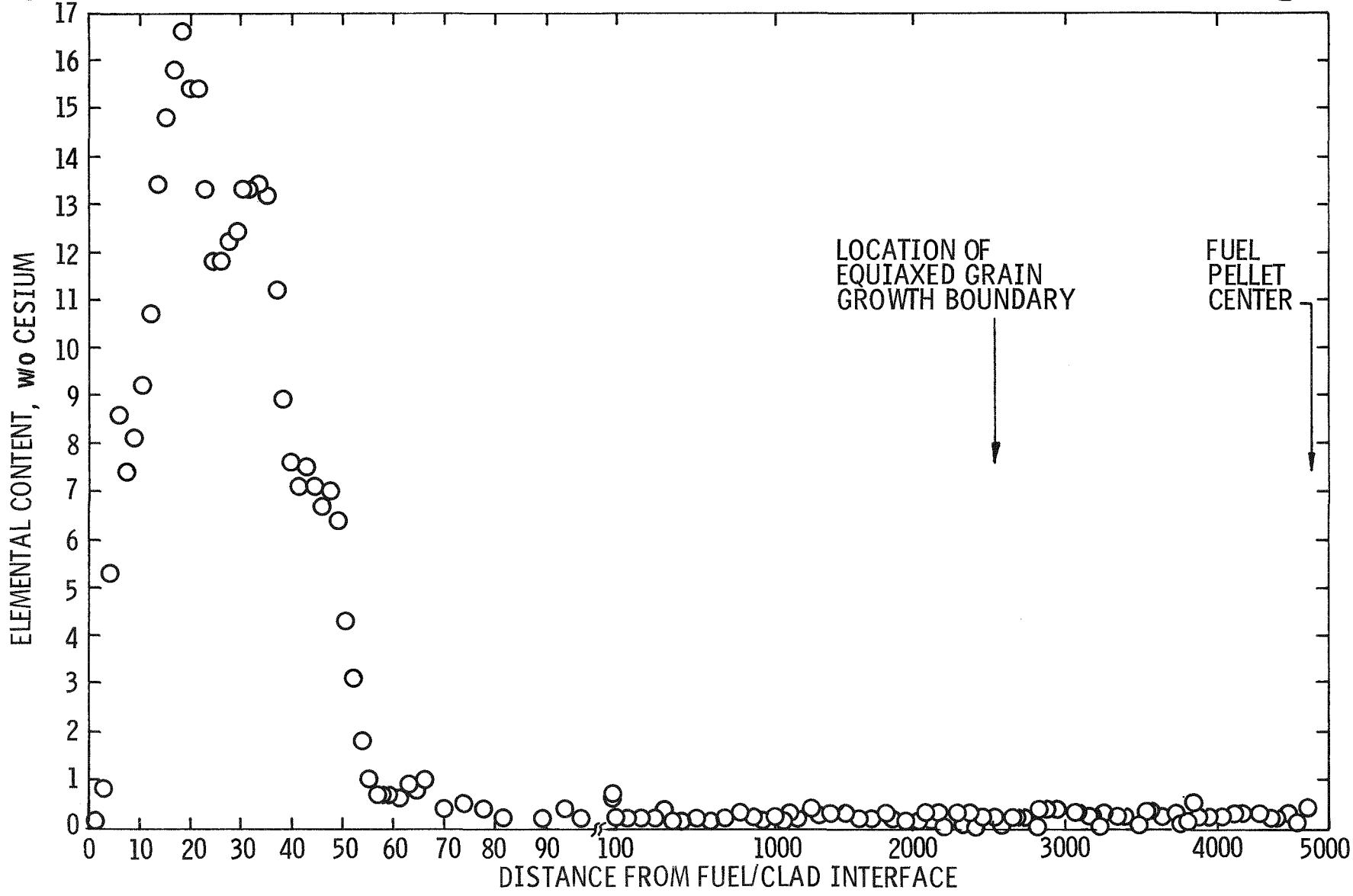

Figure 4-98 CONCENTRATION PROFILE OF CESIUM FROM FUEL/CLAD INTERFACE TO PELLET CENTER IN ROD JCN-196 SAMPLE AT 75-5/8 INCHES. (NOTE CHANGE OF ABSCISSA SCALE)

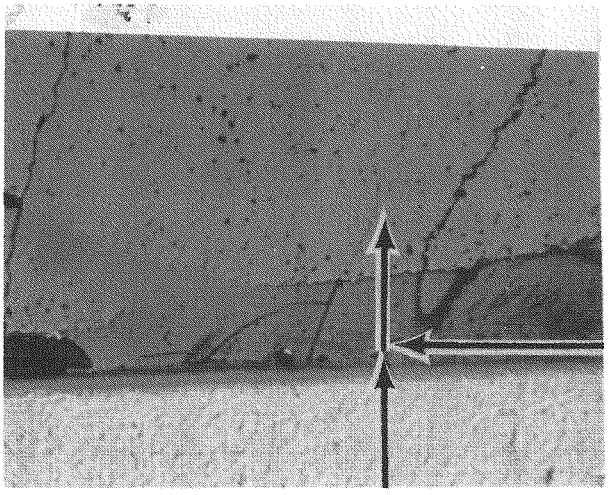

a) PHOTOMICROGRAPH (20μ)

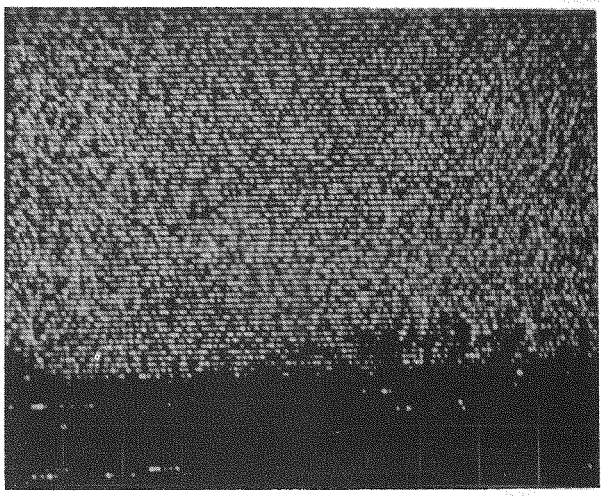

b) $U_{M\alpha}$ X-RAY IMAGE

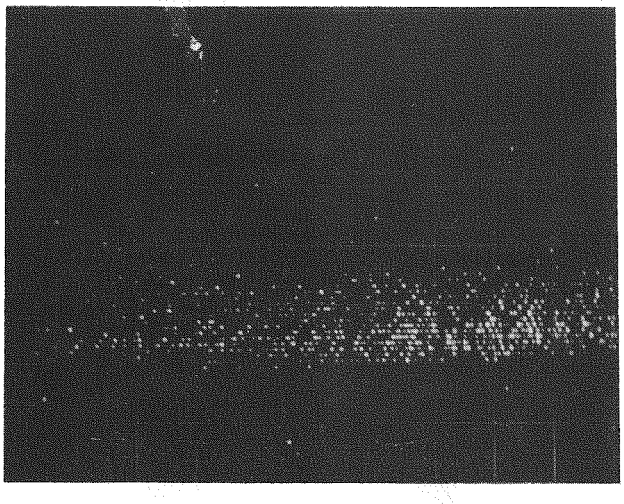

c) $Cs_{L\alpha}$ X-RAY IMAGE

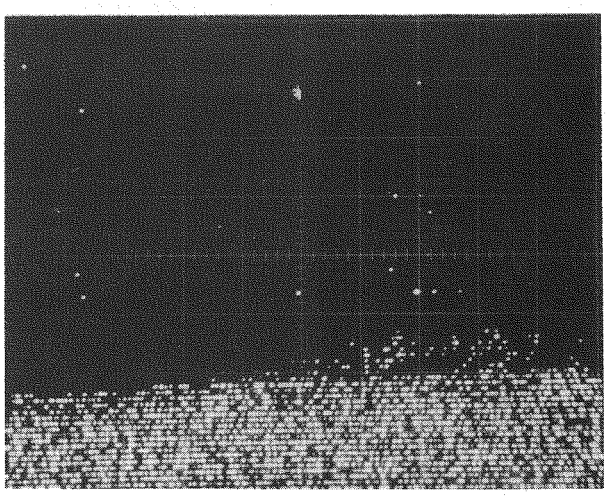

d) $Zr_{L\alpha}$ X-RAY IMAGE

Figure 4-99 MICROPROBE ANALYSIS OF FUEL/CLAD BONDING IN ROD JBY-097 AT 44-1/8 FROM BOTTOM. PHOTOMICROGRAPH SHOWS PATH OF ANALYSIS. X-RAY IMAGES OF AREA ALSO SHOWN.

Gross migration of cesium, heretofore, has been observed in cases of high temperature operation to high burnup. Neimark, et al.[12] observed significant migration of fission product cesium to the UO_2 blanket pellets during irradiation of mixed-oxide fuel pins in EBR-II. The fuel pins were irradiated at >12 kw/ft up to about 100,000 Mwd/MTU. The blanket UO_2 pellets were found to have reacted with the cesium. Similar observations were made by Karnesky et al.[13] and Langer[14] et al. It is noteworthy that the fuel in all the above cases was UO_2-PuO_2. The only reported case of reaction of cesium with UO_2 fuel was published by Bazin, et al.[15] who described Zircaloy clad fuel rods containing pellets irradiated at high power levels (an average of 18 kw/ft) to a wide range of burnups. The post-irradiation examination indicated a cesium-rich reaction layer between the fuel and the zirconium oxide layer adjacent to the cladding. It was also found that the extent of fuel bonding was very infrequent and extremely localized below a burnup of 10,000 Mwd/MTU. A quantitative analysis of a bonded fuel area showed the composition to be similar to that observed in Maine Yankee fuel rods. It appears that no elements other than uranium, cesium, zirconium and oxygen were detected in the reaction zone.

While the data presented above suggest that cesium migration or redistribution occurs only with high fuel temperatures, reaction between the oxide fuel and cesium appears to occur at significantly lower temperatures (between 500 and 1000°C). Cesium has been found to form cesium uranate (Cs_2UO_4) readily at 725°C in the presence of hyperstoichiometric oxide.[16]

The formation of Cs_2UO_4 on the blanket pellets has been suggested as the cause of some of the fuel rod failures in the C series EBR-II experiments[17]. Cs_2UO_4 is of relatively low density and thus, the formation of this compound results in large local volume change which subsequently leads to cladding failures. In the case of Maine Yankee fuel rods, the formation of fuel-clad reaction zones may have, indirectly, contributed to fuel rod perforations in that the resulting fuel bonding could have enhanced local stress concentrations during power increases.

In addition to the formation of Cs_2UO_4, cesium has also been found to form compounds with molybdenum and iodine. Out-of-pile tests carried out by Adamson and Aitken [18] have shown that the cesium migration behavior is sensitive to the O/M ratio of the fuel. With hypostoichiometric fuel, cesium is expected to behave predominantly as the free element migrating rapidly to the coolest position in the fuel rod. With a hyperstoichiometric fuel, cesium reacts with the fuel to form the uranate and is relatively immobile. With nearly stoichiometric oxide, a new compound, $CsUO_3$ may be formed, which is volatile and mobile.

Adamson and Aitken[18] also reported that, in the presence of iodine, the formation of cesium fuel compounds does not prevent or limit the formation of the more stable (but volatile) cesium iodide and the cesium combined as the iodide showed no tendency to react with the fuel.

It appears that in the case of Maine Yankee fuel which was of stoichiometric composition, cesium migration could have occurred as the free element or as an oxide with uranium, and as the iodide. However, it is believed that cesium did not reach the cladding inner surface as the free element because no gross axial redistribution of cesium was observed.

The behavior of cesium in the presence of tellurium was reported[18] to be more complex, with concommitant associations among cesium, tellurium and fuel. A compound of cesium and molybdenum, namely, cesium molybdate (Cs_2MoO_4), has been found to form with O/M <2. It is believed that gaseous Cs_2MoO_4 may be sufficiently stable at high temperatures to provide an additional transport mode for cesium in oxide fuels. However, cesium migration via this compound, is not believed to have been significant in Maine Yankee fuel rods, since no molybdenum was observed in the bonded fuel region.

It should be emphasized that the complex fuel chemistry discussed above is based on out-of-pile studies and very little is known of how it is affected by the radiation environment of a fuel rod. Nevertheless, these observations are significant as they are consistent with the results from the SEM examination of the clad inner surface of slit clad sections (Section 4.7). The particles adhering to the cladding were found to be mixtures of either cesium, tellurium, uranium or zirconium (probably combined with oxygen) or just a compound of cesium with iodine.

In summary, the results of microprobe analysis of the bonded fuel regions and examination of the data reported in the literature, lead to the following conclusions:

1. The Maine Yankee fuel rods which exhibited high fission gas release must have experienced high fuel temperatures (but still below temperatures associated with columnar grain growth, as only equiaxed grain growth was observed) during irradiation, to explain the observed cesium redistribution to the fuel-clad interface. The duration of the high temperature operation does not appear to be a critical factor in the reaction at the fuel-clad interface, since cesium-fuel compounds have been found to form at relatively low temperatures (between 500 and 1000^{o}C).

2. The migration behavior of cesium is sensitive to the stoichiometry of the fuel. In the case of the Maine Yankee fuel, which was stoichiometric, cesium could have migrated as the free element or as an oxide with uranium and as the iodide. The presence of bonded fuel without iodine and the presence of cesium iodide on the clad surface tends to support both forms of migration.

3. The migration of cesium as molybdate is not believed to have occurred in the Maine Yankee fuel rods, since no concentrations of molybdenum in the reaction zone were observed.

4. Cesium uranate has been reported to form readily with hypo-stoichiometric UO_2. Based on the Maine Yankee fuel observations, the formation of a complex oxide of cesium, uranium and zirconium also seems to be possible with stoichiometric UO_2.

5. The formation of cesium uranate or a similar compound may have contributed to clad perforation in Maine Yankee fuel rods by enhancing local stress concentration in bonded regions at pellet interfaces. Also, cesium uranate is lower in density than UO_2 so that the formation of the uranate could cause local volume increases and resulting fuel-clad gap closure, which could also contribute to local clad stress concentration.

4.11 Density Measurements on Irradiated Fuel

The densities of fifteen fuel pellet samples were measured in the hot cell to determine the extent of densification/swelling experienced by the fuel. The fuel samples were selected from high and low gas release rods and from various axial locations of the rods. The sample selection afforded a separation of fuel densification from swelling and other variables such as temperature and fission rate.

The density measurements were made using the BMI in-cell mercury pycnometer which consists of a mercury reservoir, a specimen chamber and an evacuation system. The procedure used involved the following steps:

1. The mercury reservoir was filled with mercury and weighed accurately.

2. The specimen chamber and the reservoir were then clamped together, and the chamber was evacuated and then filled with mercury from the reservoir. The reservoir was then weighed again. From the difference in the two weights, the amount of mercury used to fill the chamber and hence the volume of specimen chamber was calculated.

3. The fuel specimen of known weight was then placed in the specimen chamber and steps (1) and (2) were repeated. From the data obtained, the volume of the fuel specimen, and hence the density, was calculated. The apparatus and the method were checked for accuracy by measuring the density of a standard periodically.

The fuel samples were obtained from 1/2 in. long sections cut from the fuel rods at desired axial locations. All of the fuel was then removed from the cut sections. The fuel particles were screened to remove fine particles prior to the density measurement. The density data obtained on the samples are shown in Table 4-15. Also shown are the pre-irradiated rod average fuel density and the calculated sample burnup based on Cs-137 gamma scan data. The initial fuel density was estimated from the measured pre-irradiated fuel stack weight in each rod. The data shown in Table 4-15 indicate that the increase in fuel density during irradiation ranged from 2.4 to 5.55% TD. An analysis of the data is presented in Section 6.

4.12 Burnup Analyses

During the first campaign, burnup measurements by the Neodymium-148 Method were obtained by analysis of two fuel samples taken from a sound rod, JBP-005, adjacent to the location of an incipient cladding crack. During the second campaign, three half-inch fuel samples from two other sound rods, JCN-196 and HBU-169, were analyzed with the objective of determining the accuracy of burnup values derived from gamma scans. The results from all of the five fuel samples are shown below:

Rod	Calculated Rod Average Burnup	Sample Location Inches from Rod Bottom	Measured Sample Burnup Mwd/MTU(1)
JBP-005	13,231	94-7/16 - 95-7/16	14,900
		95-7/16 - 95-7/16	14,800
JCN-196	12,904	94 - 94-1/2	15,660
		127 - 127-1/2	8,230
HBU-169	12,410	94 - 94-1/2	14,240

(1) All burnup values based on Nd-148 method.

Table 4-15

Densification/Swelling
of Maine Yankee Core I Fuel

Rod S/N	Sample Location (in. from Bottom of Rod)	Calculated Burnup Mwd/MTU	Mercury Immersion Density, % TD		
			Initial*	Final+	Δ
HBU-169	133-1/2 - 134	5,340	91.95	97.4	5.45
	93-1/2 - 94	14,410		96.3	4.35
	2-1/2 - 3	5,590		97.5	5.55
	125-1/2 - 126	9,050		96.3	4.35
JCN-196	133-1/2 - 134	5,680	92.5	97.1	4.6
	76-5/8 - 77-1/8	15,225		96.5	4.0
	125-1/2 - 126	9,700		96.1	3.6
JBY-097	2-1/2 - 3	5,680	92.8	97.2	4.4
	88-3/8 - 88-7/8	14,900		96.6	3.8
JBP-004	133-1/2 - 134	5,840	93.3	96.3	3.0
	93-1/2 - 94	15,320		97.1	3.8
	76-1/2 - 77	15,610		97.5	4.2
	2-1/2 - 3	5,710		95.7	2.4
	120-1/2 - 121	11,260		97.1	3.8
	7-3/4 - 8-1/4	9,050		96.9	3.6

* Using the fuel rod stack weight to calculate an average geometric density (assuming nominal fuel dimensions) then adding 0.5% TD to adjust from geometric to immersion density.

\+ As-measured in the hot cell.

A comparison of the local burnup results with the corresponding relative gamma activities (from both gross gamma scans and specific isotope scans) show the following:

1. The burnup values calculated from the gamma scans are in reasonable agreement with the measured values from the respective rods. (e.g., the value calculated for the ∿95-in. location of Rod JBP-005 was 15,800 Mwd/MTU using the gross gamma scan and the rod average burnup calculated from Physics data.) This indicates that the actual power history of the fuel rods was not grossly different from that calculated from Physics data.

2. The results on the lower burnup sample from Rod JCN-196 are consistent only with the Cs-137 scan for the rod. This is based on a comparison of the burnup values calculated from the gross gamma scan and the specific isotope gamma scans assuming that the gamma activity at a given location is proportional to burnup. The burnup at 127 in. is calculated from the measured burnup at 94 in. and the ratio of gamma activity at 127 in. to that at 94 in. The results are shown below:

Type of Scan	γ Activity at 127 in. Relative to 94 in. Location	Calculated Burnup at 127 in. Mwd/MTU
Gross Gamma	0.640	10,022
Zr Nb-95	0.708	11,087
Cs-137	0.543	8,503

It can be seen that the burnup value derived from the Cs-137 scan is in excellent agreement with the measured value of 8,230 Mwd/MTU. This confirms the previous conclusions that Cs-137 scan is a more accurate representation of the axial burnup profile than the gross gamma scan or the Zr/Nb-95 scan.

5.0 FUEL ROD IRRADIATION HISTORIES

5.1 Power Histories at Incipient Crack Locations

In the overall hot cell program, three sound rods (JBP-005, JBY-097 and JBP-122) exhibited cladding cracks which undoubtedly represent evidence of incipient perforation. The irradiation history of the three rods, particularly the local power at the crack locations, has been examined in some detail to determine the possible role of fuel duty in the perforation mechanism. To obtain local heat rating values for this analysis, the core power at different burnup periods and the axially averaged power factor for the rods (relative to core power) were ascertained from core follow calculations. These were then multiplied by an appropriate axial power shape factor obtained for the respective assemblies from axial shape calculations based on in-core instrumentation. Fig. 5-1 presents the resulting steady state power history of the three incipient crack locations, covering the core average burnup range from 5,627 Mwd/MTU to 8,300 Mwd/MTU, when the majority of the rod perforations were occurring based on coolant iodine activity data. The axial power profiles at different burnups are plotted in Fig. 5-2 and Fig. 5-3 for Rod JBP-122 and Rod JBY-097, respectively. (As Rod JBP-005 is a high power rod from Assembly B-042, its power profiles are similar to those of JBP-122.)

Fig. 5-1 indicates two periods of high power operation occurred at core average burnups of ∿6,700 Mwd/MTU and ∿8,300 Mwd/MTU, corresponding to the first escalation to 88% of full power and the first escalation to 95% of full power, respectively. These are also the periods associated with the largest coolant iodine activity increases (see Fig. 1-1). Not surprisingly, Fig. 5-2 and 5-3 show that the incipient crack locations coincide with the peak axial power locations in the rods during these periods.

In view of the hot cell examination evidence of a PCI perforation mechanism, the most significant point about the power histories in Fig. 5-1 is that the heat rating in the crack regions ranged from 7.9 to 8.3 kw/ft

Figure 5-1 STEADY STATE POWER HISTORY OF INCIPIENT CRACK LOCATIONS

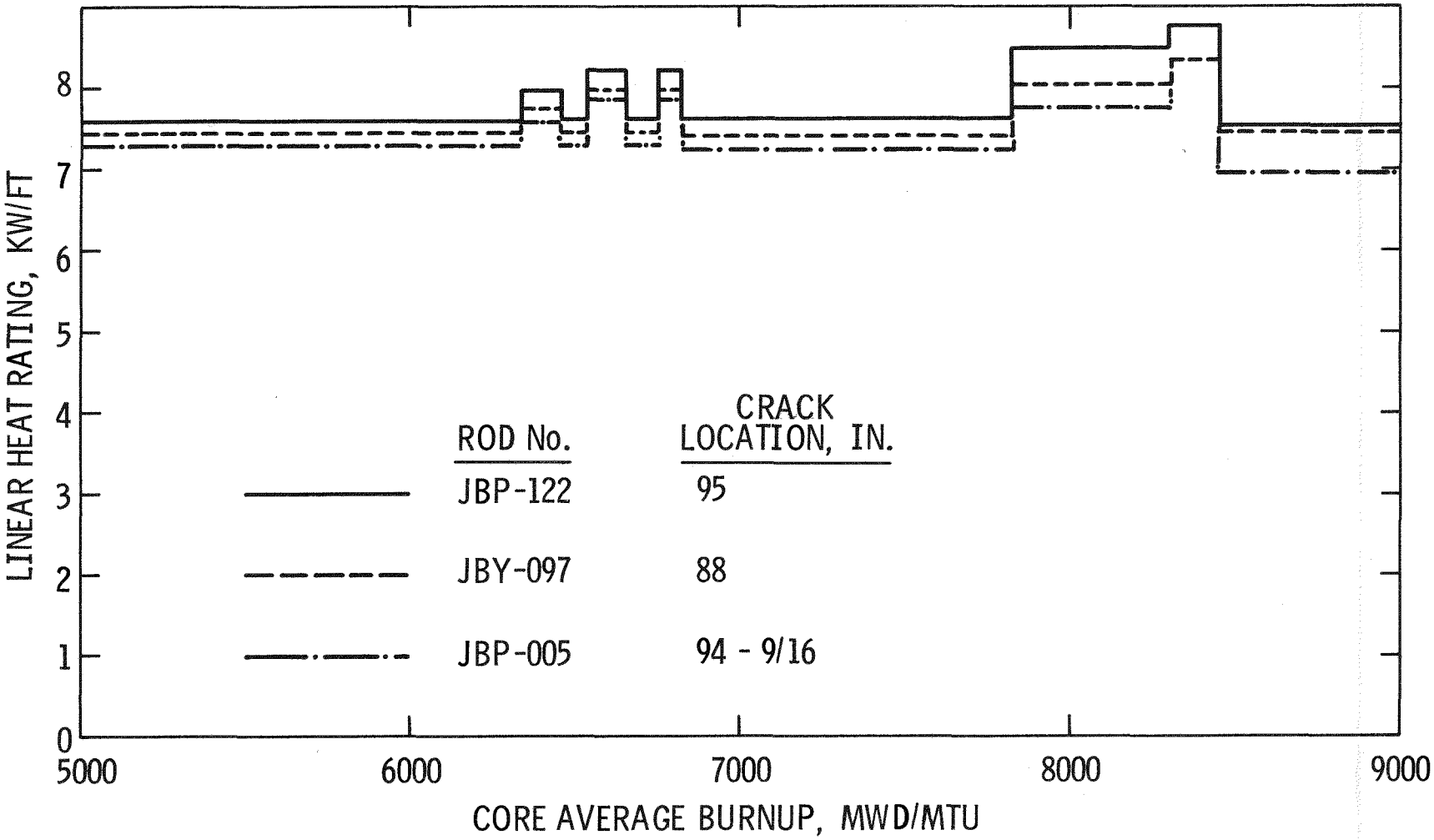

Figure 5-2 AXIAL POWER PROFILES OF ROD JBP-122 IN THE 5000-8300 MWD/MTU CORE BURNUP PERIOD

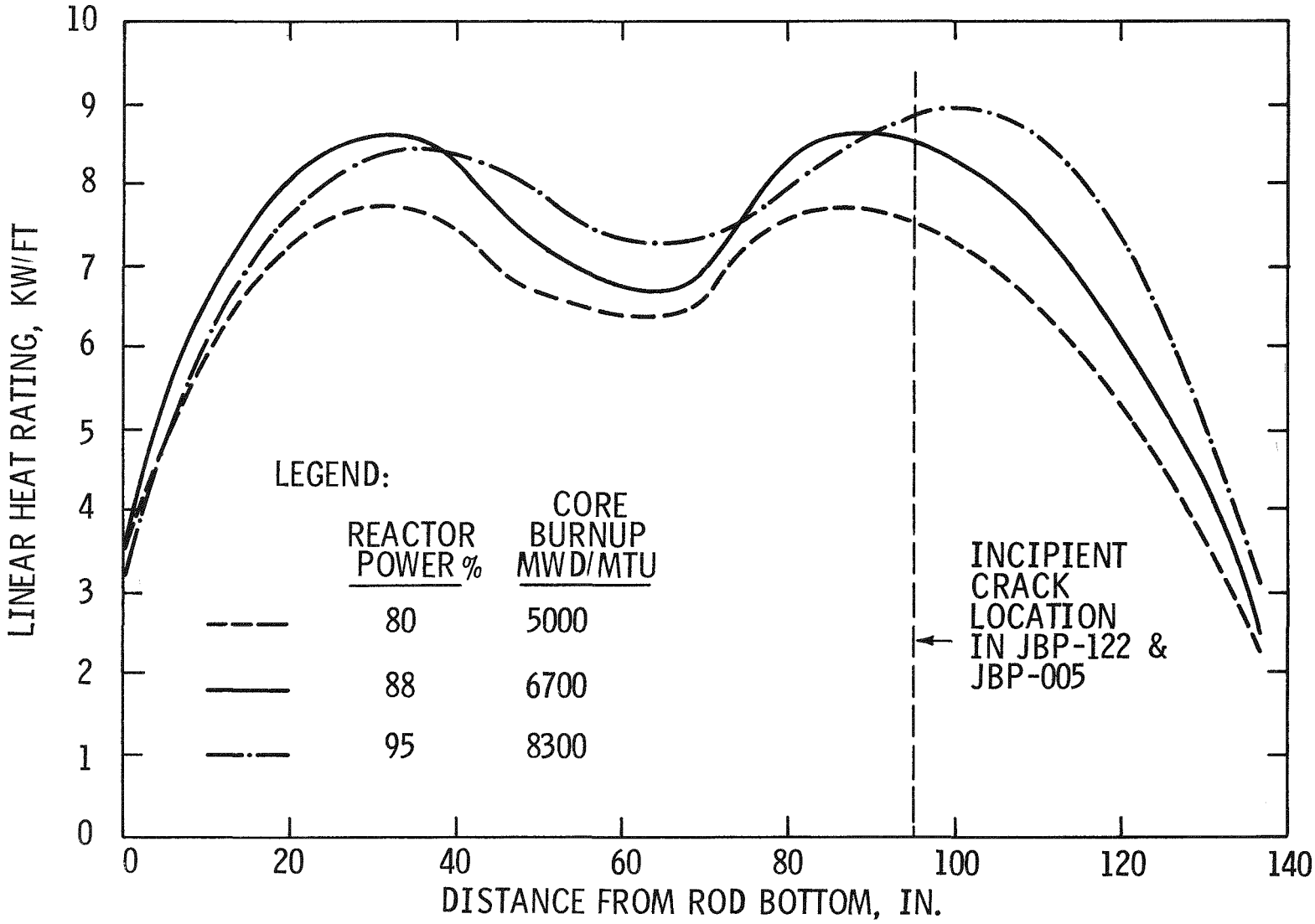

Figure 5-3 AXIAL POWER PROFILES OF ROD JBY-097 IN THE 5000-8300 MWD/MTU CORE BURNUP PERIOD

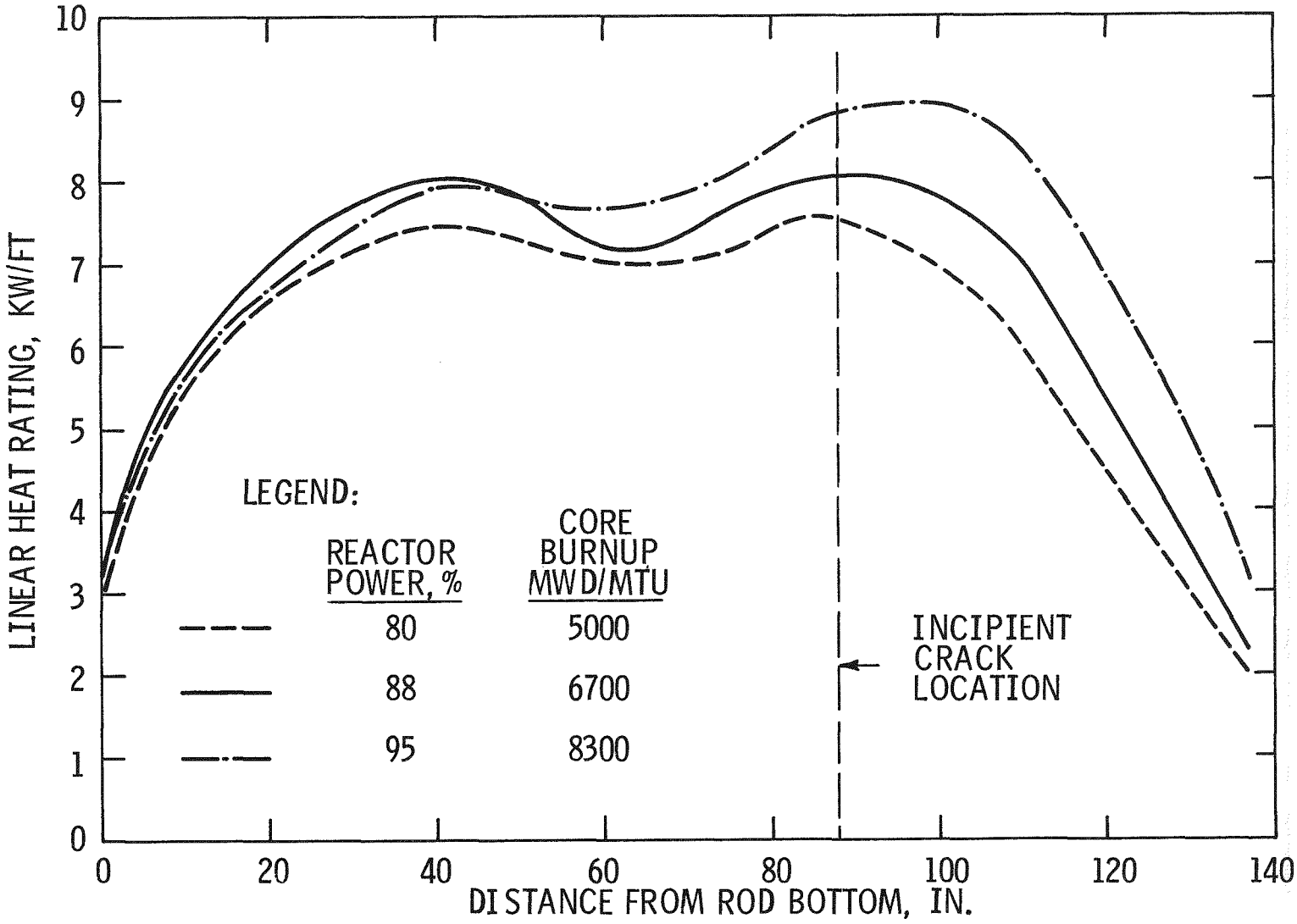

at 88% power (6,700 Mwd/MTU) and from 8.3 to 8.7 kw/ft at 95% power (8,300 Mwd/MTU). Also, core power change data from Maine Yankee confirms that in the case of the escalation to 88%, the power was raised from 20% to 85% at a rate not exceeding 10%/hour (the core had operated briefly at 85% prior to this period); and from 85% to 88%, the power change was gradual over a 16-hour interval. Similarly, the power escalation to 95% was also accomplished slowly involving a linear increase from 88% over a 2-day period. Such modest heat ratings and small rates of power change alone are not normally associated with a PCI perforation mechanism.

The above discussion has dealt only with an analysis of steady state power data. From the standpoint of a PCI mechanism, power transients are of equal, if not greater, importance. An examination of the Maine Yankee Core I power history uncovered only one power transient of possible significance, which occurred after four days of operation at 88% at ∿6,700 Mwd/MTU average core burnup. At that time, the CEA Bank 4 control rods (the Fig. 1-2 core map shows these to be located in Batch A assemblies) were inserted to reduce power level. Upon their withdrawal to the original positions, the transient resulted in an axial xenon oscillation which peaked the axial power distribution towards the top of the core. The peak location was estimated to be between 94 to 104 inches from the bottom of the core. From an analysis of the data, the estimated change in peak local heat rating from the reduced level in the unrodded adjacent Batch B assemblies, such as B047, was on the order of 4 kw/ft to a final peak heat rating of 8.6 kw/ft. Batch B assemblies more remotely located from CEA Bank 4 positions,such as B042 and B069, would be less affected by the transient. Although there is insufficient data to estimate the power change rate, again, such heat rating changes and peak levels alone are not usually associated with a PCI perforation mechanism.

Summarizing, the local power histories of the incipient crack locations alone do not appear to be consistent with a PCI perforation mechanism. However, as discussed in Section 6, other factors which are related to the high fission gas release behavior can also contribute significantly to such a mechanism.

5.2 Power Histories of Fuel Sections with Equiaxed UO_2 Grain Growth

As described in Section 4.8.3.3, the axial extent of equiaxed UO_2 grain growth was mapped in one of the high gas release rods, JBP-005, by metallographic examination of several sections selected from different axial locations. Fig. 5-4 presents the local power history as a function of core average burnup for each of the sections which exhibited equiaxed grain growth. It is noteworthy that the highest heat ratings achieved by fuel located approximately 10 inches from the top and bottom of the fuel stack were 5.5 and 5.8 kw/ft, respectively. Nevertheless, both positions experienced appreciable equiaxed grain growth while fuel in low gas release rods operating to a maximum of 8 to 9 kw/ft was not restructured. The fuel rod heat transfer reduction mechanism considered responsible for this behavior difference is described in Section 6, Data Analysis.

5.3 Relative Rod Powers Among the Different Maine Yankee Core I Batches

The most striking initial observation of the rod perforation pattern in Maine Yankee Core I was the distribution of perforated assemblies among the Batches (41 from B and only 1 each from A and C). The fact that Batch B assemblies generally achieved a higher burnup than the other assemblies in the core immediately suggested a power-dependent rod perforation mechanism. This was reinforced when, upon poolside disassembly of B-042 and B-069, all of the perforated rods were observed to have been located in relatively high power positions. To explore further the relationship between power and perforation incidence, an analysis was performed of the relative rod power histories during the burnup period when perforations were occurring (approximately 5,000 to 8,000 Mwd/MTU core average).

The results of the analysis are presented in Table 5-1 and summarized in Fig. 5-5. The significant points are:

1. Approximately 38% of the rods in the two Batch B assemblies, B-042 and B-069, operated above the lowest relative power of the perforated rods in these assemblies during the 5,000 to 8,000 Mwd/MTU core average burnup period.

Figure 5-4
POWER HISTORY OF METALLOGRAPHIC SECTIONS FROM ROD JBP-005
EXHIBITING EQUIAXED GRAIN GROWTH

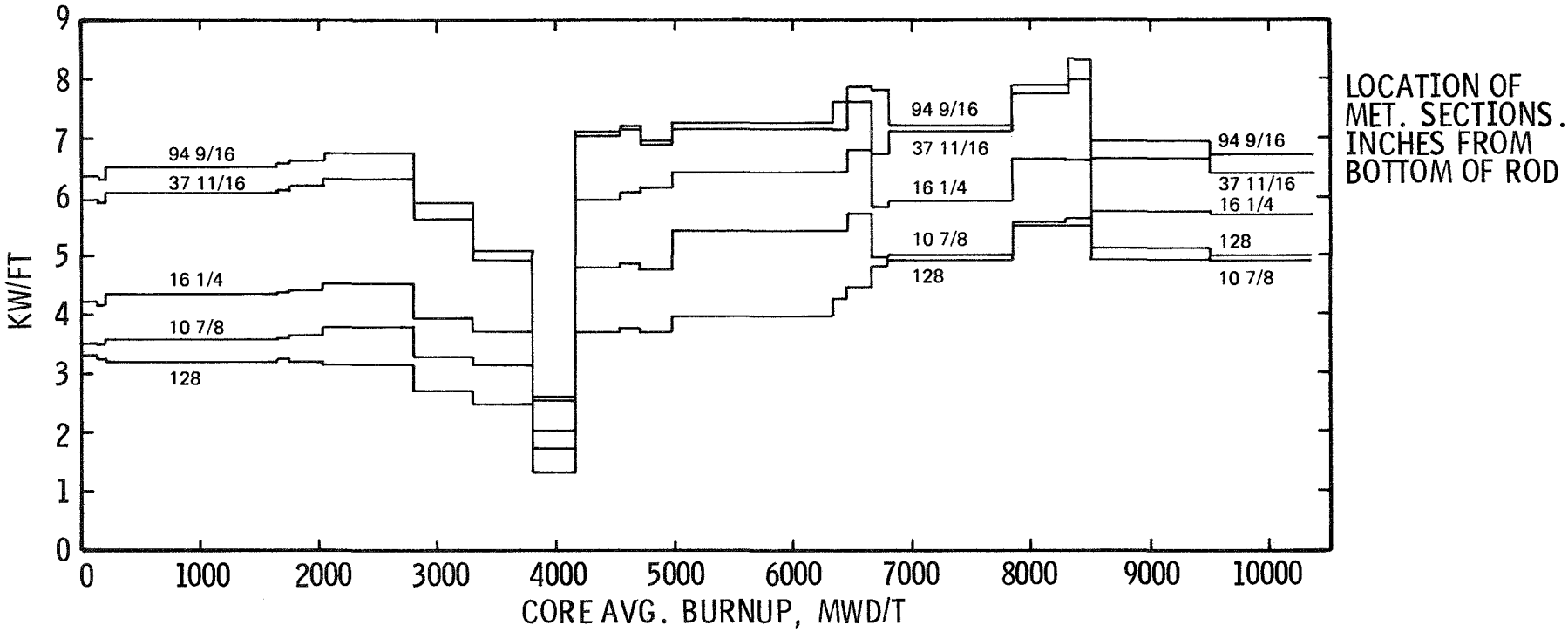

Table 5-1

Analysis of Relative Rod Power Histories* in Maine Yankee Core I During the Core Average Burnup Period from 5,000-8,000 Mwd/MTU

		Value at Indicated Burnup (Mwd/MTU)		
		5,000	6,250	8,000
1.	Minimum perforated rod relative power in B-042 and B-069	1.255	1.253	1.238
2.	Maximum relative rod power in B-042 and B-069	1.365	1.352	1.335
3.	Ratio of total number of rods in B-042 and B-069 operating at or above minimum perforated rod power-to-total number of rods in the assemblies+	0.378	0.384	0.388
4.	Ratio of perforated rods-to-total number in B-042 and B-069 operating at or above minimum.	0.124	0.122	0.121
5.	Maximum relative rod power in Batch B.	1.245	1.216	1.187
6.	Total number of rods in Batch A at or above minimum perforated rod relative power.	0	0	0
7.	Maximum relative rod power in Batch C.	1.272	1.278	1.280
8.	Total number of rods in Batch C at or above minimum perforated rod relative power.	32	56	112
9.	Ratio of number of rods in Batch C at or above minimum perforated rod relative power-to-total number of rods in Batch C.	0.0028	0.0049	0.0098

* Rod powers in this table are averages relative to the core average power.

\+ Total number of rods per Batch B assembly = 160.

Figure 5-5 ROD POWER HISTORY COMPARISON AMONG MAINE YANKEE CORE 1 BATCHES

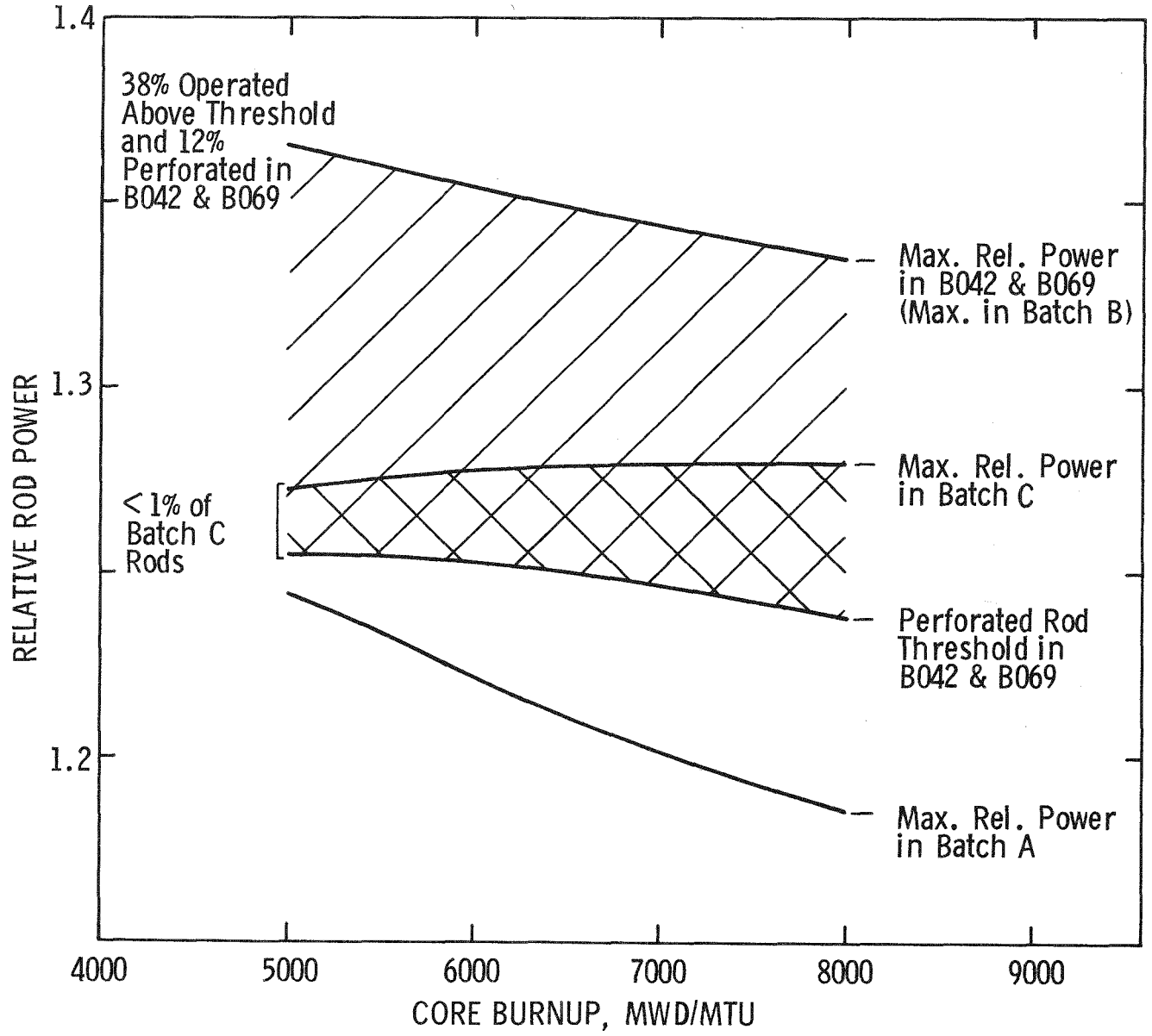

2. At any given burnup during this period, no Batch A rod and less than 1% of the Batch C rods operated at powers as high as the lowest relative power of these perforated Batch B rods.

3. Only about 12% of the Batch B rods operating above the minimum perforated rod relative power are in the perforated rod population. Applying this factor to Batch C directly would undoubtedly produce an overestimate of Batch C perforated rods. This is because the maximum relative rod power of Batch C was significantly less than that of Batch B, and the probability of perforation increases with increasing relative power.

4. Therefore, very few rods from Batches A and C would be expected to be perforated by the mechanism operating in Batch B.

Thus, the Maine Yankee poolside observations, indicating virtually all the perforated rods were from Batch B, are consistent with a strongly power dependent perforation mechanism operating during the core average burnup period from 5,000 to 8,000 Mwd/MTU.

6.0 DATA ANALYSIS

The previous sections have detailed the data generated in the program. In this section, a data analysis is presented with the objectives of:

1. Explaining why fuel rods, experiencing similar irradiation conditions and a peak heat rating between 8 and 9 kw/ft, exhibited two distinct populations of fractional fission gas release and attendant fuel temperatures,

2. Exploring differences and similarities between the two fuel rod populations,

3. Determining the relationship between the major clad perforation mechanism and the behavior of the higher gas release rods, and

4. Characterizing the performance of Maine Yankee Core I fuel to obtain data for use in fuel rod modeling.

6.1 Results of Hot Cell Examination

The key hot cell examination results upon which the data analysis is based are highlighted in Table 6.1. In addition, the pertinent information generated during the hot cell examination of the Batch B rods is displayed in the rod layouts of the assemblies B-042 and B-069 shown in Fig. 6-1 and 6-2. These include the fractional fission gas release observed, the maximum cladding ovality and creepdown from profilometry, the fuel stack shortening from gamma scanning, and the relative average rod power (life-averaged and at end-of-life) from Physics calculations.

Table 6-1

MAJOR HIGHLIGHTS OF HOT CELL EXAMINATION RESULTS

Examination	Results
Visual Examination	1. No anomalies in sound rods. The rods appeared lightly crudded. 2. Perforated rods contained blisters and bulges. 3. No cracks or splits observed except at blisters on perforated rods.
Profilometry (Spiral and Linear)	1. Data show clad creepdown of up to 3 mils (diametral). 2. Randomly-located areas of large ovality (up to 16 mils). 3. Clad ridging (max. 0.4 mils) observed in high power locations of most rods. 4. Two categories of creepdown and ovality observed among high burnup rods (>12,321 Mwd/MTU). Four high gas release Batch B rods showed diametral creepdown in the range 1.5 to 2.4 mils with maximum ovalities in the range 4-6.4 mils. Other high burnup rods showed >2.2 mil creepdown and >7.2 mil maximum ovality.
Fission Gas Collection	1. The gas release data fall into two groups <1% in 14 rods (6,750 - 13,200 Mwd/MTU) 11.3 to 15.3% in 8 rods (12,410 - 13,650 Mwd/MTU). 2. Of the 8 high gas release rods, 7 were from Batch B and one was from Batch A. The Batch A rod had low initial average fuel density based on fuel stack weight.
Gamma Scan (Gross and Specific Isotope)	1. All gamma scans showed small distributed gaps. 2. Fuel stack shortening consistent with observed densification. 3. Cs-137 scans showed peaking at pellet interfaces in high gas release rods. No peaking in low gas release rods. 4. Region of Cs peaking extended from 5 to 128 inches from rod bottom. 5. Perforated rods showed Cs peaking.

Table 6-1 (continued)

MAJOR HIGHLIGHTS OF HOT CELL EXAMINATION RESULTS

Examination	Results
Fuel-Clad Metallography	1. Incipient cladding cracks observed in three specimens from three high gas release rods. 2. All cracks were radial and appeared similar to iodine stress corrosion cracks in Zircaloy. 3. SEM fractography of the cracks confirmed cracks to be of the same type as iodine stress corrosion cracks. 4. Bonding of fuel to cladding observed at pellet interfaces in high gas release rods. No bonding in low gas release rods. 5. Equiaxed grain growth observed only in high gas release rods.
Slit Clad Examination	1. Showed fuel-clad bonding at pellet interfaces in high gas release rods. 2. Cs-137 gamma scan of the slit clad was similar to whole rod scan. 3. X-ray analysis of particles on clad showed Cs-I compounds and Cs-Te-U-Zr compounds.
Microprobe Analysis	1. Showed the reaction layers in bonded fuel to be rich in Cs adjacent to zirconium oxide layer. 2. No iodine was detected in the reaction layers.
Density Measurements	1. Showed fuel to have densified to 97.5% TD. 2. At low power positions, the EOL fuel density was higher in high gas release rods than in low gas release rods. At high power positions; the reverse was observed.
Burnup Analysis	1. Data showed good agreement with calculated values. 2. Showed Cs-137 gamma scan accurately represents axial burnup profile.

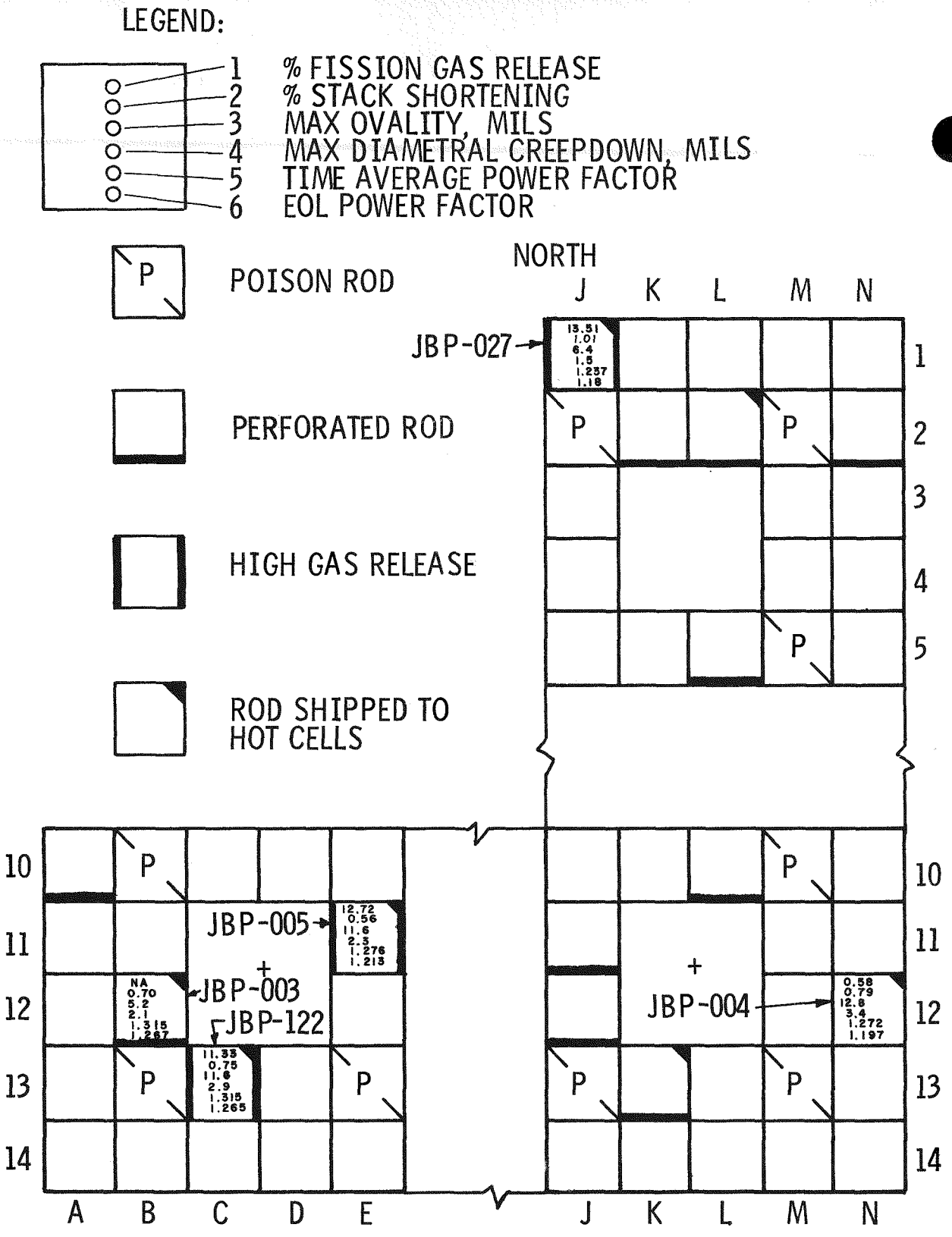

Figure 6-1
RESULTS OF HOT CELL EXAMINATION ON RODS IN ASSEMBLY B042

Figure 6-2

RESULTS OF HOT CELL EXAMINATION ON RODS IN ASSEMBLY B069

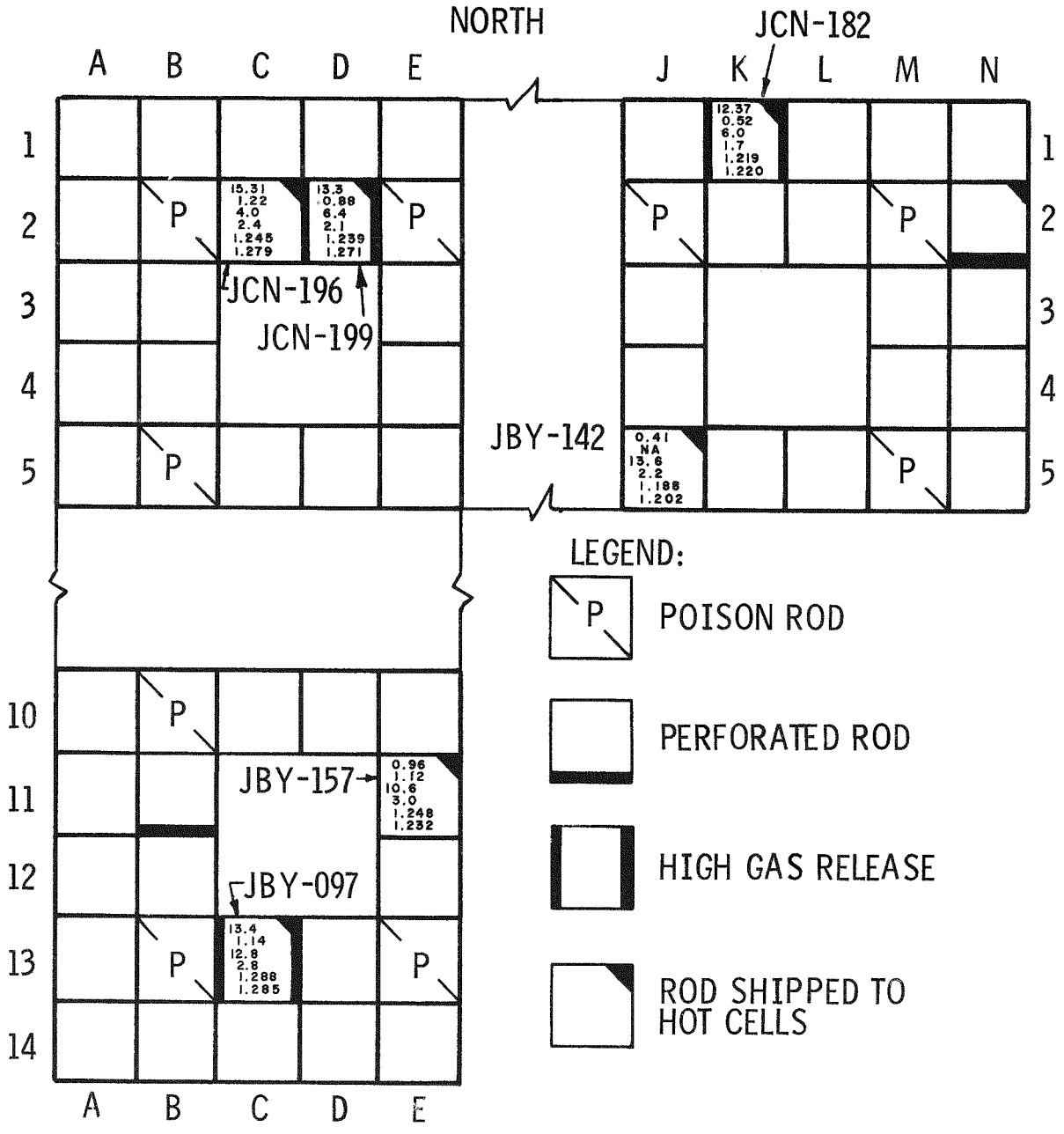

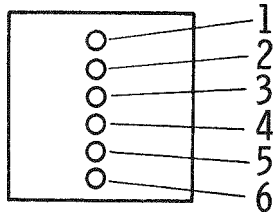

1 % FISSION GAS RELEASE
2 % STACK SHORTENING
3 MAX OVALITY, MILS
4 MAX DIAMETRAL CREEPDOWN, MILS
5 TIME AVERAGE POWER FACTOR
6 EOL POWER FACTOR

6.2 Fuel Rod Heat Transfer Reduction

6.2.1 Parameters Affecting Fission Gas Release

As referred to previously, a fuel rod heat transfer reduction process is believed responsible for the observed higher gas release population. Before describing this mechanism a discussion of parameters affecting fission gas release is in order. Since fission gas release is mainly a function of fuel temperature, the fractional releases should be dependent upon parameters which affect the fuel temperature, i.e., power, gas conductivity and hot pellet-clad gap. Rods with similar power histories are expected to have similar fuel swelling, relocation, cladding creepdown and gas conductivity, at least before any gas release differences arise among them. Therefore, fuel densification and the as-built pellet-clad gap size are the two remaining parameters that are likely to be responsible for temperature and gas release differences among rods.

Variations in the starting pellet-clad gap are largely due to variations in the as-built cladding OD. Fuels with microstructures such as those of Maine Yankee exhibit higher densification with lower initial density.[19] Thus, variations in as-built cladding OD and initial density can represent variations in operating gap conductance among the similar burnup rods. Therefore, in Fig. 6-3, the observed fractional gas releases are plotted against relative life-averaged power in fuel rod groups reflecting different combinations of as-built cladding OD and average initial fuel density. (The diameter data is derived from hot cell profilometry of the plenum region, and the average fuel densities are calculated from fuel stack weights.)

Fig. 6-3 shows the two distinct populations of fractional gas releases, namely 0.3% to 1% and 11.3% to 15.3%. It can be seen that the threshold life-averaged relative rod power for the higher gas release population is close to 1.26 for rods with nominal as-built properties. (A rod power factor of 1.26 corresponds approximately to a peak heat rating of 9 kw/ft.) For rods with greater than nominal cladding OD or

Figure 6-3
RELATIONSHIP BETWEEN FISSION GAS RELEASE
AND LIFE AVERAGE ROD POWER

LEGEND		
	CLAD OD	AVERAGE INITIAL FUEL DENSITY
○	NOMINAL (≤ 0.440 IN.)	NOMINAL (≥ 93% TD)
⊗	NOMINAL	LESS THAN NOMINAL
□	GREATER THAN NOMINAL	NOMINAL
⊠	GREATER THAN NOMINAL	LESS THAN NOMINAL

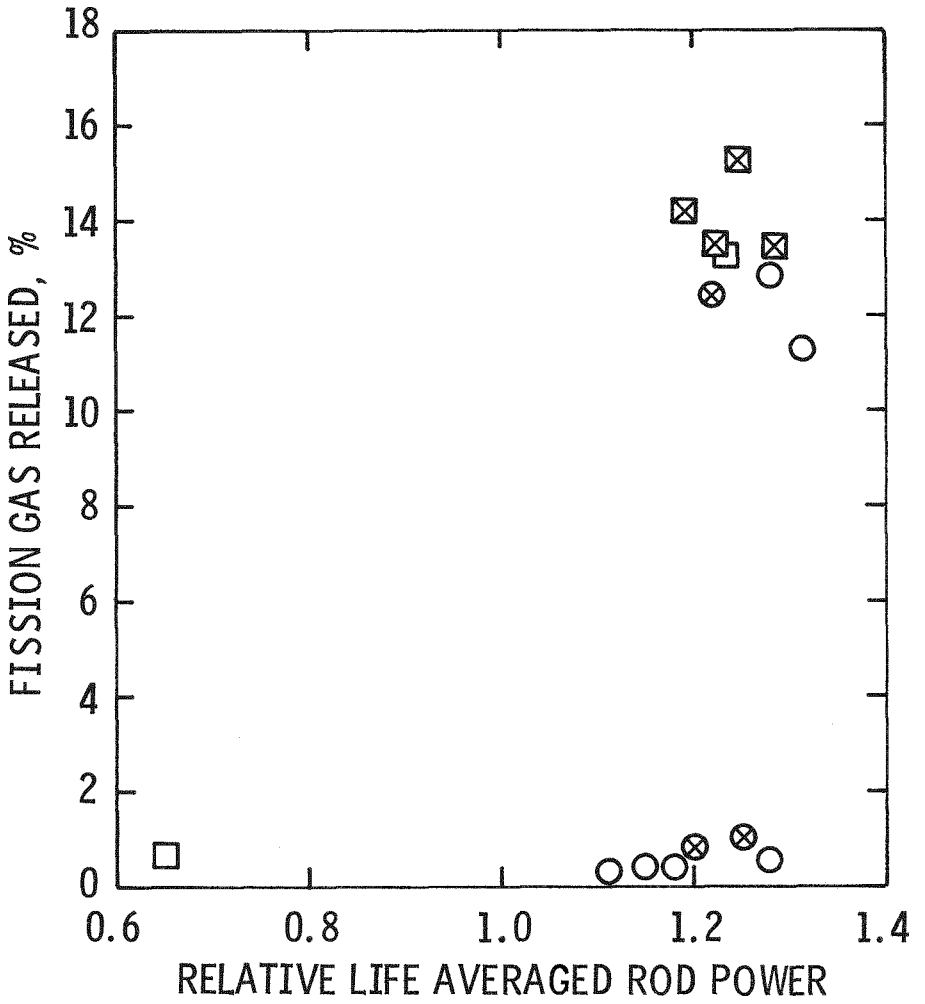

less than nominal fuel density, which are expected to result in larger hot gaps, the threshold rod power is lowered to 1.20. This relationship is consistent with a dependency of gas release on starting pellet-clad gap, fuel densification propensity and rod power, and, therefore, fuel temperature. Moreover, the two distinct ranges of gas release indicate that the temperature differences introduced initially by the variations in gap size and fuel densification were intensified during operation.

Supportive evidence for the effect of gap size variation can be found in an analysis of the cladding OD measured at the plenum region by hot cell profilometry. With the assumption that these represent the as-fabricated diameters and that the rods had nominal cladding wall thicknesses and pellet diameters, an apparent starting gap size can be inferred for the 12 Batch A and B rods having similar irradiation histories (burnups ranging from 12,321 to 13,636 Mwd/MTU). These gap sizes are plotted in Fig. 6-4 against the fractional fission gas release measured for the respective rods. It can be seen that the starting gaps of the higher gas release rods are invariably larger than those of the low gas release rods.

Figure 6-4

APPARENT INITIAL FUEL/CLAD GAP vs FRACTIONAL FISSION GAS RELEASE

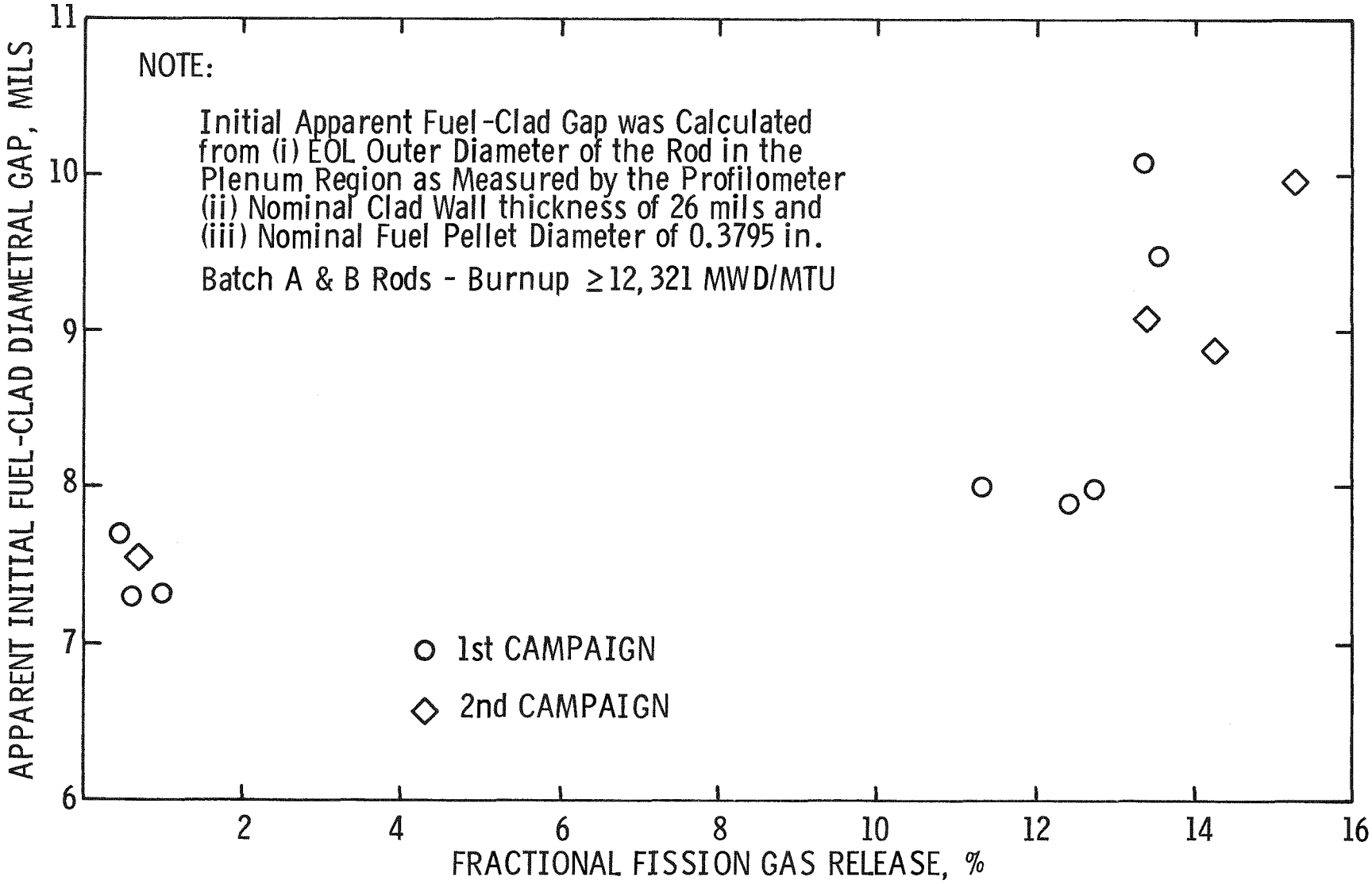

6.2.2 Mechanism of Heat Transfer Reduction

The observed difference in fission gas release behavior among rods with comparable power histories is explained by a heat transfer reduction mechanism which operated only in the high gas release rods. At some point in the high gas release rods, after the UO_2 had densified but before substantial cladding creepdown had developed, the fuel center temperature was just below the threshold for UO_2 equiaxed grain growth. A small power increase or a small reduction of gap conductance occurred and was sufficient to increase the fuel temperature and initiate equiaxed grain growth, resulting in release of a greater fraction of the inventory of fission gas in the grain growth region. This increased gas release diluted the helium fill gas surrounding the pellets, reduced the heat transfer, and caused further temperature increases and grain growth in the fuel. (The end-of-life release fractions of 11.3 to 15.3% represent a mole fraction ratio of Xe plus Kr to He of approximately 4:1 which corresponds to a fill gas thermal conductivity degradation by a factor of about 10 as shown in Fig. 6-5.) The increasing dilution of the fill gas caused sufficient temperature increase in neighboring pellets to initiate grain growth, as well. This process eventually propagated along the rod. It is apparent from the fission gas release data that rods with greater than 1% release fractions were invariably assisted by this process to reach the 11 to 15% end-of-life release fraction range.

The heat transfer reduction process was terminated by fuel thermal expansion, swelling and relocation which accompanied the increased fuel temperature and closed the hot fuel-clad gap. In addition to the gap closure, the process was arrested by the decreasing affect on gap conductance of diluting helium with fission product gas. This can be seen in Fig. 6-5, which shows the dependence of fill gas thermal conductivity on the helium mole fraction.

Figure 6-5

THE EFFECT OF FISSION GAS DILUTION ON THERMAL CONDUCTIVITY OF HELIUM GAS MIXTURE (REF. 31)

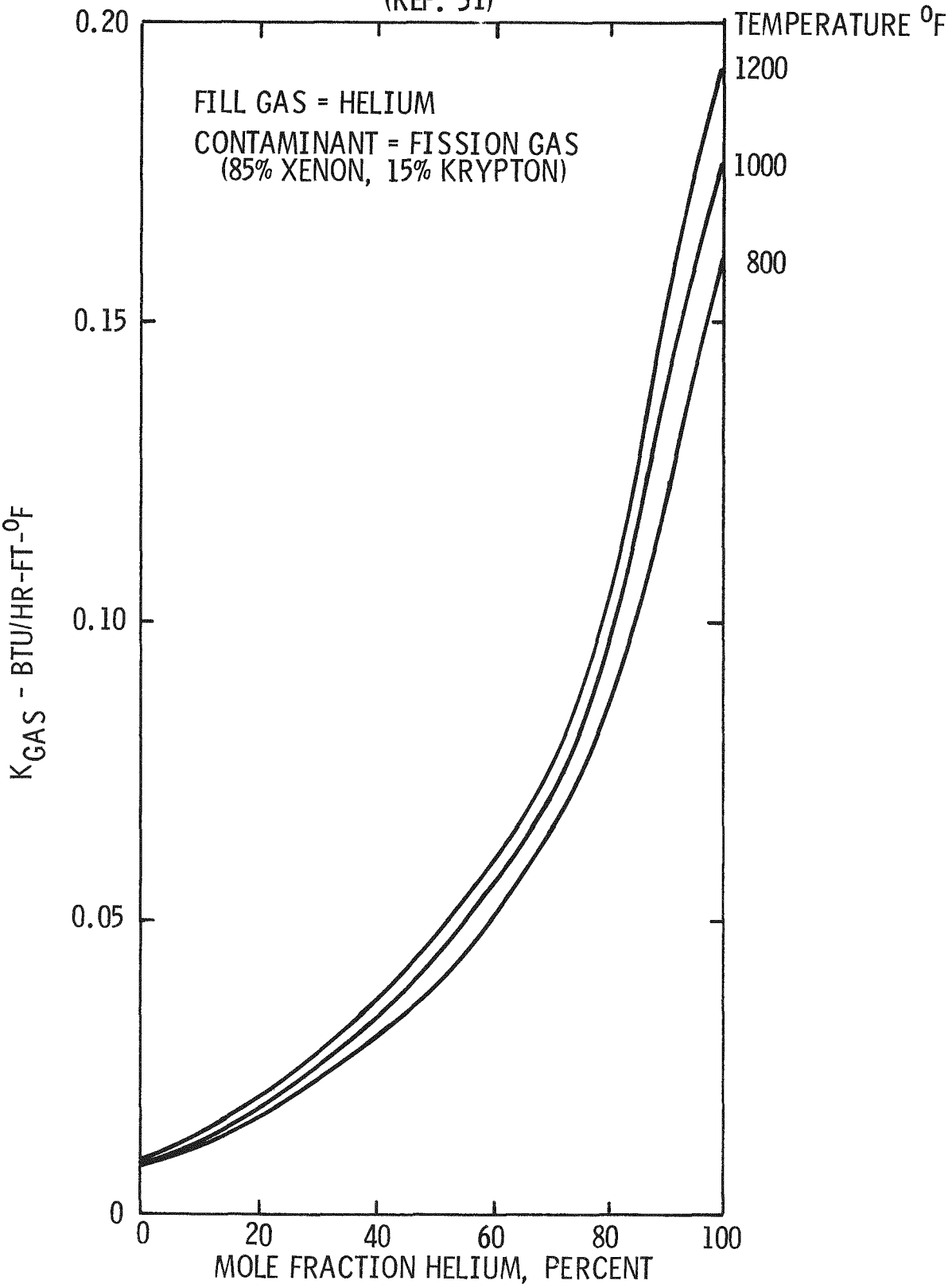

The fact that all fuel rods of a given design operating at similar power levels did not undergo heat transfer reduction is attributed to variations in the actual pellet-to-clad gap during operation due to differences in the starting gap size and propensity for UO_2 densification among rods. It is believed that larger starting gap sizes and greater UO_2 densification in-reactor led to fuel temperatures approaching that for equiaxed grain growth in the high gas release rods. The low gas release rods possessed a combination of these attributes on the low side of the distributions and tended to operate with lower fuel temperatures. Thus, while the high gas release rods experienced equiaxed grain growth in response to a fuel temperature increase, a similar increase did not initiate grain growth in the low gas release rods.

In summary, the above mechanism identifies the minimum temperature for UO_2 equiaxed grain growth as the threshold temperature above which a heat transfer reduction process becomes active. Once this threshold is reached, the accelerated fission gas release magnifies the temperature differences among fuel rods caused initially by variations in the starting pellet-clad gap size (as indicated by cladding OD) and propensity for fuel densification (as indicated by initial fuel density). Fig. 6-3 shows that for nominal fuel density and cladding OD, the threshold temperature was generally not reached unless the life averaged rod power factor exceeded 1.26. For greater than nominal cladding OD and less than nominal initial density, as in Rod HBU-169, this critical temperature was reached at a rod power factor of 1.20. Thus, the Maine Yankee Core I fuel had a combination of irradiation history and fuel parameters (in particular, the propensity for fuel densification) that placed some fuel pellet centerline temperatures near the threshold temperature for equiaxed grain growth. Consequently, pellets operating at high power with nominal initial pellet-clad gap and propensity to densify and pellets at lower power having higher propensity to densify and a larger initial pellet-clad gap experienced an increase in fission gas release, either spontaneously or in response to a power change. This initial increase in gas release caused further temperature increase and grain growth in the fuel and permitted propagation of the local heat transfer effect to the entire rod until a substantial volume of the fuel operated above the equiaxed grain growth temperature. The fuel rod

heat transfer reduction was arrested through the decreasing effect on gap conductance of fission gas release and the pellet-clad gap closure due to the temperature increase.

6.3 Fuel Densification and Swelling Behavior

Post-irradiation densities of fuel pellets taken from various axial locations of three higher gas release and one low gas release rod were measured by the mercury immersion method (see Table 4-15). In this section, the fuel densification/swelling behavior of the two different fission gas release populations is characterized, in part, to explain the heat transfer reduction process. Interestingly, the analysis of the data has also afforded a means of determining the separate effects of temperature and fission rate on UO_2 densification.

In the EEI/EPRI Densification Program [19], as well as in the in-reactor tests performed by CE[20], it was observed that fuel pellets irradiated to identical burnups differed in their rate and extent of densification. The results did not allow separation of effects due to fission rate and temperature since the higher fuel temperature was caused by higher fission rate. In the present case, pellets from similar burnup locations of high and low gas release rods operated at similar fission rates but had different temperatures. Thus, a comparison of the densification behavior of these pellets permits a separation of the two effects.

The mercury immersion density data are plotted in Fig. 6-6, as a function of calculated burnups based on the Cs-137 gamma scans. The initial densities shown are the rod average densities which were calculated using the fuel rod stack weight and nominal fuel dimensions, and then adding 0.5% TD to adjust from geometric to immersion density.*

---

* The maximum uncertainty stemming from the use of nominal fuel dimensions is estimated to be $\pm$ 0.17% TD based on the stack length tolerance.

Figure 6-6

IMMERSION DENSITY OF IRRADIATED FUEL SAMPLES TAKEN FROM VARIOUS AXIAL LOCATIONS OF MAINE YANKEE FUEL RODS

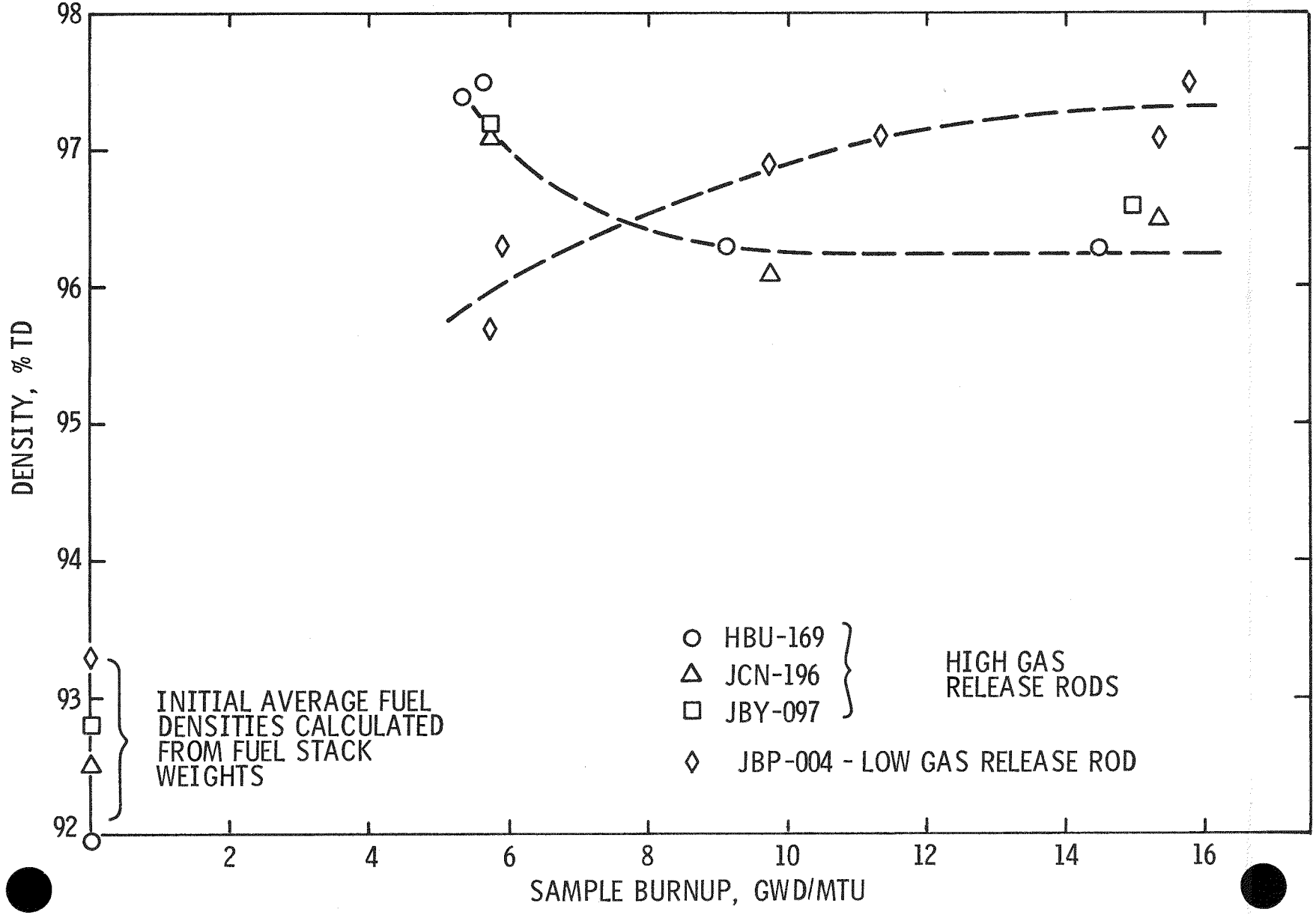

The observed fuel density increases range from 2.5 to 5.5%. It is also evident from Fig. 6-6 that the densification behavior of the fuel from high gas release rods is different from that of the low gas release rod. As noted in the EEI/EPRI and CE programs [19,20], pellets whose pores are mostly small in size are subject to more densification if their initial densities are lower. In this case, it is true only for the low burnup positions of the rods. Also, these earlier investigations showed that for a given densifying fuel type, though the density increases vary with the variation of initial density, approximately the same terminal density is reached. This is certainly not true in this case. Explanations for this apparent anomalous behavior are presented in the following discussion of the data.

In Fig. 6-6 data points at 5,300 - 5,900 Mwd/MTU correspond to axial locations of 2-1/2 to 3 and 133-1/2 to 134 inches from the bottom of the rods, where the local power was low. At these low power locations, the pellets from the high gas release rods densified to 97 to 97.5% TD compared to 95.7 to 96.3% in the low gas release rod. Pellets from both high and low gas release rods operated at similar fission rates, since power shape and history of the low and high gas release rods were similar. Therefore, up to the onset of heat transfer reduction, the pellets from both groups were likely to have operated at very similar fission rates and temperature, and most probably densified by the same amounts. However, after the onset of heat transfer reduction in the high gas release rods, the fuel temperature in these rods increased (even at the low burnup extremities, 5,300 - 5,900 Mwd/MTU, where no equiaxed grain growth was observed). Thus, the low burnup pellets in the high gas release rods subsequently operated at temperatures substantially above those of similar pellets in the low gas release rod. It is concluded, therefore, that this later higher operating temperature in the high gas release rods was responsible for greater densification in these pellets. This observation supports the conclusion that the temperature, as opposed to the fission rate, is the primary variable which led to the observed differences in densification behavior at constant burnup in the EEI/EPRI program[19].

Fig. 6-6 also shows that in the case of the fuel pellets from the low gas release rod, fuel densification increased with increasing burnup. Since the irradiation time was the same for all pellets, this is equivalent to increasing densification with increasing life-averaged heat rating. This relationship, therefore, is attributed to the effect of increasing temperature reflecting higher power operation of the samples taken from the higher burnup regions of the rod. (While this dependency could also be due to increasing total fluence of fission spikes, such an effect is generally completed within the first 4,000 Mwd/MTU burnup[19,21].) In addition, fuel densities plotted in the figure reflect the combined influence of swelling and densification so that the greater densification due to higher temperature operation exceeds the additional swelling component, and the pellets show a net density increase with burnup.

In contrast to the trend of the low gas release rod, the pellets from the high gas release rods show lower density at a burnup of ∿9,400 Mwd/MTU than at ∿5,600 Mwd/MTU. Also, there is essentially no change in density on increasing burnup from 9,400 Mwd/MTU to ∿15,000 Mwd/MTU. Pellets from high gas release rods, even at the low power positions, operated at temperatures above the range in which densification is thought to be temperature dependent. Since burnup was sufficient to complete densification, no variation in densification was expected with higher burnup. Thus, it can be assumed that the lower density at higher burnup resulted from higher swelling.

Metallographic observations have confirmed that fuel pellets above 8,000 Mwd/MTU burnup restructured with equiaxed grain growth extending to ∿50% of the radius. The structures developed significant volumes of grain boundary porosity due to the coalescence and growth of gaseous fission products. Therefore, the swelling of the restructured region is responsible for the decreases in density between 5,600 and 9,400 Mwd/MTU burnup. Assuming a swelling rate of 0.4% $\Delta V/V$ per 10^{20} fissions-cm^{-3} [22] for the unrestructured fuel and taking account of volume fractions for the restructured and unrestructured regions, the average swelling rate of the restructured region is calculated to be 1.6% $\Delta V/V$ per 10^{20} fissions-cm^{-3}.

The data indicate that swelling reached its maximum value within ∿10,000 Mwd/MTU, as no further decrease in density is observed above ∿10,000 Mwd/MTU. A possible explanation for saturation of swelling at a low burnup of ∿10,000 Mwd/MTU is that swelling and higher temperature operation in the peak power location (∿15,000 Mwd/MTU) of the high gas release rods led to closing of the pellet-clad gap and subsequent mechanical interaction. Thus, lower overall swelling of the peak power location may be the consequence of restrained swelling of the fuel, compared to unrestrained swelling in the lower power locations (∿10,000 Mwd/MTU).

In summary, the fuel density data show that the pellets densified from 2.5 to 5.5%, depending upon axial location within the fuel rods. The pellets at the low burnup extremities of the high gas release rods exhibited an end-of-life density of approximately 1.5% higher than those of the low gas release rod. This difference is attributed to the temperature dependence of the densification process. The data also confirm that the amount of densification increases with decreasing initial density. This supports the role of densification propensity in accounting for the initiation of fuel rod heat transfer reduction in the high gas release rods, but not in the low gas release rods with similar power history. Analysis of the fuel density data also indicates there was significant fuel swelling in the high power regions of the high gas release rods subsequent to the onset of the heat transfer reduction process, thus supporting the role cited for such swelling in arresting the process.

6.4 Grain Growth Data Analysis

Metallographic data indicate that only rods with high gas release exhibited significant amounts of UO_2 equiaxed grain growth. In this section, the grain growth characteristics of Maine Yankee Core I fuel are examined to establish a "best estimate" temperature for the onset of equiaxed grain growth. (This includes a mechanistic evaluation and a temperature analysis of the equiaxed grain growth data.)

6.4.1 Measured Grain Size and Boundary for Equiaxed Grain Growth

Radial profiles for grain size are plotted for three axial positions from Rod JBP-005 in Fig. 6-7. The grain size was measured by the linear intercept method, and the reported size is the mean intercept of ∿300 grains.

To locate the equiaxed grain growth outer boundary in the metallographic specimens a particular location was classified as a region of equiaxed grain growth if the grains grew and fission gas bubbles were observed in the grain boundaries. At the outer boundary of the equiaxed grain growth region, reported in this investigation, grains grew from 1.6 to 2 times their initial size. (Grain growth of this magnitude was also observed in the peak power region of low gas release rods with no fission gas bubbles at the grain boundaries.) Thus, at the outer boundary of equiaxed grain growth the grain sizes ranged from ∿4.8 to 6 μm.

As is evident from Fig. 6-7 at the 10-7/8 in. and 94-9/16 in. axial locations of the Rod JBP-005, the fuel restructured up to ∿0.6 of its radius. In the fuel cross section 6 in. from the bottom of the rod, a gradual increase in grain size was observed from the surface to the center of the fuel. But, in accordance with the criteria, the grain size increase was not classified as equiaxed grain growth.

In the equiaxed grain growth region, the grain size was generally observed to increase toward the center of the fuel. The fuel cross section at 94-9/16 in. shows this trend.

Figure 6-7
GRAIN SIZE AS A FUNCTION OF PELLET RADIAL LOCATION AT VARIOUS AXIAL LOCATIONS OF ROD JBP-005

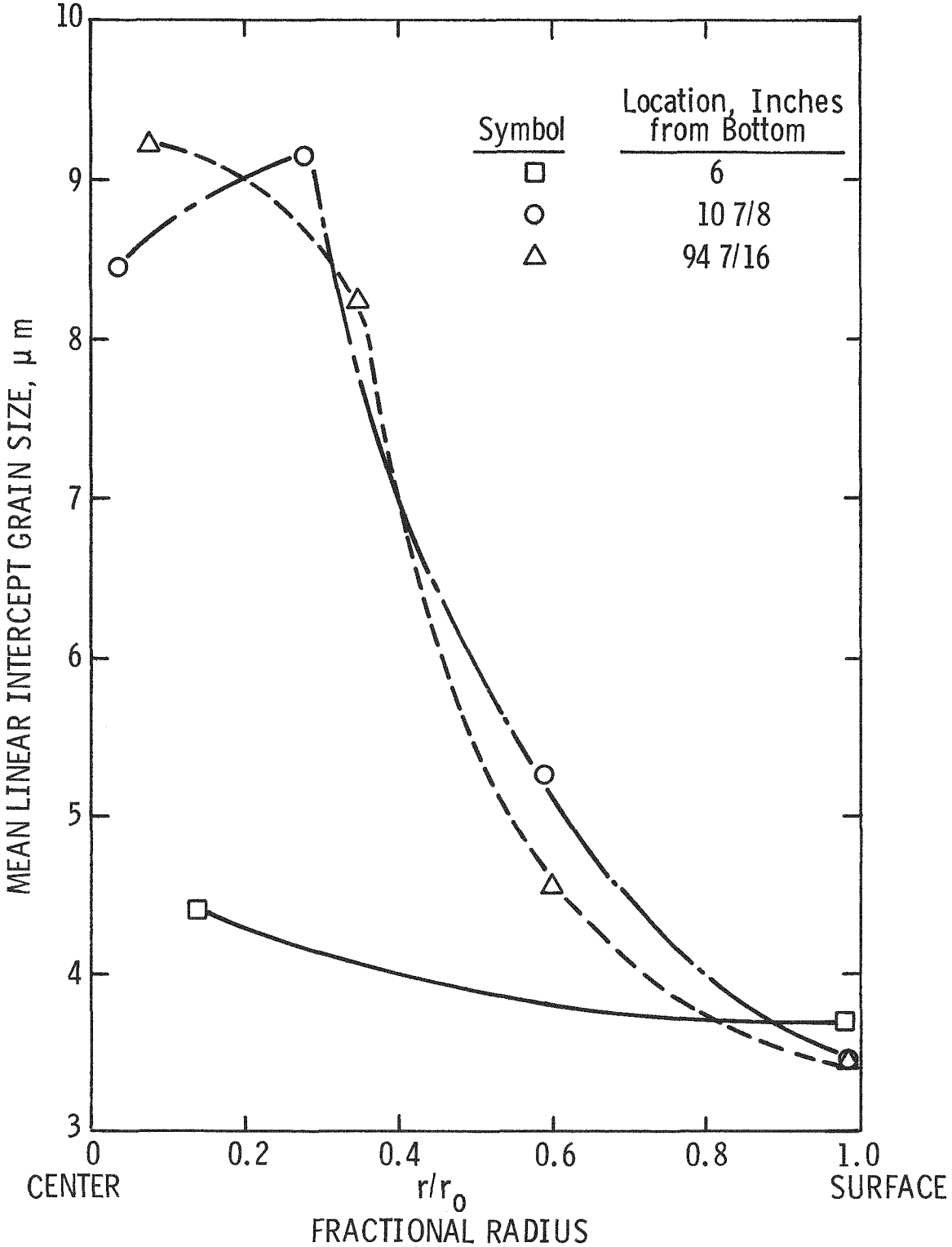

In some instances, e.g., at 10-7/8 in., the grain size at the pellet center was somewhat smaller than at off-center positions in spite of the higher temperature at the former location. One possible explanation for this effect is a higher grain growth retardation caused by fission product release in the pellet center compared with the off-center position. The temperature history of the fuel pellets at this axial location may be such that appreciable agglomeration of gaseous fission products took place at the grain boundaries near the center before the onset of grain growth. But, at the fractional radius (r/r_o) of 0.24 the temperature was lower than required for fission product pinning. On the other hand, in the peak power location of the rod, before the heat transfer reduction, the temperature at off-center locations ($\sim r/r_o$ = 0.2 to 0.4) might have been higher than required for fission product accumulation in the grain boundaries. Therefore, fission product pinning may have been equalized over the cross section, and the grain sizes observed are as expected from thermal profiles alone.

6.4.2 Mechanistic Estimation of Grain Growth Temperature

Estimates of fuel temperatures are often made from the observed microstructural changes in the fuel, such as equiaxed and columnar grain growth. The temperatures associated with the equiaxed and columnar grain growth boundaries are somewhat uncertain, and a range of temperature has been proposed in the literature [23-27]. The most frequently proposed temperature ranges are: 1300-1500°C for the onset of equiaxed grain growth and 1600-1800°C for the transition to columnar grain growth. In the Maine Yankee Core I fuel, no columnar grain growth was observed at any fuel cross section, and, therefore the following discussion is restricted to considerations of equiaxed grain growth.

Part of the differences in the reported grain growth temperatures originate from differences in fabrication methods, initial grain sizes and porosity characteristics of fuels. Based on a review of the available grain growth data of UO_2, Beyer and Hann [28] concluded that a temperature between 1400 and 1500°C is the most consistent recommended value for onset of equiaxed grain growth. Taking into account a best estimate columnar

grain growth temperature and a 300°C difference between columnar and equiaxed grain growth, they selected 1400°C as the temperature to initiate equiaxed grain growth.

However, the above recommendation does not include the effects of initial grain size and porosity characteristics of fuels. In general, the grain growth is faster the smaller the initial grain size [29]. It is also known that pores retard movement of grain boundaries. Thus, densifying fuel in which most of the sintering porosity is removed in the early period of irradiation is likely to show faster grain growth compared to a nondensifying fuel in which pores remain for longer period and continue to inhibit grain growth. Both of these factors suggest that the grain growth in the Maine Yankee fuel occurred at temperatures lower than 1400°C, as the fuel substantially densified and had a small initial grain size of approximately 3 μm.

Recently, Ainscough, et al. [25] have reported in- and out-of-reactor grain growth kinetics in UO_2. Their results show that in- and out-of-reactor, grain growth in UO_2 continues until a limiting grain size is achieved. The limiting grain size increases with increasing temperature, but, in-reactor, limiting grain size at the same temperature is lower than the corresponding value out-of-reactor due to grain boundary pinning by the fission products. The time for the limiting grain size to be reached in-reactor is significantly less than that for out-of-reactor. Taking into account the fission-product pinning effect, Ainscough, et al.[25] predicted limiting grain sizes of 5.4, 7.0, 9.9 and 14.3 μm for temperatures of 1200, 1300, 1400 and 1500°C, respectively. The above prediction is for a UO_2 fuel of 5 μm initial grain size and operated under a heat rating of 8 kw/ft. According to their prediction, a specimen having an initial grain size of 10 μm is not likely to show any observable grain growth below 1500°C. On the other hand, an initial grain size of 5 μm would show measurable grain growth at 1300°C. Their out-of-reactor data show that the minimum temperature of grain growth is higher than 1200°C, since no grain growth was observed after annealing for two years at 1200°C.

Based on the above considerations, a temperature of 1300°C has been selected as the best estimate temperature for the initiation of grain growth in Maine Yankee fuel. However, based on the criterion of also observing intergranular fission gas bubbles to identify the outer boundary of the equiaxed grain growth region, the boundary temperature is estimated to be 1350°C. In the peak heat rating position, the calculated (best estimate) pellet center temperature is approximately 230°C higher than the temperature at the outer boundary of the equiaxed region yielding an estimated pellet center temperature of 1580°C. This is lower than the best estimate columnar grain growth temperature of 1650°C measured by Christensen [27], and is, therefore, consistent with the observation of no columnar grain formation in the pellet center.

6.4.3 Temperature Analysis of Equiaxed Grain Growth

A temperature analysis of the equiaxed grain growth data was performed to obtain an alternate estimate of fuel temperatures associated with the grain growth boundary. This involved using the fuel rod dimensional information and the fission gas release data generated during the hot cell examination to estimate fuel-clad gaps and fuel temperatures at selected periods of the Maine Yankee Core I operation. The temperature calculational technique outlined in Reference 30, the "CE Fuel Evaluation Model Topical Report", was utilized to calculate the fuel rod temperature distributions for a given fuel-clad gap. The gas mixture conductivity curves, the fuel conductivity integral curves and the fuel-clad thermal expansion coefficients presented in the reference were also utilized in the temperature calculation. The fuel rod dimensional information, based on the post-irradiation pellet-clad gap data (Fig. 6-8), the fuel densification/swelling data (Section 6.3) and the cladding creepdown data (Section 6.6) provided the pellet-clad gap required in the analysis. The gas composition within the rods was established by the fission gas release data. The linear heat rating levels along these rods were obtained from the power history data discussed in Section 5.

Figure 6-8
POST IRRADIATION DIAMETRAL PELLET/CLAD GAP vs AXIAL LOCATION

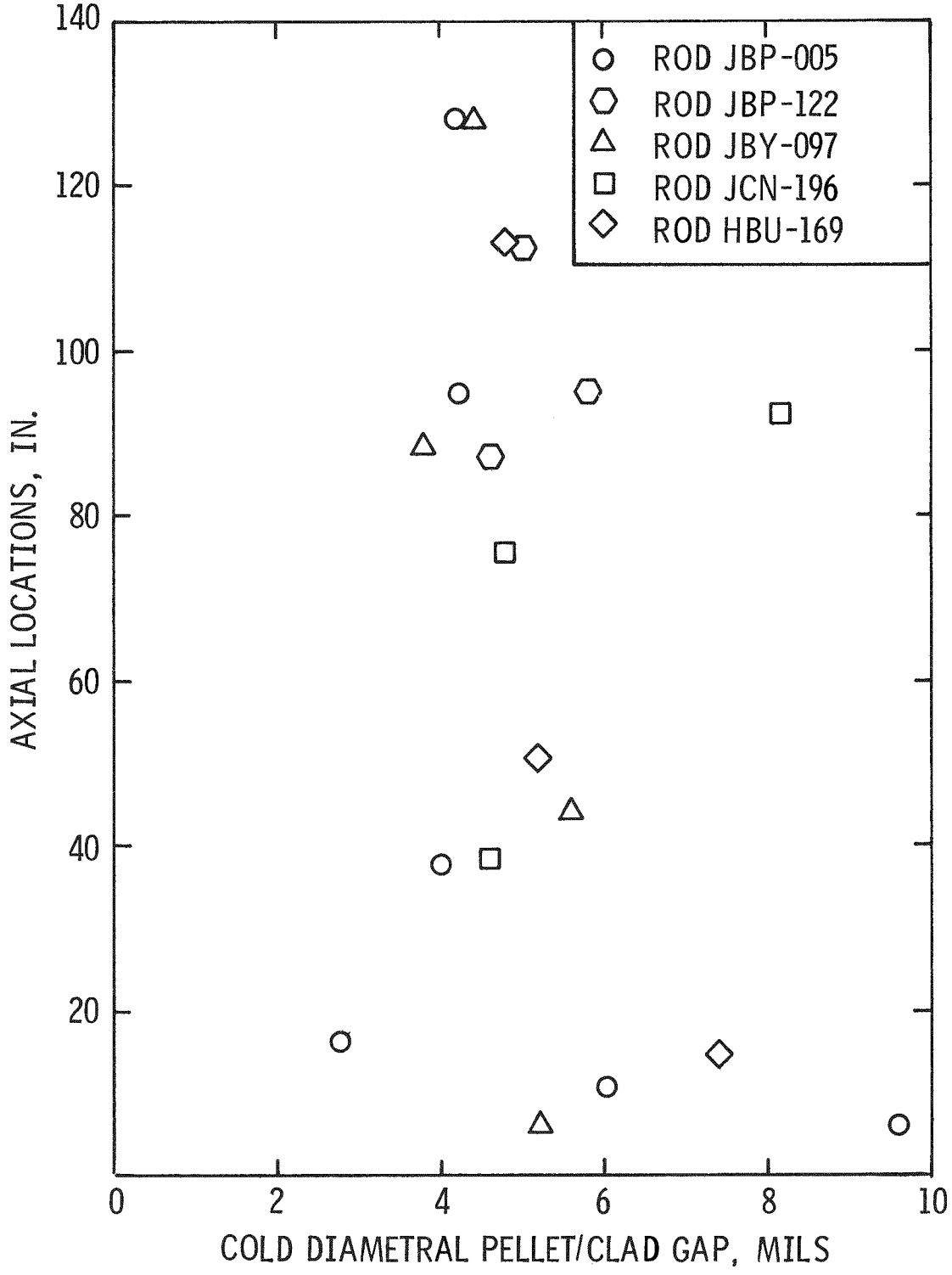

The temperature calculational technique outlined above produced temperature distributions which were then compared to the outer boundaries of the grain growth. This indicated that the best estimate temperature corresponding to the grain growth boundaries is 1350 $\pm$ 50°C, and is consistent with the result of the mechanistic evaluation.

A similar temperature estimate was also made for the high burnup rods with low gas release, showing that the fuel centerline temperature in the peak power region was about 1300°C, which is quite close to the minimum temperature for equiaxed grain growth.

It is also worth noting at this point that the axial profile of equiaxed grain growth shown in Fig. 4-78 indicates that low power pellets operated at temperatures close to, or higher than, that of high power pellets in rods with high gas release. Since the pellet-clad gaps in the low power regions are greater than those of the high power regions due to the nature of gap closure mechanisms, they contribute to lower gap conductances. These correspond to greater temperature differentials (ΔT) across the pellet-clad gap. In the high gas release rods (low gas conductivity), the increase in ΔT due to the larger pellet-clad gap was apparently sufficient to cause the observed high temperatures in the low power pellets.

In summary, the analysis of the grain growth data indicates that before heat transfer reduction, the peak power regions of the high burnup Maine Yankee Core I fuel rods operated near the temperature required to initiate equiaxed grain growth. The mechanistic evaluation and temperature analysis of the equiaxed grain growth data yield a "best estimate" equiaxed grain growth temperature of 1350°C.

6.5 Grain Growth Fission Gas Release Correlation

With the estimate of the equiaxed grain growth temperature, a quantitative correlation between gas release and equiaxed grain growth in the fuel can be formulated to benchmark performance codes.

All Maine Yankee Core I fuel rods without equiaxed grain growth had a fractional gas release of less than 1%. Fuel which experienced equiaxed grain growth showed gas releases from 11.3 to 15.3% with approximately 25% of the fuel volume restructured. With the assumption that the release fractions remained fairly constant after restructuring, the data would indicate that approximately 50% of the fission gas generated in the equiaxed grain growth region was released.

The combined observation of the Maine Yankee Core I equiaxed grain growth and fission gas release data yields the following correlation between temperature and gas release: Less than 1% of the gases generated are released at temperatures below 1350^{o}C and 50% are released at temperatures above 1350^{o}C (but below the columnar grain growth temperature). It should be noted that this correlation between gas release and temperature is interpreted from the grain growth and gas release data. Since grain growth temperature is affected by as-built grain sizes impurity levels and porosity, it may not apply to fuels with different grain growth behavior from that of Maine Yankee Core I.

6.6 Fuel Rod Dimensional Behavior

Profilometry data presented in Section 4.2 show that with notable exceptions high burnup rods with high and low gas release have essentially the same end-of-life cladding creepdown, ovality and ridging patterns. The data are analyzed below from the standpoint of fuel performance evaluation and the exceptions are explained in light of the fuel rod heat transfer reduction process.

6.6.1 Cladding Creepdown and Ovality

Representative cladding diameter profiles for a high gas release rod (JBP-005) and a low gas release rod (JBY-157) are shown in Fig. 6.9. The creepdown values are similar and reasonable for unpressurized fuel rods and the Maine Yankee Core I irradiation history. One of the test cases studied as part of the Phase II effort on the "Light Water Reactor Fuel Rod Modeling Code Evaluation" sponsored by EPRI is based on a high burnup Maine Yankee rod. Utilizing the recommended creep equation, cladding creepdown predictions in the Phase II report [31] compared reasonably well with the measured values.

The values of maximum ovality for each rod listed in Table 4-2 are plotted against the corresponding maximum cladding creepdown in Fig. 6-10. It can be seen that ovality increases sharply after diametral creepdown exceeds 1.5 mils; this correlation is also seen consistently in the profilometry traces of individual rods. The maximum cladding ovality observed was 16 mils. Considering the as-built pellet clad gap dimensions, the gap opening due to densification and the calculated gap closure due to fuel thermal expansion and relocation, this value approaches the limiting ovality imposed by pellet-clad contact at operating temperature.

As mentioned in Section 4.2, four of the high gas release rods, namely, JCN-182, JCN-199, JBP-027 and JCN-196 exhibited less creepdown and significantly lower maximum ovalities than the other four high gas release rods which had creepdown and ovalities similar to those of the low gas release rods. The axial cladding creepdown profile of these four low creepdown rods and that of a high burnup, low gas release rod are presented in Fig. 6-11. Based on the understanding of the fuel rod heat transfer reduction process and the subsequent fuel behavior, this cladding creepdown anomaly can be explained in the following manner:

Figure 6-9
REPRESENTATIVE POST-IRRADIATION
CLADDING DIAMETER PROFILES

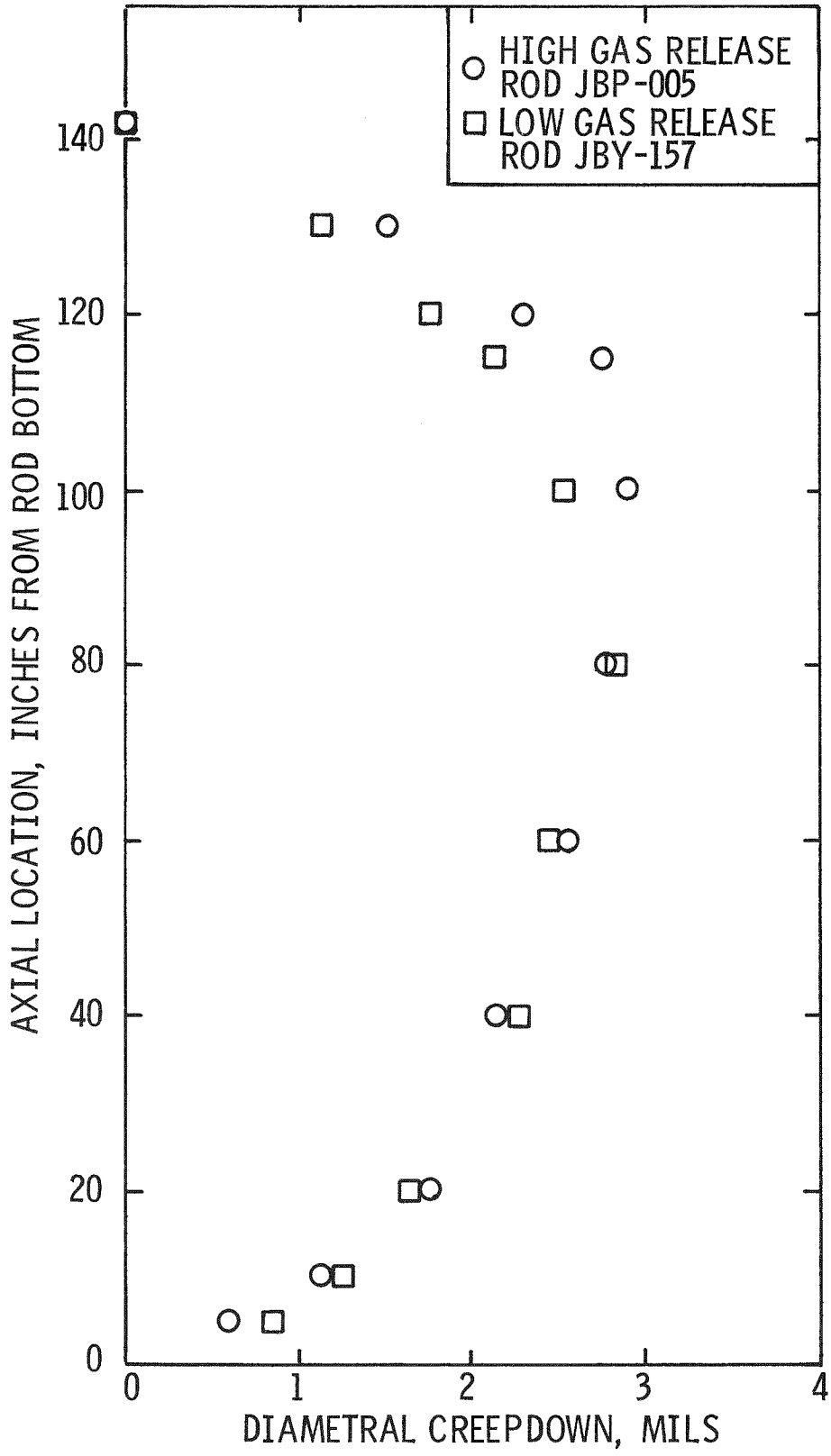

Figure 6-10
RELATIONSHIP BETWEEN CLADDING CREEPDOWN AND OVALITY

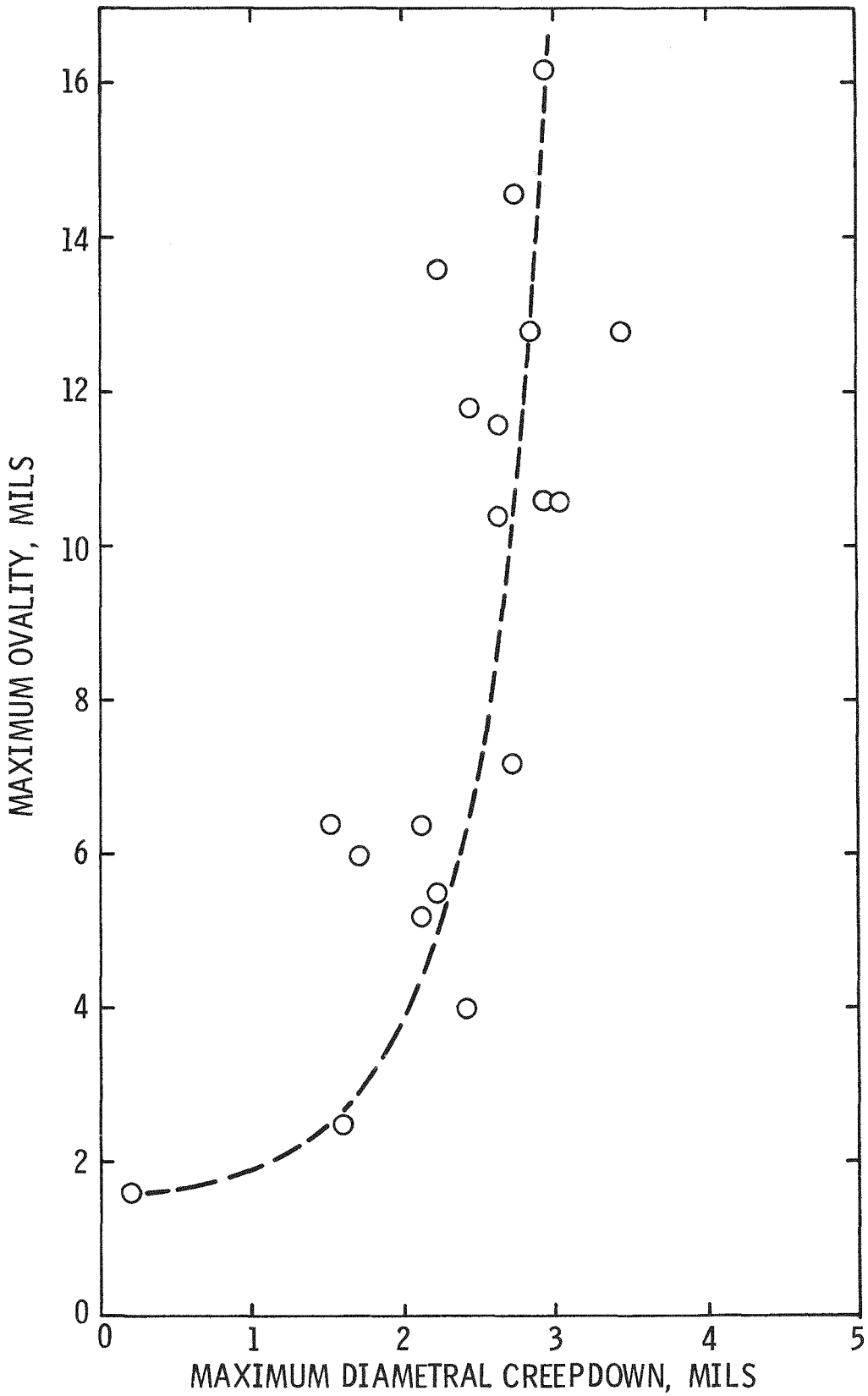

Figure 6-11
ANOMALOUS CLADDING CREEPDOWN OF FOUR HIGH GAS RELEASE RODS

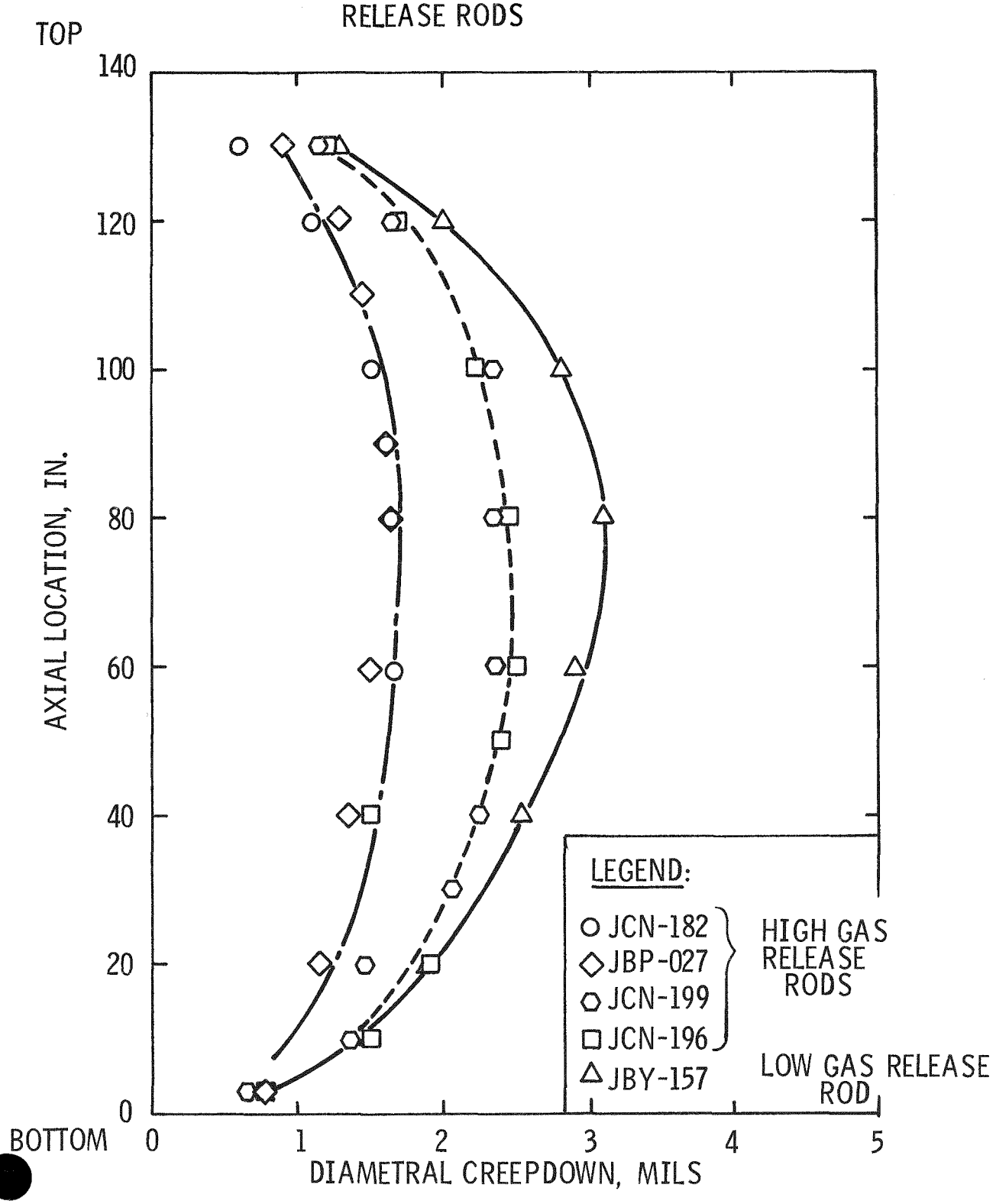

1. Once the rod experienced the reduction in heat transfer, the pellet-clad gap at power would be reduced by the added thermal expansion and fuel swelling. Therefore, fuel-clad contact at the pellet interfaces in rods with the heat transfer reduction would occur relatively early. The pellet-clad contact could arrest or slow cladding creepdown and cladding ovalization. The length of time during which such cladding creepdown support would continue (following the reduction of heat transfer) depends on the parameters which affect the pellet-clad gap at power, e.g., fuel temperature.

2. From the profiles shown in Fig. 6-11, it is concluded that Rods JCN-182 and JBP-027 probably underwent the heat transfer reduction (and/or cladding creepdown arrest) earlier, and Rods JCN-199 and JCN-196 followed later. This suggests the initiation of a relative late-in-life ($\sim$8,000 Mwd/MTU) fuel rod heat transfer reduction process for the latter case. This is not unreasonable, since the core power went to 95% of rating for the first time at 8,300 Mwd/MTU.

The above explanation suggests, then, that the four "normal" high gas release rods had either (1) experienced the reduction in heat transfer near the end of Maine Yankee Cycle-I operation or (2) had operated cooler after the reduction in heat transfer, and, therefore, possessed a larger pellet-clad gap (at power) which allowed continuous cladding creepdown. The first possibility is unlikely, since this requires the reduction in heat transfer to occur at a time when the core power was relatively low (80% of rating) and the gap relatively small. The second possibility would be supported if the four low creepdown rods had a power history that tended to provide less pellet-clad gap (following the reduction in heat transfer) than that of the four "normal" high gas release rods. Interestingly, all the low creepdown rods (all from the Batch B assemblies) are located on the north side of their respective assemblies, while the "normal" Batch B high gas release rods are on the south side (see Fig. 6-1 and 6-2). An examination of the relative rod power histories indicates that as burnup proceeded, those rods with low creepdown generally maintained their relative power or underwent a smaller reduction in power than did the "normal" high gas release rods.

The above analysis shows that the observed less than expected cladding creepdown of four of the eight high gas release rods could be related to the fuel rod heat transfer reduction phenomenon. The temperature increase following reduction of heat transfer was sustained for some time, decreasing the pellet-clad gap (at power) significantly, thus promoting pellet-clad interaction which slowed or arrested cladding creepdown. However, in the case of the four "normal" high gas release rods, high fuel temperatures were not sustained and cladding creepdown arrest did not occur for as extended a period of time.

6.6.2 Ridging

Cladding ridge heights on the order of 0.1 mil (maximum of 0.25 mil) were observed in the spiral profilometry traces of high power regions of both higher and low gas release rods. Also, pronounced ridges up to 0.4 mil were seen in linear profilometry traces at pellet interfaces from higher gas release rods. (As no linear profilometry traces were made on the low gas release rods, it is not known whether these larger ridges are restricted only to the higher gas release rods.)

The linear profilometry traces obtained for the higher gas release rods indicate that ridges were generally localized and not continuous around the circumference, and they appeared in both the minor and the major axes of these oval rods at pellet interfaces (though mostly in the minor axis). Also, the ovality in these regions is variable. This suggests that the fuel tended to relocate and expand outward to meet the oval clad and possessed an ovality of its own. Diameter measurements from the photomacrographs of the fuel cross sections are consistent with this observation.

Cladding crack characteristics described in Table 4-14 show that the cracks were found in both the major and minor axes of the oval tubes and were located at pellet interfaces near radial fuel cracks, which are generally recognized to be points of maximum stress. In one case, JBY-097, the cladding crack was associated with a prominent ridge, 0.4 mil high, but the ridge was at the minor axis of the oval, while the crack was at the major axis. The presence of the ridge is indicative of strong fuel-clad contact, and it is not surprising that a cladding crack was found in the same transverse plane.

6.7 Fuel Rod Heat Transfer Reduction, Pellet-Clad Interaction and Fuel Rod Perforation

At this point in the data analysis, it is reasonable to inquire whether there is a causal relationship between fuel rod heat transfer reduction, and a PCI fuel rod perforation mechanism. Any such connection should be explored by considering two kinds of effects which could result from the fuel rod heat transfer reduction: (1) prompt effects, e.g., PCI due to immediate large temperature increases (temperature ramps),and (2) delayed effects, e.g., enhanced PCI at subsequent power changes due to fuel-clad bonding.

6.7.1 Fuel Rod Heat Transfer Reduction and PCI

The pellet population within a rod represents many combinations of power, initial pellet density and gap size. It is, therefore, reasonable to expect variations in gap size along a given rod. Other factors, such as cladding ovalization and pellet non-concentricity during operation, add to the variety of conditions available at the start of the heat transfer reduction process. The region initiating the temperature increase could be one of large gap, while another region with a different pellet-clad configuration could undergo a prompt temperature rise to directly produce higher stresses in the cladding.

As observed in the hot cell examination, the reduction in heat transfer resulted in cesium and iodine redistribution to the fuel-clad interface. In time, the presence of cesium causes fuel-clad bonding at pellet interfaces and local fuel volume increases in the cesium-rich reaction zone. Therefore, another consequence of the heat transfer reduction is that in subsequent power changes enhanced PCI is possible through localized cladding stress due to the fuel-clad bonding and the local fuel volume increase. In both the prompt and the delayed mechanisms the presence of iodine (and possibly cesium) at pellet interfaces could contribute to stress corrosion cracking.

6.7.2 Fuel Rod Heat Transfer Reduction and Fuel Rod Perforation

The above analysis shows that the reduction in heat transfer could have induced and enhanced PCI through a temperature ramp and/or fission product redistribution. Consequently, it could be the underlying mechanism responsible for the Maine Yankee Core I rod perforations. To explore this, the threshold power for high fission gas release and rod perforation are compared.

In the analysis of the fission gas release data and the heat transfer reduction process, it was found that there exists a threshold power at which the reduction of heat transfer becomes operative.

As shown in Section 6.2, the threshold in terms of the relative life-averaged rod power for nominal cladding diameter and nominal fuel density is about 1.27; however, it could be as low as 1.20 for high cladding diameter and low fuel density (Rod HBU-169). Therefore, if the heat transfer reduction process is indeed responsible for the majority of rod perforations, these heat transfer reduction threshold powers should be comparable to those of rod perforation.

Evidence which supports such a concept can be found in Table 6-2 which presents the life-averaged rod power factors of the perforated rods whose identity was confirmed by bundle disassembly at poolside. It is seen that except for the Batch C rod, the lowest power factor for perforated rods is 1.20, and the majority of the rod power factors are greater than 1.26.

Summarizing, this analysis shows that PCI following the onset of the heat transfer reduction could stem from two factors: (1) The temperature ramp and (2) fuel-clad bonding. The attendant iodine and cesium release could contribute to stress corrosion cracking. Therefore, the heat transfer reduction process is likely a key factor in the causation chain responsible for Maine Yankee Core I rod perforations. This conclusion is supported by the comparable threshold powers of fuel rod heat transfer reduction and rod perforation.

Table 6-2

Maine Yankee Perforated Rod Powers

Assembly Number	Rod Serial Number	Life-Averaged Relative Power *	End-of-Life Rod Average Burnup (Mwd/MTU
B-042	JBP-015	1.31	13,559
	JBP-016	1.32	13,667
	JBP-077	1.27	13,155
	JBP-048	1.28	13,293
	JBP-044	1.24	12,896
	JBP-032	1.23	12,786
	JBP-021	1.28	13,271
	JBP-033	1.28	13,229
	JBP-003	1.32	13,629
	JBP-043	1.28	13,270
	JBP-084	1.31	13,526
B-069	JCN-151	1.23	12,744
	JBY-163	1.27	13,152
	JBY-013	1.25	13,005
	JBY-145	1.31	13,535
A-047	HBV-001	1.20	12,453
C-231	KCA-109	.93	9,661

* Relative to core average power (core average burnup-10,368 Mwd/MTU).

6.8 Power Dependency of Cladding Blisters and Incipient Cracks

Based on a PCI mechanism, one would expect a power dependency in the location where initial cladding perforation occurred. Data on iodine activities, power profiles, blister patterns and incipient cracks were examined with this in view.

The coolant iodine activity history gives an indication of the time at which rod perforation occurred and the relative magnitude of the number of perforated rods involved. Based on the Maine Yankee iodine activity history (see Fig. 1-1), a majority of the perforations occurred within the burnup interval of 6,700 Mwd/MTU and 8,300 Mwd/MTU.

The pattern of blisters in perforated rods is presented in Fig. 6-12. Though some blisters were probably caused by secondary hydriding, the blister locations still give an indication of the general area where the initial cladding perforation occurred. This is because through-wall cladding cracks are transformed into hydride blisters by secondary hydriding. Fig. 6-12 shows that most of the blisters are located in the region 70 to 110 in. from the bottom.

Thus, the combined observation of iodine activity history and perforated rod blister patterns suggest that initial cladding perforations in the 6700 to 8300 Mwd/MTU burnup period tended to locate in the 70 to 110 in. region. Therefore, if there is a power dependence in the perforation locations, peak power locations in the 6700 to 8300 Mwd/MTU burnup period should agree closely with the locations of the blisters. From the typical axial power profile for the 6700 to 8300 burnup period presented in Fig. 6-12, it can be seen that the blister locations, indeed, tend to coincide with the peak power locations.

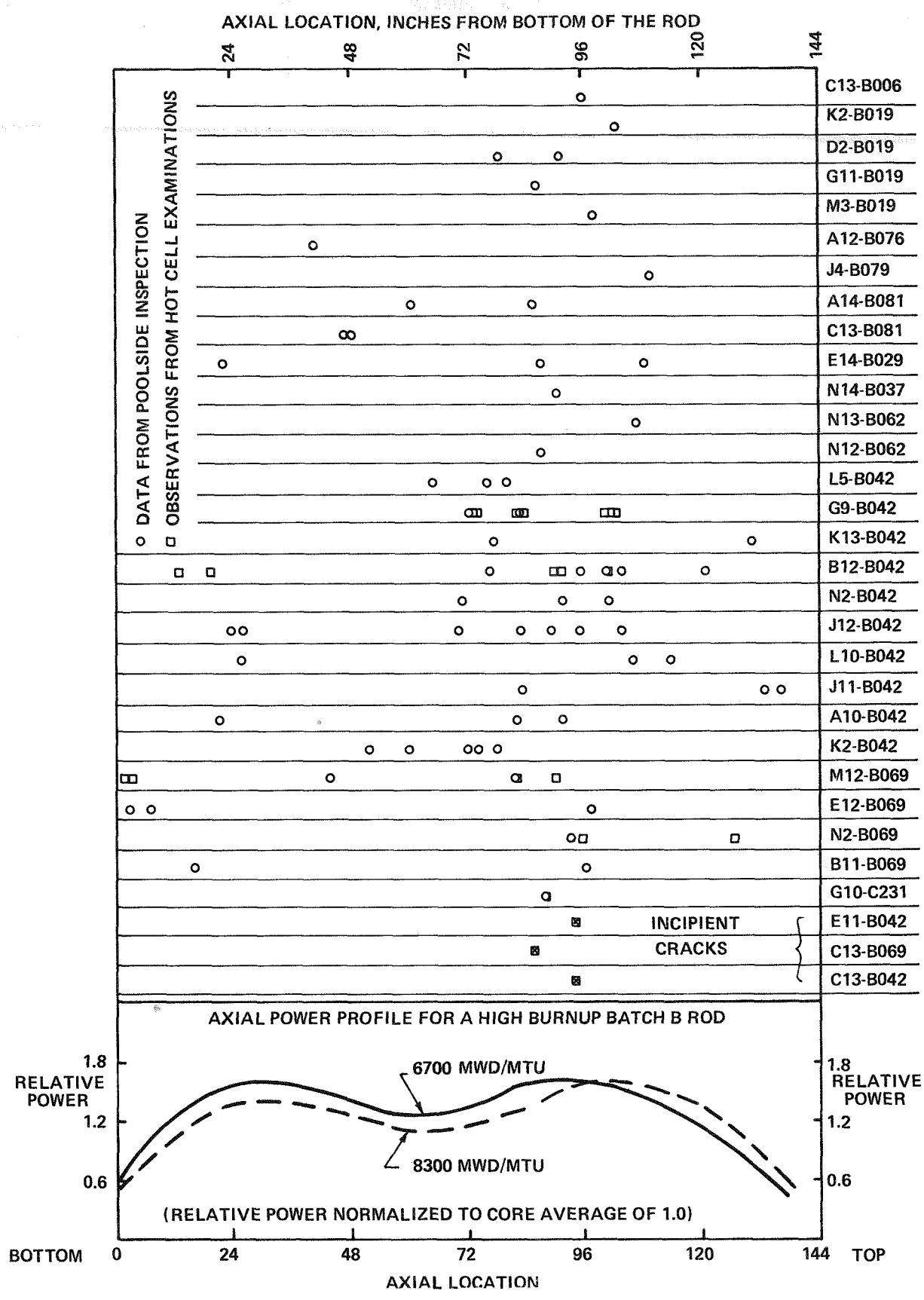

Figure 6-12 AXIAL LOCATION OF ALL BLISTERS OBSERVED DURING MAINE YANKEE POOLSIDE INSPECTION AND HOT CELL EXAMINATION

Three incipient cracks were observed in the hot cell examinations. All three were found in the high gas release rods and exhibited characteristics consistent with iodine-assisted stress corrosion cracking as detailed in Section 4.8. The axial locations of these incipient cracks are located in the region between 88 in. and 94 in. Thus, the location of incipient cracks fall within the peak power region which existed in the 6,700 to 8,300 Mwd/MTU period.

In summary, the patterns of blisters, perforated rods, the locations of incipient cracks, and the history of iodine activities are consistent with a power dependent mechanism causing the initial clad perforations in the Maine Yankee Core I fuel rods.

CAUSE(S) OF INITIAL CLAD PERFORATIONS

During the course of the Maine Yankee Core I fuel examination program, three prime candidates for the cause of initial clad perforation were considered:

1. Direct cracking of cladding by PCI involving fission product (cesium and/or iodine) assisted stress corrosion.

2. Primary hydriding involving an internal source of hydrogen such as moisture in the UO_2 pellets.

3. Cladding predamage due to localized hydriding followed by perforation as a result of stresses induced by PCI.

The following sections describe the typical phenomenology and characteristic patterns associated with these mechanisms and discusses whether the pertinent evidence gathered in this program is consistent with these descriptions.

7.1 Pellet-Cladding Interaction (Stress Corrosion)

As described in a report of BWR fuel experience,[32] clad perforations caused by PCI characteristically occur after a burnup of 5,000 Mwd/MTU. The defects are evident as axial cladding cracks or blisters which may form subsequent to perforation by fine cracks. The location of perforated assemblies and rods is strongly correlated with high power operation, and the cladding defects tend to be located in the peak power regions. A review by Robertson [33] of defect mechanisms in Zircaloy-clad UO_2 fuel indicates that the cladding cracks are initiated at those locations on the inside surface of the cladding where pellet interfaces and radial cracks in the pellets concentrate stresses. These stresses can be aggravated by pellet chips and other discontinuities at the fuel-clad interfaces. Clad perforation, as indicated by activity release to the coolant, usually occurs within hours after a power ramp.

PCI has been cited as a major cause of initial clad perforations in BWRs [32] and Canadian reactors [33]. Environmentally-assisted stress corrosion has not been explicitly involved in the BWR case; for example the PCI-caused perforations in BWRs up to the early 1970's are attributed, in part, to a low strain-to-fracture capability of the cladding before a higher temperature annealing heat treatment was instituted in fabrication. The Canadians [33], on the other hand, appear convinced by in-pile and out-of-pile evidence that most of their power ramp-related perforations involve iodine-assisted stress corrosion cracking. As noted by Robertson [33], where there is sufficient iodine available, clad cracking by stress corrosion is likely to occur at a lower stress than that required for cracking by a purely mechanical influence. Moreover, perforating cracks due to purely mechanical interaction require relatively large and rapid power increases.

In Maine Yankee Core I, the irradiation history, the strong correlation of perforated rods with high power operation, and the hot cell examination evidence (especially the incipient crack characteristics) are consistent with a PCI perforation mechanism directly causing cladding cracks with volatile fission product stress corrosion assistance. Although no primary axial cladding splits were observed during the poolside or hot cell examination of perforated rods, fine incipient cracks penetrating up to two-thirds of the wall were found in three sound, high power rods at pellet interfaces. As noted earlier, the perforated rod blisters tend to be located in the high power regions and are sufficiently large to mask cracks such as those observed in the sound rods. Garlick [34] has presented evidence that radial cracks are preferential sites for the initiation of secondary hydriding attack once the cladding is breached and water enters the rod. Thus, some of the blisters in the high power regions could have been originally the sites of fully or partially penetrating cracks.

While the Maine Yankee power history and coolant iodine activity data appear to be consistent with the normal pattern of PCI-caused clad perforations, the two power escalations leading to most of the iodine activity releases involved relatively small power changes (less than 1 kw/ft) over long time intervals (2 days) to relatively modest final heat rating levels (less than 9 kw/ft) as described in Section 5. Such conditions alone are not believed sufficient to cause the classical PCI clad perforation.

Since all three rods which exhibited cladding cracks also displayed high gas releases resulting from temperature increases following a heat transfer reduction phenomenon, it is considered likely that these cracks and most of the Maine Yankee Core I initial clad perforations were caused by a PCI mechanism. All such rods also exhibited evidence of cesium and iodine redistribution. It is possible, therefore, that relatively large iodine and cesium concentrations coupled with high local cladding stresses caused by a large fuel temperature increase, rather than a large power increase, resulted in PCI stress corrosion cracking in the three rods. In effect, then, though the actual power changes which triggered the heat transfer reduction process were small, the temperature change experienced by the fuel was equivalent to that normally associated with a larger power change. (The fuel material adhering to the cladding at the pellet interfaces of these rods may also have played a role in aggravating the local stress concentrations resulting from PCI.) Of the mechanisms considered, this is believed to be the most likely to have caused most of the initial clad perforations observed in Maine Yankee Core I.

The predominant occurrence of perforated rods in Batch B assemblies may be explained by the fact that the susceptibility for heat transfer reduction was greatest when the fuel had reached maximum densification (about midway through Core I operation). At the same time, the fuel had to be operating at sufficiently high power to trigger the heat transfer reduction. As discussed in Section 5, both Batches A and C fuel operated at a significantly lower power than Batch B during this time period. Thus, Batch B fuel was more likely to meet the prerequisites for the perforation mechanism.

Power history data indicate that no Batch A rod ran as high in power as the lowest power perforated Batch B rod in Assemblies B-042 and B-069 during the average core burnup exposure period from 5,000 to 8,000 Mwd/MTU, when the major iodine activity releases occurred. Also, during this period less than 1% of the Batch C rods operated at or above such a threshold relative power for perforation, while in the two Batch B assemblies 38% of the rods operated above this power. This relative power distribution pattern is consistent with and supports the conclusion that the heat transfer reduction phenomenon was involved in this most likely perforation mechanism.

7.2 Primary Hydriding

Clad perforations caused by excessive hydrogeneous impurity levels inside the fuel rod usually occur at low burnup, mostly before 5,000 Mwd/MTU. The cladding is penetrated from the inside surface by a localized hydride nodule (the so-called "sunburst") or blister which may crack or form a crater. The hydrogen migrates outwards down the temperature gradient and spreads out at the cladding external surface. BWR experience [32,35] indicates that when there is hydrogen (moisture) contamination, the location of perforated assemblies and rods do not strongly correlate with operating power and are randomly distributed. The blisters, however, tend to be located in the high power regions of the affected rods. This picture is complicated by secondary hydriding caused by water ingress into perforated rods which produces a more random distribution of blisters along the length of the rods.

If in sound rods a limited localized hydriding attack had occurred, exhaustion of the hydrogen supply and the migration of hydrogen to the external surface could leave major internal cladding defects in the form of cracks and laminations with little hydride precipitate remaining. Such remnants would go undetected unless signaled by an eddy current test and examined metallographically.

Joon [36] has reported that the minimum moisture level in the fuel required to cause clad perforation by primary hydriding is 2 mg H_2O/cm^3 of cold void volume in the rod based on a survey of perforated fuel in the Halden BWR. On the other hand, out-of-pile tests by Garzarolli, et al., [35] indicate that as low as 1 mg H_2O/cm^3 will support a localized hydriding attack (not necessarily directly causing perforations). These levels are equivalent, respectively to 26 ppm and 13 ppm on a UO_2 basis in the Maine Yankee fuel design.

In contrast with this pattern, the Maine Yankee coolant iodine activities (Fig. 1-1) indicate that virtually all the initial clad perforations occurred after a core average burnup of 5,000 Mwd/MTU. Although the blisters tend to be located in the high power regions of the perforated rods (see Fig. 6-12) the perforated assemblies and rods are strongly correlated with the highest power operation. Furthermore, the fuel moisture levels from manufacturing inspection and archive examination [1] are well below the Joon threshold for clad perforation. For example, the core-wide average pellet moisture content was 6.8 ppm, while the level among Batch B pellets averaged 5.2 ppm.

Based on hot cell examination, only one rod can be cited as probably having been perforated by primary hydriding. This is the sole perforated Batch C Rod, KCA-109. Its only cladding breach is a hydride blister with the characteristic hydride distribution at the external surface. The virtual absence of cladding creepdown of this rod also indicates that perforation occurred early-in-life.

Although the sound rods were eddy current tested by systems capable of detecting major internal surface cladding defects, no remnant cracks attributable to localized hydriding were found in the hot cell examination.

7.3 Cladding Predamage/Pellet Cladding Interaction

A partially-penetrating hydride blister may introduce sufficient cladding damage to lead to perforation later as a result of stresses imposed by PCI. This mechanism is suggested as a possible cause of initial clad perforation by Proebstle [37] et al. and Pickman [38] where evidence indicates: (1) The presence of moderate moisture concentrations (instead of gross contamination) in the fuel, (2) a correlation of perforated rods with high power operation, and (3) the detection of perforations shortly after a power ramp. In this case, the perforations would not occur early-in-life but would be expected at higher burnups, say, greater than 5,000 Mwd/MTU.

Niehoff and VonJan [39] attribute the perforated rods observed in the KWL*and KRB*first cores to such a mechanism. The rod perforation rates in the first and succeeding cycles were nearly constant and were correlated with high operating rod power. The fact that leaking fuel was essentially eliminated in subsequent reloads when excessive moisture contents were prevented by changes in manufacturing procedures is offered as strong evidence that, indeed, the clad perforation mechanism involved a localized hydriding predamage phenomenon.

The power-dependent pattern of perforated rods in Maine Yankee Core I appears on the surface to be consistent with this two-stage mechanism. However, as pointed out in the above discussion of the direct primary hydride perforation mechanism, the eddy current tests and extensive destructive examination did not reveal any internal surface cladding defect which could be related to a partially penetrating localized hydriding attack.

Thus, it is difficult to reconcile all of the evidence gathered in this investigation with primary hydriding, either directly penetrating the cladding or contributing to a later cladding breach as a result of PCI.

---

* German BWRs: KWL = Lingen, KRB = Gundremingen

7.4 Events Leading to Clad Perforations

By way of summarizing the evaluation of the evidence obtained from the overall program and the results of the data analysis, the following sequence of events is believed to have led to the predominant Maine Yankee Core I fuel rod perforation pattern. Some of the phenomena presented are recognized as conjectural, e.g., the complex internal fuel rod chemical processes and species associated with the observed fission product redistribution; nevertheless, they are listed to lend coherence to the sequence of events.

1. Approximately midway during the Core I operation (after an average core burnup of 5,000 Mwd/MTU) most of the UO_2 pellets in the higher power Batch B rods completed their densification.

2. The small cladding creepdown which had occurred up to this point could not compensate for densification. This led to an increase in fuel-clad gap and therefore, a decrease in the gap conductance. Thus, the fuel temperature tended to increase for a given power level.

3. In some of the higher power Batch B rods, those with greater UO_2 densification propensity and larger as-fabricated fuel-clad gaps, the temperature of the fuel (not necessarily in the peak power location) was just below that required to initiate UO_2 equiaxed grain growth ($\sim 1350^{o}C$).

4. During this critical period, a small power increase or a small reduction in gap conductance was sufficient to increase the fuel temperature and initiate equiaxed grain growth. This resulted in a local release of a fraction of the fission gas inventory in the grain growth region leading to a reduction in the helium fill gas conductivity.

5. The temperature of the fuel, thus, was increased by the reduced heat transfer and the grain growth process spread radially and axially to affect a larger volume of the fuel resulting in more gas release and additional reduction in fuel rod heat transfer.

6. The release of fission gases was accompanied by the release of other volatile fission products, including cesium and iodine, from the grain growth region as gaseous species. The iodine was probably chemically combined with cesium and released as the iodide. Most of the cesium in excess of that required for the iodine may have been released as compounds with oxygen and uranium, which are volatile at fuel temperatures.

7. The cesium compounds condensed and formed small discrete deposits on the cladding surface. In time, these cesium-rich deposits promoted a complex reaction involving both the UO_2 and the Zircaloy cladding resulting in fuel-clad bonding at the deposit location.

8. Cesium iodide on the cladding internal surface was radiolytically and thermally decomposed providing a source of free iodine for a possible stress corrosion attack of the Zircaloy cladding.

9. The heat transfer reduction process resulted in PCI in the high power Batch B rods at or near the peak power position by means of one or both of the following mechanisms. (The evidence does not permit a distinction between the two.):

a. Heat transfer reduction was triggered by the first escalations to 88% and 95% core power, respectively, and PCI leading to clad perforation promptly followed without any contribution from fuel-clad bonding.

b. Heat transfer reduction occurred earlier,and PCI leading to clad perforation occurred later, during the power escalations, and was intensified by fuel-clad bonding.

In both cases, the fuel temperature increase caused by the heat transfer reduction was a major contributor to PCI. Also, redistributed fission products, such as iodine and cesium, were available in both cases to participate in an SCC process.

10. In some of these high power Batch B rods the local stress concentrations at pellet interfaces (with or without enhancement from fuel-clad bonding) was sufficient to cause a small axial crack (~3/16 in. long) by SCC (most probably iodine-assisted) normal to and originating at the cladding internal surface.

11. In rods where the crack fully penetrated the cladding, water entered and proceeded via a secondary hydriding mechanism to cause the blisters and bulges observed on the perforated rods. Even the initial SCC crack probably hydrided, thus obscuring evidence of the primary perforation mechanism.

12. In some rods, the initial SCC cracks only partially penetrated the cladding (i.e., the cracks were incipient). If such cracks had occurred before the first escalation to 95%, they might very well have propagated through the cladding on going to this higher power due to higher PCI cladding stresses and/or further supply of aggressive fission products to the crack tip. On the other hand, incipient SCC cracks formed during this power escalation probably survived the remainder of Core I operation because the core power was restricted to the 80% level to end-of-cycle.

From the above sequence, it is apparent that fuel rod heat transfer reduction was the underlying mechanism in the overall chain of events leading to the observed perforated fuel rod pattern in Core I. The major factor tending to promote heat transfer reduction was the propensity for fuel densification. Low helium pressure in the rods resulted in little dilution of the released fission gases. A recurrence of the Maine Yankee Core I fuel experience is highly unlikely in view of current PWR fuel designs incorporating nondensifying fuel in pressurized rods.

8.0 REFERENCES

1. N. Fuhrman and V. Pasupathi, "Evaluation of Fuel Rod Performance in Maine Yankee Core I", Report on Work Performed Up to July 1975, CENPD-221, December 1975.

2. M. L. Picklesimer, "Anodizing for Controlled Microstructure Contrast by Color", The Microscope, Vol. 15, Fourth Quarter (October 1967) pp. 472-479.

3. P. D. Kaufman, Paul Danielson and E. F. Baroch, "Improved Metallography of Zirconium Alloys", Zirconium in Nuclear Applications, ASTM STP 551, ASTM, 1974, pp. 52-62.

4. A. S. Bain, et al., "Fuel Designs to Eliminate Defects on Power Increases", Paper No. 56, British Nuclear Energy Society International Conference on Nuclear Fuel Performance, London, October 1973.

5. S. B. Dalgaard, "Long Term Corrosion and Hydriding of Zircaloy-4 Fuel Clad in Commercial Pressurized Water Reactors With Forced Convective Heat Transfer", Paper presented at the Electrochemical Society Meeting, May 2-7, 1976, Washington, D. C.

6. J. B. Melehan, "Yankee Core Evaluation Program Final Report" WCAP-3017-6094, January 1971.

7. W. W. Kirk, "Appearance of Hydrides in Corrosion Tested Zircaloy-2", WAPD-ZH-20, 1959.

8. L. A. Hartman and R. E. Westerman, "Quantitative Metallography of Hydride Phase in Zircaloy-2 Process Tubes", HW-74949, November 1963.

9. J. C. Wood, B. A. Syrett, I. M. London and J. Baird, "Environmentally Induced Fracture of Zircaloy by Iodine and Cesium" The Effects of Strain Rate, Localized Stresses and Temperature", Journal of Nuclear Materials, Vol. 57 (1975) 155-179.

10. A. Garlick, "Fracture of Zircaloy Cladding Under Simulated Power Ramp Conditions", Journal of Nuclear Materials, Vol. 49 (1973/74) 209-224.

11. B. Cox and J. C. Wood, "Iodine Induced Cracking of Zircaloy Fuel Cladding--A Review", Corrosion Problems in Energy Conversion and Generation - Symposium of Electrochemical Society, October 1974.

12. L. A. Niemark, J. D. B. Lambert, W. F. Murphy and C. W. Renfro, "Performance of Mixed-Oxide Fuel Elements to 11 at % Burnup", Nuclear Technology,Vol.16, October 1972, pp. 75-88.

13. R. A. Karnesky, R. D. Leggett, S. A. Chastain and J. W. Weber, "Cesium Migration in Mixed-Oxide Fuel Pins", ANS Transactions, Vol. 22, 1975 pp. 229-231.

14. S. Langer, N. L. Baldwin, J. R. Lindgren, R. V. Strain, G. Hayner, R. Bono, L. Neimark, "Volatile Fission Product Migration and Plateout in GCFR Rod Irradiations", ANS Transactions, Vol. 15, 1972, p. 850.

15. J. Bazin, J. Jouan and N. Vignesoult, "Oxide-Cladding Reactions and Their Effect on Water Reactor Fuel Column Behavior, "ANS Transactions, Vol. 20, 1975, p. 235.

16. I. Johnson and C. E. Johnson, "Cesium Interaction with Irradiated Oxide Fuel Pins", ANS Transactions, Vol. 17, 1973, p. 194.

17. J. D. B. Lambert, L. A. Neimark, R. V. Strain, "A Failure Mechanism in Mixed-Oxide Fuel Elements", ANS Transactions, Vol. 17, 1973, p. 193.

18. M. G. Adamson and E. A. Aitken, "Chemical State and Thermomigration Behavior of Fission Product Cesium in Oxide Fuel Systems, ANS Transactions, Vol. 17, 1973, p. 195.

19. D. W. Brite, et al., EEI/EPRI Fuel Densification Project--Final Report, EPRI-131, March 1975.

20. S. D. Harkness, S. R. Pati, M. G. Andrews and W. P. Chernock, "In-Pile Densification of UO_2", Submitted for the Proceedings of the European Nuclear Conference, Paris, April 21-25, 1975.

21. A. Hanevik, P. Arneson and K. D. Knudsen, "In-Reactor Measurement of Fuel Stack Shortening", Paper No. 89, British Nuclear Energy Society, International Conference on Nuclear Fuel Performance October 197

22. D. A. Collins, R. Hargreaves, "Performance-Limiting Phenomena in Irradiated UO_2,"Paper No. 50, British Nuclear Energy Society International Conference on Nuclear Fuel Performance, London, October 1973.

23. J. P. Stora and P. Chenebault, Programme Cyrane-Mesure de l'integrate de conductibile thermique d' UO_2 fritta jusqua 2300^{o}C--Evolution des gaz de fission a puissance constante, CEA-R-3618 (1968).

24. Jean-Claude Janner. et al., "Irradiation of Uranium Dioxide in a Resistant Cladding-Effects of Initial Diametral Gap on Overall Behavior", CEA-R-3358 (October 1967).

25. J. B. Ainscough, et al., "Isothermal Grain Growth Kinetics in Sintered UO_2 Pellets', Journal of Nuclear Materials, Vol. 49, p. 117-128 (1973/74).

26. R. N. Duncan, "Rabbit Capsule Irradiation of UO_2" CVNA-142 (June 1962).

27. J. A. Christensen, "Columnar Grain Growth in Oxide Fuels", ANS Transactions, Vol. 15, 1972, p. 214.

28. C. E. Beyer and C. R. Hann, "Prediction of Fission Gas Release from UO_2 Fuel", BNWL-1875 (November 1974).

29. J. E. Burke, Transactions AIME Vol. 180, p. 73 (1949).

30. Combustion Engineering Report, "C-E Fuel Evaluation Model Topical Report", CENPD-139, Rev. 01, July 1, 1974.

31. M. G. Andrews, et al., "Light Water Reactor Fuel Rod Modeling Code Evaluation, Phase II Topical Report", CENPD-218, April 1976.

32. H. E. Williamson and R. A. Proebstle, "Results with BWR Fuel Improvements", Joint ANS/CNA Topical Meeting on Commercial Fuel Technology Today, Toronto, Canada, April 28-30, 1975.

33. J. A. L. Robertson, "Nuclear Fuel Failures, Their Causes and Remedies", Joint ANS/CNA Topical Meeting on Commercial Nuclear Fuel Technology Today, Toronto, Canada, April 28-30, 1975.

34. A. Garlick, "Stress Corrosion Cracking of Zirconium Alloys in Iodine Vapor", Paper #3 in Effects of Environment on Material Properties in Nuclear Systems, Proceedings of the International Conference on Corrosion organized by the British Nuclear Society, July 1-2, 1971, London.

35. F. Garzarolli, et al., "BWR Fuel Experience: 2, Correlation of Fuel Performance to Manufacturing Variables", Paper No. 71, British Nuclear Energy Society, International Conference on Nuclear Fuel Performance, London, October 1973.

36. K. Joon, "Primary Hydride Failure of Zircaloy-Clad Fuel Rods", Reactortagung, Hamburg, April 1972.

37. R. A. Proebstle, et al., "The Mechanism of Defection of Zircaloy-Clad Fuel Rods by Internal Hydriding", Joint ANS/CNA Topical Meeting on Commercial Nuclear Fuel Technology Today, Toronto, Canada, April 28-30, 1975.

38. D. O. Pickman, "Internal Cladding Corrosion Effects", Advanced Course on In-Reactor Behavior of Water Reactor Fuels, Netherlands-Norwegian Reactor School (1974).

39. P. Niehoff and R. F.Von Jan, "BWR Fuel Experience 1, Correlation of Fuel Performance to Operational History", Paper No. 74, British Nuclear Energy Society, International Conference on Nuclear Fuel Performance, London, October 1973.

APPENDIX A

DETAIL OF

POOLSIDE INSPECTION PROGRAM RESULTS

Table A-1

Initial Poolside Inspection

Perforated Rod Summary

Assembly Number	Rod Position	Fuel Lot	Calculated Axial Average Rod Burnup (Mwd/MTU)	Rod Power (Shutdown)*
B-081	A14	623	12,244	1.202
	C13	623	12,454	1.259
B-079	J4	618	13,072	1.234
B-076	A12	623	9,944	1.041
B-069	B11	617	13,152	1.275
	N2	622	12,744	1.230
B-062	N12	621	12,137	1.204
	N13	621	12,112	1.207
B-037	N14	612	13,169	1.216
B-029	E14	610	11,952	1.188
B-019	D2	606	13,499	1.264
	G11	606	12,120	1.118
	K2	606	13,509	1.259
	M3	606	13,623	1.266
B-006	C13	603	13,576	1.268
B-042	N2	614	13,155	1.207
	K2	614	13,559	1.255
	A10	614	12,786	1.183

* Relative to core average of 1.

Table A-2

Maine Yankee Bundle Disassembly Program
Perforated Rod Summary

Assembly Number	Rod Position	Rod Serial Number	Fuel Lot Number	Shutdown Conditions	
				Relative Power (1)	Rod Average Burnup (MWD/MTU) (2)
B-042	K2	JBP-015	614	1.255	13559
	L2	JBP-016	614	1.264	13667
	N2	JBP-077	614	1.207	13155
	L5	JBP-048	614	1.229	13293
	G9	JBP-044	614	1.223	12896
	A10	JBP-032	614	1.183	12786
	L10	JBP-021	614	1.224	13271
	J11	JBP-033	614	1.206	13229
	B12	JBP-003	614	1.267	13629
	J12	JBP-043	614	1.224	13270
	K13	JBP-084	614	1.245	13526
B-069	N2	JCN-151	622	1.230	12744
	B11	JBY-163	617	1.275	13152
	E12	JBY-013	617	1.252	13005
	M12	JBY-145	617	1.284	13535
A-047	F7	HBV-001	516	1.073	12453
C-231	G10	KCA-109	719	0.969	9661

(1) Rod average relative to core average. Core power varied during the cycle (see Fig 1-1) and at the maximum power reached (95%), the core average linear heat generation rate was 5.6 kw/ft.

(2) Core average burnup--10,368 Mwd/MTU.

NORTH

	A	B	C	D	E	F	G	H	I	J	K	L	M	N
1		E,V	E	E						E, V	E	E	E,V	E,V
2			E	E,V				E		E,V	V	V	E,V	E,V
3		E	GT		E					E	GT		E	E,V
4	E	E, V			E	E				E, V			E,V	E
5			E	E						E	E	V,E		E,V
6	E				E		E	E, V		E				
7					E	E	GT		E					E, V
8		E, V				E			E		E		E	
9						E	E, V	E				E		
10	E, V	E,V	E	E,V	E,V				E	E	E	V,E		
11	E	E,V	GT		E, V	E		E		E, V	GT		E,V	E
12	E,V	E, V			E,V					V,E			E	E, V
13			E,V	E, V		E		E			V	E	E, V	E, V
14		E, V	E, V		E, V				E		E	E	E	

LEGEND

E EDDY CURRENT TESTED

V VISUALLY EXAMINED

PERFORATED ROD

POISON ROD

ROD NOT REMOVED

ROD SHIPPED TO HOT CELLS

GT GUIDE TUBE LOCATION

Figure A-1

ASSEMBLY B042 EXAMINATION SUMMARY

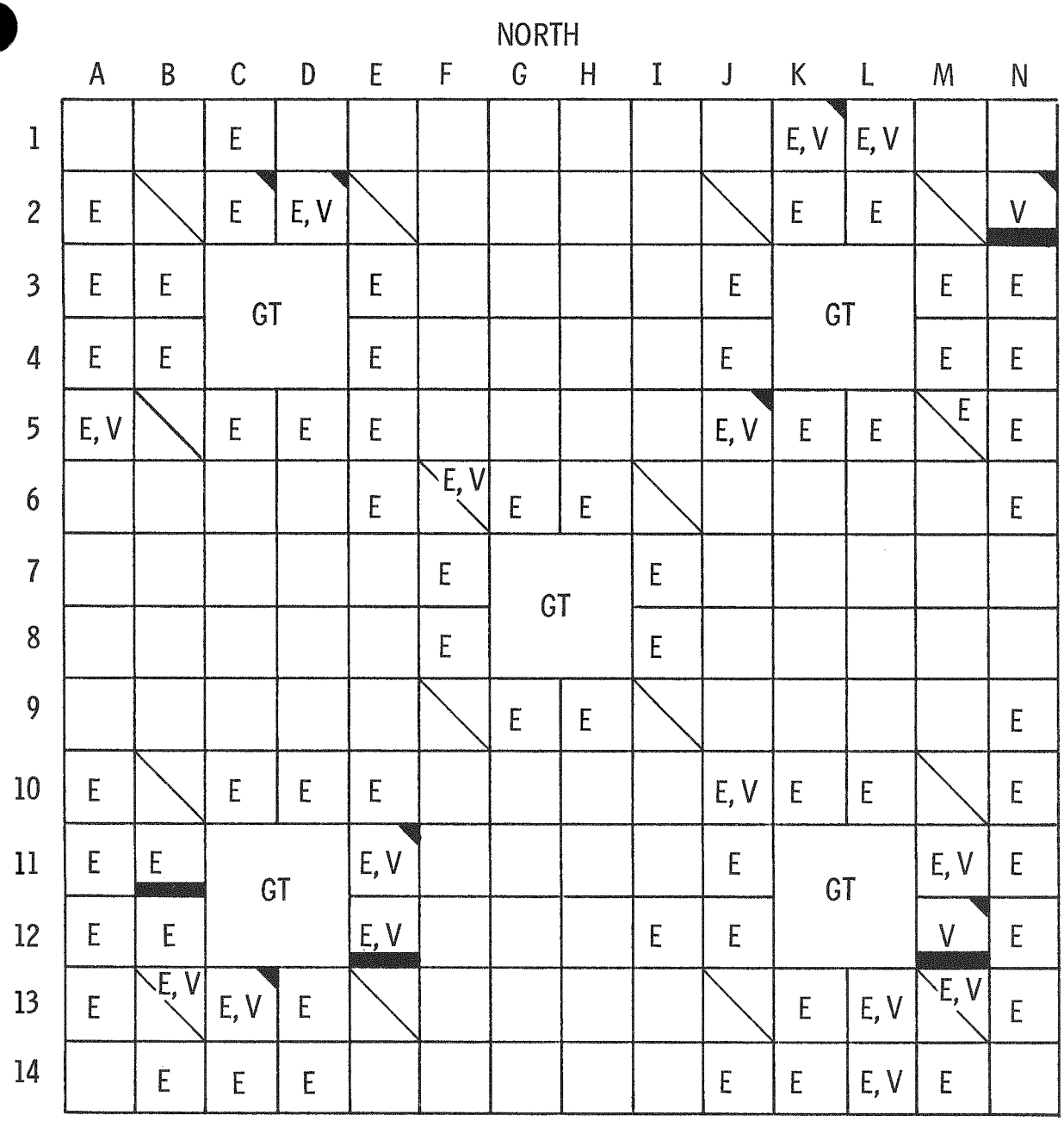

Figure A-2
ASSEMBLY B069 EXAMINATION SUMMARY

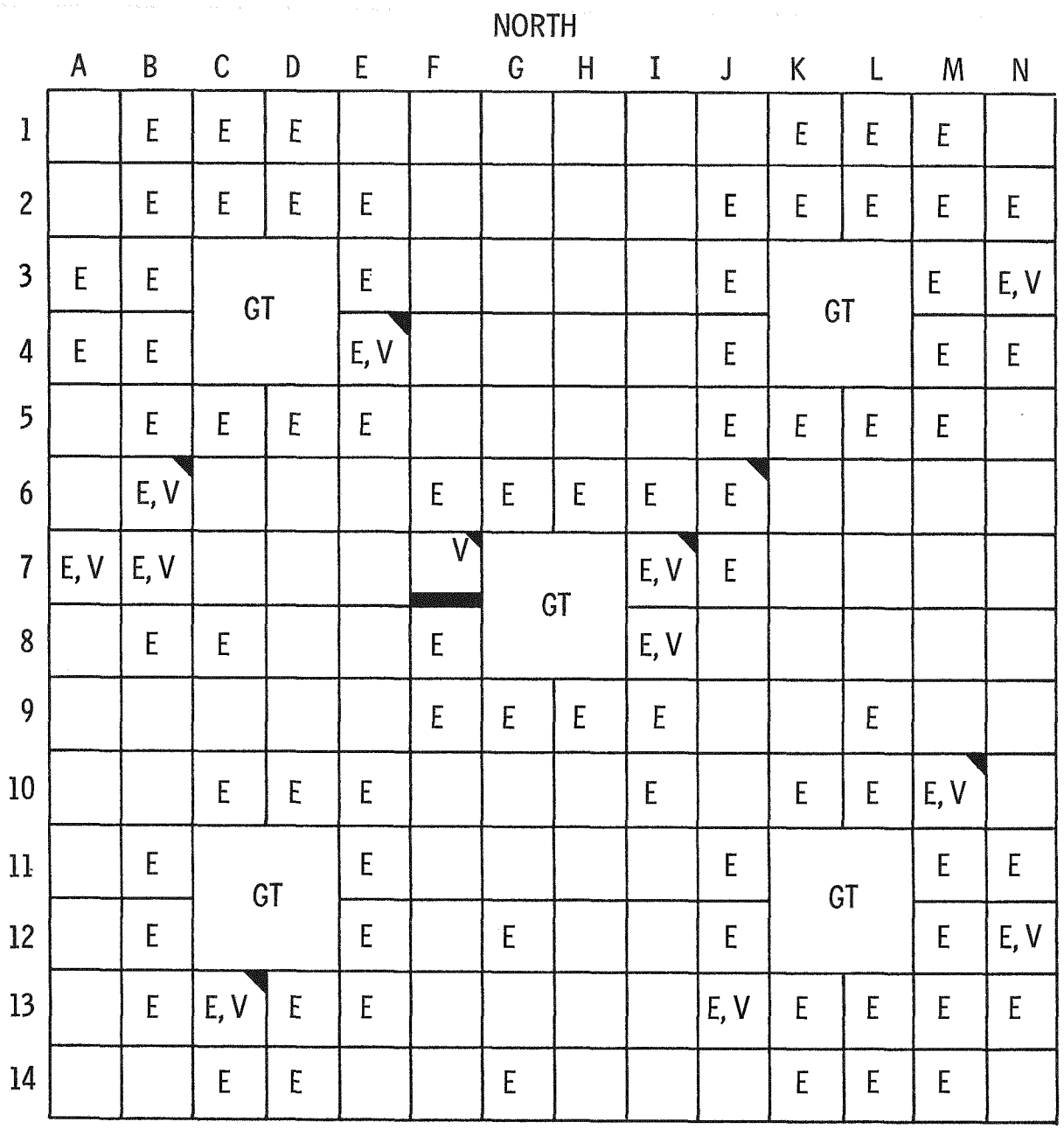

Figure A-3
ASSEMBLY A047 EXAMINATION SUMMARY

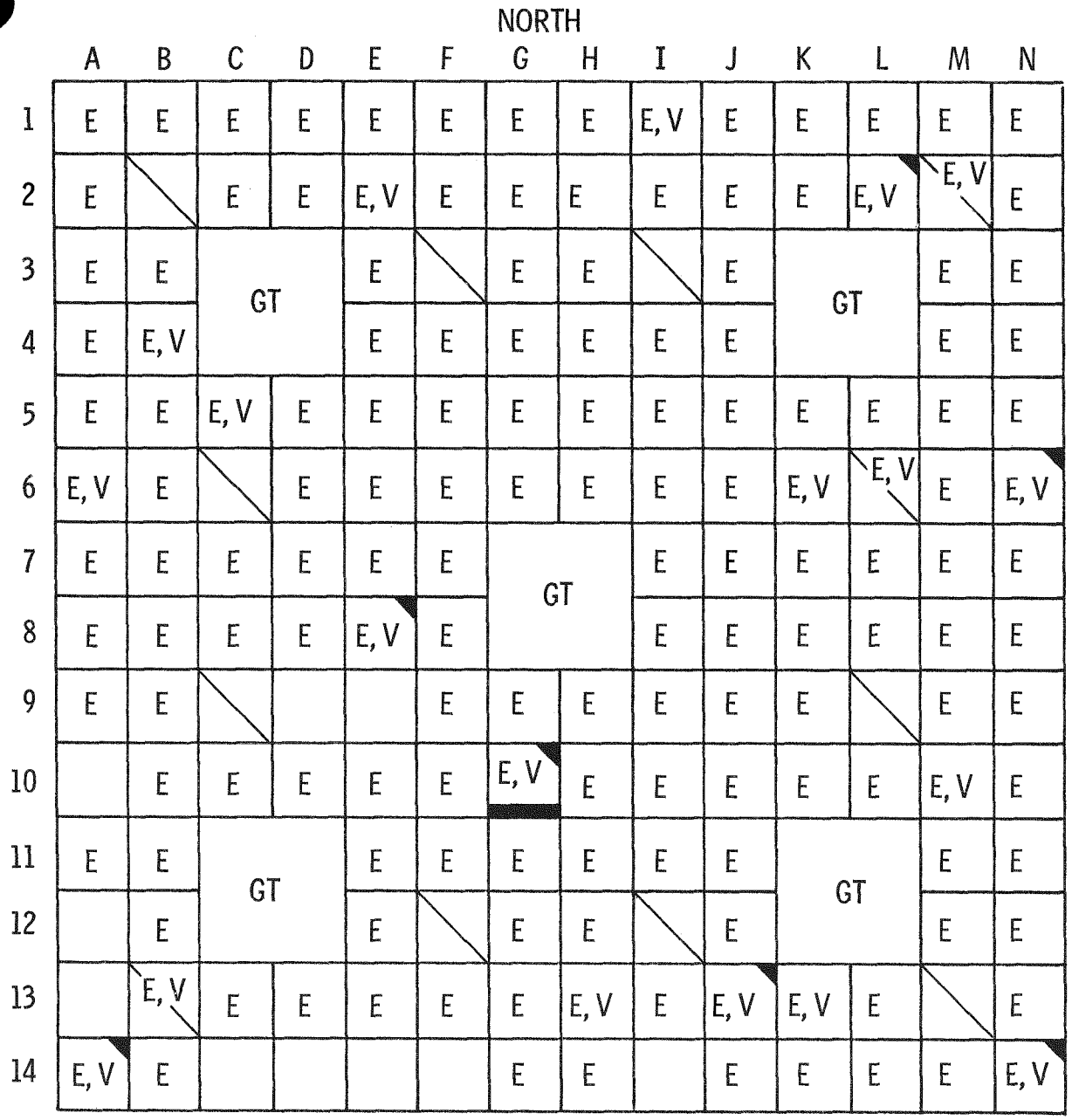

Figure A-4
ASSEMBLY C-231 EXAMINATION SUMMARY

APPENDIX B

POOLSIDE EDDY CURRENT DATA

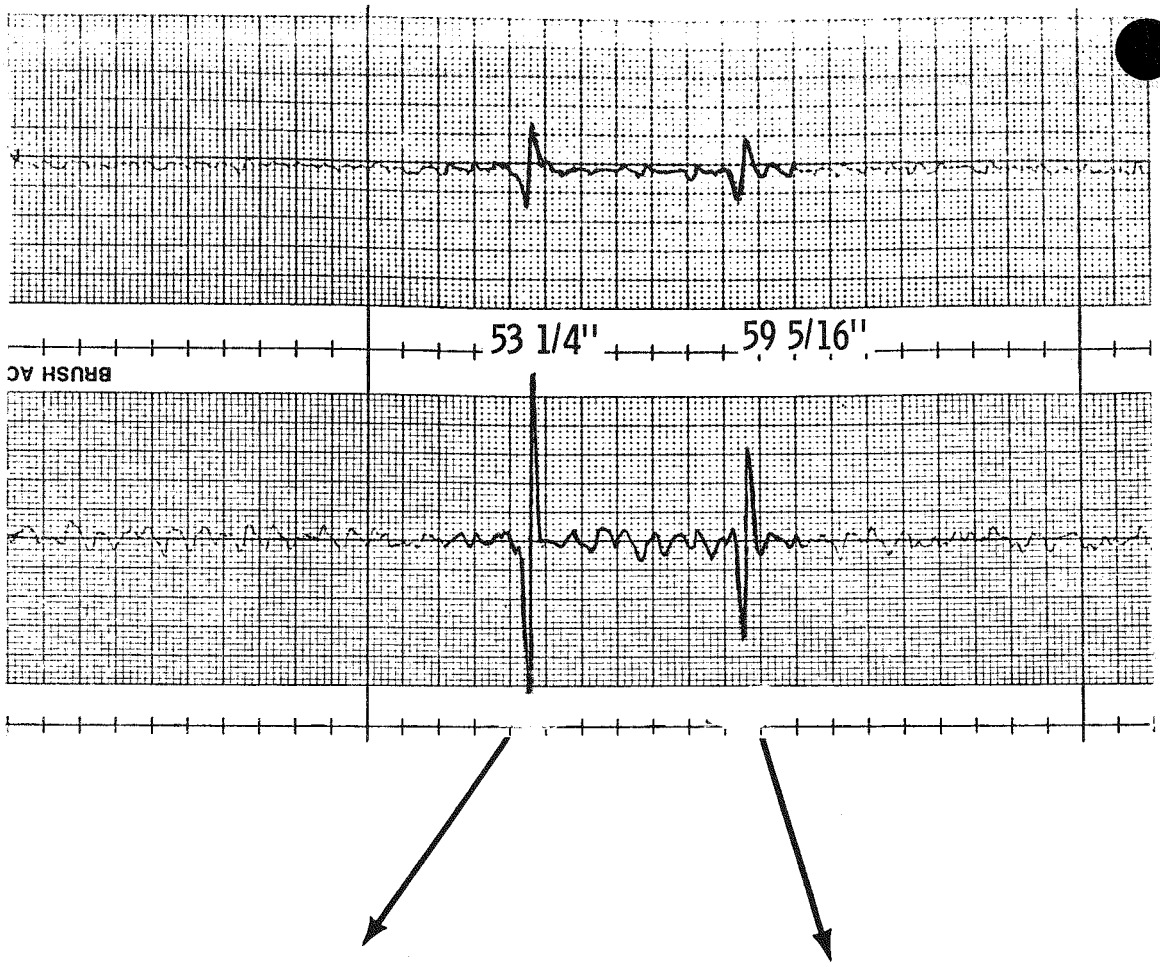

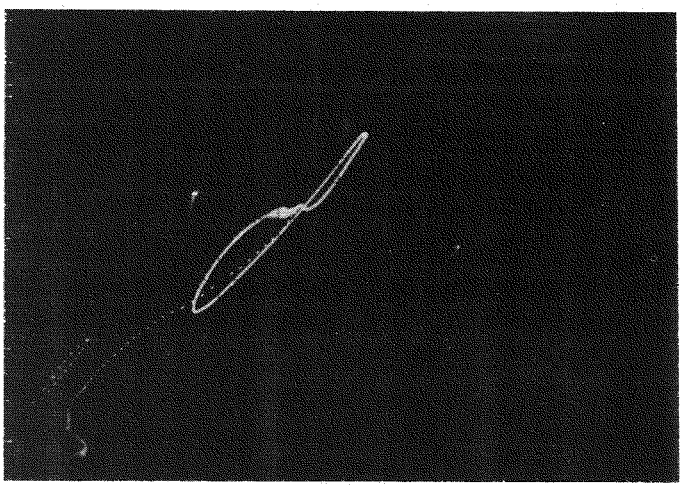

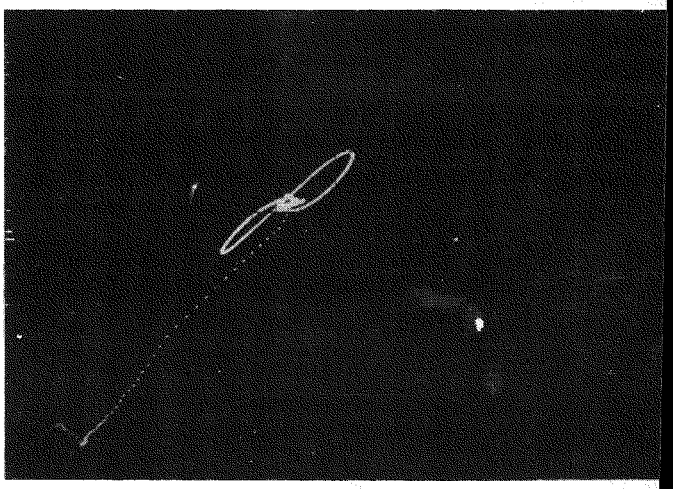

1 v/div. 100 KHZ 53 1/4" 1 v/div. 100 KHZ 59 5/16"

Figure B-1 POOLSIDE EDDY CURRENT DATA FOR ROD JBP-027 FROM B-042 SHOWING SIGNALS AT 53 1/4 AND 59 5/16 INCHES FROM THE BOTTOM OF THE ROD. (TOP - RECORDER TRACES, BOTTOM - CORRESPONDING OSCILLOSCOPE SIGNATURES)

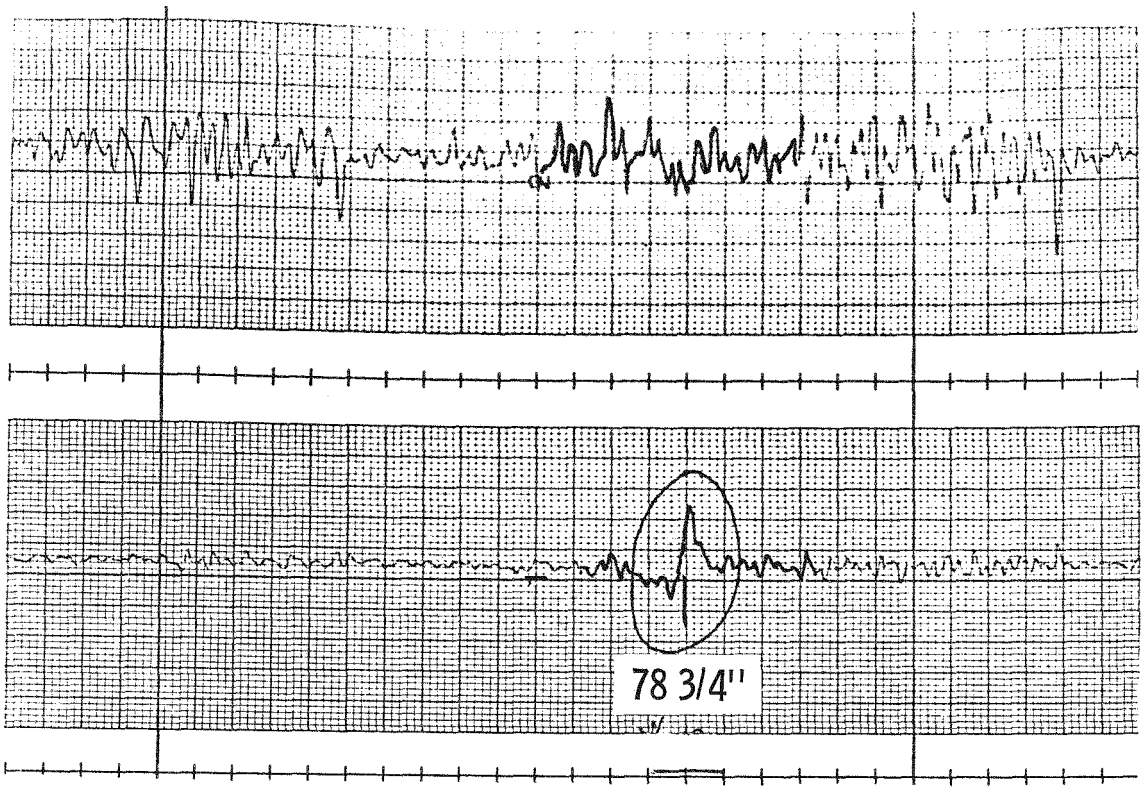

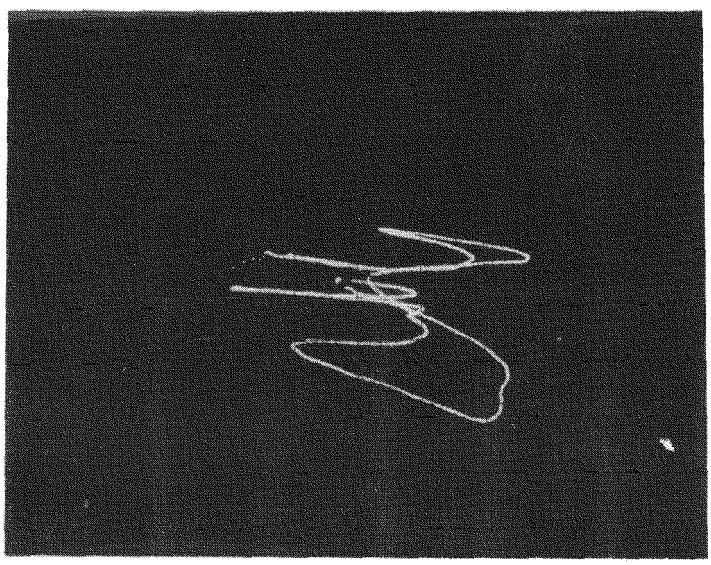

0.5 v/div. 100 KHZ 78 3/4"

Figure B-2 POOLSIDE EDDY CURRENT DATA FOR ROD JCN-182 FROM B-069 SHOWING SIGNAL AT 78 3/4 INCHES FROM THE BOTTOM OF ROD. (TOP - RECORDER TRACES, BOTTOM - CORRESPONDING OSCILLOSCOPE SIGNATURE)

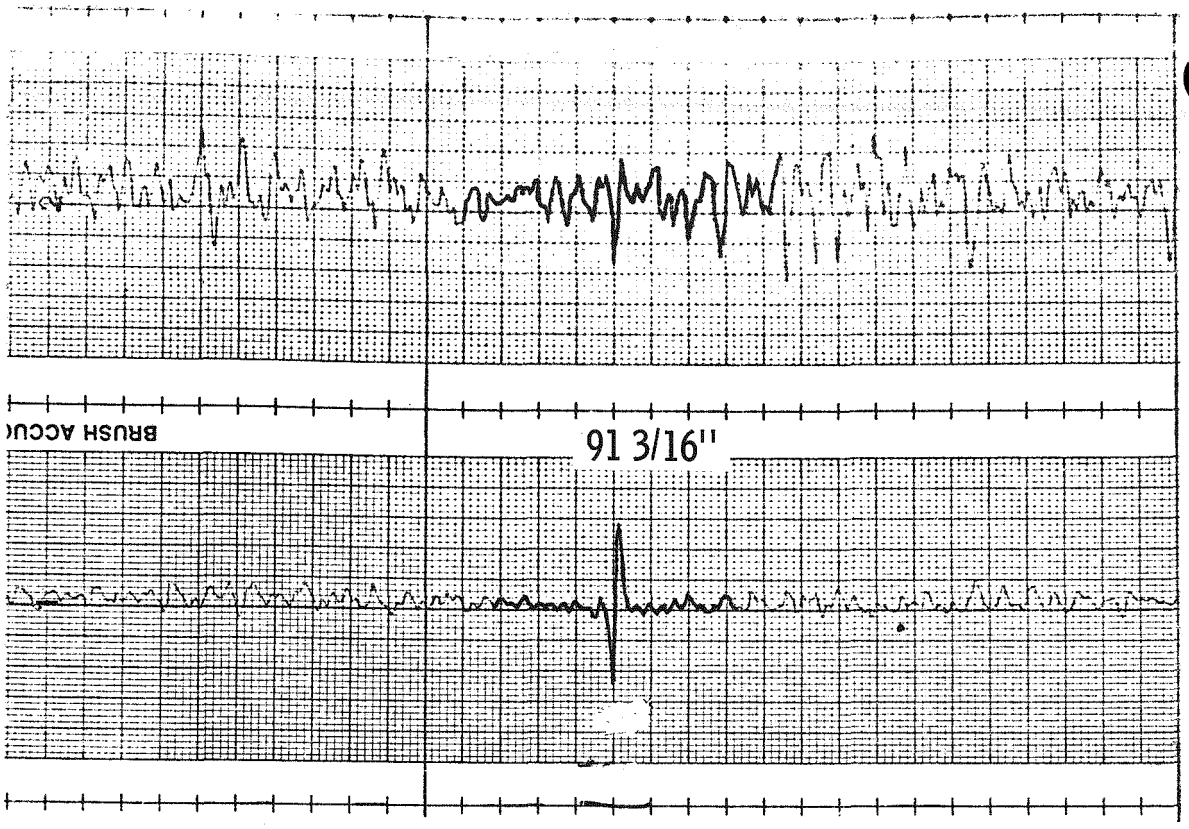

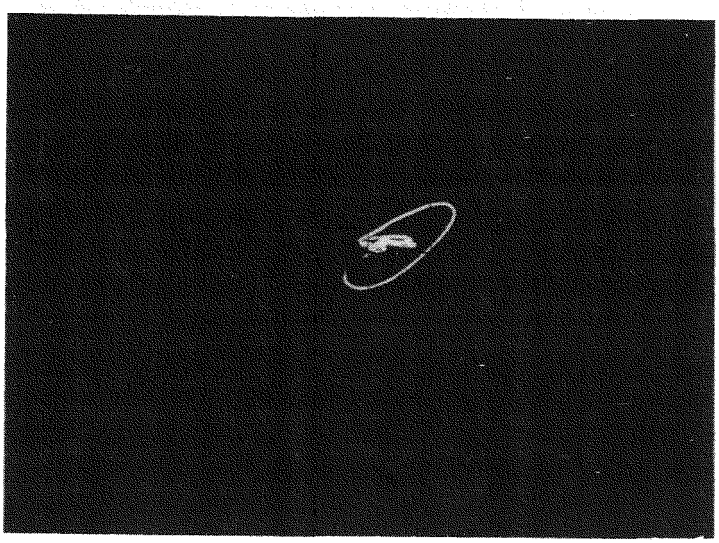

2 v/div. 100 KHZ 91 3/16"

Figure B-3 POOLSIDE EDDY CURRENT DATA FOR ROD JCN-199 FROM B-069 SHOWING SIGNAL AT 91 3/16 INCHES FROM THE BOTTOM OF THE ROD. (TOP - RECORDER TRACES, BOTTOM - CORRESPONDI OSCILLOSCOPE SIGNATURE)

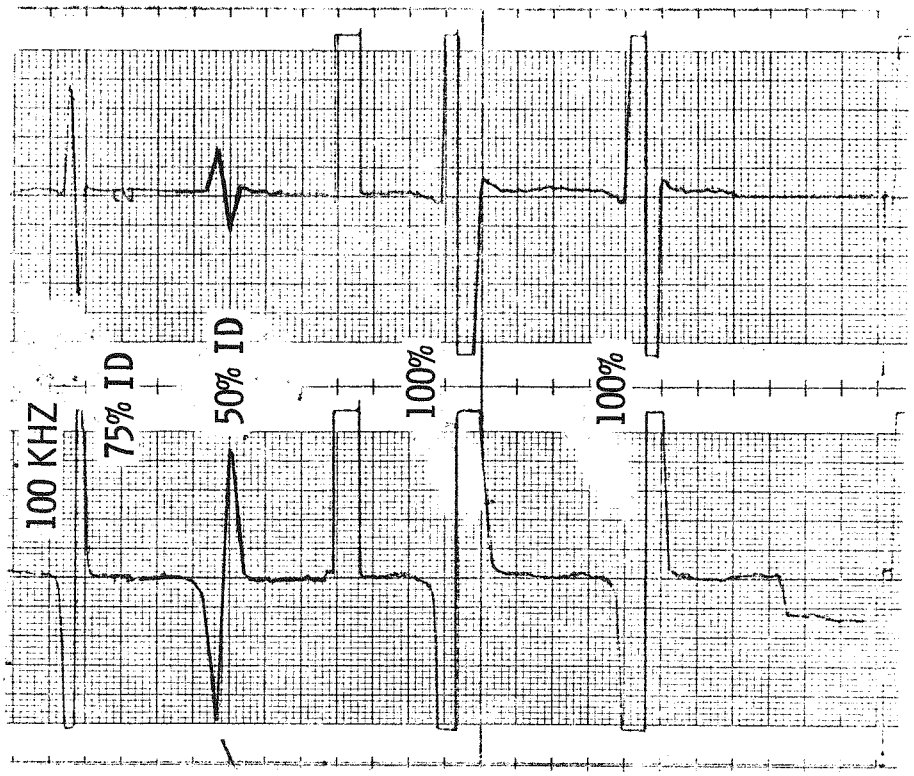

100 KHZ 50% ID TEST PHASE

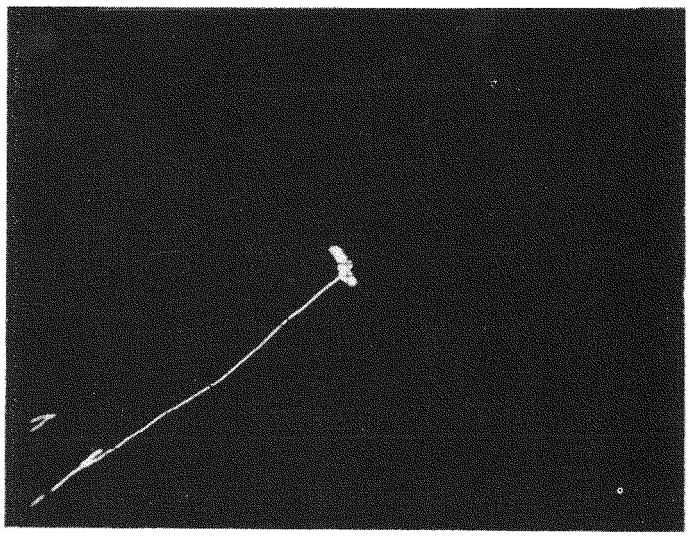

1 v/div. 1/4" LONG NOTCH

Figure B-4 POOLSIDE EDDY CURRENT SIGNAL FOR AN INTERNAL SURFACE CALIBRATION STANDARD NOTCH (50% OF WALL THICKNESS x 1/4 INCH LONG) (TOP - RECORDER TRACE, BOTTOM - CORRESPONDING OSCILLOSCOPE SIGNATURE)